Hydrogen interaction with TiC-coated metals for fusion technology application

Thesis

Hydrogen interaction with TiC-coated metals for fusion technology application

Thesis submitted by
Marco Caorlin,
dottore in Fisica (Milano),
for the degree of
Doctor of Philosophy
26 March 1992

Oxford Research Unit
Materials Discipline
The Open University

Date of submission: 26 March 1992
Date of award: 21 May 1992

A mio padre

To my father

Renato

Declaration

Part of the data and models contained in this thesis and referring to the work carried out at Ispra were published in two papers:

1. "HYDROGEN RELEASE FROM TiC-COATED METALS", by M. Caorlin, J. Camposilvan, F. Reiter, Proc. 15th SOFT, Utrecht 1988, A.M. Van Ingen, A. Nijsen-Vis, H.T. Klippel Eds., Elsevier Science Publishers, 1989, page 1057.

2. "SOLUBILITY AND DIFFUSIVITY OF HYDROGEN AND DEUTERIUM IN TZM", by S. Tominetti, M. Caorlin, J. Camposilvan, A. Perujo, F. Reiter, J. Nucl. Mater. 176-177, (1990), page 672.

Acknowledgements

This work has been made possible thanks to the financial support of the Commission of the European Communities and of the Open University which also provided access to their laboratories at Ispra and Oxford.

There are definitely many persons I feel I need to thank for providing various sorts of help over these years. It is a long list, but it is worth writing it out.

I wish to thank my supervisors, Dr N St J Braithwaite, Dr F Reiter and Dr D A Blackburn, for constant help and encouragement over all the duration of this thesis, and for proofreading this manuscript.

More in detail, I feel indebted with Dr F Reiter of JRC Ispra, who patiently followed me and gave me any type of support from the very beginning of this long dream.

Thanks also to Dr D A Blackburn, who allowed me to start the whole research project and who has always been a constant source of ideas and suggestions even after his departure.

The difficult job of Dr Nick Braithwaite, who took over as internal supervisor after Dr Blackburn had left, is acknowledged. He was essential in getting things going, in all situations, quickly and efficiently. Among other things, he also acted as an invaluable relief valve during my numerous down-and-out moments by providing me with free pub meals and laughter. For this and more I am grateful.

Thanks to Prof Gerald Elliott, Unit Director at Oxford, for patiently hosting me at the Unit laboratory and to Dr Heinz Dworschak, NFC Division Head at Ispra, for encouragement and support.

Thanks to Dr David Grant for friendship, help and hospitality well beyond his duty and to Dr Alan LeClaire for kindly providing the right contacts at Oxford and for helpful discussions.

I would also like to acknowledge the initial help by Dr Derek Cummings, who was precious with suggestions while I was working towards having the Oxford rig up and running again after a long sleep.

I also want to aknowledge the invaluable technical assistance after dramatic hardware failure of any type provided by Alan Knight and Ted Beaver at Oxford and of J Camposilvan and Gianni Cueroni at Ispra.

I need to thank Dr A Perujo and Stefano Tominetti at Ispra for running some experiments for me and for practical and moral support and M Ottaviani at JET, Culham, for helpful suggestions.

Thanks for fast and efficient computer problem-solving to the ACS advisory service at Walton Hall. Also thanks are addressed to Naomi Williams at Walton Hall and to Takao Sasaki at JRC Ispra for SEM work with my specimens. Other analysis work on the specimens by F Brossa, A Manara and M Mariotto at Ispra has to be acknowledged.

Invaluable moral support by all at the Oxford Research Unit, and particularly by Nageena, is acknowledged.

I would also like to thank Goran, Carlo, Marina, Franco, Luigi, Gabriella, Susana, Roberta and many more at JET, Culham, for additional moral support.

Abstract

The interaction of gaseous hydrogen with TiC coatings deposited on metals by Chemical Vapour Deposition was studied. The prime aim of this study was to determine whether such coatings could affect the rate of absorption and desorption by the metallic substrate. Developing and testing simple models for the experiments in terms of diffusivity D, Sieverts' constant K_s and surface reaction rates k_1, k_2, was another goal of the work. Both aims are closely linked to the use of tritium in present and future fusion devices.

Two manometric techniques were used. At Ispra, the hydrogen pressure increase in a closed vessel was recorded in time, after loading the sample with hydrogen to equilibrium and evacuating the chamber. Loading pressures between 10^3 Pa and 10^5 Pa were used, with temperatures in the range 673 K – 873 K. At Oxford, a similar equilibrium state was perturbed by an imposed periodic volume variation. The corresponding pressure response, in a closed chamber containing the specimen immersed in hydrogen, was recorded in time. Pressures between 4 Pa and 74 Pa were used and the temperature range was 883 K – 1083 K. The substrates used were the AISI 316L steel and the molybdenum alloy TZM at Ispra, while only TZM at Oxford.

With both methods, a marked increase of the times to reach equilibrium was detected with respect to uncoated samples, while the equilibrium absorption behaviour of the coated specimens was not significantly different from that of the bare ones.

Very low diffusivity values were obtained for hydrogen in TiC. For the Ispra samples, the temperature dependence found is

$$D/(\mathrm{m^2 s^{-1}}) = 1.08 \times 10^{-12} \exp\left(-\frac{6800}{T/K}\right)$$

while that determined at Oxford, for different TiC specimens, is

$$D/(\mathrm{m^2 s^{-1}}) = 9.60 \times 10^{-12} \exp\left(-\frac{6010}{T/K}\right) \ .$$

The surface rate constants determined at Ispra are represented by

$$k_1/(\mathrm{mol\,m^{-2} s^{-1} Pa^{-1}}) = 4.10 \times 10^{-8} \exp\left(-\frac{4560}{T/K}\right) \ ,$$

$$k_2/(\mathrm{m^4\,mol^{-1} s^{-1}}) = 6.90 \times 10^{-12} \exp\left(-\frac{5070}{T/K}\right)$$

and those found at Oxford by

$$k_1/(\mathrm{mol\,m^{-2} s^{-1} Pa^{-1}}) = 5.40 \times 10^{-5} \exp\left(-\frac{10250}{T/K}\right) \ ,$$

$$k_2/(\mathrm{m^4\,mol^{-1} s^{-1}}) = 2.90 \times 10^{-9} \exp\left(-\frac{5070}{T/K}\right) \ .$$

The Sieverts' constant K_s for hydrogen in TiC determined at Oxford is represented by

$$K_s/(\mathrm{mol\,m^{-3} Pa^{-1/2}}) = 2.90 \times 10^{-9} \exp\left(-\frac{5070}{T/K}\right) \ .$$

This give values lower than for the steel substrate for a factor of 200, and for the TZM substrate for a factor of 2000.

The results suggest that TiC would impede hydrogen permeation through steel more effectively in surface-limited regimes. TZM was also studied and was shown to be a possible permeation barrier itself. Trapping was also qualitatively detected in TZM.

Contents

List of Figures

Glossary

The main symbols used in this thesis are listed in the following in alphabetical order. For each symbol the number of the equation where it is first encountered is given, together with a short explanation, when possible.

Roman symbols

Symbol	Equation	Meaning
a	(4.2)	Radius of a cylindrical metal specimen
A	(2.4)	Electrical resistance calibration constant
A	(3.9)	Fit parameter in oscillating time law
A	(4.54)	Specimen surface area
a_1	(4.110)	See text (Oxford model)
a_2	(4.110)	See text (Oxford model)
A_s	(2.18)	SPRT calibration constant
A_{s1}	(5.26)	Molar mass of medium 1
A_{s2}	(5.26)	Molar mass of medium 2
B	(2.4)	Electrical resistance calibration constant
B	(3.9)	Fit parameter in oscillating time law
b_1	(4.110)	See text (Oxford model)
b_2	(4.111)	See text (Oxford model)
B_s	(2.19)	SPRT calibration constant
c	(1.1)	Hydrogen subsurface concentration
c	(1.12)	Hydrogen bulk concentration
c	(4.1)	Hydrogen bulk concentration in an infinite cylinder

$\bar{c}$	(4.6)	Average hydrogen concentration in a cylinder
C	(3.9)	Fit parameter in oscillating time law (fine offset)
$\mathcal{C}$	(4.116)	Determinant of algebraic system (Oxford model) – see text
c_1	(1.29)	Hydrogen bulk concentration in medium 1
c_{1f}	(4.48)	Hydrogen final concentration in medium 1
c_{1s}	(1.32)	Hydrogen saturation concentration in medium 1
c_2	(1.29)	Hydrogen bulk concentration in medium 2
$\bar{c}_2$	(4.45)	Average hydrogen concentration in medium 2
$c_{20}(x)$	(4.91)	Amplitude of the oscillating part of the hydrogen concentration in medium 2 (Oxford experiment)
c_{2e}	(4.87)	Hydrogen equilibrium concentration in medium 2 (Oxford experiment)
c_{2f}	(4.28)	Hydrogen final concentration in medium 2
c_{2s}	(1.32)	Hydrogen saturation concentration in medium 2
c_{eq}	(1.2)	Hydrogen equilibrium concentration in a solid
c_f	(4.3)	Hydrogen final concentration
c_i	(4.2)	Hydrogen initial concentration
c_{ji}	(4.25)	Hydrogen initial concentration in medium j
c_s	(1.17)	Hydrogen saturation concentration
d	(4.25)	Coating thickness
D	(1.12)	Hydrogen diffusivity in a solid
$\mathcal{D}$	(4.134)	Determinant of algebraic system (Oxford model) – see text
$\mathcal{D}_0$	(4.153)	Auxiliary parameter, Oxford model – see text
D_0	(1.15)	Hydrogen diffusivity pre-exponential coefficient
D_1	(1.29)	Hydrogen diffusivity in medium 1
$\mathcal{D}_1$	(4.154)	Auxiliary parameter, Oxford model – see text
D_2	(1.29)	Hydrogen diffusivity in medium 2
$\mathcal{D}_2$	(4.155)	Auxiliary parameter, Oxford model – see text
D_{app}	(1.127)	Apparent hydrogen diffusivity in a solid
$\mathcal{D}_E$	(4.156)	Auxiliary parameter, Oxford model – see text

$D(R)$	(2.12)	Discriminant for temperature calculation
E	(1.37)	Young's modulus of the coating
E_C	(1.5)	Hydrogen sticking activation energy
f	(3.9)	Fitting time law for oscillating quantities
f_1	(5.27)	Pressure term - contribution to final pressure
f_2	(5.27)	Pressure term - contribution to final pressure
$F(x)$	(4.9)	Hydrogen release function, Ispra DL model
$F(x)$	(4.104)	See text (Oxford model)
$F_1(t/\tau_d)$	(4.44)	Hydrogen normalised concentration in medium 1
$F_2(t/\tau_d)$	(4.46)	Hydrogen normalised average concentration in medium 2
G	(1.6)	Gas atom
G_2	(1.6)	Gas molecule
$G(x)$	(4.105)	See text (Oxford model)
$G(x, t/\tau_d)$	(4.40)	Normalised hydrogen concentration in medium 2
h	(4.7)	Cylinder height
$H(x)$	(4.106)	See text (Oxford model)
H_d	(6.1)	Diffusion-limited hydrogen permeation reduction factor
H_s	(6.3)	Surface-limited hydrogen permeation reduction factor
i^-	(1.29)	Interface location approached from medium 1
i^+	(1.29)	Interface location approached from medium 2
$I(x)$	(4.107)	See text (Oxford model)
I_y	(3.11)	Generalised amplitude for oscillating quantity y
j	(1.21)	Hydrogen permeation flux through a foil
j_d	(6.1)	Diffusion-limited flux through a bilayer foil
J_d	(1.12)	Hydrogen diffusive flux in a solid
J_n	(4.4)	Bessel function of the first kind and order n
J_s	(1.1)	Hydrogen stationary flux through a solid surface
k^0	(5.16)	Partition factor at $p_0 = 0$ (Ispra)
K_0	(1.3)	Sieverts' constant pre-exponential factor

k^1	(5.16)	Pressure coefficient of the partition factor k (Ispra)
k_1	(1.1)	Surface absorption rate constant
k_1'	(6.4)	Surface absorption rate constant of the downstream side of a permeation membrane
$k_1{}^*$	(4.82)	Normalised surface absorption rate constant
k_2	(1.1)	Surface desorption rate constant
k_3	(1.31)	Interface reaction rate constant
k_4	(1.31)	Interface reaction rate constant
k	(1.30)	Partition coefficient
k_A	(1.17)	Trapping rate constant
k_B	(1.17)	Detrapping rate constant
k^B	(1.8)	Boltzmann's constant
K_s	(1.2)	Sieverts' constant
K_s^*	(4.83)	Normalised Sieverts' constant
$K_{s,app}$	(1.27)	Apparent Sieverts' constant
ℓ	(1.21)	Permeation foil thickness
ℓ_1	(6.2)	Thickness of medium 1 in a permeation foil
ℓ_2	(6.2)	Thickness of medium 2 in a permeation foil
m	(1.16)	Mass of a diffusing species
m_V	(4.89)	Volume modulation factor
N	(1.17)	Number of traps per unit volume of a solid
$\mathcal{N}$	(4.152)	Auxiliary parameter, Oxford model – see text
N_A	(1.17)	Avogadro's number
p	(1.1)	Hydrogen partial pressure
P	(3.1)	Normalised hydrogen partial pressure
p_0	(4.21)	Hydrogen loading pressure
p_0	(4.94)	Pressure oscillation amplitude (Oxford)
p_1	(1.21)	Upstream hydrogen partial pressure
p_1	(2.1)	Hydrogen pressure before expansion
p_2	(1.21)	Downstream hydrogen partial pressure
p_2	(2.1)	Hydrogen pressure after expansion
p_b	(3.7)	Hydrogen pressure in a blank run

p_c	(4.55)	Integration constant (a pressure term)
p_e	(4.87)	Hydrogen equilibrium pressure in medium 2 (Oxford experiment)
p_f	(4.21)	Hydrogen final pressure
P_f	(4.20)	Normalised hydrogen final pressure
p_i	(4.56)	Hydrogen initial pressure
P_i	(4.15)	Normalised hydrogen initial pressure, before pumpdown
p_L	(4.73)	Ultimate pressure of the vacuum system
p_{min}	(5.2)	Pressure corresponding to minimum of parabola – see text
p_n	(3.7)	Hydrogen net pressure
P_r	(4.14)	Normalised hydrogen residual pressure, after pumpdown
q	(4.103)	See text (Oxford model)
Q	(2.3)	Activation molar energy of diffusion
Q_1	(5.27)	Hydrogen heat of solution in medium 1
Q_2	(5.27)	Hydrogen heat of solution in medium 2
Q_s	(1.3)	Hydrogen heat of solution
Q_d	(1.15)	Hydrogen activation energy for diffusion in a solid
r	(4.1)	Radial coordinate in a cylindrical system
R	(1.3)	Gas constant
$R(\theta')$	(2.4)	Electrical resistance of a metal at the temperature θ'
R_{H_e}	(4.144)	Ratio of pseudo-volume to equilibrium volume (Oxford)
R_i	(2.21)	Impurity-dependent part of electrical resistance
R_o	(2.4)	Electrical resistance of a metal at 0 °C
R_{os}	(2.17)	Ice-point resistance of the SPRT
R_T	(2.21)	Temperature-dependent part of electrical resistance
s	(1.4)	Hydrogen sticking coefficient
S	(1.22)	Hydrogen solubility

s_0	(1.5)	Hydrogen sticking coefficient pre-exponential factor
S_0	(5.1)	Hydrogen residual solubility in TZM
$S_P(p)$	(4.73)	Pumping speed
t	(1.13)	Time
t_b	(3.5)	Pressure reading time in a blank run
t_B	(3.3)	Base time for pressure readings
t_i	(3.9)	i-th time reading
t_n	(3.6)	Pressure reading time in a net P vs t curve
t_R	(3.3)	Release time
t_{RH}	(3.4)	Rescaled release time
T	(1.3)	Temperature
T	(4.86)	Temperature in the cold part of the experimental chamber (Oxford rig)
T_1	(2.1)	Hydrogen temperature before expansion
T_2	(2.1)	Hydrogen temperature after expansion
T_A	(3.1)	Temperature in the hot part of the Ispra rig
T_B	(3.1)	Temperature in the cold part of the Ispra rig
T_N	(3.1)	Normalising temperature for the Ispra rig
u	(4.50)	Modified partition factor
U	(2.1)	Reference volume
U	(4.68)	Surface model parameter (Ispra SL model)
$\mathcal{U}_1$	(4.150)	Auxiliary parameter, Oxford model – see text
$\mathcal{U}_2$	(4.151)	Auxiliary parameter, Oxford model – see text
V	(2.1)	Experimental chamber volume of the Ispra rig
V_0	(4.88)	Amplitude of the volume oscillation (Oxford experiment)
V_1	(4.47)	Substrate volume (medium 1)
V_2	(4.47)	Coating volume (medium 2)
V_A	(3.1)	Volume of the hot part of the Ispra rig vessel
V_B	(3.1)	Volume of the cold part of the Ispra rig vessel
V_e	(2.31)	Equilibrium volume, Oxford rig
V_{H_2}	(4.143)	Pseudo-volume (Oxford)

V_s	(4.6)	Cylindrical specimen volume
$V(t)$	(4.88)	Temporal law for the volume oscillation (Oxford experiment)
$\mathcal{W}_1$	(4.148)	Auxiliary parameter, Oxford model – see text
$\mathcal{W}_2$	(4.149)	Auxiliary parameter, Oxford model – see text
$W(\theta')$	(2.5)	Normalised resistance at the temperature θ'
$W_s(\theta')$	(2.22)	SPRT normalised resistance at the temperature θ'
x	(1.12)	Spatial coordinate in a solid
X	(4.128)	Auxiliary parameter (Oxford) – see text
x_i	(3.8)	i-th reading of the generalised independent variable
y	(3.8)	generalised dependent variable
Y	(4.129)	Auxiliary parameter (Oxford) – see text
y_i	(3.8)	i-th reading of the dependent variable y
$y(x)$	(4.92)	See text (Oxford model)
z	(1.17)	Concentration of trapped hydrogen
z	(4.7)	Axial coordinate in a cylindrical system
$z(x)$	(4.93)	see text (Oxford model)
Z	(2.20)	Cragoe's function
z_e	(1.22)	Equilibrium concentration of trapped hydrogen

Greek symbols

Symbol	Equation	Meaning
α	(2.5)	Callendar's equation coefficient
α	(4.130)	Coefficient of algebraic system (Oxford)
α_n	(4.4)	n-th zero of the Bessel function J_0
α_s	(2.18)	Callendar's equation coefficient for the SPRT
β	(4.131)	Coefficient of algebraic system (Oxford)
β	(5.14)	Fit parameter in the Ispra SL model
γ	(4.146)	Flow regime number (Oxford)
γ	(5.26)	Sieverts' constant when solubility expressed

		in atomic fraction
δ	(2.5)	Callendar's equation coefficient
Δp	(4.77)	Pressure term from hydrogen desorbed and lost to the pumps
ΔP	(4.17)	Normalised pressure term from hydrogen desorbed and lost to the pumps
ΔP_d	(4.16)	Normalised pressure rise caused by gas release
ΔP_p	(4.16)	Normalised pressure drop caused by pumpdown
δ_s	(2.19)	Callendar's equation coefficient for the SPRT
Δt	(4.14)	Pumpdown duration
ΔT	(1.37)	Temperature change
ΔT	(2.3)	Temperature measurement resolution
$\Delta \alpha$	(1.37)	Thermal expansion coefficients difference
$\Delta \theta'$	(2.10)	Temperature correction
ϵ	(1.8)	Ratio of number of absorption sites to number of host atoms
ϵ	(4.88)	Empirical phase difference (Oxford experiment)
ε	(3.5)	Time tolerance
η	(1.8)	Hydrogen concentration in atomic fraction
η_1	(5.24)	Hydrogen solubility in medium 1, in atomic fraction
η_2	(5.24)	Hydrogen solubility in medium 2, in atomic fraction
θ	(2.11)	Corrected temperature in degrees °C
θ	(4.7)	Angular coordinate in a cylindrical system
θ	(4.138)	Phase advance (Oxford)
θ_1	(2.20)	Corrected temperature in degrees °C
θ_2	(2.20)	Corrected temperature in degrees °C
θ'	(2.4)	Temperature in degrees °C
λ	(4.120)	Auxiliary angle (Oxford) – see text
Λ	(4.124)	Amplitude ratio – Oxford model
μ_g	(1.7)	Gas chemical potential (gaseous phase)

μ_{0g}	(1.9)	Gas chemical potential reference value (gaseous phase)
μ_s	(1.7)	Gas chemical potential (dissolved phase)
μ_{s0}	(1.8)	Gas chemical potential reference value (dissolved phase)
μ_{s01}	(5.23)	Gas chemical potential reference value (dissolved phase) in medium 1
μ_{s02}	(5.23)	Gas chemical potential reference value (dissolved phase) in medium 2
ν	(1.37)	Poisson's ratio of the coating
ν	(3.9)	Oscillation frequency in the Oxford experiment
π	(3.9)	Length to diameter ratio for a circle
ρ	(2.29)	AISI 316L steel density
ρ_{s1}	(5.26)	Density of medium 1
ρ_{s2}	(5.26)	Density of medium 2
σ	(1.37)	Amount of stress on the coating
σ_i	(3.8)	Standard deviation of i-th measurement y_i
σ_R	(2.14)	Standard deviation of resistance R
$\sigma(x)$	(4.121)	Auxiliary angle (Oxford) – see text
σ_θ	(2.16)	Standard deviation of temperature θ
τ_d	(4.4)	Diffusion characteristic time in a cylinder (Ispra)
τ_d	(4.41)	Diffusion characteristic time in a coating (Ispra)
τ_d	(4.142)	Diffusion characteristic time in a coating (Oxford)
τ_s	(4.62)	Surface release characteristic time (Ispra)
τ_s	(4.145)	Surface characteristic time (Oxford)
τ_s^0	(4.71)	Limit as $p_0 \to 0$ of the surface release characteristic time (Ispra)
ϕ	(1.4)	Hydrogen sticking kinetic constant
ϕ	(4.94)	Phase lag of pressure with respect to volume oscillation (Oxford)
Φ_1	(6.1)	Hydrogen permeability of medium 1
Φ_2	(6.2)	Hydrogen permeability of medium 2

$\phi_2(x)$	(4.91)	Phase of the oscillating part of the hydrogen concentration in medium 2 (Oxford)
ϕ_y	(3.10)	Generalised phase for oscillating quantity y
χ^2	(3.8)	Sum of squared residues
Ω	(4.88)	Angular frequency of the volume oscillation (Oxford experiment)

Chapter 1

Introduction

This thesis deals with the interaction of gaseous molecular hydrogen with titanium carbide (TiC) -coated metals and comprises six chapters.

The work has been carried out at the Joint Research Centre of the Commission of European Communities, Ispra Establishment (Italy) and at the Oxford Research Unit of the Open University, Oxford (UK). Two different experimental techniques have been used, therefore some of the chapters have been split into two parts. Nevertheless, the same basic principles have been used for the mathematical modelling of the experiments. In addition, some results obtained at Ispra have been used as a starting point in the experiments carried out at Oxford.

An outline of key general background topics is presented in this introductory chapter, together with the goals of the work. The second chapter describes the experimental facilities used, while chapter 3 details the methods and procedures used with each rig. Then chapter 4 presents the mathematical models, with analytical solutions, used for interpreting the experiments and based on the theory given further on in this introduction. Results of the experiments are detailed and discussed in the fifth chapter and a final chapter is devoted to the conclusions.

The material contained in this introduction provides background information on data and theory in the field of hydrogen-material interactions that are relevant to this work.

To create this basis of information the reasons and interests for this work are explained. A survey of the basic ideas about hydrogen-solid interactions is given and a mathematical description of the main processes involved is provided. Data

from the relevant literature are briefly reviewed, with attention only to experimental data for key materials. The goal of the work is explained and the means used to this end are anticipated.

1.1 General background

There are many reasons to carry out experimental and theoretical research in the field of hydrogen-materials interaction since hydrogen isotopes are present in a wide variety of technological processes as background, as catalyser and/or as main components. The susceptibility of several materials to the absorption of hydrogen isotopes and to their permeation is an incentive for this study, especially for metals and alloys which can suffer hydrogen embrittlement. There is a special interest in the case of tritium, the artificial, therefore expensive, radioactive isotope which decays to yield helium. The introduction of helium in metals via tritium decay is much more detrimental from the point of view of embrittlement owing to the low solubility of helium in metals coupled to its tendency to agglomerate forming bubbles and blisters which contribute to degrade the integrity of the metal.

This is all the more true for thermonuclear fusion devices, where the fuel is a high temperature deuterium-tritium plasma. As a result, energetic deuterium and tritium atoms and ions can enter the confinement structures by implantation. This leads to loss of fuel, erosion and radiation damage of the structures, hydrogen and helium embrittlement of metallic components, loss of radioactive compounds such as tritiated water (HTO) to the outside, contamination of the plasma discharge by eroded wall material and subsequent cooling by high Z (atomic number) bremsstrahlung. In addition, tritium produced in the breeding blanket by neutrons interacting with lithium nuclei is bound to enter the metal structures and to be lost to the outside.

Tritium inventory in the metallic components should be kept under close control throughout the fusion reactor lifetime, bearing in mind the risk of accidents and the need for maintenance.

It is also evident that means should be sought to impede the penetration of hydrogen isotopes into metal components and the permeation through them to the outside. This is required for any fusion reactor, but particularly for future designs

that will call for the use of vanadium-titanium alloys, with the aim of reducing the amount of long-lived induced radioactive products. In fact, vanadium and titanium can absorb enormous amounts of hydrogen, for instance up to two hydrogen atoms per titanium atom.

For fusion device applications there is a strong need to predict and control the deuterium/tritium Inventory in, Permeation through and Recycling from the structures, where in general I and P should be minimised. Computer codes have been devised to simulate possible fusion reactor operation and have been used to predict and control IPR. Recent work with the PERI code by Saibene and co-workers ([1] and references therein), has shown that an encouraging agreement can be obtained between experiment and numerical simulation for deuterium discharges in the beryllium-covered JET[1] device.

Codes such as PERI rely on basic data as input parameters, which can be determined in well-controlled laboratory-scale experiments. These experiments would also improve the understanding of the key processes and would allow one to test simple models so as to be able to scale the acquired knowledge to realistic fusion device conditions.

Many of the above considerations also apply in general to other situations where hydrogen is part of the process environment.

The goal of this work is to carry out experiments and to develop simple models for materials which can possibly impede the absorption/release and permeation of hydrogen. Carbides and oxides, e.g. alumina (Al_2O_3) are known to act as a barrier to the permeation of hydrogen. However, they are generally brittle and tend to develop cracks and to spall under thermal cycling. Furthermore, oxides may be unstable in a hydrogen environment.

For these reasons this work is devoted to carbides and in particular to titanium carbide, TiC, for which the published data are by far much scarcer than those for oxides.

Owing to its high hardness and wear resistance, TiC is widely used in the coating deposition industry and is often used as a compliance interlayer between metallic

[1]JET is the acronym of Joint European Torus, the leading thermonuclear fusion experiment in Europe, located at Culham, Oxfordshire, UK, and financially supported by european countries and by the Commission of the European Communities.

substrates and harder carbides, such as silicon carbide, SiC.

1.2 Modelling hydrogen-materials interaction

The main phenomena occurring when a mixture of gaseous hydrogen and energetic hydrogen plasma encounters a solid are shown in a simplified way in Figure 1.1.

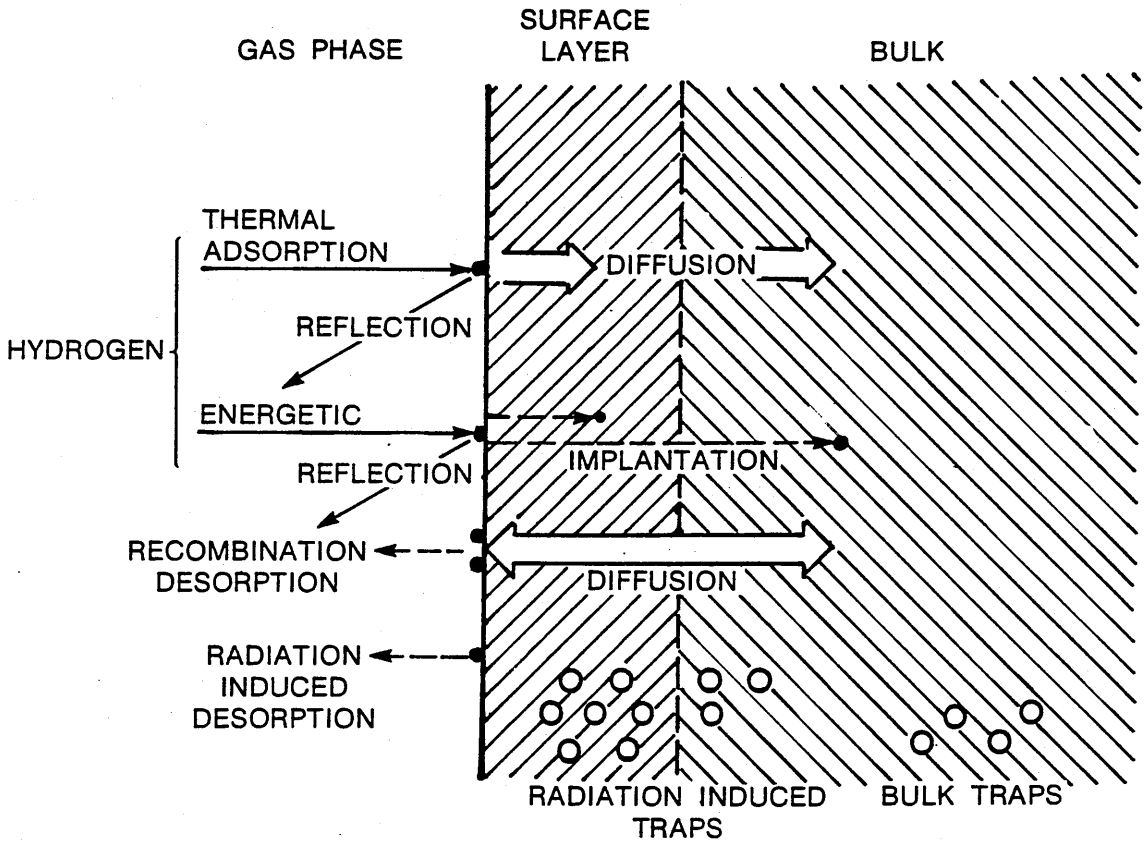

Figure 1.1 Simplified picture of the processes involved in the interaction of a hydrogen plasma and gas mixture with a solid (based on [2]).

The surface of a solid is generally defined as the two-dimensional interfacial boundary between the solid and the gas/plasma phase. The physical properties of all solids vary with the depth into the solid, down to a depth at which these properties become those of the bulk of the solid and are on average constant in space. In other words, a layer exists just below the two-dimensional surface of the

solid and is markedly different from the bulk of the solid. This layer is referred to as a 'surface layer' as indicated in Figure 1.1 and is due to several causes, such as modification by implantation and natural oxide formation, or deposition of a coating layer.

The layer is some 100 Å thick in the case of natural oxides or implantation, depending on the experimental conditions, but may be much thicker for purposely deposited coatings. It is not uniform, since oxides preponderate in the outermost region and the density of the implanted products diminishes with depth after first passing through a maximum.

As shown in Figure 1.1, some of the hydrogen impinging on the surface is reflected, while some of the energetic fraction may penetrate into the solid and be implanted. Part of the thermal hydrogen is adsorbed on the surface and can jump into the subsurface from where, as can occur to the implanted part, it can then migrate towards the bulk of the solid or back towards the surface. On adsorption, dissociation of hydrogen molecules can take place at the surface where also recombination of atoms into molecules prior to desorption occurs. Energy and momentum transmitted by impinging particles and radiation can stimulate and enhance the desorption of single atoms without the need of recombination.

From the wealth of processes mentioned, which occur on or through the surface and in the 'surface layer' it is evident that the surface and the surface layer are important since they may affect the dynamics of the interaction between hydrogen and the material. Through suitable modification of the surface and of the surface layer it may be possible to intervene to modify the way hydrogen interacts with the solid.

The work reported here is only concerned with thermal hydrogen molecules impinging on a solid surface, hence the effects of implantation are not dealt with. In this way, both experiments and models are considerably simplified. The work is nevertheless useful and relevant to fusion and hydrogen plasma applications since in similar environments diffusion and bulk processes, as well as surface recombinative desorption, will be present for example as soon as the discharge is switched off. Complicating effects caused by implantation can then be studied subsequently, once enough knowledge has been obtained from simpler gas-material work such as this

one.

In general, the behaviour of gaseous thermal hydrogen in contact with metals is governed by two groups of processes:

1. those taking place on and through the two-dimensional surface of the sample which are referred to as **surface processes** and

2. those occurring in the bulk of the sample and are therefore referred to as **bulk processes.**

The latter class includes interstitial and grain boundary diffusion caused by concentration gradients, thermomigration or Soret effect and trapping at defects.

Both classes are included in Figure 1.2, where the potential energy of hydrogen in an endothermic occluder is shown as a function of the penetration depth in the metal, referred to half the energy of a gaseous hydrogen molecule at rest. The level represented by the dashed top line and labelled H, is that of a hydrogen atom at rest in the gaseous phase (half a dissociated H_2 molecule), while the level represented by a solid horizontal line on the left side of the figure is that of half a H_2 molecule. The energies U_s, $2U_m$, U_d, U_c, U_t and U_p are associated respectively to solution in the metal lattice, dissociation of a gas molecule, bulk diffusion, adsorption, trapping and precipitation as hydride or in clusters. According to the sign of the solution enthalpy U_s, the metal is classified as an **endothermic** ($U_s > 0$) or an **exothermic** ($U_s < 0$) occluder of hydrogen.

In the following sections, a mathematical description of the hydrogen fluxes associated with surface and bulk processes is given, which also defines the nomenclature adopted throughout this work. In particular, bulk diffusion, trapping at defects and solid-to-solid interface reactions are dealt with in the section on bulk processes.

1.2.1 Surface processes

Surface processes is a broad term, used to indicate all processes that take place on and through the two dimensional surface of a solid. They include for example adsorption, desorption, jumping into solution and back from bulk solution sites into the surface. Figure 1.3 outlines the main surface processes and gives expressions for the fluxes associated with them.

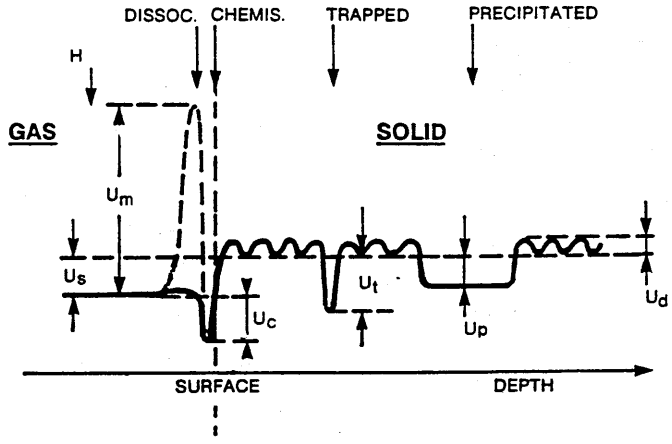

Figure 1.2 Variation of the potential energy with depth into a metal (based on [3]).

According to such a picture, a hydrogen molecule splits into two atoms on the surface, process (1), before entering the bulk, process (3), while the reverse processes (2) and (4) take place on the way back to the gas phase. In Figure 1.3, **c** represents the subsurface atomic hydrogen concentration, **p** is the molecular hydrogen partial pressure. The surface coverage $\theta = N_H/N_s$ is defined as the ratio of the number N_H of adsorbed H atoms to the number N_s of adsorption sites. Processes (5) to (8) in Figure 1.3 are only important for high values of the coverage θ. Notice that the coverage θ cannot exceed 1, i.e. $\theta_{max} = 1$ when all the adsorption sites are occupied. Processes (5) and (6) have been shown [5] to be responsible for the permeation's through a foil being proportional to $\sqrt{p}$ even at very high pressures, when the surface has become saturated with adsorbed atoms. The kinetic parameters k_j, where j=1,2,...,8 are dependent only on temperature.

The hydrogen flux J_s across the specimen surface is defined as the amount of hydrogen crossing that surface per unit time and area. All of the fluxes shown in Figure 1.3 should be accounted for in order to obtain an expression for J_s, but a simpler and more effective version is

$$J_s = k_1 p - k_2 c^2 \ , \tag{1.1}$$

where p is the H_2 partial pressure and c the H subsurface concentration. Here, the net current density J_s is computed as the difference between the dissociative adsorption and recombinative desorption rates. It can be interpreted as the rate

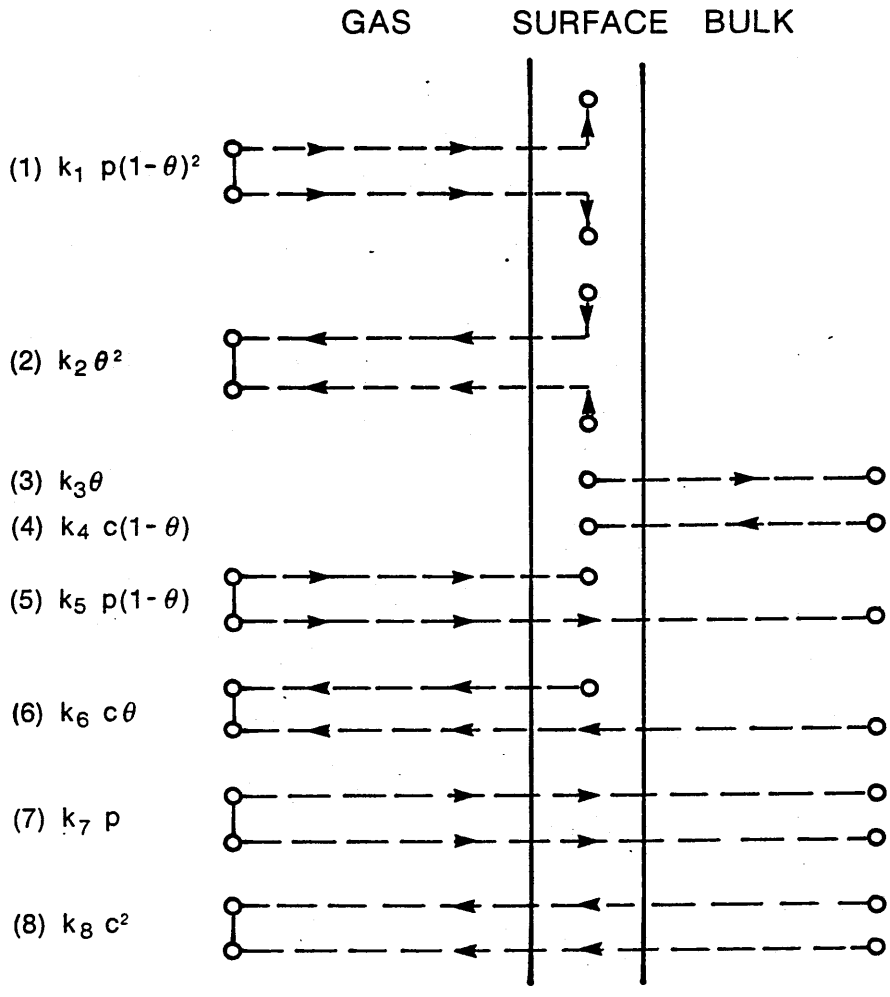

Figure 1.3 Schematic picture of surface processes in hydrogen-metal interaction (based on [4]).

of a "chemical reaction" with rate constants k_1, k_2, which are different from those depicted in Figure 1.3. A possible link with those will be suggested further on in this subsection.

The units used for J_s and c throughout this work are

$$[c] = \text{mol m}^{-3} \ ,$$

$$[J_s] = \text{mol m}^{-2}\text{s}^{-1}$$

and for the surface constants k_1, k_2

$$[k_1] = \text{mol m}^{-2}\text{s}^{-1}\text{Pa}^{-1} \ ,$$

$$[k_2] = \mathrm{m^4 s^{-1} mol^{-1}} \ .$$

It has to be noticed that at equilibrium $J_s = 0$, thus Sieverts' law holds

$$c_{eq} = K_s \sqrt{p} \tag{1.2}$$

where $K_s = \sqrt{(k_1/k_2)}$ is Sieverts' constant, which is expressed throughout this work in mol $\mathrm{m^{-3}}$ $\mathrm{Pa^{-1/2}}$. Then c_{eq} is the hydrogen solubility in the material.

In general, the Sieverts' constant K_s is a function of the temperature T according to the Arrhenius' law

$$K_s = K_0 \ \exp\left(-\frac{Q_s}{RT}\right) \ , \tag{1.3}$$

Q_s being the heat of solution and where $R = 8.314$ J $\mathrm{mol^{-1}}$ $\mathrm{K^{-1}}$.

A possible justification for the surface model given by equation (1.1) was proposed by Waelbroeck [6] for low surface coverage, $\theta \ll 1$, and under the hypothesis of equilibrium between surface and subsurface, briefly referred to as SSE. The latter hypothesis implies that the fluxes associated to processes (3) and (4) in Figure 1.3 are equal and therefore for low surface coverage θ the subsurface concentration c is directly proportional to θ. Hence all the fluxes but (3) and (4) in Figure 1.3 are linearly proportional to c^2 or to p. According to Pick [7], computer simulation, supported by experimental data as input, showed that this is true for niobium, i.e. that at any time t, apart from a very fast initial transient, $c(t) = \alpha\theta(t)/(1 - \theta(t))$, which for low coverage, $\theta \ll 1$, reduces to $c(t) = \alpha\theta(t)$.

Making use of a surface roughness factor σ, defined as the ratio of the true surface area to the geometrical one, the so-called recombination coefficient K_r was introduced as $\sigma K_r = k_2$. Owing to the great importance of k_2 there have been some attempts at computing it, by assuming one of the surface processes in Figure 1.3 to dominate. According to Pick [8], the rate of adsorption $k_1 p$ is given by the kinetic theory of gases, with $k_1 = \phi \ s$, through the sticking coefficient s and with $\phi = 4.385/\sqrt{2T}$ mol $\mathrm{m^{-2}}$ $\mathrm{s^{-1}}$ $\mathrm{Pa^{-1}}$; since $k_2 = k_1/K_s^2$ he finds

$$k_2 = \phi \frac{s}{K_s^2} \ . \tag{1.4}$$

For clean nickel and molybdenum surfaces [9, 10] it has been shown experimentally that the sticking coefficient s is not thermally activated and is very close to unity, so that the temperature dependence of k_2 is given by the solubility coefficient K_s.

This gives a theoretical maximum for k_2 since in general the surface of a metal is poisoned by impurities which alter the surface potentials in such a way that the sticking becomes thermally activated with energy $2E_C$ [8]

$$s = s_0 \exp\left(-\frac{2\,E_C}{RT}\right) \ . \tag{1.5}$$

Surface processes have been modelled in detail by Le Claire [11] and have been recently reviewed by Richards [4], who gives more general expressions for the fluxes shown in Figure 1.3 and in particular for the energies involved.

Experimental evidence is available in the literature (see [12], or [11] and references therein) which show that surface processes are important, i.e. slow compared to bulk processes, at low hydrogen pressures in the gas phase.

1.2.2 Bulk processes

Atomic and molecular solution

After crossing the surface of a solid, hydrogen jumps into the subsurface, where it occupies solution sites of the host lattice. The solubility S of a gas in the material is of fundamental interest as it may give a precise information on the state of the gas, atomic or molecular, within the sample. The solubility also affects the steady state permeation, as shown further on in the section for diffusion-limited regimes. It is a bulk property and as already anticipated in 1.2.1, it is defined as the concentration c_{eq} of gas dissolved in the sample at equilibrium, under a given pressure p and at the temperature T. If the gas is dissolved as atoms in the material then Sieverts' law (1.2) holds, which means that the solubility S varies linearly as the square root of the equilibrium pressure p. The solubility, or Sieverts', constant K_s is given by (1.3).

In general, atomic absorption of a diatomic gas G_2 by a solid is represented by the reaction

$$G_2(g) \rightleftharpoons 2G(s) \ . \tag{1.6}$$

At equilibrium, equations (1.2), (1.3) can be obtained by equating the gas chemical potential in the gaseous phase μ_g to that in the solid (dissolved) phase μ_s, as follows

$$\mu_g = 2\mu_s \ , \tag{1.7}$$

where the factor 2 is due to the presence of two atoms G of the gas dissolved in the solid. It has been shown [14] that

$$\mu_s = \mu_{s0} + k^B T \ln\left(\frac{\eta/\epsilon}{1-\eta/\epsilon}\right) \quad , \tag{1.8}$$

where ϵ is the ratio of the number of absorption sites to the number of host atoms. For octahedral absorption sites, $\epsilon = 1$ in a fcc lattice while $\epsilon = 3$ in a bcc lattice. In addition, η is the hydrogen concentration expressed in atomic fraction, i.e. $\eta = 2A_s c/\rho_s$ if c is the hydrogen concentration expressed in mol/m^3, A_s and ρ_s are the host molar mass and density. The term μ_{s0} only depends on temperature T and k^B is Boltzmann's constant. For the hydrogen potential in the gaseous phase [14] at the pressure p

$$\mu_g = \mu_{g0} + k^B T \ln\left(p/\mathrm{Pa}\right) \quad . \tag{1.9}$$

Equating the two potentials according to equation (1.7) gives

$$\frac{\eta/\epsilon}{1-\eta/\epsilon} = \sqrt{p/\mathrm{Pa}}\exp\left(\frac{\mu_{g0}-\mu_{s0}}{k^B T}\right) \tag{1.10}$$

and for a dilute solution $\eta/\epsilon \ll 1$, so that equation (1.10) becomes

$$\eta/\epsilon = \sqrt{p/\mathrm{Pa}}\ \exp\left(\frac{\mu_{g0}-\mu_{s0}}{k^B T}\right) \quad , \tag{1.11}$$

which is equivalent to (1.2) and (1.3).

If the solution is molecular then the factor 2 in equation (1.7) disappears and equations (1.10) and (1.11) become linear in p.

All this is true for diatomic gases in metals and it has been confirmed experimentally even for liquid metals and for some carbides, whereas for glasses, polymers and some liquid salts the solubility S varies linearly as the pressure p. This is interpreted as an indication that the gas is dissolved in molecular form in these materials.

The picture is not clear for oxides, definite and complete evidence in this sense being still lacking. Nonetheless, some investigators have reported a $\sqrt{p}$ dependence of the deuterium solubility in uranium dioxide single crystals [15], while other authors conclude that hydrogen dissolves as molecules in steel and iron oxides [16]. Porosity of the oxide layer could be an important factor in such behaviour.

Another example of the lack of definite and clear information on oxides, is the disagreement existing in the literature as to the form of hydrogen and deuterium

dissolved in Li_2O, a ceramic oxide of potential use as solid breeding blanket material in a fusion reactor. While Ihle and Wu [17] report the deuterium solubility in Li_2O single crystals to vary linearly with the deuterium pressure, the solubility of hydrogen in sintered Li_2O pellets was found to obey Sieverts' law by Katsuta [18].

Diffusion

The flux J_d inside a solid caused by a concentration gradient $\partial c/\partial x$ is given by Fick's law

$$J_d = -D\frac{\partial c}{\partial x} \ , \tag{1.12}$$

where the diffusion coefficient D is expressed in $m^2\ s^{-1}$ and J_d has the same dimensions and units as J_s. Together with a continuity equation

$$\frac{\partial c}{\partial t} + \frac{\partial J_d}{\partial x} = 0 \ , \tag{1.13}$$

and with the assumption of constant D, this gives the diffusion equation

$$\frac{\partial c}{\partial t} = D\frac{\partial^2 c}{\partial x^2} \ . \tag{1.14}$$

Equation (1.14) coupled to appropriate boundary and initial conditions can be solved to give the variation in time t and space x within the solid of the concentration $c(x,t)$. The diffusivity D of the gas in the solid is a function of the temperature T according to the Arrhenius' law

$$D(T) = D_0 \exp\left(-\frac{Q_d}{RT}\right) \ . \tag{1.15}$$

The pre-exponential factor D_0 depends on the mass m of the diffusing species and classically

$$D_0 \propto \frac{1}{\sqrt{m}} \tag{1.16}$$

so that heavier species diffuse more slowly.

As the diffusive flux J_d is linear in the concentration c, whereas the surface release flux is quadratic in c, it is reasonable to expect that diffusion is rate-controlling at high concentration and that surface processes become rate-controlling at low concentration.

Trapping

Trapping has been invoked to explain differences in measured diffusivities during gas absorption and desorption experiments and also to account for extremely low and spread out diffusivities in iron and steels at temperatures below 550 K.

Internal trapping is a process that delays the flow of hydrogen in a solid via the capture and release of hydrogen atoms by sites others than the ordinary solution ones. Examples of such sites are located at dislocations, voids, particle inclusions and grain boundaries.

For a single type of point-like traps uniformly distributed throughout the solid, reversible trapping is described by assuming that part of the hydrogen in the solid is mobile, with concentration $c(x,t)$, while the rest is immobile (i.e. non-diffusible) in the traps and has a concentration $z(x,t)$. Exchange between these two states occurs through a reversible reaction with rate constants k_A for trapping and k_B for detrapping. These rate constants are assumed to vary with the temperature, but not with the concentrations c and z. The variation in time of the concentration of trapped hydrogen, $\partial z/\partial t$ is the difference between a trapping and a detrapping term. The former is proportional, through k_A, to the mobile concentration c and to the fraction of unoccupied trapping sites $1-zN_A/N$, where N is the number of traps per unit volume and N_A is Avogadro's number. The latter is similarly proportional to the trapped concentration z times the fraction of available solution sites, $1-c/c_s$, where c_s is a saturation concentration. The rate equation is then

$$\frac{\partial z}{\partial t} = k_A c\left(1-\frac{zN_A}{N}\right) - k_B z\,(1-c/c_s) \quad , \tag{1.17}$$

in which irreversible trapping is described by setting $k_B = 0$. The continuity equation becomes

$$\frac{\partial\,(c+z)}{\partial t} + \frac{\partial J_d}{\partial x} = 0 \quad , \tag{1.18}$$

which gives the diffusion equation with trapping term

$$\frac{\partial c}{\partial t} = D\frac{\partial^2 c}{\partial x^2} - \frac{\partial z}{\partial t} \quad . \tag{1.19}$$

The system of equations (1.17,1.19) is nonlinear owing to the product cz and can only be solved numerically. It becomes linear for low mobile concentration and low

trap occupation, i.e. if $zN_A/N \ll 1$ and $c/c_S \ll 1$ then equation (1.17) becomes

$$\frac{\partial z}{\partial t} = k_A c - k_B z \ , \tag{1.20}$$

in which case analytical solutions may be obtained [13].

It is evident that the effect of trapping is to increase the solubility by providing additional sites to accommodate hydrogen and to increase the time necessary for hydrogen to move in the solid, therefore creating an "apparent" decrease of the diffusivity. In other words, the "apparent" diffusion coefficient D_{app} measured when trapping is present is smaller than D.

On the other hand, trapping does not affect the steady state permeation through a foil of thickness ℓ which separates two chambers at pressures p_1 upstream and p_2 downstream. The permeation flux j across the foil can be found by solving equation (1.19) subject to the condition $\partial/\partial t = 0$. If the flow regime is controlled by diffusion on both sides of the foil, the flux is given by Richardson's law

$$j = \frac{DK_s}{\ell}\left(\sqrt{p_1} - \sqrt{p_2}\right) \ , \tag{1.21}$$

which does not depend on trapping parameters N, k_A and k_B. The permeability $\Phi = DK_s$ is therefore unaffected by trapping.

The effect of trapping on the solubility can be found from (1.17). At equilibrium $\partial z/\partial t = 0$, hence

$$z_e = \frac{k_A c_e}{k_B + \left(k_A N_A/N - k_B/c_s\right) c_e} \tag{1.22}$$

and, recalling that at equilibrium (1.2) holds,

$$z_e = \frac{k_A K_s \sqrt{p_e}}{k_B + \left(k_A N_A/N - k_B/c_s\right) K_s \sqrt{p_e}} \ . \tag{1.23}$$

The solubility is therefore

$$S = c_e + z_e = K_s\sqrt{p_e}\left[1 + \frac{k_A}{k_B + \left(k_A N_A/N - k_B/c_s\right) K_s\sqrt{p_e}}\right] \ . \tag{1.24}$$

For very large pressures p_e, S takes the form

$$S \simeq K_s\sqrt{p_e} + \frac{k_A}{k_A N_A/N - k_B/c_s} \ , \tag{1.25}$$

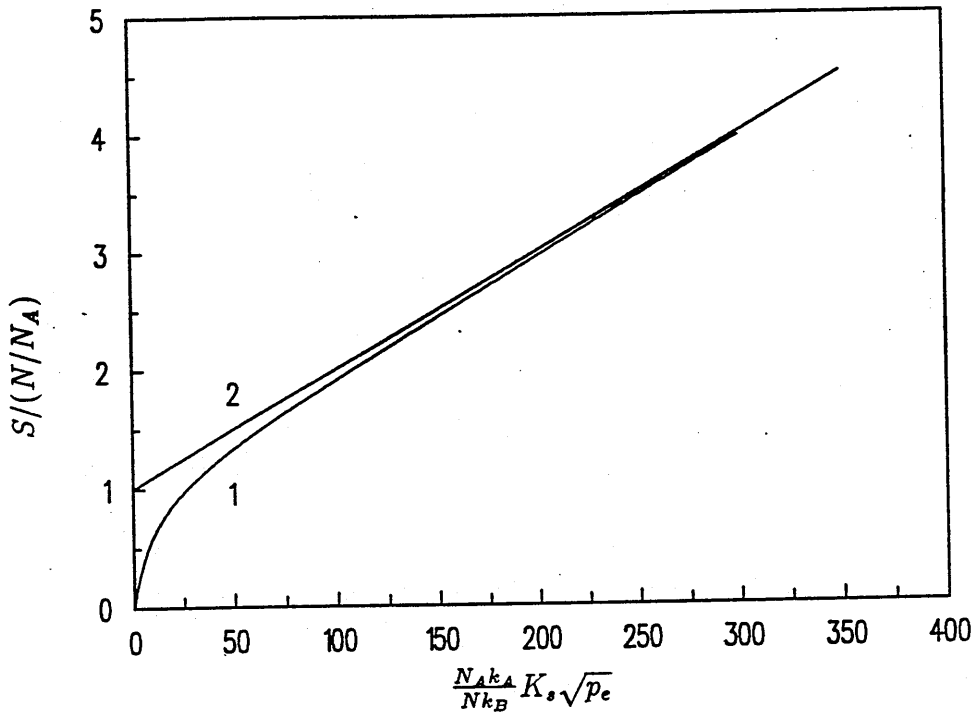

Figure 1.4 Effect of trapping on the hydrogen solubility in a solid. Key to symbols: 1 - equation (1.24), 2 - high pressure approximation, equation (1.25).

which extrapolates to $p_e = 0$ by yielding an intercept equal to N/N_A when $1/c_s$ is negligible.

The low pressure approximation is

$$S \simeq K_s \sqrt{p_e} \left(1 + \frac{k_A}{k_B}\right) \quad , \tag{1.26}$$

so that Sieverts' law still holds but proportionality to $\sqrt{p_e}$ occurs through the modified Sieverts' constant $S/\sqrt{p_e} = (1 + k_A/k_B)K_s$. This reduces to K_s for low trap occupation i.e. if $z_e N_A/N \ll 1$, or when $k_A \ll k_B$.

In general, for endothermic hydrogen occluders the term c_s is so large that $1/c_s$ is negligible compared to the other terms. Under such approximation, the normalised solubility SN_A/N from equation (1.24) and its high pressure asymptote given by (1.25) are plotted in Figure 1.4, as functions of the square root of the dimensionless equilibrium pressure $[(N_A k_A)/(N k_B)]K_s\sqrt{p_e}$.

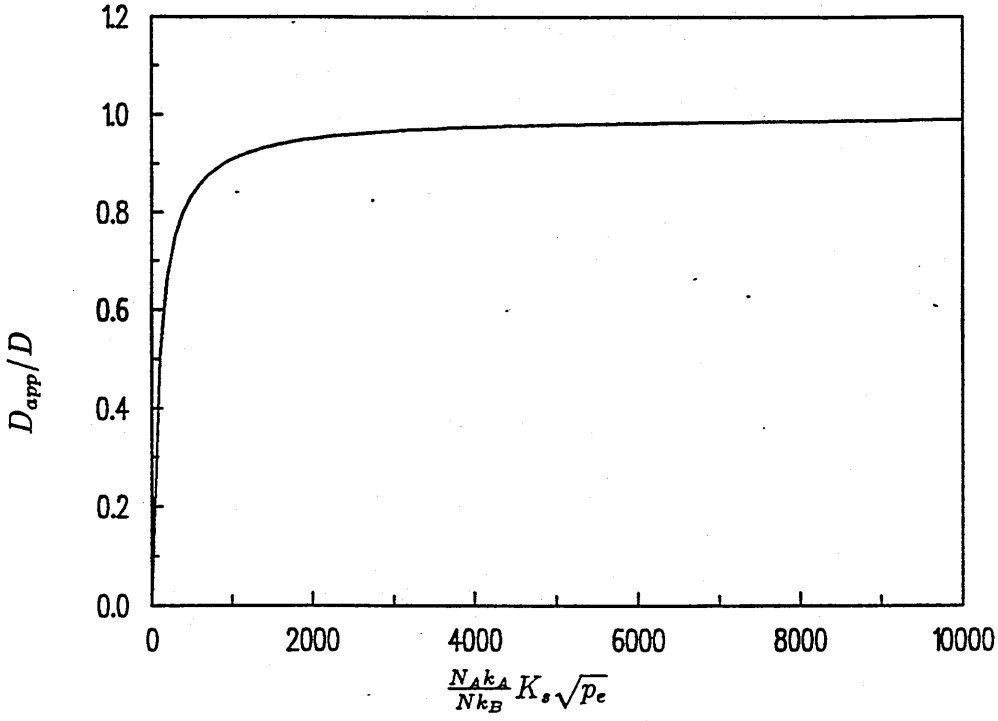

Figure 1.5 Effect of trapping on the hydrogen apparent diffusivity in a solid.

The effect of trapping on the "apparent" diffusivity D_{app} cannot be found by analytical methods, because of the nonlinearity of the diffusion equation with trapping terms. A shortcut is to recall that the permeability $\Phi = DK_s$ is not affected by trapping. Hence, if an apparent Sieverts' constant is defined as $K_{s,app} = S/\sqrt{p_e}$ where S is given by (1.24), the apparent diffusivity is

$$D_{app} = \frac{DK_s}{K_{s,app}} \quad . \tag{1.27}$$

More explicitly

$$\frac{D_{app}}{D} = \frac{1}{1 + \frac{k_A N}{k_B N + k_A N_A K_s \sqrt{p_e}}} \quad , \tag{1.28}$$

where the term $1/c_s$ has been neglected.

The ratio D_{app}/D from equation (1.28) is plotted in Figure 1.5 as function of the square root of the dimensionless equilibrium pressure $[(N_A k_A)/(N k_B)] K_s \sqrt{p_e}$. It is important to mention that the effect of trapping on D_{app} vanishes at high pressures.

Interface reactions

The aim of this work is to study coated metals, hence solid/solid interfaces must be accounted for in the mathematical modelling of hydrogen flow. In this work, it is assumed that hydrogen is dissolved atomically in the TiC coating as well as in the metallic substrate. This assumption is suggested by the compact and pore-free structure of the coatings used. In addition, if hydrogen dissolves as molecules in the coating layer then the solubility for the coated specimen does not follow Sieverts' law and can be represented by a parabola when plotted versus the square root of the equilibrium pressure. Thus, if the experiments show that Sieverts' law holds for the coated specimen, then either hydrogen dissolves atomically also in the coating or the solubility constant[2] $K_{h,2}$ in the coating is much smaller than $K_{s,1}V_1/(V_2\sqrt{p})$, where $K_{s,1}$ is Sieverts' constant in the metallic substrate.

Interface behaviour is still an open subject in the field of hydrogen-material interaction, as no experimental evidence has been obtained showing what are the boundary conditions to describe hydrogen dissolved between two solid phases.

If no hydrogen accumulation occurs at the interface, mass conservation implies the continuity of the diffusive flux at the interface. Hence for two different media 1 and 2 with hydrogen diffusivities D_1, D_2 and concentrations c_1, c_2

$$D_1 \frac{\partial c_1}{\partial x}\Big|_{i^-} = D_2 \frac{\partial c_2}{\partial x}\Big|_{i^+} \quad , \tag{1.29}$$

where the subscripts i^- and i^+ indicate the approaching to the interface location from left (medium 1) and from right (medium 2) respectively.

If hydrogen migration is not dominated by reactions at the interface, which are therefore assumed to be infinitely fast, it is fair to assume that such reactions are in dynamic equilibrium. This implies continuity of the chemical potential across the interface, which is equivalent to a discontinuity in the concentration at the interface

$$\frac{c_1\big|_{i^-}}{c_2\big|_{i^+}} = k \tag{1.30}$$

making use of the partition coefficient k, which is equal to the ratio of the solubility coefficients $k = K_{s1}/K_{s2}$.

[2]The subscript h here refers to Henry's law, according to which the solubility is linear with the pressure p, $S = K_h p$.

If interface reactions are considered to be rate-determining, equation (1.30) can be substituted for by a reaction rate equation such as

$$- D_1 \frac{\partial c_1}{\partial x} \mid_{i-} = k_3 c_1 \mid_{i-} - k_4 c_2 \mid_{i+} \tag{1.31}$$

where again $k = k_4/k_3$ is the partition coefficient. The latter is very important since it describes how hydrogen is distributed at equilibrium in the two solid phases, the higher the solubility coefficient in a medium the higher its hydrogen concentration.

Equations (1.30) and (1.31) hold for dilute solutions, i.e. for concentrations c that are much smaller than the concentration of available solution sites c_s. If this is not so, steric factors $1 - c/c_s$ have to be introduced, so that equation (1.31) becomes

$$- D_1 \frac{\partial c_1}{\partial x} \mid_{i-} = k_3 c_1 \mid_{i-} \left(1 - \frac{c_2 \mid_{i+}}{c_{2s}}\right) - k_4 c_2 \mid_{i+} \left(1 - \frac{c_1 \mid_{i-}}{c_{1s}}\right) \quad . \tag{1.32}$$

At equilibrium this gives

$$\frac{c_1 \mid_{i-}}{c_2 \mid_{i+}} = k \frac{(1 - c_1 \mid_{i-} / c_{1s})}{(1 - c_2 \mid_{i+} / c_{2s})} \quad , \tag{1.33}$$

which again expresses the continuity of hydrogen chemical potential across the interface.

1.3 Available data

As outlined in the previous sections, the flow of hydrogen through a solid is commonly described in terms of diffusion, solution and surface reactions. Hence, the relevant parameters concerning hydrogen-materials interactions are the solubility and/or the Sieverts' constant K_s, the diffusivity D and the surface rate k_2. This is the amount of information needed for instance to evaluate the steady state permeation flux j_P through a symmetric foil of thickness d, continuously evacuated downstream and kept at a constant pressure p upstream. This is given by Richardson's law $j_P = K_s D \sqrt{p}/d$ in diffusion-limited regimes or by $j_P = \frac{1}{2} k_2 K_s^2 p$ in surface-limited regimes[3]. In intermediate regimes the same input data D, K_s, k_2 need to

[3]This holds in surface-controlled regimes for a *symmetric* membrane, i.e. one for which the rate constant k_2 has the same value on its two sides.

be fed to a computer code to solve a partial differential equation with nonlinear boundary conditions.

This section is a short review of available data on D, K_s and k_2 for the materials under study, including substrates and coating.

1.3.1 Data for AISI 316 steel, molybdenum and TZM

a) Steel 316

The austenitic steels AISI 304 and 316 have been studied by many authors, mainly because of the large use these steels have in the nuclear industry for fission and fusion applications. The techniques used to study the interaction of hydrogen with these steels were mostly based on the measurement of steady state permeation through a foil of known thickness d, pumped downstream and kept at constant pressure p upstream. Diffusivities D were obtained by the time-lag method [13] and solubility coefficients K_s were then computed from Richardson's law, as the ratio of permeability to diffusivity Φ/D where the permeability is $\Phi = d\, j_P/\sqrt{p}$. This procedure was followed despite the fact that the pressure dependence found for the permeation flux j_P, often departed from the Richardson's limit $p^{1/2}$, with exponents as high as 0.7, which indicates the presence of other processes. As shown by Le Claire [11], surface effects may cause the pressure exponent n to vary from 0.5 to 1 as the input pressure is decreased. Indeed, when n is significantly different from 0.5 there must be considerable concern about the accuracy of the results obtained by a straightforward application of both Richardson's law and the time-lag method to determine the Sieverts' constant K_s and the diffusivity D from the graphically measured time-lag $t_L = d^2/(6D)$. This adds to the inherent growth of the uncertainty in diffusivity and solubility values determined, indirectly, by this method [19].

For the AISI 316 steel, diffusivities and solubilities are reasonably well known, within less than a factor of 10. Discrepancies may be attributed to a variety of reasons such as surface cleanliness, history and pre-treatment or technique used.

In Figure 1.6 the Sieverts' constant for the AISI 316L steel is shown as obtained with a permeation technique (Forcey, line 1) [20] and by means of evolution after loading to saturation (Reiter, line 3) [21]. It is also worth noting the agreement

with the values by Grant [22], obtained for a slightly different steel, the AISI 316, by means of a pressure-modulated permeation technique in which surface effects were separated from bulk diffusion. It has to be pointed out, however, that in the paper by Forcey et al. ([20], pages 121 and 122), some misprint must have crept into the equations for the temperature dependence of permeability Φ, diffusivity D and solubility constant K_s, as the relationship $\Phi = DK_s$ is not verified for pre-exponential factors. In addition, while there seems to be agreement between data points on the graph and the equations for D and Φ, it is not so for K_s. Therefore, in this work the pre-exponential factor for K_s given by Forcey [20] is not used. The ratio Φ/D has been used instead, to draw the K_s straight line shown in Figure 1.6.

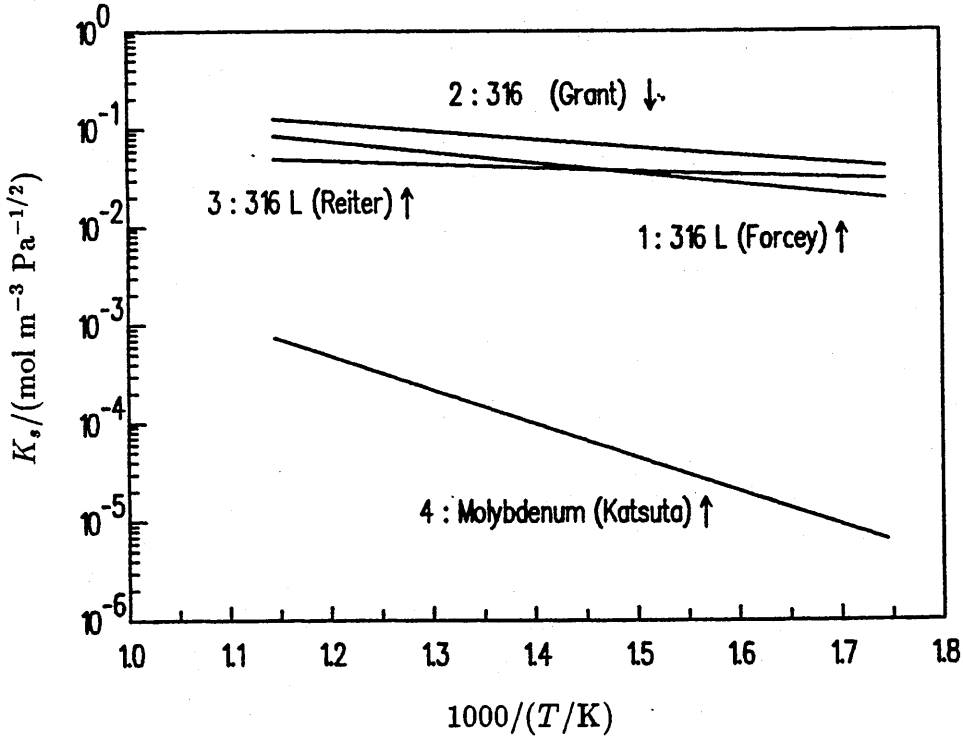

Figure 1.6 Solubility constant of hydrogen isotopes in the AISI 316 steel and in molybdenum: 1 - Forcey [20], 2 - Grant [22], 3 - Reiter [21], 4 - Katsuta, [28].

For the diffusivity in the AISI 316 steel, Figure 1.7[4] presents Arrhenius plots of

[4]Here and throughout this work, the term "Log" is used to indicate the common logarithm.

the data from the same authors [20, 21, 22].

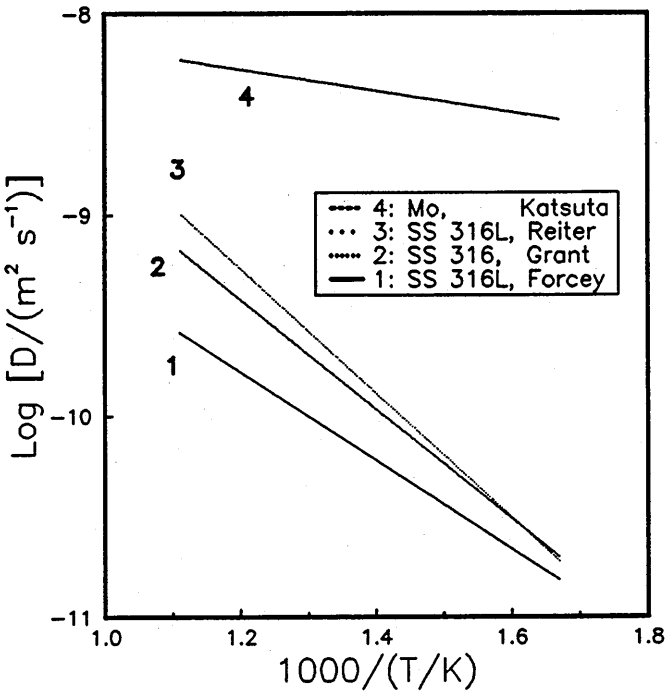

Figure 1.7 Diffusivity of hydrogen isotopes in the steel AISI 316 and in molybdenum: 1 - Forcey [20], 2 - Grant [22], 3 - Reiter [21], 4 - Katsuta, [28].

The data by Reiter [21] have been taken as representative of the AISI 316L steel used as substrate in this work, since they have been obtained on the same steel batch used here and with the same technique. They have also been confirmed prior to deposition of the TiC coating, by a small number of experiments. The expressions for K_s and D from [21], used throughout this work, are as follows:

$$K_s/(\text{mol m}^{-3}\text{Pa}^{-1/2}) = 0.128 \exp\left(-\frac{6900}{RT}\right) , \tag{1.34}$$

$$D/(\text{m}^2\text{s}^{-1}) = 2.99 \times 10^{-6} \exp\left(-\frac{59700}{RT}\right) , \tag{1.35}$$

where $R = 8.314$ J mol^{-1}K^{-1}.

The surface rate constant k_2 for steels 304 and 316 has been measured by several authors using different methods and under different experimental conditions. When presented in an Arrhenius plot the values found fall in a belt spanning four orders of magnitude and lying well below the theoretical maximum, obtained by setting

$s = 1$ in equation (1.4) and using for K_s the data by Reiter [21] for steel and by Katsuta [28] for molybdenum, as shown in Figure 1.8. The slope in this graph is also

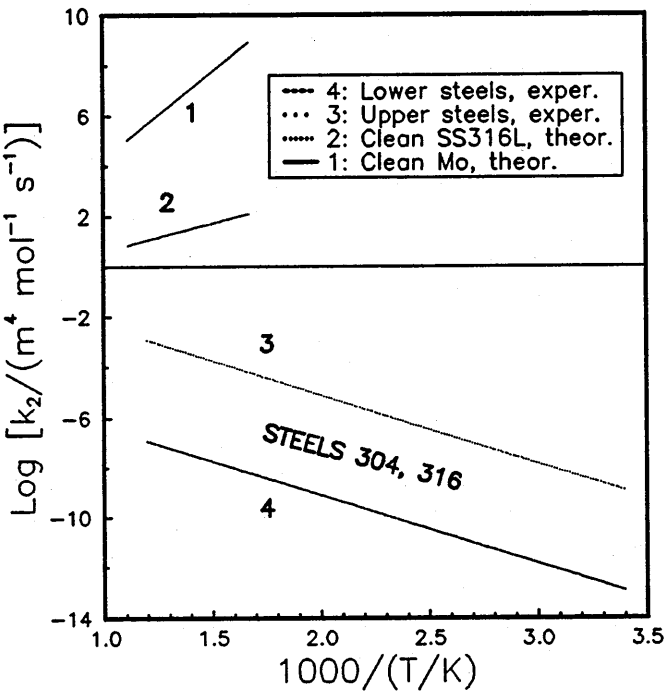

Figure 1.8 Surface desorption rate constants of hydrogen isotopes in the AISI 316 steel and in molybdenum as functions of the inverse temperature: 1 - theoretical maximum for molybdenum, $s = 1$, K_s by Katsuta [28], 2 - theoretical maximum for steel, K_s by Reiter, 3 and 4 - belt containing experimental values for indicated steels, by various authors.

opposite to the theoretical maximum one, a fact which is interpreted by a thermally activated sticking coefficient due to altered surface energy levels [8].

Recent work by Yamawaki and coworkers [23] is in agreement with such a picture. By measuring the permeation through nickel and steel membranes and simultaneously the surface composition by means of *in situ* Auger analysis they found that k_2 increases as the amount of surface impurities (mainly oxygen for stainless steel and sulphur for nickel) is diminished. They gave values of k_2 for a clean surface which are 2-3 orders of magnitude higher than the belt reported for steel in Figure 1.8. They also linearly extrapolated the value of 2 E_C to zero impurity coverage to obtain 0.7 eV instead of zero as predicted by Pick's model [8]. From this, they concluded that surface impurities are not the only factor responsible for the surface

barrier to adsorption.

It is important to point out again that they did not actually measure the value of 2 E_C at zero surface impurity coverage, and that their data have a rather large scatter. In addition, the value of k_2 at zero surface impurity coverage was also not directly measured. Instead, at a given temperature the dependence of k_2 on the concentration of surface impurity was assumed to be exponentially decreasing as the impurity concentration increased. Then an extrapolated value of k_2 to zero oxygen surface concentration, or for a clean surface, was extracted by fitting that decreasing exponential to the data. Their extrapolated results seem at least questionable from a quantitative point of view and ought to be confirmed by measured data with clean surfaces.

b) Molybdenum and TZM

TZM is the designation of a high temperature molybdenum alloy with small titanium and zirconium additions, below 1 per cent by weight [24]. Despite being a potential fusion reactor material [25, 26], almost no data on the interaction of TZM with hydrogen isotopes are available, though low solubility and permeability are expected owing to the dominant presence of molybdenum.

A rather large amount of data is available on the latter, showing inconsistencies attributed to surface and/or trapping effects [27]. It is known that on a molybdenum surface a protective oxide layer forms which is volatile above 773 K. Permeabilities Φ seem consistent, but diffusivities D vary by several orders of magnitude between different authors. Surface effects are present even after argon ion-beam cleaning and palladium coating, though these treatments yield the highest measured diffusivity [28]. For hydrogen at temperatures between 673 K and 1473 K, polycrystalline molybdenum shows a higher permeability than a single crystal by a factor 2.6 and a slightly higher diffusivity, by less than 25 per cent [29]. Remembering Richardson's permeability law $\Phi = K_s D$ where K_s is the solubility constant, and since D increases less than Φ on passing from single- to polycrystals, an increase in K_s is not to be ruled out. However, direct measurements indicate that the difference in K_s between single- and polycrystals is not meaningful [30].

A few investigations have been reported on molybdenum-based alloys with tita-

nium, zirconium, niobium and vanadium in the molybdenum-rich region [31, 32, 33]. These elements increase the molybdenum permeability and solubility and cause the heat of solution Q_s to undergo a change of sign for amounts of the addition higher than 1 per cent. The ruling parameter seems to be the electron to atom ratio e/A, i.e. the ratio of the number e of conduction electrons to the number A of atoms of different species present in the alloy. The sign change occurs at a value of e/A between 5.6 for Mo-Ti, corresponding to 20 per cent titanium, and 5.8 for Mo-Zr, corresponding to about 9.55 per cent zirconium [31]. As expected because of its high 'apparent' solubility, zirconium is the most effective in changing the sign of the heat of solution Q_s and, when this happens, the solubility is higher than in molybdenum by not more than one order of magnitude and is therefore still in the low-solubility range. Small boron and carbon additions are reported to decrease the deuterium diffusivity, an effect which is attributed to trapping at carbide and boride centres [34]; it is worth recalling that dispersed oxides and carbides exist in the bulk of TZM to prevent grain growth. Thermal desorption spectroscopy measurements of deuterium in TZM [26] indicate bulk trapping, but this conclusion derives from an interpretation which uses diffusivity and solubility data taken from separate experiments [28, 30] on molybdenum.

TZM has received attention as a hydrogen permeation barrier material [35], because of its low permeation to hydrogen. The permeation is reported to be higher in the alloy Mo-0.5% Ti than in molybdenum at 1.08×10^5 Pa (810 torr) input pressure in the temperature range 1173-1450 K [33].

For comparison with steel values, the data for molybdenum by Katsuta [28] have been added in Figures 1.6, 1.7, 1.8, the latter only showing the theoretical maximum for unit sticking coefficient. Katsuta's work is generally taken as a reference for molybdenum data because of the care used in trying to remove surface effects (*in situ* cleaning by Ar^+ sputtering followed by Pd coating).

No data on the surface-limited release of hydrogen from TZM were found in the literature, but Kitajima and co-workers [37] reported the values they measured for K_r in a set of experiments on a hydrogen glow discharge with several conditioning treatments of the specimen. The values of K_r for molybdenum were estimated from the pressure drop in time during the discharge, on the assumption that the flow was

controlled by surface recombinative desorption. For molybdenum at 13.3 Pa in the temperature range 300 K - 600 K the values obtained are similar to those for the AISI 304 and 316 steels and also show the same slope on an Arrhenius plot. They were reported to be strongly influenced by surface impurity layers, which could be removed, at least partly, by means of Ar glow discharge cleaning.

The ideal substrate material for vapour deposition for the purpose of studying hydrogen interaction with a coating should have low hydrogen absorption, so that hydrogen is predominantly located in the coating layer, and a high hydrogen migration speed, so that migration through the substrate can be considered as virtually instantaneous. From the data survey it is evident that owing to the lower solubility and the higher diffusivity with respect to the AISI 316 steel, molybdenum is a better choice. The higher recrystallisation temperature, well above the deposition temperature, makes TZM even more attractive.

1.3.2 Data for Carbides

Data for carbides are scarce, mainly because they are difficult to shape into a vacuum-tight membrane for permeation work and also owing to the unrealistically long measuring times possibly caused by low diffusivities and permeabilities. Some work was carried out in the late seventies by Elleman's group [36, 38] on SiC of various shapes and types, at temperatures above 1100 K. Hydrogen, deuterium and tritium were used: deuterium permeation through tubes and tritium evolution after nuclear charging were studied. Sieverts' law was reported to hold, even though the pressure coefficient obtained was 0.61 ± 0.6. The striking facts are the high solubility, K_s being several orders of magnitude higher than for nickel and stainless steels, and the exothermal behaviour typical of hydride formers. This is identified by a positive slope of the solubility coefficient in an Arrhenius plot, as shown in Figure 1.9 for massive and vapour-deposited SiC.

It has to be noted that there is strong disagreement between these two sets of data. Further and more recent work on hydrogen in sintered SiC and Si_3N_4 [39] confirmed Sieverts' law to hold but gave much lower and almost temperature-independent values for the solubility. Unfortunately the latter were given only in graphical form, the only value quoted being for an unspecified pressure, so these

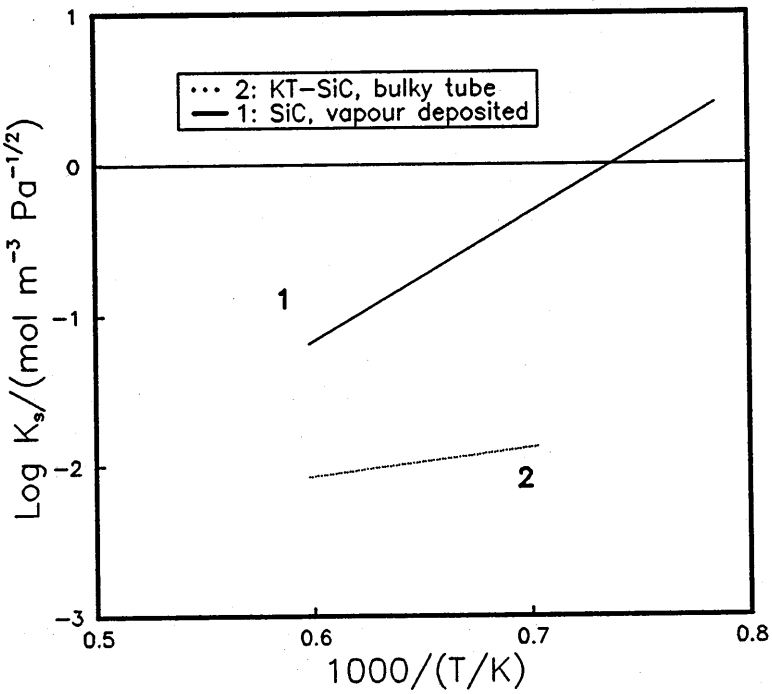

Figure 1.9 Solubility constant of hydrogen isotopes in SiC: 1 - Causey [36], 2 - Verghese [38].

data cannot be included in Figure 1.9. That work however seems to confirm that vapour-deposited materials show a higher solubility than sintered ones. No data are available on the solubility in TiC.

Diffusivities of hydrogen isotopes in carbides [36, 38, 40, 41] are shown in Figure 1.10 in Arrhenius plot. Again, a strong difference is observed for different types of SiC, but the common features are evidently the very low values of the diffusivity relative to those for metals (compare to Figure 1.7) and the huge activation energies for SiC, which suggests some form of chemical bonding of hydrogen to the material. Details are lacking on the method and procedure adopted for obtaining the TiC data. It is reported only [41] that the diffusivity is estimated from the measurement of desorbed deuterium after 6 keV D^+ ion bombardment up to the saturation fluence. The following equation for the diffusivity in the temperature range from room temperature up to 773 K, is then given:

$$D/(\mathrm{m}^2\ \mathrm{s}^{-1}) = 1.31 \times 10^{-16} \exp\left(-\frac{12760}{RT}\right) \quad , \tag{1.36}$$

where R is the gas constant expressed in J mol^{-1}K^{-1}.

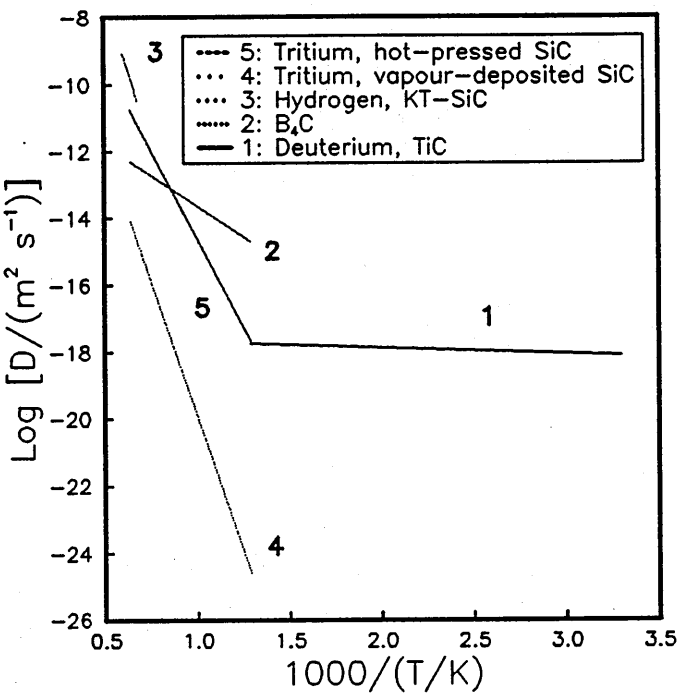

Figure 1.10 Diffusivity of hydrogen isotopes in carbides: 1 - TiC, Sone [41], 2 - B_4C, Riehm [40], 3 - SiC, Verghese [38], 4 and 5 - SiC, Causey, [36].

Kitajima [37] carried out hydrogen-glow experiments with molybdenum coated by 1 to 2 μm TiC produced by radio frequency magnetron sputtering. He observed a large pressure drop during the discharge caused by the reemission being almost negligible as compared to the implantation, even after the sample had been cleaned for a long time in an Ar glow discharge. He concluded that this was caused by the hydrogen atoms being very stably trapped in the TiC lattice. No consideration was made of the possibility that TiC might itself have had a very low surface recombination rate constant K_r.

1.4 Aim of the present work

The aim of this work is to study the influence of ceramic coatings on the release of hydrogen from alloys relevant to fusion technology. Coatings for which low outgassing rates are expected, and that are reported to impede the penetration of hydrogen in the metallic substrate, are of particular interest. The obvious goal when applying

such coatings, is to try improving the metal surface properties, especially from the hydrogen absorption viewpoint, without affecting the metallic bulk properties. In view of the main characteristic of these coatings, which is to slow down the hydrogen release from a sample, in order to reduce experiment times it is necessary to resort to thin coatings, with thicknesses in the micron range, deposited on metals. The bare substrate needs to be studied as well. Chemical Vapour Deposition (CVD) has been chosen since it is a well known and developed method, available on industrial scale, whereby dense and compact coatings can be obtained on metallic substrates.

Real coating-to-substrate interfaces are required to investigate the hydrogen behaviour in their presence and to assess the feasibility of simple modelling. Indeed, real interfaces never are step-like and might undergo changes in time owing to thermal effects.

In order to study the influence of the substrate on the hydrogen release, two different metallic substrates are required, with different thermal expansion coefficients. Coating integrity and good adhesion to the substrate require that the substrate thermal expansion coefficient value be close to that of the coating.

Availability and cost suggested the study of titanium carbide (TiC) as a coating.

In the present work, two manometric experimental techniques have been used to study the interaction of hydrogen with TiC-coated metallic substrates. They are described in detail in the next two chapters, but as a useful short anticipation it can be said that the technique used at the JRC of Ispra is based on recording the pressure increase in a closed ultra-high-vacuum (UHV) vessel after loading the specimen to saturation. The hydrogen release is triggered by a quick evacuation of the experimental chamber where the specimen is kept at a constant temperature. This is therefore a method based on the study of transients provoked artificially between two equilibrium states.

In contrast to this technique, at the Oxford Research Unit the method relies on the cyclic variation of the volume of a closed UHV chamber containing the specimen at the required temperature and base pressure. The resulting pressure response is recorded at different oscillation frequencies. In particular, the phase difference between pressure and volume oscillations is measured. This is a frequency response method for forced oscillations around a stationary state.

Both techniques need modelling of the experiment, whereby parameters such as diffusivity, solubility and surface reaction rate constants can be obtained after data fitting.

This work is meant as a first step towards a study of more realistic and complex carbon-based compounds used in fusion technology applications.

1.5 Mechanical integrity of the coating layer

The TiC coating deposition takes place at 1323 K and on cooling to room temperature the differential thermal expansion causes compressive stresses to build up inside the coating. Assuming that both the coating and the substrate behave elastically, the amount of stress to which the coating is subject is roughly given by [42]

$$\sigma = E\Delta T\frac{\Delta\alpha}{1-\nu} \quad . \tag{1.37}$$

Here E and ν are the coating Young's modulus and Poisson's ratio, ΔT is the temperature change and $\Delta\alpha$ is the difference between the substrate and the coating average linear thermal expansion coefficients. These data are not known for a coating, therefore values taken from tests on bulk specimen have been used to estimate σ. For TiC one has $\nu = 0.191$ and E can vary between 270 and 470 GN m^{-2}, depending on the degree of porosity of the sample. By using $\Delta\alpha = 10^{-5}\mathrm{K}^{-1}$ and $\Delta T = 800$ K one has

$$\sigma = \frac{E}{100} = (2.7 - 4.7)\ \mathrm{GNm}^{-2} \quad , \tag{1.38}$$

to be compared to the theoretical fracture stress $E/20$ [43] and to the TiC compressive strength S_c at room temperature, taken from the literature [43, 44]

$$S_c = (1.4 - 2.8)\ \mathrm{G\,N\,m}^{-2} \quad . \tag{1.39}$$

Higher values of S_c have been reported, of about 5.5 GNm^{-2}, depending on the surface treatment. Tensile strengths are lower than compressive ones, nearly by an order of magnitude. A temperature change ΔT of only 800 K is considered to compute σ since TiC, as most ceramics, behaves elastically below the ductile-to-brittle transition temperature T_{DB}. For TiC single crystals T_{DB} is about 0.3 T_m, where

T_m = 3340 K is the melting temperature, while for polycrystals an approximate value is 1073 K, depending on the departure from stoichiometry [43]. As a consequence, the sample at room temperature is in a stressed state and cracks might already have developed in the coating on cooling after deposition. Heating the sample up to the deposition temperature may have a beneficial effect since stresses should relax. Thermal cycling below the deposition temperature should have little or no effect on the coating integrity.

The linear thermal expansion coefficient for TZM is $\alpha = 5.6 \times 10^{-6}$ K^{-1}, i.e. lower than that of steel, hence cooling to room temperature from the deposition temperature causes tensile stresses in the coating. Since in this case $\Delta\alpha = -1.8 \times 10^{-6}$ K^{-1}, where the minus sign refers to a tensile stress, one has

$$\sigma = (0.5 - 0.8) \text{ GNm}^{-2} \ . \tag{1.40}$$

1.6 Expected problems

The sort of problem expected in this work is mainly related to the type of material under study, which is a ceramic carbon-containing coating expected to act as a hydrogen permeation barrier. The preparation of the samples by external agencies adds to this a lack of flexibility and the need to check the samples and it also increases the times required for the study.

In particular, the coating thickness determination, which directly affects the results and their extrapolability, is a difficult task since carbon is hard to detect with quantitative analysis and the range of thicknesses used requires powerful techniques. Crack development in the coating is another source of concern which requires the sample to be checked. Finally, the thermal stability of the coating, interdiffusion of the substrate and the coating components and the effect on composition of hydrogen charging-unloading cycles might pose other serious questions.

1.7 Summary

In this chapter the reasons for this work have been discussed and background information on the interaction of hydrogen with solids has been given. Such information

includes an outline of the theory used to model the behaviour of hydrogen when in contact with a solid, as well as a short review of available data for the materials to be studied.

The goal of the work has been described and accordingly some sources of concern have been anticipated.

Chapter 2

Experimental apparatus and specimens

The experimental rigs used at JRC Ispra and at the Oxford Research Unit are briefly and separately described, stressing only the general layout and some criteria underlying their conception. Details are given on the most important parts of the equipment. The measurement of temperature by resistance thermometry is also addressed. Specimen production and preparation are discussed. The experimental methods used with these rigs are described in chapter 3.

2.1 JRC Ispra rig and specimens

2.1.1 The rig: general description

The apparatus is schematically shown in Figure 2.1. It is a computer-controlled UHV-installation, devised to study the hydrogen absorption and desorption behaviour of solids with low hydrogen solubility, such as nickel, iron and their alloys. It is composed of four main parts:

- the pumping units UHV1, UHV2
- the gas inlet unit LV2, LNT, HgM
- the gas analysis unit V2, MV, V3, BAG, QMF, and
- the experimental chamber V1.

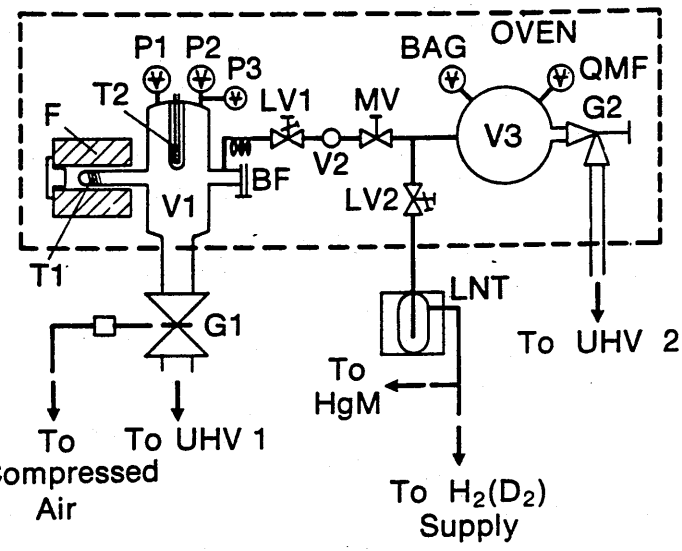

BAG	Bayard-Alpert Gauge	MV	Manually Actuated Magnetic Valve
BF	Blanking Flange	P1, P2	Capacitive Manometers
F	Furnace	P3	Spinning Rotor Gauge
G1	Electropneumatic Gate Valve	QMF	Quadrupole Mass Filter
G2	Manually Actuated Gate Valve	T1, T2	Pt-Resistance Thermometers
HgM	U-tube Hg manometer	UHV	Pumping Units
LNT	Liquid Nitrogen Trap	V1	Experimental Chamber
LV1, 2	Manually Actuated Leak Valves	V2, V3	Expansion Volumes

Figure 2.1 Schematic view of the apparatus.

The latter two are detailed in Figure 2.1, since they are the most important parts of the apparatus and they are delimited by a dashed line indicating the bakeable parts.

In both pumping systems the forevacuum is obtained by a two-stage rotary pump provided with an inert gas (argon) inlet that operates automatically or is manually actuated, in order to prevent hydrocarbon contamination of the vessel. UHV is then reached by means of two water-cooled turbomolecular pumps, with nominal speeds of 500 and 330 l/s. The task of the pumping units is to evacuate the vessels V1 and V3 in 30 seconds, through the low impedance valves G1 and G2, down to less than 10^{-3} Pa starting from pressures as high as 10^{5} Pa. Residual pressures lower than 10^{-7} Pa prior to system bakeout at 300 °C and of less than 10^{-8} Pa afterwards

have been obtained before any experiment. The only elastomer present is a Vitilan O-ring inside the pneumatic gate valve G1. A steel safety support rigidly secures the vessel V1 and the furnace F to G1 so to avoid any risk of damage due to the violent action of G1 when operating.

Hydrogen with a nominal purity of 99.9999 % by weight is fed through the manual leak valve LV2 and through a nickel-plated, vacuum-sealed, glass liquid nitrogen trap (LNT), where the impurities present in the glass ducts (mainly Hg and H_2O) are condensed. The gas pressure may be measured by the U-tube Hg-manometer HgM, and is limited to about 1.2 bar by a Hg venting device.

The experimental chamber V1 is mainly made out of glass in order to reduce the background pressure due to wall outgassing and has a cylindrical shape with four ports. Two of them support the pressure heads (P1,P2,P3), the third terminates with a blanking flange BF and is used for inserting the sample holder and the sample; the fourth extends horizontally into the furnace F and carries a doubly wound platinum wire. This is the platinum resistance thermometer T1 which is described in the next subsection.

The temperature in the furnace F can also be checked by means of a nickel-nickel/chromium thermocouple placed on the quartz side-arm which supports the thermometer T1 and contains the sample. Both the sample-holder and the side-arm are made of quartz, whereas the rest of the glassware is of pyrex. A second platinum resistance thermometer T2 immersed in the vessel V1 measures the gas temperature in the cold part of V1.

The volume V1 has been calibrated by repeated hydrogen expansion from a known reference volume $U = 1.044 \times 10^{-3}$ m^3, measured by filling with water and weighing. If p_1, T_1 and p_2, T_2 respectively are the hydrogen pressure and temperature before and after the expansion, the volume V of V1 is

$$V = U \left(\frac{p_1 T_2}{p_2 T_1} - 1 \right) \quad . \tag{2.1}$$

The average of several measurements was

$$V = (5.495 \pm 0.004) \times 10^{-3}\,\mathrm{m}^3 \quad . \tag{2.2}$$

Pressures in the range 10^{-5} - 10^{5} Pa can be measured by means of two fast-response absolute capacitance manometers P1, P2 covering five decades each be-

tween 10^5 and 10^{-3} Pa and of one spinning rotor gauge P3 between 10^2 and 10^{-5} Pa.

The spectrometric unit comprises a spherical glass vessel V3 with a volume of about 6 litres, containing a Bayard-Alpert type gauge BAG and the quadrupole mass filter head QMF used for gas analysis. The quadrupole operates at pressures lower than 10^{-2} Pa, so small quantities of gas have to be expanded from the small volume V2 (some cm^3) into V3 through the manual valve MV. Several spectra are recorded before and during the expansion, so that background subtraction and extrapolation to the time at which MV is opened can be performed. In this way the influence of the QMF gauge head and of outgassing from the walls of V3 is greatly reduced.

A section view of the furnace F is shown in Figure 2.2. The heating element is an

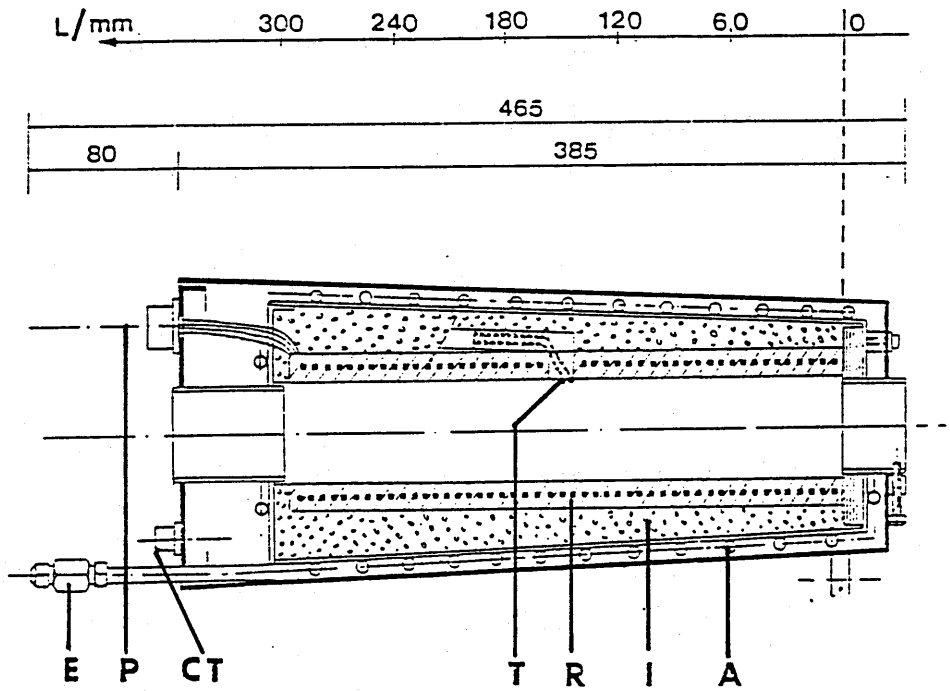

Figure 2.2 Lengthwise section view of the furnace F. Key to symbols: A – cooling water jacket, CT – thermocouple connections (output), E – cooling water inlet and outlet, I – insulating layer, P – power input from mains, R – heating coils, T – thermocouples.

electrical resistance wire spirally wound inside a refractory tube. A thick insulating layer and a water cooling jacket provide good thermal insulation from the ambient. Two nickel/chromium-nickel thermocouples placed between the heating coils in the

middle of the heated tube are devoted to temperature regulation and checking. The supplier's specifications gave a 0.1 m long homogeneous temperature region, within a tolerance of ± 4 °C, when the furnace is placed vertically. For horizontal positioning no figures were given, so several temperature profile measurements have been carried out at different temperatures and with different insulation conditions. The tests were performed by means of a calibrated chromel-alumel thermocouple. It turned out that the horizontal furnace has a flat temperature profile region about 0.04 m long centred at the abscissa L=150 mm in Figure 2.2. This can be seen in Figure 2.3 where different temperature profiles have been assembled. The furnace was therefore positioned so that the thermometer T1 was centred on the point L=150 mm. A proportional temperature controller provides a temperature stability of ± 1 K.

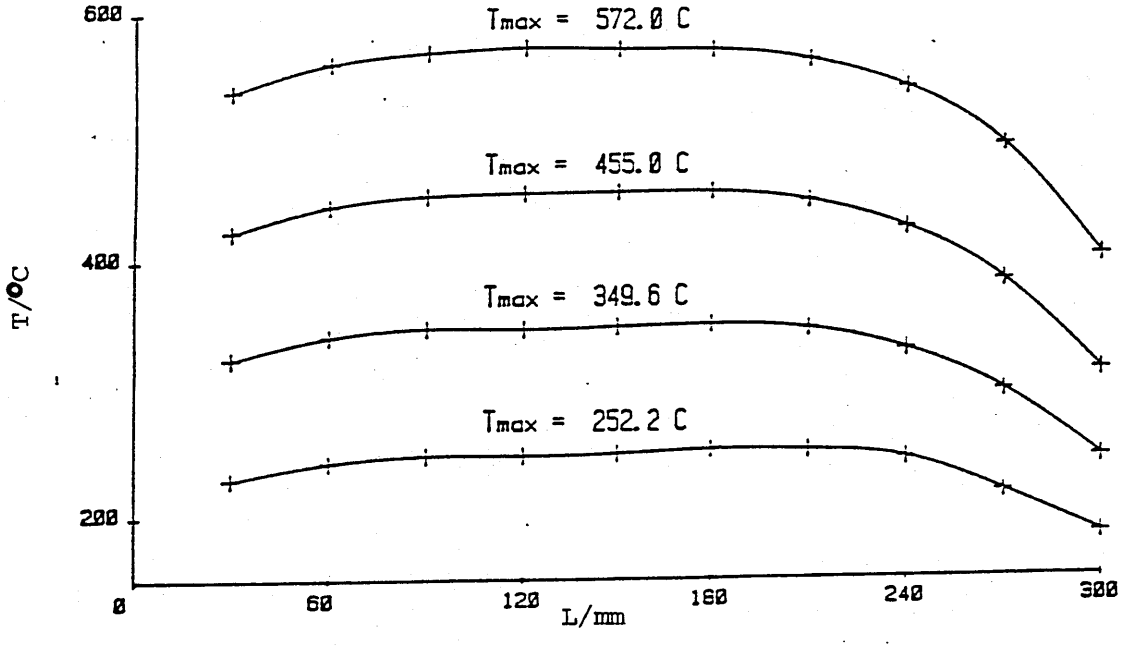

Figure 2.3 Furnace axial horizontal temperature profiles.

2.1.2 Temperature measurement

The measurement of the temperature plays an important role in this study since the gas-material interaction can be strongly temperature dependent. Therefore a high precision is needed in temperature measurement. For example, the temperature resolution required to measure hydrogen diffusivity in nickel to 1 percent is

$$\Delta T = 0.01\ RT^2/Q \tag{2.3}$$

where $Q = 2.15$ kJ mol^{-1} is the activation molar energy of diffusion, R is the gas constant and the temperature T is expressed in K. This would give 0.5 K at 473 K and 1.7 K at 873 K.

The instrument needed to measure the sample temperature should satisfy the following requirements:

1. working interval from 0 °C to 650 °C;
2. high stability and reproducibility, of the order of some mK per hour, to allow a repeat of the same run with no sample after a long time;
3. high precision, of the order of some tenths of K due to the alleged strong temperature dependence of the processes to study.

The use of thermocouples was therefore limited to checking and regulation only and a four-terminal Platinum Resistance Thermometer, referred to as PRT in the following, was built and calibrated to suit our particular requirements.

Resistance thermometry

The well-known variation of the electrical resistance of a metal with the temperature is used, through the empirical law

$$R(\theta') = R_o(1 + A\theta' - B\theta'^2)\ , \tag{2.4}$$

which links the resistance of a metal wire R measured in Ω to the temperature θ', measured in degrees °C. Calibration at three fixed points [45] gives the constants R_o, A, B, all of them positive. It is worth noticing that R_o is the resistance value

at $\theta' = 0$, the so-called ice-point. Alternatively, setting $W(\theta') = R(\theta')/R_o$ in (2.4) gives Callendar's equation

$$\theta' = \frac{W(\theta') - 1}{\alpha} + \delta \left(\frac{\theta'}{100} - 1 \right) \frac{\theta'}{100} \ , \tag{2.5}$$

with

$$\alpha = \frac{W(100) - 1}{100} = A - 100B \tag{2.6}$$

$$\delta = 10^4 \frac{B}{\alpha} \tag{2.7}$$

and hence

$$A = 1 + \frac{\delta}{100} \ , \tag{2.8}$$

$$B = \alpha \delta 10^{-4} \ . \tag{2.9}$$

Experiments [45] showed small deviations of "Callendar's temperature" θ' with respect to thermodynamic (gas thermometry) temperature, so that a correction $\Delta\theta'$ is required

$$\Delta\theta' = 0.045 \frac{\theta'}{100} \left(\frac{\theta'}{100} - 1 \right) \left(\frac{\theta'}{419.58} - 1 \right) \left(\frac{\theta'}{630.74} - 1 \right) \ , \tag{2.10}$$

to give the corrected temperature

$$\theta = \theta' + \Delta\theta' \ . \tag{2.11}$$

The correction $\Delta\theta'$ is always smaller in magnitude than 0.05 °C. The values of R_o, α and δ or alternatively of R_o, A and B, characterize the PRT, δ being related to the state of the platinum wire and α to its purity, with which it increases. A Standard PRT (SPRT) to be used as reference for calibration requires $\alpha \geq 3.925 \times 10^{-3}\ ^\circ\mathrm{C}^{-1}$ [45].

After calibration, the measurement of the resistance R gives the temperature θ'

$$\theta' = \frac{A - \sqrt{D(R)}}{2B} \ , \tag{2.12}$$

with

$$D(R) = A^2 - 4B \left(\frac{R}{R_o} - 1 \right) \ . \tag{2.13}$$

Accidental errors in R measurement are statistically averaged out by considering only the arithmetic average $< R >$ and the standard deviation σ_R of a large number of readings. Uncertainty analysis [46], gives

$$< \theta(R) >= \theta(< R >) + \sigma_R^2 \frac{B}{R_o^2 [D(< R >]^{3/2}} \ , \tag{2.14}$$

where

$$\theta(< R >) = \frac{A - \sqrt{D(< R >)}}{2B} \tag{2.15}$$

and

$$\sigma_\theta = \frac{\sigma_R}{R_o \sqrt{D(< R >)}} \ , \tag{2.16}$$

where the prime $'$ has been dropped for simplicity.

PRT construction, annealing and calibration

A quartz tube was weld-closed at one edge and a double groove, devised to house the platinum wire, was spirally drawn on its outer surface with a diamond tool. Seven small quartz pegs at the beginning and at the end of this spiral served as fixed support for the wire. This was doubly wound inside the grooves to gather its two edges so that the resulting four leads could follow the same path. In this way winding the wire was easier. In order to separate the two pairs of leads, the weldings to the sensor wire were executed at diametrically opposed positions on the quartz tube causing a length difference between the two coils of half a turn. The two edges of the sensor wire were directly discharge-welded onto the four platinum leads, the latter being then inserted into thin fibreglass protection sheaths. The four platinum terminals were then brazed to shielded copper cables and the platinum-copper junctions were placed into an ice bath in a Dewar flask. A quartz case was provided for easier handling and to prevent damage and contamination of the platinum wire. The thermometer was fitted in a resistance measuring network, composed of a standard PRT calibrated at the Physikalische Technische Bundesanstalt, Braunschweig, used as a reference during the calibration, in series with a reference resistor used

to measure the intensity of the current flowing in the circuit. This was provided by a computer driven digital-to-analogue power supply which closed the circuit. A computer driven scanner and a digital voltmeter (DVM) were used to measure in turn the voltages across the three resistors. After acquisition and processing the computer programme combined the voltages using Ohm's law to give the required resistances. Each single measurement was repeated with inverted polarity and with the same intensity and the average was taken to eliminate emfs due to heterogeneity in the circuit combined with thermal gradients.

Stabilization of the platinum sensor was achieved by one bakeout in air at about 850 °C followed by several others at 650 °C, each one lasting more than 24 hours. Between two successive bakeouts the 0 °C resistance was measured and the relative variation $\Delta R_o/R_o$ was taken as an indication of the stability so far achieved. An equivalent drift of the order of 1 mK/hr, which is what is required for a reference SPRT [45], was finally achieved.

The calibration was carried out at the ice-point (0.00 °C) and at the steam point (100.0 °C). The use of a SPRT coupled to a procedure based on Matthiessen's addition rule [48] provided the information required to determine the third parameter of the empirical law (2.4). The measurements were repeated with 1 mA and 2 mA for the measuring current in order to evaluate the Joule self-heating effect, which proved to be negligible. The SPRT was previously checked through several 0 °C resistance measurements which confirmed the old calibration. Then the coefficients were updated according to the modification of the sulfur boiling point, changed in 1968 from 444.600 °C to 444.674 °C. The revised coefficients are then

$$R_{os} = 11.3816\,\Omega \ , \tag{2.17}$$

$$A_s = 3.9839 \times 10^{-3}\,°C^{-1}\,, \alpha_s = 3.9249 \times 10^{-3}\,°C^{-1} \ , \tag{2.18}$$

$$B_s = 5.897 \times 10^{-7}\,°C^{-2}\,, \delta_s = 1.50245°C \ . \tag{2.19}$$

The universal Cragoe's function Z(θ_1,θ_2,θ) [47]

$$Z(\theta_1, \theta_2, \theta) = \frac{R(\theta) - R(\theta_1)}{R(\theta_2) - R(\theta_1)} \ , \tag{2.20}$$

depends on θ, θ_1, θ_2 only and is the same for every PRT calibrated at the temperatures θ_1, θ_2. This is due to Matthiessen's rule [48]

$$R(\theta) = R_i + R_T(\theta) \ , \tag{2.21}$$

according to which the electrical resistance of a metal is the sum of a temperature-dependent part $R_T(\theta)$ and a term R_i depending on the impurities contained in the metal. The function $Z(\theta_1,\theta_2,\theta)$ is supplied by the SPRT with $\theta_1 = 0\,°C$, $\theta_2 = 99.4\,°C$ (the effective calibration temperature due to altitude effects):

$$W_s(\theta') = 1 + A_s\theta' - B_s\theta'^2 \tag{2.22}$$

so that

$$Z(\theta_1, \theta_2, \theta') = \frac{W_s(\theta') - 1}{W_s(\theta_2) - 1} \tag{2.23}$$

which, by means of (2.22), becomes

$$Z(\theta_1, \theta_2, \theta') = \frac{(A_s - B_s\theta')\,\theta'}{W_s(\theta_2) - 1}, \tag{2.24}$$

where $F = W_s(\theta_2) - 1 = 0.390173$. As for the PRT, one has

$$W(\theta') = 1 + [W(\theta_2) - 1]\ Z(\theta_1, \theta_2, \theta') \tag{2.25}$$

with $G = W(\theta_2) - 1 = 0.381991$ from the PRT calibration measurements. Hence the coefficients are $A = A_sG/F$ and $B = B_sG/F$ or

$$R_o = 20.2787\ \Omega \ , \tag{2.26}$$

$$A = 3.9813 \times 10^{-3}\ °C^{-1}\ ,\ \alpha = 3.9224 \times 10^{-3}\ °C^{-1} \ , \tag{2.27}$$

$$B = 5.8931 \times 10^{-7}\ °C^{-2}\ ,\ \delta = 1.50243\ °C \ . \tag{2.28}$$

Previous checks on R_o performed after very long experimental runs showed that these runs had a stabilizing effect on the sensor wire, by slightly increasing the values of α and δ.

2.1.3 Specimens

TiC-coated metallic cylinders and the bare metallic substrates have been studied. Two different substrates have been chosen with markedly different thermal expansion coefficients, different expected hydrogen solubilities and diffusivities and that are both relevant to fusion technology application. They are the austenitic stainless steel AISI 316L and the molybdenum-based alloy TZM. The specifications for each type of specimen are reported below.

AISI 316L

The nominal composition of the AISI 316L steel in wt% is [21] Fe=65.31, Cr=17.3, Ni=12.4, Mn=1.8, Mo=2.3, Cu=0.2, Co=0.17, C=0.024, Si=0.46, P=0.03, S=0.001. Its melting point is 1400 °C, the structure is FCC and its linear thermal expansion coefficient varies from 15×10^{-6} to 22×10^{-6} °C^{-1} in the temperature range (20-1000) °C [49].

The steel cylinders were 0.06 m long, with a diameter of 0.006 m and an average mass $m = 13.51 \times 10^{-3}$ kg, which gives an average density $< \rho >= 7.957 \times 10^3$ kg/m^3. This is exactly the value obtained at the temperature $T = 293$ K, by means of the formula [49]

$$\rho = 8084 - 0.4209\,T - 3.89 \times 10^{-5}\,T^2 \tag{2.29}$$

where ρ is in kg m^{-3} and T in K.

TZM

The nominal composition of the TZM alloy in wt% is Mo=99.2, Ti=0.5, Zr=0.08, C=0.01-0.04. Its melting point is taken to be approximately the same [24] as for molybdenum, i.e. 2610 °C, the structure is BCC, the linear thermal expansion coefficient is about 5.6×10^{-6} °C^{-1} in the temperature range (20-1000) °C.

The TZM cylinders used were 0.06 m long, with a diameter of 0.005 m and an average mass $m = 11.95 \times 10^{-3}$ kg, which gives a density of 10.15×10^3 kg m^{-3}. This is fairly close to the value for molybdenum of 10.20×10^3 kg m^{-3} at 293 K.

Treatment

Both types of substrate have been mechanically smoothed and chemically cleaned before testing. Other samples, treated in the same way, have been coated with titanium carbide (TiC) by HTM Biel, Switzerland.

TiC-coated specimens

The coating production takes place at 1323 K in a vapour phase by Chemical Vapour Deposition (CVD) according to the reaction

$$H_2 + CH_4 + TiCl_4 \rightarrow TiC + 4HCl \uparrow + H_2 \uparrow \tag{2.30}$$

where hydrogen is added as a catalyser. In this way dense, compact coatings can be obtained on very complex shapes. The melting point of TiC is at 3340 K, its density is 4.91×10^3 kg m^{-3} and it has an average linear thermal expansion coefficient of 7.4×10^{-6} °C^{-1} [43].

Three thicknesses have been obtained, on both types of substrate, nominally of 0.5, 1 and 3 μm.

2.2 The Oxford rig and specimens

2.2.1 General description of the apparatus

The rig used at the Oxford Research Unit had previously been developed and converted from a permeation-type into an absorption-desorption apparatus [50]. It was put into operation for this thesis after a long period of inactivity. It was thoroughly checked and several parts had to be replaced as they turned out to be inoperative. However the basic original design and philosophy were not affected.

The apparatus is schematically presented in Figure 2.4. It comprises a UHV part, enclosed in a rectangle labelled OVEN in the figure, and below that, a low-vacuum part, which extends from the palladium-thimble PT through the valve V9

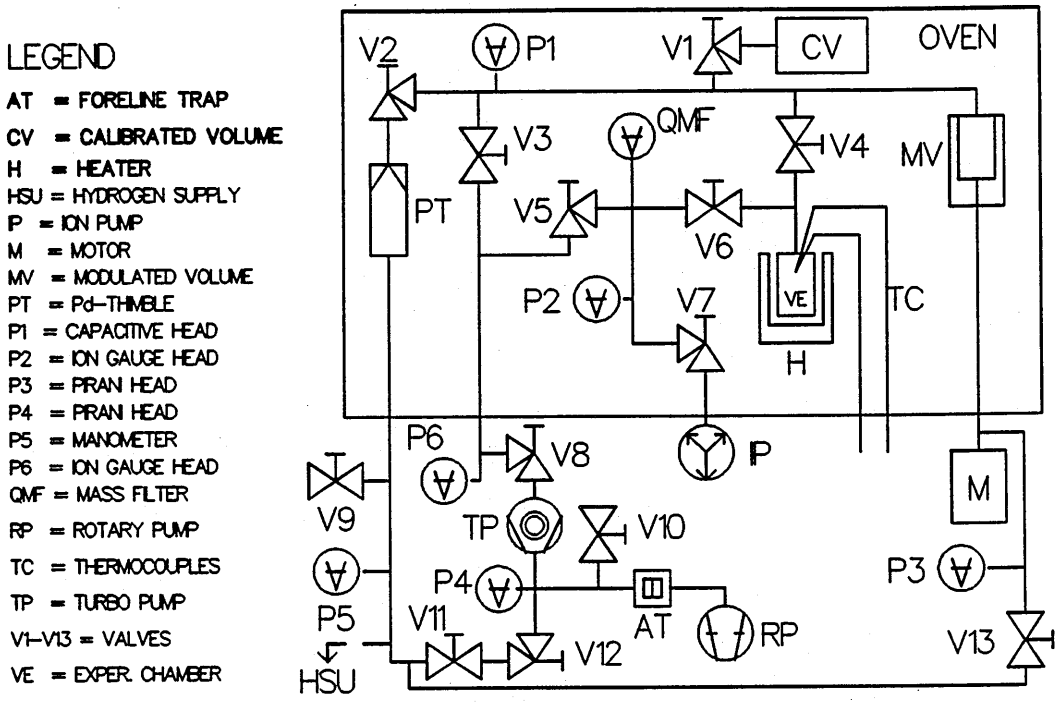

Figure 2.4 Schematic view of the Oxford volume-modulation apparatus.

and the Pirani gauge P4 to the rotary pump RP and through the valve V13 to the variable volume MV which contains the modulating bellows.

The pumping system is composed of the rotary pump RP, with a pumping speed of 16 m^3/h, the foreline trap AT and the turbomolecular pump TP, with a pumping speed of 0.36 m^3/h. Ultimate pressures on top of the two pumps are less than 10^{-2} Pa for the rotary pump RP and less than 10^{-8} Pa for the turbopump TP. The sorption trap AT is filled with type 5A molecular sieve pellets (1/8", calcium alumino-silicate) and acts as a filter for water vapour and backstreaming hydrocarbons from the rotary pump RP into the turbopump TP. The pumping system can be vented to air by means of the manual valve V10 and is separated from the experimental vessel by the manual valve V8. The ion pump IP provides additional pumping capability, through the valve V7. The low vacuum part of the rig can be pumped with the rotary pump RP and the pressure is monitored by the Pirani gauges P3 and P4 from atmospheric pressure down to 1 Pa and by the manometer P5 between 10^3 and 10^5 Pa.

Pressures in the high-vacuum part of the rig are measured by the ion gauges P2 and P6 in the range 1 Pa to 10^{-9} Pa and thanks to the quadrupole mass spectrometer QMF at pressures below 10^{-2} Pa. The fast-response absolute capacitance manometer P1 is kept at a fixed temperature of 323 K and is used for quantitative pressure readings during a volume-modulation run. With a precision of four and a half digits, this manometer covers the range 10^{-3} Pa – 100 Pa.

The experimental chamber VE has a volume of about 9×10^{-5} m^3 and can be isolated from the rest of the vessel by means of the manual valves V4 and V6. The cylindrical chamber VE is electrically heated by a furnace H constituted by a cold-ends sheathed thermocoax heating element, wound in a double spiral around VE and kept in position by a cylindrical tube. This is fixed to the chamber with three screws and it is wrapped in alternated layers of asbestos tape and aluminium foil to reduce heat losses by conduction and radiation towards the outside. A radial gradient larger than 5×10^4 K/m has been achieved in air at 900 K. Temperatures up to 1173 K can be reached to $\pm$ 1 K, by means of a three-term temperature controller.

Temperatures inside the chamber VE are measured by three calibrated chromel-alumel thermocouples TC, with reference junctions kept in a thermostatic bath at 318 K. Thermocouple voltages are converted into temperatures by a third degree Lagrange polynomial interpolation in a calibration conversion table. A fourth thermocouple is devoted to temperature regulation. All thermocouples are in contact with the specimens inside the chamber VE.

The total volume can be varied by up to 25 per cent thanks to the motor M, which drives a linear motion feedthrough and then the bellows. The total volume has been measured by the same method adopted at Ispra and reported in 2.1.1. This consists in recording the pressure with P1 before and after successive gas expansions from the calibrated volume CV into the vessel through the toggle valve V1. Such calibrations have been carried out at different pressures. The volume of CV has been determined, again by weighing the amount of water contained in it, to be about $U = 1.59 \times 10^{-4}$ m^3. By means of equation (2.1), the average of several measurements has given a total modulated volume

$$V_e = (1.345 \pm 0.015) \times 10^{-3} \mathrm{m}^3 \ , \tag{2.31}$$

obtained with valves V2, V6 closed and V4 open. The UHV components of the apparatus are made of stainless steel, apart from the chamber VE, made of Fecralloy to reduce hydrogen absorption and desorption by the inner walls of the rig during the experiments.

Hydrogen from the supply cylinder is fed to the experimental vessel after being purified through the palladium-thimble PT, which is heated by a cold-ends sheathed thermocoax wire to 423 K - 473 K. The temperature is monitored through another chromel-alumel thermocouple, not shown in the figure, which is also used for temperature regulation. The gas composition can be checked with the quadrupole filter QMF, by spilling small amounts of gas through the leak valve V6 under dynamic vacuum conditions in the QMF branch of the apparatus.

The rig can be baked out by the modular movable OVEN at a maximum temperature of 443 K, this limitation being imposed by the presence of epoxy resin in the capacitive head P1. Additional heating of the UHV parts outside the OVEN is achieved by electric heating tapes, wrapped around the steel UHV components.

The endowment is completed by a computer which drives the experiments through a six and a half digits digital voltmeter and a scanner. These are coupled to

- a modulator control unit, which controls the motor M,
- a dual auto-offset amplifier which offsets the pressure and volume signals before starting a modulation run at a given frequency,
- a digital-to-analogue converter used by the computer to control the furnace temperature and to provide the required modulation sine wave to the modulator control unit,
- an opto-isolator, for triggering the offset of pressure and volume signals.

2.2.2 Specimens

Cylindrical specimen of TZM coated with 8 μm TiC have been studied. The TZM specifications have already been given in 2.1.3. The only difference is the size of the cylinders, which have a radius of 5×10^{-3} m while the height is 1.5×10^{-2} m.

According to the supplier's specification, after chemical cleaning of the substrate, coating took place at 1300 K for two hours at 10 mbar above atmospheric pressure, in a mixture of gas with the following composition in per cent by volume:

$$H_2 - 77.6,\ TiCl_4 - 2.6,\ Ar - 11.3,\ CH_4 - 8.5\ .$$

Again, hydrogen is added as a catalyser.

It is to be recalled that the gas pressure is markedly different from that reported for the coating deposited by the other supplier.

2.3 Summary

The experimental rigs used for this thesis at the JRC Ispra and at the Oxford Research Unit have been described in this chapter.

Both are computer-controlled UHV rigs, devised to study the hydrogen absorption and desorption behaviour of solid specimens.

Temperature measurement by platinum resistance thermometers has been addressed as it is relevant to the Ispra rig.

The characteristics of the specimens studied have been described.

Chapter 3

Experimental Methods and Procedures

A separate description is given of the experimental methods and the procedures used at JRC Ispra and at the Oxford Research Unit. After some generalities on the methods, the way a single experiment runs is described with particular stress on the measured observables and their handling. The computer programmes that run the experiments are briefly presented and quantitative mass spectra recording and analysis are addressed. Intermediate procedures on raw data are also discussed together with data fitting computer programmes. The techniques used to characterise the samples are concisely recalled and results of the characterisation tests are given. Problems and questions arising from these results are discussed.

3.1 JRC Ispra procedures and sample characterisation

3.1.1 The method

A first aim of the experiment was to determine the concentration of hydrogen absorbed at equilibrium by a sample under given experimental conditions (pressure and temperature), a quantity which is referred to as the hydrogen solubility in that material. It is also required to study the dependence of the solubility on the experimental conditions. This involves investigating equilibrium properties of the sample-gas system.

A second task was to study the kinetics of approach to the equilibrium state, by

measuring the evolution in time of the absorption/desorption process. The dependence of this transient on the experimental conditions was also to be investigated.

A simple way to determine the solubility would be to measure the pressure drop caused by gas absorption by a specimen placed in a closed chamber containing the gas, at the required experimental conditions. As anticipated in chapter 1, the solubility of the materials to be studied is expected to be low, hence the pressure drop due to absorption would be so small that it would be masked by temperature fluctuations and by systematic errors in the pressure reading. Here therefore, the desorption transient is recorded in time after a sharp perturbation of a previous high-pressure equilibrium state.

Single run description

The method used is an improved version of Eichenauer's gas evolution technique [51]. A sample of the material under study is loaded with hydrogen at a given temperature T and loading pressure p_0 in a closed vessel, which is then emptied by a short but thorough pumpdown, thereby triggering the release of hydrogen previously absorbed by the specimen. The pressure increase $p(t)$ in the experimental chamber is recorded as a function of time t, together with the temperatures of the specimen and of the gas, till a new equilibrium state is reached at the final pressure p_f. This sequence is repeated for different combinations of temperature T and loading pressure p_0.

Improvements with respect to Eichenauer's version are a higher and cleaner vacuum, an almost total computer control of the rig and of the experiments, modelling accounting for surface effects, non-linear least squares data fitting software which allows the use of the full pressure curve for automatic processing. This software also allows a precise correction for the gas lost during the pumpdown, without resorting to extra runs with different pumpdown times.

A single run is qualitatively shown in Figure 3.1, where the pressure evolution in time is given. For clarity, time and pressure axes are not to scale in that figure. For example, the ratio of p_0 to p_f depends on the hydrogen solubility of the material and can be as high as 10^4. In what follows, numbers in parentheses refer to the phases of a single run described in Figure 3.1.

After system bakeout and thermal cleaning at 973 K and at less than 10^{-7} Pa, the

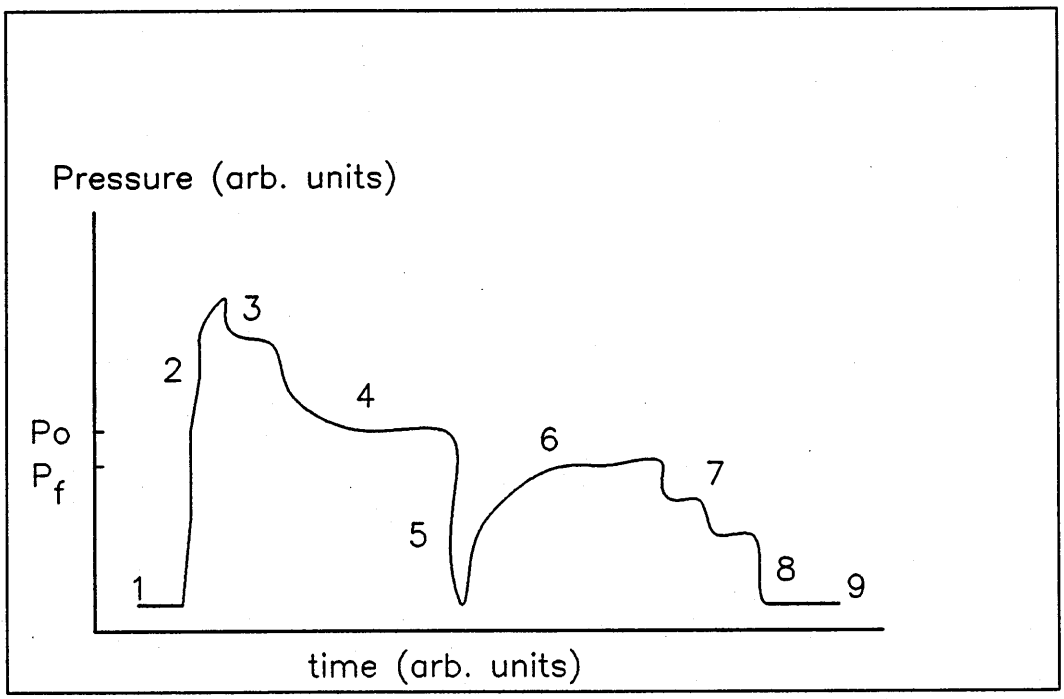

Figure 3.1 Qualitative presentation of a single absorption/desorption experiment.

required test temperature is set and a sufficient time is allowed for its stabilisation (1) under dynamic high vacuum conditions. In this period, the capacitive manometers are zeroed and full-scale adjusted. After isolating the pumping system, hydrogen is admitted (2) to the closed vessel and part is drawn (3) for purity check by mass analysis. The loading phase is started (4) by allowing the system to evolve towards equilibrium at the loading pressure p_0, for a sufficient time t_L. In this period some hydrogen penetrates in solution into the metal.

This equilibrium is perturbed (5) through a sharp decrease of the pressure by means of the pumping system. After 30 seconds the pumps are isolated again and the pressure versus time curve due to gas desorption (6) from the sample is recorded, for a time t_R sufficient to reach a new equilibrium at the final pressure p_f. Again, a sample of the gas is mass-analysed for composition (7), after which the vessel is evacuated (8) and thermally cleaned (9) before starting another run.

During a desorption run, the time t, the pressure p and the temperatures T_A, T_B in the hot and in the cold part of the vessel are measured. Small fluctuations in the pressure due to temperature effects are eliminated by combining p, T_A and T_B into

a *normalised pressure* P as follows

$$P(t) = p(t)\frac{T_N}{V}\left[\frac{V_A}{T_A} + \frac{V_B}{T_B}\right] \quad , \tag{3.1}$$

where $V = V_A + V_B$ is the total volume of the vessel and the subscripts A, B refer to its hot and cold parts and T_N is an arbitrary normalising temperature, taken equal to 293.15 K. As a rule, $V_A/V = 0.04$ and $V_B/V = 0.96$, whereas $T_A/T_B > 2$, depending on the run temperature. The small amount of gas released during the pumpdown and lost to the pumps is accounted for by the data processing computer programmes.

When dealing with a completely unknown gas-material system, trial experiments have to be carried out in order to determine the minimum loading and release times t_L, t_R to achieve equilibrium during loading and release. In particular, t_L needs to be large enough for the concentration in the sample to become uniform throughout the specimen. Therefore a trial run with an estimate of these times is carried out and then repeated with increasing values of t_L and t_R until the measured pressure curves attain the same final value p_f no matter what are the values of t_L and t_R. This task is made more difficult by the background contribution from the walls of the vessel. To maximise the signal-to-noise ratio, very good initial vacuum conditions are required, together with the use of low-outgassing materials such as pyrex and quartz in the construction of the vessel. Samples having the highest mass compatible with the vessel dimensions and with the size of the thermally flat region inside it are used to that end. The current design allows up to four cylinders, each 6 cm long, to be accommodated in the sample holder. Nonetheless, due to the low hydrogen solubility of the materials studied, the background was still not negligible, typically about 10 per cent and in some extreme cases 60 per cent of the total signal. For this reason, a blank run, with no samples in the rig, has to be carried out in exactly the same experimental conditions of pressure, temperature, initial vacuum (pumping time between two consecutive runs) and loading time as are used in the actual runs. The blank run is then subtracted from the run with samples, to yield the net contribution from the samples under additivity hypotheses.

Gas analysis

A quantitative spectrometric analysis of the gas used is required before and after each run:

1. to check the purity of the gas used so that measures can be taken to reduce as much as possible the amount of impurities, as they might strongly affect the dynamics of the hydrogen interaction with the sample; in particular, the gas should be free of oxygen and carbon, since even small amounts of these elements on the sample surface may act as a barrier to the penetration of hydrogen into the metal;

2. to correct, if necessary, the total pressure curve measured by capacitive manometers, into a hydrogen partial pressure curve, to which the mathematical analysis can be applied.

The upper limit on the pressure during gas analysis imposed by the use of the quadrupole mass filter, about 10^{-2} Pa, makes it necessary to follow a procedure based on gas expansion between two volumes having a volume ratio of about 10^{-2}. Account was taken of the variation of the gas composition during analysis because of outgassing from the walls and the hot filament or due to chemical reactions catalyzed by the hot filament, such as methane production from hydrogen and carbon, according to

$$C + 2H_2 \rightleftharpoons CH_4. \tag{3.2}$$

For such correction, each single spectrum scan was carried out once before expanding the gas to be analysed in order to determine the background composition, then several times during and after the expansion. The mass peak heights measured at different times were extrapolated to the time t=0 at which the expansion was started, this time being determined from the pressure increase during the expansion, as measured by a Bayard-Alpert gauge. An example of such extrapolated spectrum is shown in Figure 3.2 for the gas released after a run. The decimal logarithm of the ionic current is plotted in arbitrary units versus the mass/charge ratio m/q expressed in multiples of the value m_H/e for a proton.

After a complex analysis involving the use of standard cracking patterns, a hydrogen composition of more than 99.9 wt% was found, the main impurity being

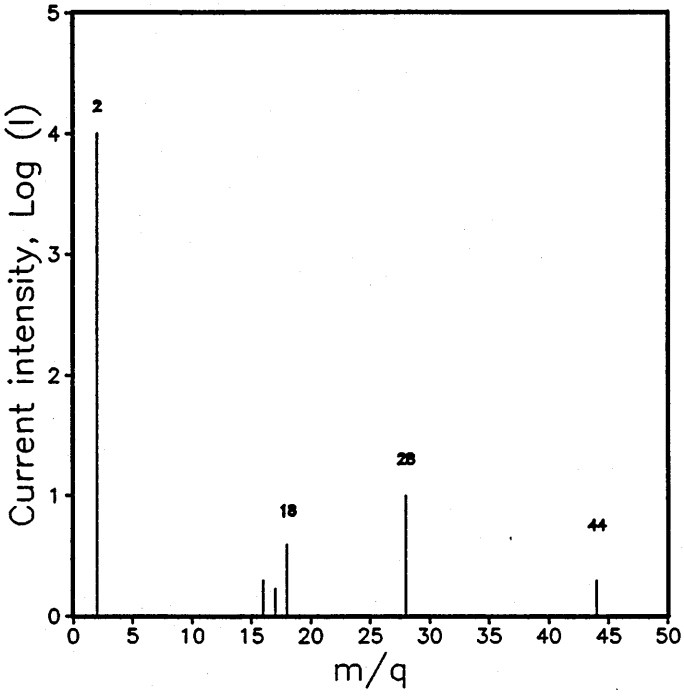

Figure 3.2 Extrapolated mass spectrum of the gas released after a run.

water in the range 100-200 wt ppm. Peaks at $m/q = 28$ and $m/q = 44$ corresponding to N_2, CO and CO_2, were already present as background in the analysis vessel, before the expansion was started.

The control computer programmes

Apart from temperature setting/control and gas inlet procedures, each run is totally computer-controlled by a number of FORTRAN programmes, running on the laboratory minicomputer under a real time operating system, which allows multiprogramming by time-slicing and time-scheduled operation of the instruments controlled. To this end an internal clock is used, with a minimum schedule interval of 10 ms. This clock is also used for time reading before or after reading an instrument.

Very quick pressure readings are needed during the release phase, since the pressure variation in time is very fast especially at the early stages of the release. Pressure reading has also priority over time and temperature readings. The time spacing between two consecutive measurements varies all along a release run, with 480 measurements divided into 4 sets of 120 equispaced measurements. The spacing doubles

from one set to the following, beginning with a base time t_B computed from the release time t_R as follows

$$t_R = 120\, t_B\, (1 + 2 + 4 + 8) \quad , \tag{3.3}$$

which takes the appealing form

$$t_B = 2\, t_{RH} \tag{3.4}$$

where t_R, t_B and t_{RH} are in seconds and $t_{RH} = t_R/3600$ is a rescaled release time, which has the value of the release time expressed in hours.

A single computer code controls twin rigs in the laboratory and can launch a set of four control programmes for each rig, two programmes for the loading phase and two programmes for the release phase. These programmes have been developed over the years by several members of the laboratory including the author. Each set of programmes "knows" the rig it is controlling and has access to information on the specimen-gas system under study.

A run starts after initialisation of instruments and programmes, by initiating the loading phase. In this period the computer just controls the run, by taking equispaced readings which are not used in the data processing steps. A *master* programme carries out this task and other general procedures such as data storage, printout production, control and regulation of the measuring current in the thermometer electrical circuits. It also schedules, at given fixed times, a *slave* programme which is only in charge of instrument reading and quick data processing and which passes the control of the rig back to his master together with the data just measured.

At the beginning of the loading phase, the master stops to prompt the user to insert the gas and reads the loading pressure p_0 at the end. It then opens the pneumatic gate valve G1 (see Figure 2.1) for 30 seconds so that the pumping system can evacuate the vessel and then closes it again. At this moment the control is transferred to another master-slave pair, designed for quantitative measurements during a release run and with a base time t_B. Again the control of the rig is swapped between master and slave till the time t_R has elapsed. The data are stored in a sequential disc-file for further processing.

3.1.2 Data processing

Each data file is treated prior to processing. Times are converted from absolute to relative values, referred to the time when the valve G1 is opened and the gas release is started. A new file is then created after deducting the blank run pressure $p_b(t_b)$ at the time t_b from the total (wall+sample) pressure $p(t)$ to give the net pressure $p_n(t_n)$ at the time t_n.

Thus, provided t and t_b are not too different, i.e. that

$$| t - t_b | < \varepsilon \, , \tag{3.5}$$

where we have taken $\varepsilon = 10^{-2}$ s, the time t_n is

$$t_n = \frac{t + t_b}{2} \tag{3.6}$$

and the net pressure at time t_n is

$$p_n(t_n) = p(t) - p_b(t_b) \, . \tag{3.7}$$

Relationship (3.5) tells when two time readings t and t_b are considered coincident.

An example of the blank correction is given in Figure 3.3 for hydrogen in TZM at 873 K and 10^5 Pa.

In order to decide whether the loading/release times used were sufficient to reach saturation, the pressure curves from several runs with increasing loading/release times were compared. Saturation of the sample was reflected by a final pressure which did not vary with increasing loading times.

To ascertain the presence of surface effects several runs at the same temperature but with different loading pressures were compared. Indeed, in a diffusion-limited release one would expect that normalised pressure curves $P(t)/P_f$ all overlap when plotted versus the time t. The fact that the normalised pressure increases with time more slowly as the loading pressure is lowered can be attributed to surface processes, as it is shown in the chapter on modelling.

Another preliminary check was carried out on the scaling of the final pressure P_f versus the loading pressure p_0. This scaling may be indicative of the state of hydrogen within the sample. The state can be modelled as atomic when P_f varies as $\sqrt{p_0}$ and as molecular if it varies as p_0. Any other dependence is suspicious

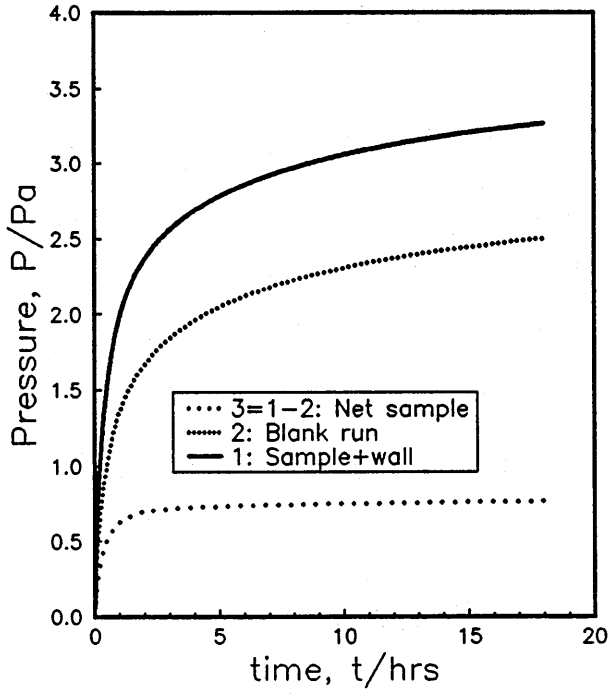

Figure 3.3 Pressure increase correction due to wall effects (worst case).

and is a serious hint that something was not working properly. For instance, other effects may contribute to the final pressure, such as surface contaminants giving off hydrogen.

Approximate values for the physical parameters involved in the theoretical models of the experiment (such as the diffusion coefficient, the solubility Sieverts' constant or the surface rate constants) have been determined . These are required as input in the subsequent non-linear data fitting software. They have been obtained by considering only a small portion of the release curve P vs t and an approximate form of the analytical solution valid for very long or short times. Then data fitting has been carried out with two models. An analysis of the trend of the fit parameters as a function of the loading pressure is useful to obtain a better estimate of these parameters. Results have been accepted on the basis of fit accuracy tables whereby the fitted curve was compared to the experimental one and accepted if a reasonable agreement could be achieved, say to within a few per cent.

Data fitting is carried out using a least-squares fit of a function $y(x, \underline{a})$ which is non-linear in the parameters $\underline{a}=(a_j)$, j=1,...,k. Here x is the independent variable,

i.e. the time t in our case, and y represents the normalised pressure. The value of $\underline{a}$ is chosen to minimise the sum χ^2 of the residues of the N experimental data points

$$\chi^2 = \sum_{i=1}^{N} \frac{[y_i - y(x_i)]^2}{\sigma_i^2} \quad , \tag{3.8}$$

where σ_i is the standard deviation of each data point y_i. This is equivalent to finding the minimum of the function χ^2 in the k-dimensional parameters hyperspace. The fitting programmes heavily rely on the iterative call of the powerful CURFIT subroutine [46], till convergence of the parameters is reached within a given tolerance, say 10^{-6}. It is of paramount importance to choose *independent* parameters, otherwise the algorithm may not converge at all, or converge locally to values that do not represent a true minimum.

3.1.3 Sample characterisation

Tests to characterise samples were essential especially as sample preparation was carried out by external suppliers. The following items were considered to be of direct importance in this experimental investigation:

1. state and morphology of the coating surface, with particular attention to degradation and crack formation,
2. determination of the actual coating thickness, needed for data processing and preliminary evaluation, especially in a diffusion-limited regime,
3. coating-to-substrate interface,
4. substrate composition after the coating deposition,
5. effect of thermal cycling in vacuum and in hydrogen on the previous items.

The coating surface was examined by high magnification optical microscopy and by scanning electron microscopy (SEM). The droplet-like morphology reported in the literature [52] characteristic of TiC by CVD was observed, as it appears in Figures 3.4 and 3.5, with apparent drop size of the order of the coating thickness. Crack formation was not detected in the samples tested, neither before nor after hydrogen

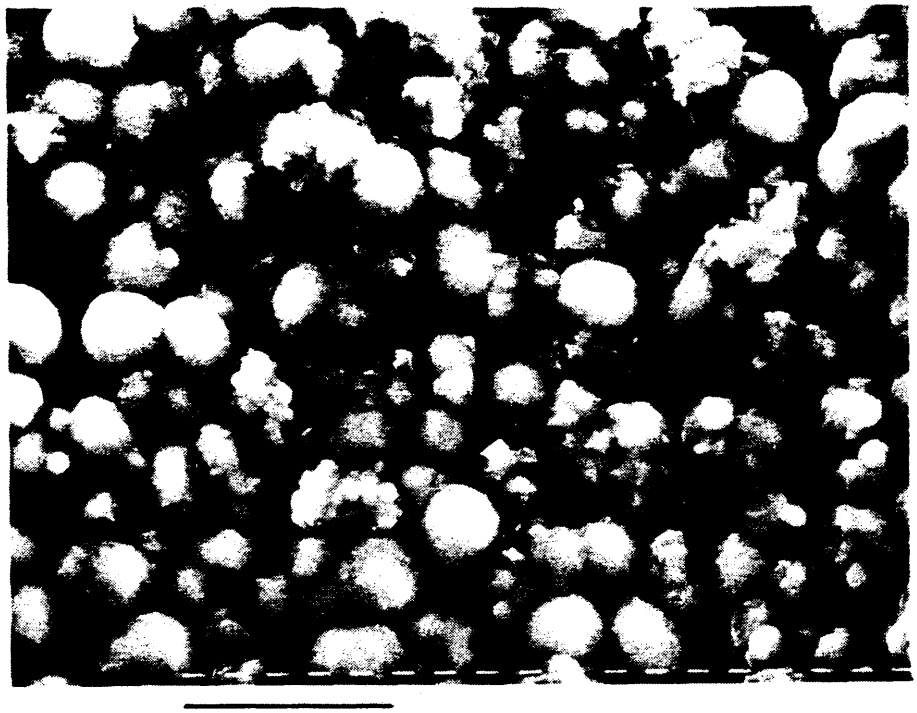

Figure 3.4 SEM picture of one as-received TiC-coated AISI 316L sample. The nominal coating thickness is 4 μm, the magnification is $\times$2700. The black segment is 10 μm long.

thermal treatment, whereas this did seem to affect the surface morphology, which acquired a spiky appearance. This is shown in Figures 3.4 and 3.5, wherein the surface morphology of one as-received coated sample is compared to that of one tested for long period in a hydrogen atmosphere and which has undergone several temperature cycles between room temperature and 873 K.

To determine the thickness, sections of samples have been inspected and analysed. Three thicknesses for the coatings on three different samples of AISI 316L steel, have been measured to be 0.5, 3 and 5 μm within a tolerance of $\pm$ 20 per cent. Whereas the TiC thickness was of 1 μm $\pm$ 20 per cent on the TZM specimen. These figures were determined from optical and SEM contrast estimates and then confirmed in the SEM by X-ray EDS line profiles of the metallic elements Cr, Fe, Mo, Ti. Traces of Cr and Fe could be detected in the TiC coating, with possible Mo and Cr segregation at the substrate/coating interface. This was rather sharp, i.e. with a width of less than 30 per cent of the thickness. The substrate was also

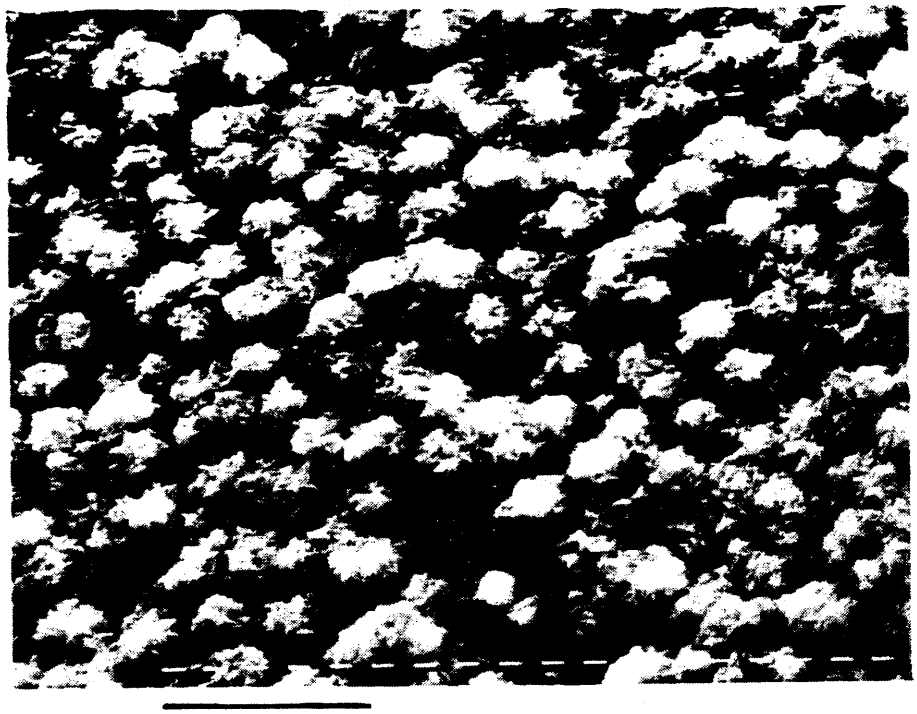

Figure 3.5 SEM picture of one TiC-coated AISI 316L sample after prolonged testing in hydrogen at high temperature and after repeated thermal cycling between room temperature and 873 K. The nominal coating thickness is 3 μm, the magnification is $\times$2700. The black segment is 10 μm long.

analysed with EDS and the composition agreed within 1 per cent with the supplier's specification for an AISI 316 steel, apart from carbon which was not detectable. No Ti penetration in the substrate was detected. As for TiC-coated TZM rods, quantitative Electron Probe Microanalysis showed that the substrate was composed of Mo with small traces of Ti, while Zr was outside the detection range of the machine. The composition was the same as in the uncoated TZM samples.

The SEM X-ray analysis was limited to elements with atomic number Z greater than 11 so that no data on the presence and the distribution of carbon could be obtained. For this, some qualitative analysis by Auger Electron Spectroscopy (AES) coupled to Ar^+ sputter-depth profiling was carried out. This was intended only as a complement to the previous investigations with the aim of revealing the effective presence of carbon in the coating. Indeed, a quantitative analysis of AES spectra would call for the quantitative determination of the atomic sensitivity factors in

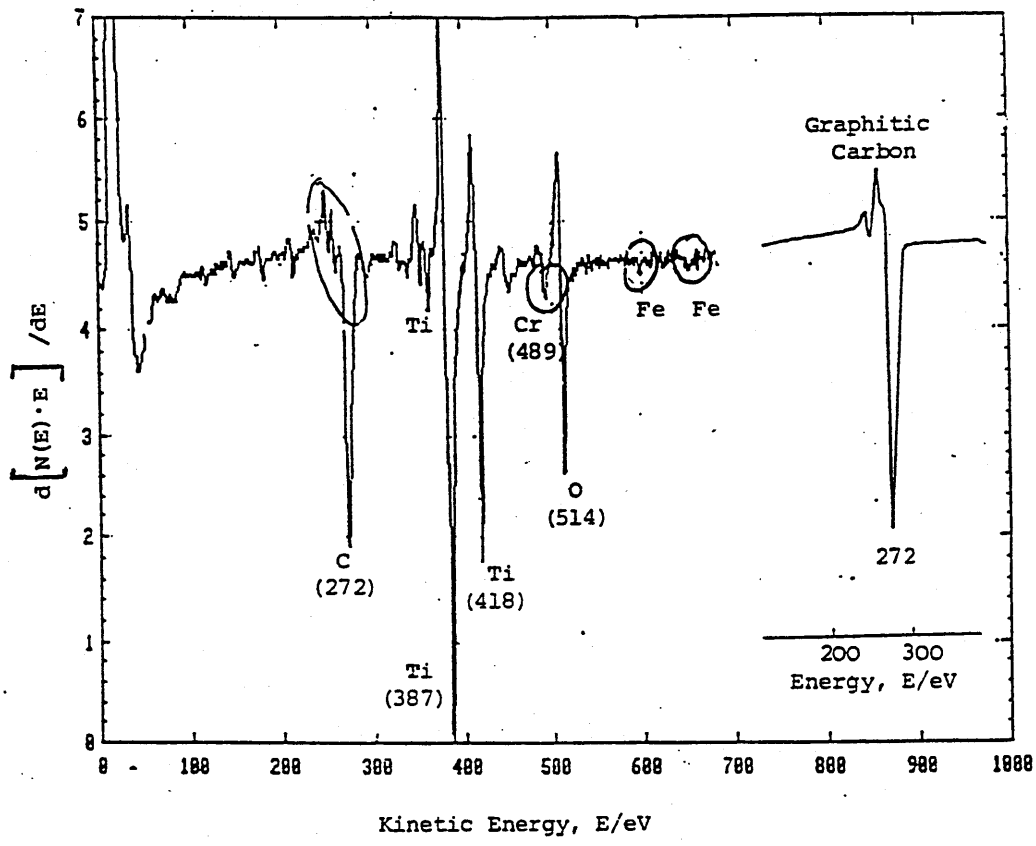

Figure 3.6 Differentiated AES spectrum of the TiC surface of one as-received coated AISI 316L rod. The nominal coating thickness is 0.5 μm. Numbers in parentheses give the energy of a given peak. Compare the shape of the multiple C peak at 272 eV with that in the insert for graphitic carbon.

the material under study, since the Ti peaks' energy position, shape and height in a Ti matrix are not the same as in a TiC matrix. The same is true for the C peak in a C matrix and in a TiC matrix. Special techniques, based on the use of standard specimens, would be needed to resolve overlapping peaks. Typical is the case of the N and Ti peaks at an energy of 387 eV. A calibration of the depth scale i.e. of the erosion rate in the matrix under study would be required when sputter-depth profiling with Ar^+ ions. Preferential sputtering of C over Ti should also be considered. Many of these data are not currently known and are not available in the literature.

An AES survey on the surface of one as-received 0.5 μm thick TiC coating on steel showed the presence of oxygen, graphitic carbon and carbidic titanium. This conclusion came from the peak energy position and shape, after comparison to literature data, as can be noticed in Figure 3.6.

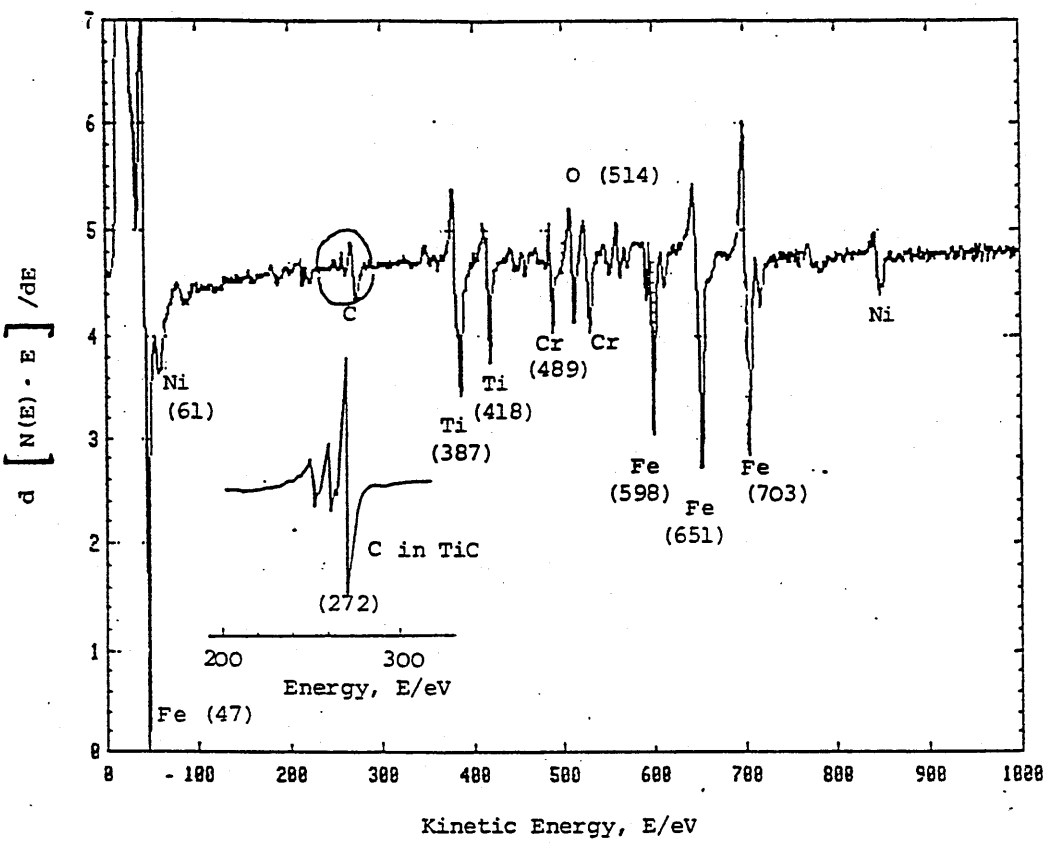

Figure 3.7 Differentiated AES spectrum of the TiC/steel interface of one as-received coated AISI 316L rod. The nominal coating thickness is 0.5 μm. Numbers in parentheses give the energy of a given peak. Compare the shape of the multiple C peak at 272 eV with that in the insert for carbidic carbon.

The carbon peak turned into carbidic (TiC) on moving into the coating and through the substrate/coating interface by sputter-profiling. At the interface the iron peak began to increase, the carbon peak decreased and was substituted for by oxygen whereas the titanium peak was still present, as depicted in Figure 3.7. This would suggest some preferential Ti deposition during the early stages of the CVD treatment, to form some Ti-O compound. Traces of Cl (from CVD treatment), Ar (from sputtering), Fe and Cr (from the substrate during CVD) were detected in the coating. From the C and Ti peak heights at 272 and 418 eV respectively and using sensitivities by [52] from a $TiC_{0.94}$ single crystal, a composition of $TiC_{0.936}$ for the coating was found.

Another AES analysis on a 3 μm-thick TiC coating deposited on the same AISI 316L steel, was carried out after a very long experimental campaign which involved repeated thermal cycles in hydrogen and vacuum. It showed that Ti and C had the

same depth in the coating and it was confirmed by an AES line scan on a section of the same sample, thus ruling out any preferential sputtering of C over Ti by Ar ions. An interface composed of Ti, C and Fe but no O was detected. The C peak height was not constant in depth inside the coating.

These qualitative results may suggest that thermal treatment in hydrogen may have some influence on the coating composition by triggering migration of C and O atoms. In any case this does not seem to have any effect on the hydrogen release characteristics, as it is shown in a later chapter. It would nevertheless be important to carry out a detailed and quantitative study of the thermal stability, i.e. on the effects that thermal treatments have on these coatings. In particular, it would be of interest to determine if an oxide interface is present between the coating and the substrate after TiC deposition and whether and under which conditions this can be removed by thermal treatments.

3.2 Procedures and sample characterisation at Oxford

3.2.1 The method

The aim of the experiments carried out at Oxford is the same as that of the work executed at Ispra, that is to study the interaction of gaseous hydrogen with a TiC coating and, by interpreting the experiments with suitable models, to determine values for solubility S, diffusivity D and surface rate constants k_1, k_2 as functions of pressure and temperature.

The means used to achieve this task are different, as at Oxford an equilibrium state is reached at the required pressure and temperature and then the volume of the closed experimental chamber which contains the specimen under study is varied periodically. In other words, while at Ispra the pressure transient is recorded after an equilibrium state is quickly and abruptly perturbed, at Oxford the same equilibrium is perturbed by a sinusoidal variation of the volume, readings of the pressure being taken after the transients have died out.

Restricting the volume oscillation to small amplitudes compared to the equi-

librium value, allows one to linearise the equations describing the hydrogen flow between the gas and the solid phases. In this way, the flow can be modelled analytically, with the simultaneous inclusion of both bulk diffusion and surface reactions.

A second difference is that the pressure around which the oscillation is executed can be chosen *a priori*, by successive approximations. This involves filling the chamber with hydrogen at the required temperature and pressure, waiting for equilibrium to be reached, then correcting the pressure by slowly pumping out or admitting hydrogen as appropriate till equilibrium is reached at the required pressure. This is not possible with the method used at Ispra, where only the loading pressure p_0 is chosen *a priori*.

The method used at Oxford was developed by Cummings and Blackburn [50]. Improvements performed in the course of this thesis work are mentioned as appropriate in this section.

Description of an experiment and of the control computer programme

In the following, reference is made to Figure 2.4.

The specimen under study is placed in the experimental chamber VE and then good vacuum conditions are obtained by baking out the whole rig while pumping it, down to the ultimate pressure of the system. Residual pressures below 10^{-7} Pa have been obtained in this way.

The rig is then computer-driven by means of the control programme. This requires as input the experiment temperature, the number of runs, each one with a fixed frequency, the frequency range, the temperature ramp rate and the plateau time. This time is needed for pressure equilibration before starting a run. A maximum ramp rate of 300 K/h is allowed.

The control programme ramps up the temperature. As this causes an increased outgassing by the specimen and the walls of the apparatus, the program stops and waits until good vacuum conditions have been restored. In this period the rig is again continuously evacuated, till the ultimate pressure is reached and the capacitance manometer P1 is zeroed. Ion gauges are switched off so to diminish the ultimate pressure and both gas pressure and composition are determined by the quadrupole QMF. Typical spectra revealed hydrogen, water, methane, nitrogen, carbon monox-

ide and carbon dioxide, these last four, present in trace quantities, mainly attributed to the analysis vessel. Hydrogen is the main peak however, higher by a factor of 5 than the water peak.

Purified hydrogen is then admitted through the heated palladium-thimble PT and the valve V2 at the required pressure, measured by the capacitance head P1. During this operation, the valves V3 and V6 are kept closed and the experimental chamber is not pumped. The quadrupole QMF is in operation and continuously evacuated through the valve V5, which is left open. Gas purity checks can be performed, by feeding gas through the leak valve V6, under dynamic vacuum conditions. Such qualitative gas analyses gave spectra similar to that of Figure 3.2 discussed in 3.1.1, and with the hydrogen peak dominating all the others by a factor of 1000.

The computer programme is made to resume the control of the rig, and it measures pressure and temperature at fixed times during the plateau time. The system is left to reach an equilibrium state at the pressure p_e, at which the hydrogen concentration in the specimen is uniform.

At the end of this period, which may vary from hours to days, the pressure p_e is measured and both volume and pressure signals are electronically offset by the amounts V_e and p_e. Then the volume of the chamber is caused to oscillate by means of the bellows contained in MV, at the required frequency ν. After enough time has passed to allow the transients to decay, typically the largest between twice the cycle time and fifteen minutes, readings of the offset pressure and volume are taken by the digital voltmeter and stored in the computer's memory, at given intervals of time. The computer's time base and scheduling capability are used for this. The volume signal is given by the output from the position transducer which is used to drive the linear motion feedthrough and the bellows.

Volume and pressure measurements continue for at least one period of oscillation, depending on the frequency. While the readings are taken, the volume and pressure waveforms are plotted on the screen and then dumped to the printer when the run is over. The maximum number of readings is limited to 3000 by the size of the computer memory.

At the end of the run, the oscillating piston is left in the equilibrium position and the measured data are analysed to obtain amplitudes and phases of both volume

and pressure oscillations. A standard linear-least squares analysis is used for this. The experimental volume and pressure data points y_i, with $i = 1, 2 \ldots, N$ and where N is the number of readings taken, are fitted by means of the time law

$$f(t_i) = A \sin 2\pi\nu t_i + B \cos 2\pi\nu t_i + C \ , \tag{3.9}$$

obtaining values for A, B and C. Here t_i is the i-th time reading. The term C is a fine offset constant, which completes the coarse electronic offset.

The phase ϕ_y is then given by

$$\tan \phi_y = -\frac{B}{A} \tag{3.10}$$

and the amplitude I_y is

$$I_y = \sqrt{A^2 + B^2} \ . \tag{3.11}$$

The oscillation frequency may vary between 8×10^{-5} Hz and 0.001 Hz and the lower limit can be further diminished, thanks to an improvement to the control programme carried out during the execution of this work.

Phases and amplitudes are stored on a disk file, the fitted waveforms for both volume and pressure oscillations are plotted on the screen and then dumped to the printer for a qualitative comparison to the experimental ones.

The volume oscillation is then repeated at a different frequency, till the last frequency required has been run. The programme ends by ramping the temperature to the next value or down to room temperature. Alternatively it may remain in stand-by if another experiment at the same temperature is to be carried out.

Blank runs, that is with no specimens in the rig, have been carried out. They have shown that the pressure remains constant during a run at a fixed frequency, at least at frequencies higher than 3×10^{-4} Hz. Below this value, absorption and desorption by the apparatus' internal walls spoil the signals. In addition, a positive additive correction to the phase lag, i.e. a phase advance ϵ, has been determined for each pressure and temperature. This phase advance is attributed mainly to the distance between specimen and modulating bellows. A system response time τ_{SR} has been derived as $\tau_{SR} = \epsilon/(2\pi\nu)$. This time appears to depend only on temperature and equilibrium pressure p_e.

3.2.2 Data processing

The phase and amplitude data can be retrieved from the disk file for immediate monitoring, through low-resolution graphs of phase lag and amplitude ratio versus the frequency ν or versus $\sqrt{\nu}$.

The data have then to be unpacked, since they have been stored as a long numerical packed sequence. They also have to be transformed into ASCII format. After this, they can be transferred to the mainframe computer through a terminal emulation software. On the mainframe, appropriate programmes have been written to carry out a second tidying up, to plot the data on a graphics terminal screen and on a high-resolution laser printer. Other programmes have been written for separating phase lag from amplitude ratio data, in order to transfer them to a PC for the production of alternative high-quality plots. In this way the variation of phase and amplitude ratio plots with temperature and equilibrium pressure can be examined.

A large modular programme has also been written for iterative data fitting. It includes a subroutine to read the raw phase versus frequency data, another subroutine to plot them, and several fitting subroutines, one per model. The output is both on the graphics screen and on paper, as well as on two data files. One of these files contains the values of the parameters while the other contains the experimental and the fitted curves. These files can then be transferred to a PC for high-quality plot production.

3.2.3 Specimen characterisation

The analysis of the specimens used at Oxford has been limited to high magnification optical microscopy and to SEM/EDS work.

An SEM survey of the surface of the coating for a hydrogen-treated specimen, has shown the same spiky morphology seen with the Ispra samples and the absence of either cracks or regions where the coating was missing.

The thickness has been determined by means of pictures taken with the optical microscope of sectioned and polished specimens. The same has been done by means of SEM contrast and line scans estimates of the elements molybdenum and titanium.

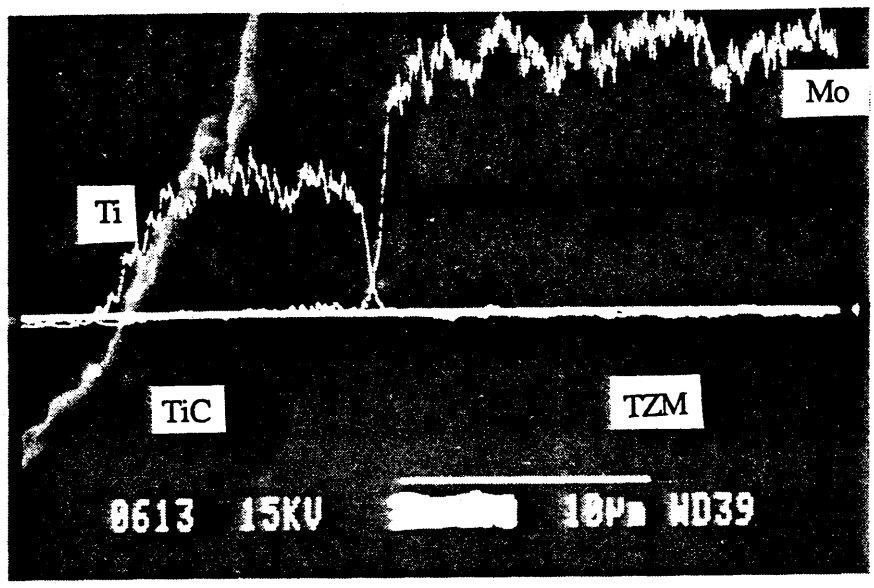

Figure 3.8 SEM picture of a section of a TiC-coated TZM specimen. The coating is on the left-hand side, the clearer TZM substrate is on the right-hand side. Line scans for titanium (left) and molybdenum (right) are also shown. The white foreground segment is 10 μm long and the effective magnification is about $\times$3300. The coating thickness is 8 μm.

An example is shown in Figure 3.8. The thickness determined by these tests is 8 μm within a 10 per cent tolerance.

The appearance of the bulk coating has been examined at the SEM on fractured specimens. A picture of this type is presented in Figure 3.9. Notice the compact columnar structure of the coating layer.

Qualitative analyses of the coating and substrate composition have been executed by X-ray EDS analysis and by X-ray maps with images on sections of the coated specimens. They confirmed the supplier's specifications, within the limits of the technique.

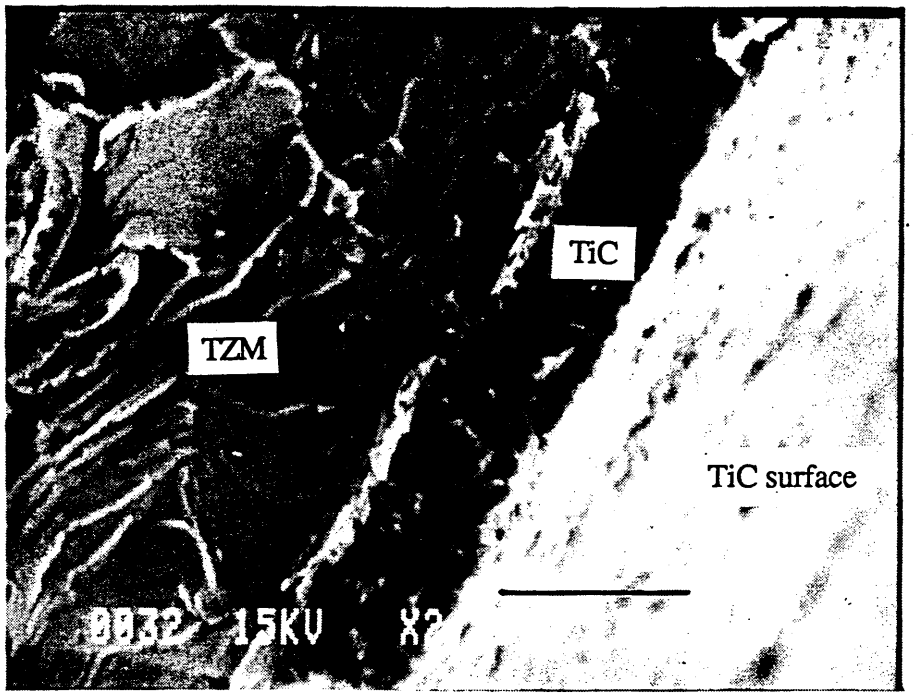

Figure 3.9 SEM picture of a section of a fractured TiC-coated TZM specimen. The clearer coating surface is on the right-hand side, the TZM substrate is on the left-hand side. The black foreground segment is 10 μm long and the effective magnification is about $\times$2500. The coating thickness is 8 μm.

3.3 Advantages and drawbacks of the techniques used

3.3.1 Advantages and drawbacks of the JRC Ispra method

The method used at JRC Ispra is simple and has been well developed over the years, by adding powerful software for non-linear least-squares data fitting and extensive modelling to account for surface effects. It can still be improved by adding modelling with trapping and mixed surface-diffusion regimes, the latter by means of computer-implemented numerical algorithms. It makes use of high precision computer-driven instruments, so that the measurements need a very limited contribution from the operator and can last even for weeks. It has proven highly stable, reliable and efficient over the years and has been shown to yield reproducible results.

On the other hand it lacks flexibility, since only loading-unloading cycles can be carried out and it may become very time-consuming, especially if hydrogen permeation barriers are to be studied. Bounds to the experimental conditions are set by the presence of a platinum thermometer for temperatures and by the background noise for pressures, heavily depending on the solubility of the material under study. Additivity hypotheses for the blank run subtraction have always appeared to be satisfactory though in principle they might seem doubtful with very low solubility materials.

3.3.2 Advantages and drawbacks of the Oxford method

The method used at Oxford is certainly more complicated than that used at Ispra and it heavily relies on sophisticated modelling of the experiment. It is also similarly time-consuming.

Advantages are

1. its flexibility, as in principle also Ispra-type transients can be studied with this apparatus, for instance by recording the transient pressure response to a sudden pressure or temperature variation;

2. the possibility of setting a priori the equilibrium pressure p_e, though this may turn out to be a very time-consuming procedure;

3. the possibility of working at low pressure;

4. the fact that phase lags increase in magnitude as the equilibrium pressure p_e is diminished, as shown in chapter 4;

5. the less crucial role of blank runs compared to an Ispra-type experiment.

Improvements can be made to overcome the following drawbacks:

1. the rig is an all-metal one, which implies a very high background outgassing, a factor particularly important apparently as the oscillation frequency is decreased;

2. heat conduction from the heated experimental chamber to the other uhv metallic components increases the noise level;

3. the current computer is under-dimensioned and more memory space and computing power would be needed;

4. the linear least-squares analysis of the pressure and volume waveforms is much too simplified;

5. account is not made for the gas' being heated to the sample temperature when in the experimental chamber.

Such improvements are surely feasible and if accomplished they would notably improve the amount and quality of information obtained by this technique.

3.4 Summary

This chapter has presented a description of the computer-driven experimental methods used at Ispra and Oxford. The way an experiment is carried out has been described, together with the computer programmes that run the rigs. Gas analysis has been addressed. Data processing has been briefly sketched. Results of the analysis carried out to characterise the samples studied have been given.

Chapter 4

Modelling

Following the ideas given in chapter 1, the mathematical models which have been used to process the experiments carried out at Ispra and Oxford are discussed. Analytical expressions are obtained for the relevant physical quantities experimentally measured.

For the transient experiments carried out at Ispra, an expression for the evolution in time of the hydrogen partial pressure in the closed experimental vessel is derived. Equilibrium and dynamical physical quantities are expressed as functions of the measured observables and of the parameters which characterise the hydrogen release. Surface processes and bulk diffusion are considered separately as being the rate-determining step, yielding two different models. Hydrogen is assumed to dissolve atomically both in the metal substrate and in the coating layer. Models for coated samples and for bare specimens are described. Coefficients thus deduced for the bare metallic substrates are then used as data for the experiments with the coated samples.

For the volume-modulation work executed at Oxford on coated specimens, a single comprehensive model is outlined, which includes diffusion in the coating layer and surface processes, with substrate/coating interface reactions taken to be in dynamic equilibrium. Again, hydrogen is assumed to dissolve atomically in the substrate and in the coating layer.

From this model, limiting cases are obtained in which diffusion or surface reactions control the hydrogen flow regime. Analytical expressions are worked out for the phase lag of the hydrogen pressure response to the volume forced oscilla-

tion which take place in the closed experimental chamber. Similar expressions are given for the ratio of pressure to volume oscillation amplitudes. Both for phase lag and amplitude ratio the emphasis is on the oscillation frequency dependence, as the method used is based on a frequency analysis, but the influence of various physical parameters is also discussed.

Although the volume-modulation model reported here does not include trapping effects, these have actually been included in a wider model [55], which has been used to rule out any strong evidence of trapping effects in the coating layer, under the experimental conditions of this work.

4.1 Diffusion-limited models for Ispra work

The basic idea in diffusion-limited models is that the slowest step in the interaction of gaseous hydrogen with a solid is bulk diffusion, all of the other processes appearing to evolve instantaneously on the time scale of diffusion. Cylindrical samples have been chosen with dimensions such that the "infinite cylinder" approximation can be used. More specifically, the ratio of top and bottom to lateral surface areas, equal to the radius-to-height ratio a/h, is very small, typically 0.04. This means that hydrogen is mainly released through the lateral surface.

The mathematical problem to be solved then consists in finding the solution of a radial diffusion equation subject to appropriate boundary and initial conditions, in a cylindrical coordinate system where the z-axis is the symmetry axis of the cylindrical specimen.

4.1.1 Diffusion in an uncoated cylinder

The diffusion-limited model for a solid homogeneous cylinder requires the solution of the radial diffusion equation in cylindrical coordinates, for an infinitely long cylinder with radius a

$$\frac{\partial c(r,t)}{\partial t} = \frac{D}{r}\frac{\partial}{\partial r}\left(r\,\frac{\partial c(r,t)}{\partial r}\right) \quad , \tag{4.1}$$

together with the initial condition

$$c(r,0) = c_i = \text{ constant} \quad 0 \leq r \leq a \tag{4.2}$$

and the boundary condition

$$c(a,t) = c_f = \text{ constant} \quad t \geq 0\,. \tag{4.3}$$

The condition (4.2) means a flat initial concentration profile, the sample being thus saturated with hydrogen, while (4.3) identifies a diffusion-limited regime, by assuming that the surface concentration immediately reaches its equilibrium final value c_f. It is worth noticing that this system describes both absorption and release, depending on the sign of the difference $c_i - c_f$.

The solution of this problem, obtained by Laplace transform techniques [13, 53] is:

$$c(r,t) = c_f + 2\ (c_i - c_f) \sum_{n=1}^{\infty} \frac{J_0\,(\alpha_n r/a)}{\alpha_n\ J_1\,(\alpha_n)} \exp\left(-\alpha_n^2 t/\tau_d\right) \tag{4.4}$$

where $J_n(x)$ is the Bessel function of the first kind and order n, while α_n ($n = 1, 2, 3, \ldots$) are the infinite[1] real roots of the equation $J_0(\alpha) = 0$. The diffusion characteristic time τ_d is defined as

$$\tau_d = \frac{a^2}{D}\,. \tag{4.5}$$

It is useful to compute the average concentration $\bar{c}(t)$ within the cylinder such that when multiplied by its volume V_s it gives the amount of gas dissolved in the solid. This is

$$\bar{c}\,(t) = \frac{1}{V_s} \int_{V_s} c(r,t)\, dV\,. \tag{4.6}$$

For an infinite cylinder this is given by

$$\bar{c}\,(t) = \lim_{h\to\infty} \left(\frac{1}{2\pi h a^2} \int_{-h}^{+h} dz \int_0^{2\pi} d\theta \int_0^a r\, c(r,t) dr \right) \tag{4.7}$$

which, after integration and evaluation of the limit, gives

$$\bar{c}\,(t) = c_f + 4\ (c_i - c_f) \sum_{n=1}^{\infty} \frac{1}{\alpha_n^2} \exp\left(-\alpha_n^2 t/\tau_d\right)\,. \tag{4.8}$$

As the time approaches infinity both $c(r,t)$ and $\bar{c}(t)$ tend to the equilibrium value c_f. The diffusion time τ_d is such that for $t > \tau_d$, $\bar{c}(t)/c_f > 0.998$.

[1] Here *infinite* refers to the number of roots.

It is also useful to define the function $F(x)$

$$F(x) = 4 \sum_{n=1}^{\infty} \frac{1}{\alpha_n^2} \exp\left(-\alpha_n^2 x\right) , \tag{4.9}$$

so that equation (4.8) becomes

$$\bar{c}(t) = c_f + (c_i - c_f) F(t/\tau_d) . \tag{4.10}$$

It is easily verified that

$$F(0) = 4 \sum_{n=1}^{\infty} \frac{1}{\alpha_n^2} = 1 \tag{4.11}$$

and that

$$\lim_{x \to +\infty} F(x) = 0 . \tag{4.12}$$

The link between average concentration and pressure

As already stated in chapter 3 the experimental chamber is made of two parts A and B with volumes V_A and V_B kept at different temperatures T_A and T_B with $T_A > T_B$, while the pressure p is measured in B. In order to account for this temperature difference and also to reduce the noise due to temperature fluctuations a normalised pressure P is used instead of the actual pressure p[2]:

$$P(t) = p(t) \frac{T_N}{V} \left[\frac{V_A}{T_A} + \frac{V_B}{T_B}\right] \tag{4.13}$$

where the normalising temperature is arbitrarily chosen as $T_N = 293.15$ K and $V = V_A + V_B$ is the vessel volume.

It is particularly useful to introduce the following normalised pressures:

- the residual pressure after a pumpdown of duration Δt

$$P_r = P(\Delta t) , \tag{4.14}$$

- the initial pressure, equivalent to the normalised loading pressure

$$P_i = P(0) , \tag{4.15}$$

[2]Here and throughout the work, uppercase P is used for normalised pressures and lowercase p for actual pressures.

- the pressure drop caused by the pumpdown, ΔP_p,
- the pressure increase due to the gas released by the sample during the pumpdown interval, ΔP_d.

From the above

$$\Delta P_p = P_i + \Delta P_d - P_r \tag{4.16}$$

or, by setting

$$\Delta P = \Delta P_p - P_i \,, \tag{4.17}$$

it is found that

$$P_r = \Delta P_d - \Delta P \,. \tag{4.18}$$

Thus, ΔP represents the fraction of gas released by the sample and lost to the pumps and is such that $-P_r < \Delta P < \Delta P_d$. The pumping speed of the system is such that P_r is lower than the minimum detectable pressure and is therefore negligible. For materials and experimental conditions such that the value of the ratio $\Delta t/\tau_d$ is much smaller than 1 also ΔP_d and hence ΔP turn out to be negligible.

Conservation of mass in the experimental chamber gives a relationship between the average concentration $\bar{c}(t)$ and the normalised pressure $P(t)$

$$P(t) + \Delta P = [\bar{c}(0) - \bar{c}(t)]\ RT_N \frac{V_s}{V} \,, \tag{4.19}$$

where R is the gas constant and V_s is the sample volume. In the limit for $t \to \infty$ it is found that $P(t) \to P_f$ which is the final pressure and $\bar{c} \to c_f$, hence (4.19) gives

$$(c_i - c_f) = (P_f + \Delta P) \frac{V}{V_s\, R\, T_N} \,. \tag{4.20}$$

Equation (4.20) is used to evaluate the solubility c_i, as it expresses the amount of hydrogen dissolved per unit volume in the cylinder at the end of the loading phase, if $c_i > c_f$. If Sieverts' law holds, the small term c_f can be evaluated from the loading pressure p_0 and the final pressure p_f

$$\frac{c_f}{c_i} = \sqrt{\frac{p_f}{p_0}} \tag{4.21}$$

so that the solubility S is given by

$$S(T, p_0) = \frac{(P_f + \Delta P)\ V}{V_s R T_N} \left[1 - \sqrt{\frac{p_f}{p_0}}\right]^{-1} \,. \tag{4.22}$$

Eventually, the time law for the normalised pressure is obtained from (4.10) and (4.19) as

$$P(t) = P_f - (P_f + \Delta P)\ F(t/\tau_d) \quad , \ t \geq \Delta t\ . \tag{4.23}$$

This formula is fitted to the experimental P versus t curve with ΔP and τ_d as parameters of the fit. Then ΔP is used together with the accurately measured value of P_f to find the solubility through (4.22) and τ_d is used to compute the diffusivity D by means of (4.5).

4.1.2 Diffusion in a coated cylinder

In the diffusion-limited model for a coated cylinder, the infinite cylinder approximation is used and the coating thickness d is assumed constant over all the cylinder. A sharp substrate-to-coating interface is considered so that the medium is composed of two regions with different properties, namely region 1 designating the metal substrate and region 2 referring to the TiC coating. A further assumption is that no hydrogen accumulation occurs at the solid/solid interface. The geometry used for the model is schematically depicted in Figure 4.1, which shows in particular the radial distance r from the cylinder symmetry axis, the solid/solid interface location at $r = a$ and the coating thickness d.

The model is represented by the following set of equations, which hold for the two media ($j = 1, 2$):

- the radial diffusion equations

$$\frac{\partial c_j}{\partial t} = D_j \nabla^2 c_j \tag{4.24}$$

  with the concentration $c_j(r,t)$ in medium j depending only on the radius r and on time t,

- the initial condition

$$c_j(r,0) = c_{ji} = \text{constant} \ , \qquad 0 \leq r \leq a + d \tag{4.25}$$

- a boundary condition at the coating/substrate interface, from chemical potential continuity, expressing equilibrium of interface reactions

$$\frac{c_1(a^-,t)}{c_2(a^+,t)} = k = \text{constant}, \quad t \geq 0 \tag{4.26}$$

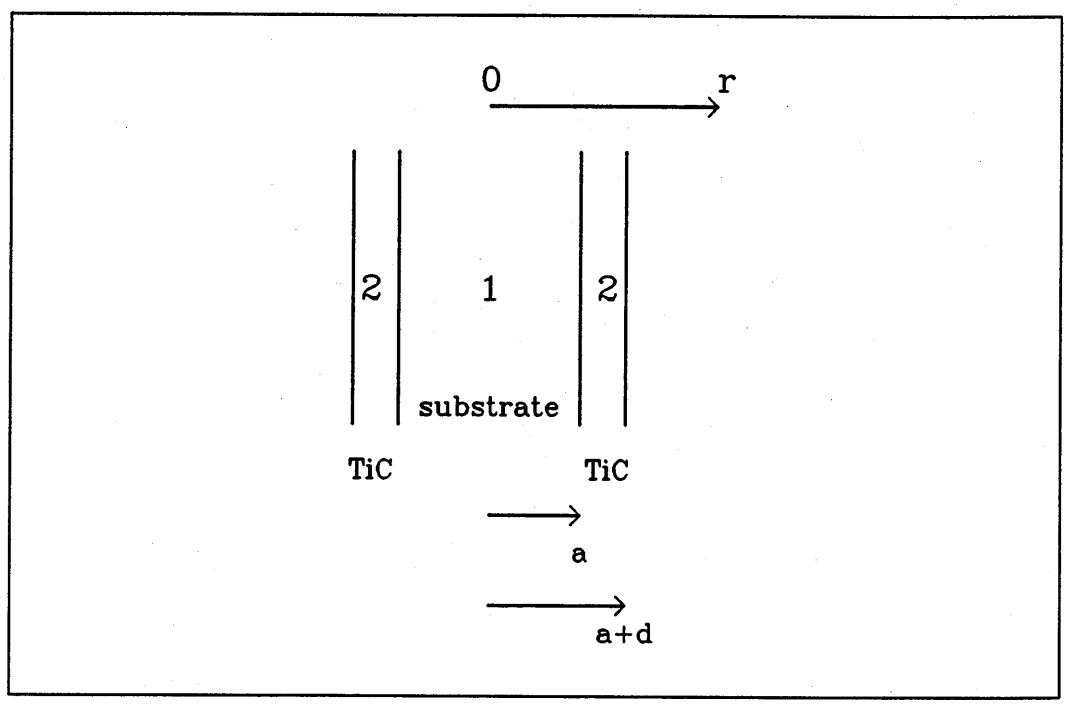

Figure 4.1 Longitudinal schematic section of the geometry for modelling of diffusion in a coated cylinder. Key: a – cylinder radius, d – coating thickness, r – radial coordinate.

- another boundary condition at the same interface, from the "no accumulation" assumption, or continuity of the diffusive flux

$$D_1 \frac{\partial c_1}{\partial r}\Big|_a^- = D_2 \frac{\partial c_2}{\partial r}\Big|_a^+ \quad , \quad t \geq 0 \tag{4.27}$$

- a boundary condition at the coating surface, which imposes a fixed subsurface concentration

$$c_2\,(a+d,t) = c_{2f} = \text{constant}, \quad t \geq 0 \ . \tag{4.28}$$

Condition (4.28) is typical of models for diffusion-limited regimes.

Again the solution can be found by Laplace Transform techniques. It is easily verified that the solution of this problem is the sum of the solutions of two similar diffusion problems a) and b) where

a) the surface concentration is kept constant and equal to c_{2f}, while the initial concentration is zero throughout the cylinder,

b) the subsurface concentration is kept equal to zero while the initial concentration is constant and equal to c_{ji}, with $j = 1, 2$.

These solutions have been given by Jaeger [54] for the particular case where the partition coefficient is $k = 1$ and therefore can be used provided we identify Jaeger's solution $v_1(r,t)$ with the rescaled concentration $c_1(r,t)/k$. In addition, since Jaeger's was a heat conduction problem, it is also required to identify his conductivity K_1 in medium 1 with the diffusivity D_1, and his K_2 with the value of the ratio D_2/k. Furthermore his specific heats c_j and densities ρ_j in medium 1 and 2 are to be related in our case by $c_1\rho_1 = 1$, $c_2\rho_2 = 1/k$.

This solution is so complex that its use is impractical. A much simpler model can be set up according to the following assumptions:

- diffusion characteristic times are much lower in the metal core than in the coating; this happens if

$$\frac{D_1}{D_2} \gg \left(\frac{a}{d}\right)^2 \simeq 10^6 \ . \tag{4.29}$$

  In such a case, hydrogen throughout the metal core can be supposed to be in dynamic equilibrium, through the chemical potential equation (4.26), with hydrogen within the coating at the interface. In other words, the hydrogen concentration in medium 1 does not depend on the radial position r but only on time t, $c_1 = c_1(t)$. These assumptions split the problem into two virtually uncoupled problems and only the problem for medium 2 remains to be solved.

- the Laplacian operator ∇^2 is approximated by $\partial^2/\partial x^2$, i.e. for any arbitrary function $f(r)$

$$\nabla^2 f = \frac{\partial^2 f}{\partial x^2} \ . \tag{4.30}$$

  In fact, the Laplacian operator in cylindrical coordinates acts on any arbitrary function $f(r)$ as follows

$$\nabla^2 f = \left(\frac{1}{r} + \frac{\partial}{\partial r}\right)\left(\frac{\partial f}{\partial r}\right) \tag{4.31}$$

  and if the radial coordinate r is related to the position coordinate in the coating x as measured from the coating/substrate interface, that is $r = a + x$, it is

found that, for any function $g(r)$

$$\frac{g(r)}{r} + \frac{\partial g}{\partial r} = \frac{g(a+x)}{(a+x)} + \frac{\partial g}{\partial x} \simeq \frac{\partial g}{\partial x} \quad . \tag{4.32}$$

Here the term in $1/r$ can be dropped if radial gradients are large enough for the condition

$$\left|\frac{\partial g}{\partial x}\right| \gg \left|\frac{g}{a}\right| \tag{4.33}$$

to hold throughout the coating layer and if the coating is thin so that $x \ll a$ (here $a/x = 1000$). Under such assumptions, equation (4.31) is substituted by (4.30).

Thus the coating geometry has been reduced to a slab and the problem to solve is now to find $c_1(t)$ and $c_2(x,t)$, $t \geq 0$, $0 \leq x \leq d$, such that:

$$\frac{\partial c_2}{\partial t} = D_2 \frac{\partial^2 c_2}{\partial x^2} \quad , \tag{4.34}$$

$$c_2(x,0) = c_{2i} = \text{constant} \quad 0 \leq x \leq d \quad , \tag{4.35}$$

$$c_2(d,t) = c_{2f} = \text{constant}, \quad t \geq 0 \quad , \tag{4.36}$$

$$\frac{\partial c_2}{\partial x}|_{0^+} = 0, \quad t \geq 0 \quad , \tag{4.37}$$

$$c_1(t) = k\, c_2(0,t), \quad t \geq 0 \quad . \tag{4.38}$$

The condition (4.37) comes from combining (1.31) to (4.38), with $k = k_4/k_3$.

Solution of the slab diffusion problem

The slab diffusion problem given by equations (4.34) to (4.37) has been solved by means of the Laplace Transform technique and the solution is

$$c_2(x,t) = c_{2i} + (c_{2f} - c_{2i})\; G(x, t/\tau_d) \quad , \tag{4.39}$$

where, having set for simplicity $\theta = t/\tau_d$,

$$G(x,\theta) = 1 + \frac{4}{\pi} \sum_{n=1}^{+\infty} \frac{(-1)^n}{2n-1} \cos\left[(2n-1)\frac{\pi x}{2d}\right] \exp\left[-(2n-1)^2\,\theta\right] \quad . \tag{4.40}$$

Here the diffusion characteristic time τ_d is defined as

$$\tau_d = \frac{4d^2}{\pi^2 D_2} \quad . \tag{4.41}$$

It is possible to show that $G(x,0) = 0$, for all $x \in (0,d)$ and that

$$\lim_{\theta \to +\infty} G(x,\theta) = 1 \ . \tag{4.42}$$

Thus, c_{2f} is the final concentration in the coating layer, reached asymptotically as $t \to \infty$. The concentration in the metal core is obtained from (4.38)

$$c_1(t) = k\left[c_{2f} + (c_{2i} - c_{2f})\ F_1(t/\tau_d)\right] \tag{4.43}$$

having set

$$F_1(\theta) = \frac{4}{\pi} \sum_{n=1}^{+\infty} \frac{(-1)^{n+1}}{2n-1} \exp\left[-(2n-1)^2\,\theta\right] \ . \tag{4.44}$$

The average concentration in the coating is given by

$$\bar{c}_2(t) = c_{2f} + (c_{2i} - c_{2f})\ F_2\left(\frac{t}{\tau_d}\right) \tag{4.45}$$

where

$$F_2(\theta) = \frac{8}{\pi^2} \sum_{n=1}^{+\infty} \frac{1}{(2n-1)^2} \exp\left[-(2n-1)^2\,\theta\right] \tag{4.46}$$

and a well known result is $F_1(0) = 1 = F_2(0)$.

By repeating the argument in 4.1.1, the time law for the normalised pressure reads

$$P(t) + \Delta P = \frac{RT_N}{V}\left\{V_2\ \left[\bar{c}_2(0) - \bar{c}_2(t)\right]\ + V_1\left[c_1(0) - c_1(t)\right]\right\} \ , \tag{4.47}$$

from which one has

$$V_1\ (c_{1i} - c_{1f}) + V_2\ (c_{2i} - c_{2f}) = (P_f + \Delta P)\frac{V}{R\,T_N} \ , \tag{4.48}$$

bearing in mind that $V_s = V_1 + V_2$ is the sample total volume (=substrate + coating). It can also be shown that the ratios of equilibrium concentrations in the two solid media is equal to the partition coefficient k,

$$\frac{c_{1i}}{c_{2i}} = \frac{c_{1f}}{c_{2f}} = k \tag{4.49}$$

so that, by introducing the modified partition factor u,

$$u = k\frac{V_1}{V_2} \ , \tag{4.50}$$

it follows that

$$(c_{2i} - c_{2f}) = \frac{V\ (P_f + \Delta P)}{(u+1)\, V_2\, R\, T_N} \tag{4.51}$$

and the solubility $S(T, p_0)$ *in the coating* is

$$S\,(T, p_0) = \frac{V\ (P_f + \Delta P)}{(u+1)\ V_2 R T_N \left[1 - \sqrt{\frac{p_f}{p_0}}\right]}\ . \tag{4.52}$$

Finally, the time evolution of the pressure reads

$$P\,(t) = P_f - \frac{P_f + \Delta P}{u+1}\{u\, F_1\left(\frac{t}{\tau_d}\right) + F_2\left(\frac{t}{\tau_d}\right)\} \tag{4.53}$$

and since P_f is accurately measured, this formula can be fitted to the experimental P vs t curve, by using ΔP, u and τ_d as parameters of the fit.

Then the values of u and ΔP found by data fitting are used to evaluate the solubility by means of (4.52), while the value found for τ_d gives the diffusivity D_2 in the coating layer through (4.41) once the coating thickness d has been measured.

The partition parameters k and u are important since they describe how hydrogen is distributed between substrate and coating. For a given volume ratio V_1/V_2 and a finite diffusivity ratio D_1/D_2 different from zero, the case $u \to \infty$ would represent a formidable permeation barrier, since hydrogen would not penetrate the coating facing it, but it would also be very difficult to study. On the other hand, the case $u \to 0$ would represent a less effective permeation barrier to hydrogen, but it would be easier to study experimentally since, from the point of view of absorption, the substrate would be virtually non-existent.

A consequence of these considerations is that hydrogen interaction tests should be carried out with a low solubility coated substrate, whereas the coating would be more effective, in practice, if applied on the surface of a higher solubility material.

4.2 Surface-limited models for Ispra work

When hydrogen flow is limited by surface reactions all bulk processes are assumed to occur instantaneously on the time scale of surface reactions, so that any concentration gradient is cancelled by diffusion and at a given time t the concentration c may be treated as uniform inside the specimen, that is $c = c(t)$. Such models are

also independent of the specimen geometry (shapeless solid, slab, sphere, cylinder) *per se* but the effective area and the volume of the specimen enter the model. Simplified extensions of such models to the case of a composite solid, such as a coated specimen, are readily obtained.

Considering a specimen with surface area A and volume V_s, placed in a closed vessel of volume V and under a hydrogen partial pressure p, mass conservation implies

$$\left(\frac{V}{RT}\right)\frac{dp}{dt} + V_s\frac{dc}{dt} = 0 \ . \tag{4.54}$$

It is a good first approximation to identify T with the temperature of the gas in the cold part of the vessel. Integration of (4.54) gives

$$p(t) = p_c - RT\frac{V_s}{V}c(t) \ , \tag{4.55}$$

where p_c is a constant determined from the initial condition $p(0) = p_i$

$$p_c = p_i + RT\frac{V_s}{V}c_i \ . \tag{4.56}$$

The variation of the concentration with time is obtained by equating the hydrogen flux out of the sample to the rate of variation of the amount of hydrogen dissolved in it:

$$V_s\frac{dc}{dt} = A\left(k_1\, p - k_2\, c^2\right) \ . \tag{4.57}$$

Substituting (4.55) for $p(t)$ in (4.57) one has

$$\frac{dc}{dt} = -k_2\frac{A}{V_s}c^2(t) - k_1\frac{ART}{V}c(t) + k_1\frac{A}{V_s}p_c \tag{4.58}$$

and this is Riccati's equation which can be written as

$$\frac{dc}{dt} = Lc^2 + Mc + N \tag{4.59}$$

with $L = -Ak_2/V_s$, $M = -k_1ART/V$, $N = k_1Ap_c/V_s$.

The solution for an initial condition $c(0) = c_i$ is

$$c(t) = c_f + \frac{(c_i - c_f)(M + 2Lc_f)}{[M + L(c_i + c_f)]\exp[-(M + 2Lc_f)t] - L(c_i - c_f)} \ , \tag{4.60}$$

where

$$c_f = \lim_{t\to\infty} c(t) = \frac{V_sRT}{2V}\frac{k_1}{k_2}\left[\sqrt{1 + 4\frac{V^2k_2p_c}{V_s^2k_1(RT)^2}} - 1\right] \ . \tag{4.61}$$

is the final concentration. By substituting (4.60) for $c(t)$ in (4.55), the pressure law

$$p(t) = p_f + (p_f - p_i)\frac{\sqrt{1 + p_c\frac{k_2}{k_1}\left[\frac{2V}{RTV_s}\right]^2}}{\frac{k_2V(c_i-c_f)}{k_1V_sRT} - \left[1 + \frac{k_2V(c_i+c_f)}{k_1V_sRT}\right]\exp\,(t/\tau_s)} \tag{4.62}$$

is obtained, where the surface release characteristic time τ_s has been defined by

$$\tau_s = -\frac{1}{M + 2Lc_f} = \frac{V}{ARTk_1}\left[1 + p_c\frac{k_2}{k_1}\left(\frac{2V}{V_sRT}\right)^2\right]^{-1/2} \tag{4.63}$$

and

$$p_f = \lim_{t\to\infty} p(t) = p_i + (c_i - c_f)\,RT\frac{V_s}{V} \tag{4.64}$$

is the final pressure.

By squaring (4.61), using (4.56) and (4.64), Sieverts' law is found

$$c_f^2 = \frac{k_1}{k_2}p_f \tag{4.65}$$

with Sieverts' constant K_s being given by $K_s^2 = k_1/k_2$. In the light of (4.54) and (4.57) it is evident that

$$\lim_{t\to\infty}\left(\frac{dc}{dt}\right) = 0 = \lim_{t\to\infty}\left(\frac{dp}{dt}\right)\ , \tag{4.66}$$

which confirms that c_f and p_f are the equilibrium, steady state concentration and pressure, respectively. Then by means of (4.64) an expression for the initial concentration c_i is obtained

$$c_i = K_s\sqrt{p_f} + (p_f - p_i)\frac{V}{RTV_s}\ . \tag{4.67}$$

In this way the pressure $p(t)$ is expressed as a function of time t, of the initial and final pressures p_i, p_f, of the vessel volume V and temperature T and of the specimen parameters A, V_s, k_1, k_2 as follows

$$p(t) = p_f + \frac{p_f - p_i}{U - (U+1)\exp\,(t/\tau_s)} \tag{4.68}$$

with

$$U = (p_f - p_i)\left[\frac{V}{K_sV_sRT}\right]^2 / \left[1 + \frac{2V\sqrt{p_f}}{K_sV_sRT}\right]\ , \tag{4.69}$$

where an equivalent expression for τ_s is

$$\tau_s = \frac{V}{ARTk_1}\left[1 + \frac{2V\sqrt{p_f}}{K_s V_s RT}\right]^{-1} \quad . \tag{4.70}$$

It is important to realise that τ_s varies with the final pressure p_f and therefore with the loading pressure p_0 through the initial concentration c_i. Specifically, τ_s increases as c_i or p_0 diminish, in contrast with what happens in the diffusion limited models where the characteristic diffusion time τ_d is independent of c_i. As a consequence, release curves obtained at the same temperature but with different loading pressures do not overlap and the release becomes slower as the loading pressure is decreased.

The model also predicts a limit curve as p_f, hence p_0, tends to zero. With the assumption $p_i = 0$, such a curve is described by the equation

$$\frac{p(t)}{p_f} = 1 - \exp\left(-t/\tau_s^0\right) \quad , \tag{4.71}$$

with

$$\tau_s^0 = \frac{V}{k_1 ART} \quad . \tag{4.72}$$

Therefore, the release curves tend to be closer and closer as the loading pressure is diminished. This is evident in Figure 4.2 where the fractional release $p(t)/p_f$, obtained by this surface-limited model, is shown as a function of the normalised time t/τ_s, for three different loading pressures of 10^5, 10^3 and 1 Pa respectively.

4.2.1 Correction for pressure losses during the pumpdown and extension to normalised pressure

If due account is made for the effect of gas pumping between the time $t_1 = 0$ and the time $t_2 = \Delta t$ with a pumping speed $S_P(p)$ which is a function of time t through the pressure $p(t)$, then by mass conservation, equation (4.54) becomes

$$\left(\frac{V}{RT}\right)\frac{dp}{dt} + V_s\frac{dc}{dt} + [p(t) - p_L]\frac{S_P}{RT} = 0 \quad , \tag{4.73}$$

where p_L is the ultimate pressure of the vacuum system.

Integrating between times $t_1 = 0$ and t one has

$$\frac{V}{RT}[p(t) - p(0)] + V_s[c(t) - c(0)] + \int_0^t \frac{S_P}{RT}[p(z) - p_L]dz = 0 \tag{4.74}$$

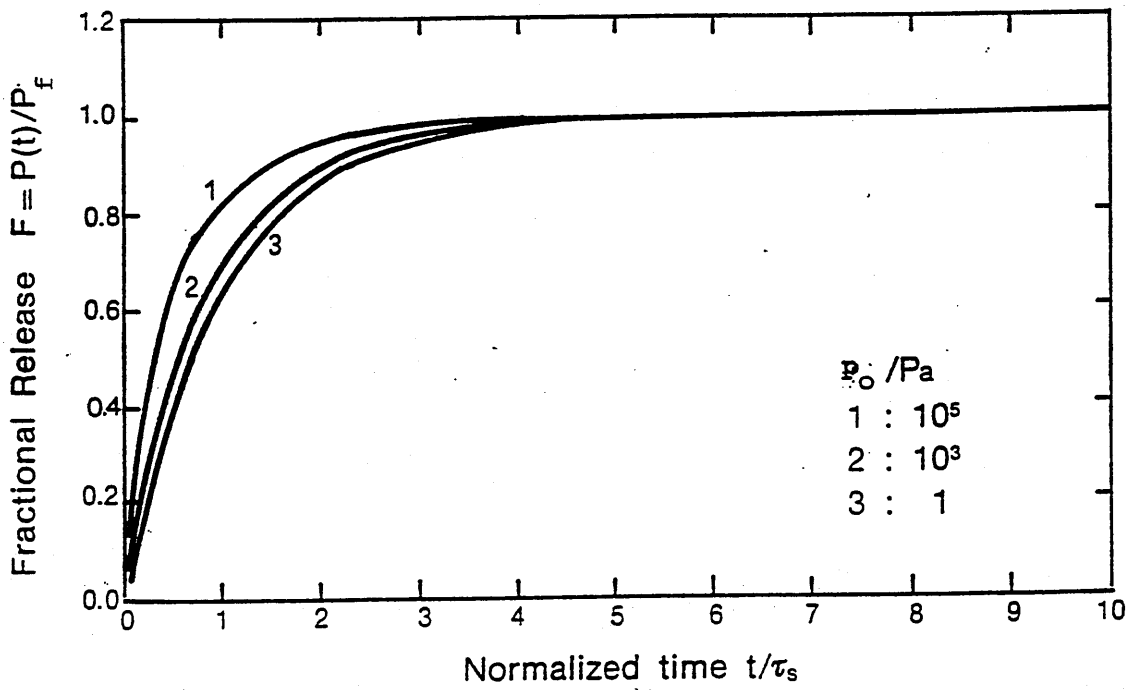

Figure 4.2 Hydrogen release at three different loading pressures, by the surface-limited model.

and at $t = \Delta t$ this becomes

$$\frac{V}{RT}[p(\Delta t) - p(0)] + V_s[c(\Delta t) - c(0)] + \int_0^{\Delta t} \frac{S_P}{RT}[p(z) - p_L]dz = 0 \ , \qquad (4.75)$$

From (4.74) recalling that $S_P(p) = 0$ for $t > \Delta t$

$$\frac{V}{RT}[p(t) - p(0)] + V_s[c(t) - c(0)] + \int_0^{\Delta t} \frac{S_P}{RT}[p(z) - p_L]dz = 0 \qquad (4.76)$$

so that equations (4.75) and (4.76) can be combined to eliminate the pumpdown integral. Then it is recalled that the residual pressure (not normalised) is $p_r = p(\Delta t)$, that the initial or loading pressure is $p_i = p(0)$, that the pressure increase caused by gas desorption from the samples is $\Delta p_d = V_s RT[c(0) - c(\Delta t)]/V$ so that the pressure drop due to the pumpdown is expressed as $\Delta p_p = p_i - p_r + \Delta p_d$. If in addition, $\Delta p = \Delta p_p - p_i$, the pressure law becomes

$$p(t) = [\frac{V_s RT}{V} c(0) - \Delta p] - RT\frac{V_s}{V} c(t) \qquad (4.77)$$

and it appears evident that this is the same as (4.55) with the provision

$$p_c = \frac{V_s}{V} RT c(0) - \Delta p \ . \qquad (4.78)$$

The treatment proceeds now as in the previous section to yield the pressure law which substitutes equation (4.68)

$$p(t) = p_f + \frac{p_f + \Delta p}{U - (U+1)\exp(t/\tau_s)} \tag{4.79}$$

As for the solubility, which is given by the initial concentration c_i, equation (4.67) is replaced by

$$c_i = K_s\sqrt{p_f} + (p_f + \Delta p)\frac{V}{RTV_s} \tag{4.80}$$

all the rest remaining unchanged.

The above formulas are modified for use with the normalised pressure $P(t)$ by setting

$$\frac{V}{T} = \frac{V_A}{T_A} + \frac{V_B}{T_B} \tag{4.81}$$

and using k_1^* and K_s^* instead of k_1, K_s respectively, defined by

$$k_1^* = k_1 \left[\frac{V}{T}\right] / \left[\frac{V}{T_N}\right] \tag{4.82}$$

and by

$$K_s^* = \sqrt{\frac{k_1^*}{k_2}} = K_s \left[\frac{V}{T}\right] / \left[\frac{V}{T_N}\right] \quad . \tag{4.83}$$

With this provision, the solubility given by (4.67) coincides with that given by (4.20) from the diffusion-limited model, as expected since the solubility does not depend on the dynamics, being an equilibrium quantity. Then equation (4.79) is fitted to the data, using τ_s and Δp as only parameters of the fit. In fact K_s^* is determined from the accurately measured value of P_f and from (4.83) with $K_s = c_i/\sqrt{p_0}$ after c_i has been determined through (4.80) or (4.20). From the values of τ_s, K_s and by (4.70), k_1 is computed and then k_2 is derived as $k_2 = k_1/K_s^2$.

4.2.2 Extension to a coated solid

The treatment and the formulas outlined in the previous subsections are extended to the case of a coated solid by setting

$$V_s = kV_1 + V_2 = V_2(1+u) \quad , \tag{4.84}$$

following the nomenclature used in discussing the diffusion model for a coated cylinder.

This extension of the model is obtained by recalling that the assumption of surface-control implies that concentrations c_1, c_2 throughout the coated specimen evolve in time through flat profiles, i.e. $c_j = c_j(t)$ for $j = 1, 2$. This assumption also implies that c_1 and c_2 are linked to one another through the partition coefficient k, $c_1(t) = kc_2(t)$.

Then the total amount of hydrogen dissolved in the cylinder at any time t is $V_s c(t) = (kV_1 + V_2)c_2(t)$. Therefore, by means of (4.84) the treatment is exactly the same as in the previous section, provided that c is identified with c_2 and K_s, K_s^* refer to the coating material.

Now V_s is an effective cylinder volume. The product $K_s^* V_s$ is used as additional parameter of the fit, together with k_1 instead of τ_s.

4.3 The model for volume-modulation work at Oxford

This section explains the model developed to interpret the volume-modulation experiments carried out at Oxford with cylindrical TiC-coated TZM specimens. The present model was inspired by an article by Cummings and Blackburn [50], with which it shares some key starting ideas. The treatment in this sections is different from that in [50] as their work was with uncoated nickel foils and because the matrix method is not used here. The present model however can be thought of as an extension of the model in [50] and it reproduces those results, after some rescaling. Trapping is not included in the present version of the model, for brevity, but it has actually been included in the treatment [55] and has been used to rule out any strong evidence of trapping effects in the present work.

It has to be mentioned that [50] contains some important misprints, as follows:

- on page 86, in equation (63) one should read $[\mathrm{Im}(V_x)/V_s]^2$ instead of $[\mathrm{Im}(V_x)]^2$;
- on page 87, in equations (89) and (90) the terms $\sinh\xi$ and $\sin\chi$ should be interchanged, while in equation (90) only, the sign of the term V_{H_2} should be changed into a minus.

4.3.1 Basic assumptions

In this subsection, the basic assumptions of the model are outlined.

In line with the nomenclature adopted describing the models in the previous sections, all physical quantities are labelled with a subscript 1 when they are referred to the substrate and with a subscript 2 in the case of the coating.

The model assumes that a uniform coating of total surface area A and thickness d entirely covers a metallic cylinder having radius a and height h. The thin coating approximation $d \ll a$, $d \ll h$ is also used in this model. The coated specimen is placed in a closed vessel having volume V_e.

In section 4.1.2 it has been shown that equation (4.34) describes radial diffusion of atomic hydrogen in a thin coating layer placed on the lateral surface of a cylinder. That equation also describes diffusion in a slab and is therefore used here, with the provision that x now indicates the distance from the interface within the coating, both for the lateral surface and for the top and bottom faces of the coated cylinder. This is necessary because in these experiments, the sample dimensions are such that the lateral surface area is comparable to the top and bottom areas, unlike the experiments carried out at Ispra. Hydrogen is released through both types of surface, and the lateral contribution to the absorption/desorption flux is not dominant. Therefore, top and bottom face contributions cannot be neglected.

As with the Ispra modelling for coated samples, diffusion in the substrate is taken to occur instantaneously with respect to all other processes. Therefore, the concentration in the substrate c_1 is assumed to be only a function of time t, $c_1 = c_1(t)$.

No hydrogen accumulation is assumed to occur at the interface and interface kinetics is again assumed to be in dynamic equilibrium, two assumptions already made in the Ispra models. Interface boundary conditions (4.37) and (4.38) are therefore again used.

The hydrogen flux through the surface is modelled by means of the two-constants reaction rate equation (1.1). This is an evident improvement with respect to the way surface adsorption and desorption were modelled at Ispra.

The surface boundary condition is now obtained by equating the surface absorption/desorption flux J_s (1.1) to the diffusion flux in the coating at the subsurface

$J_d\,|_{(x=d^-)}$. This gives

$$-D_2\frac{\partial c_2}{\partial x}\,|_{d^-} = k_2 c_2^2(d,t) - k_1 p(t)\ . \tag{4.85}$$

In this way, mixed flow regimes, where diffusion and surface reactions are both important, can be modelled.

A gas balance equation accounts for exchange of hydrogen between the gaseous phase inside the vessel at the partial pressure $p(t)$ and the dissolved phase within the coated solid, as follows

$$\frac{d}{dt}\left(\frac{pV}{RT}\right) = -V_1\frac{dc_1}{dt} - A\frac{d}{dt}\int_0^d c_2(x,t)dx\ . \tag{4.86}$$

Here, V_1 is the substrate volume, V is the volume occupied by the gas in the vessel and a good first approximation is to interpret T as the hydrogen temperature in the cold part of the experimental vessel.

The initial conditions are of equilibrium absorption/desorption. This is described by equating to zero the net flux in equation (4.85), which then yields Sieverts' law, *for the coating*

$$c_{2e} = K_s\sqrt{p_e}\ . \tag{4.87}$$

Here and throughout this section, the subscript "e" refers to such equilibrium conditions.

In each single experimental run, the total vessel volume V is made to vary sinusoidally with an angular frequency Ω around the equilibrium value V_e. Hence

$$V(t) = V_e - V_0\sin(\Omega t - \epsilon)\ , \tag{4.88}$$

describes the volume oscillation in time t. The oscillation amplitude V_0 is small, typically 10 per cent of the equilibrium value V_e. Allowance is made in (4.88) for a small delay $\tau_{SR} = \epsilon/\Omega$, where ϵ is an empirical factor incorporating the effect of propagation delay in the gas, to account for the distance between the specimen and the piston which actually varies the volume. The system response time τ_{SR} can be determined by blank runs, i.e. runs without samples in the chamber, carried out in exactly the same experimental conditions as those with specimens.

If there is no interaction with the solid specimen

$$p(t) = \frac{p_e}{1 - m_V\sin(\Omega t - \epsilon)}\ , \tag{4.89}$$

where $m_V = V_0/V_e$ is the volume modulation, $p_e = n_e RT/V_e$ is the equilibrium pressure and n_e is the number of moles of hydrogen in the vessel at equilibrium. Expanding in series

$$p(t) = p_e \left\{1 + m_V \sin(\Omega t - \epsilon) + O({m_V}^2)\right\} \ , \tag{4.90}$$

according to which, for a 10 per cent modulation, $m_V = 0.1$, the error made by truncating after the linear term is not greater than 1.11 per cent. Hence, for small modulations, the pressure oscillates in phase with the volume, apart from the small phase difference ϵ, and with amplitude $m_V p_e$.

If there is absorption/desorption, it is assumed that, after transients have died out, the pressure lags behind the volume by an amount ϕ, called phase lag, and has amplitude p_0. Phase and amplitude are the experimentally measured quantities. It is required to determine an expression for ϕ and p_0 in the linear approximation, which holds for small amplitudes, $m_V \ll 1$.

4.3.2 The linear approximation for small oscillations

In the linear approximation, all terms proportional to $(m_V)^\alpha$ or to $(p_0/p_e)^\alpha$ with $\alpha > 1$ are neglected. Established oscillating solutions are sought, hence the concentration $c_2(x,t)$ within the coating is taken to have the form

$$c_2\,(x,t) = c_{2e} + c_{20}(x) \sin\left[\Omega t - \phi_2\,(x)\right] \ . \tag{4.91}$$

At this stage it is particularly useful to define

$$y(x) = c_{20}(x) \sin \phi_2(x) \tag{4.92}$$

and

$$z(x) = c_{20}(x) \cos \phi_2(x) \ . \tag{4.93}$$

With this provision, the linearised surface boundary condition reads

$$D_2 \cos \Omega t \, \frac{\partial y}{\partial x} \, |_{d^-} \, - D_2 \sin \Omega t \, \frac{\partial z}{\partial x} \, |_{d^-} = \\ \left[2k_2 c_{2e} z\,(d) - k_1 p_0 \cos \phi\right] \sin \Omega t + \left[k_1 p_0 \sin \phi - 2k_2 c_{2e} y\,(d)\right] \cos \Omega t \ . \tag{4.94}$$

As this condition holds $\forall\, t$, the coefficients of $\sin \Omega t$ and of $\cos \Omega t$ must be simultaneously and separately equal to zero. This gives

$$D_2 \frac{\partial y}{\partial x} |_{d-} = k_1 p_0 \sin \phi - 2k_2 c_{2e} y(d) \tag{4.95}$$

$$D_2 \frac{\partial z}{\partial x} |_{d-} = k_1 p_0 \cos \phi - 2k_2 c_{2e} z(d) \ . \tag{4.96}$$

Similarly, the linearised diffusion equation in the coating is

$$D_2 \sin \Omega t \frac{d^2 z}{dx^2} - D_2 \cos \Omega t \frac{d^2 y}{dx^2} = \Omega \left[z(x) \cos \Omega t + y(x) \sin \Omega t \right] \tag{4.97}$$

and hence

$$D_2 \frac{d^2 z}{dx^2} = \Omega\, y(x) \tag{4.98}$$

$$D_2 \frac{\mathrm{d}^2 y}{\mathrm{d}x^2} = -\Omega\, z(x) \ . \tag{4.99}$$

Eventually, the boundary condition (4.37) at the interface, $x = 0$, yields

$$\cos \Omega t \frac{\partial y}{\partial x} |_{0+} - \sin \Omega t \frac{\partial z}{\partial x} |_{0+} = 0 \tag{4.100}$$

and this gives

$$\frac{\partial y}{\partial x} |_{0+} = 0 \tag{4.101}$$

$$\frac{\partial z}{\partial x} |_{0+} = 0 \ . \tag{4.102}$$

4.3.3 Solution of the linearised diffusion problem in the coating

The concentration in the coating, i.e $\forall\, x \in (0, d)$, is found by solving the system of differential equations (4.98), (4.99), subject to boundary conditions given by (4.101), (4.102), (4.95) and (4.96). This defines the linearised diffusion problem.

The solution is found by further differentiation of either (4.98) or (4.99), followed by substitution into the other to obtain one differential equation for only one of the variables y and z. By defining, for simplicity

$$q = \sqrt{\frac{\Omega}{2D_2}} \tag{4.103}$$

and introducing the functions

$$F(x) = \sinh(qx)\cos(qx) \ , \tag{4.104}$$

$$G(x) = \cosh(qx)\sin(qx) \ , \tag{4.105}$$

$$H(x) = \cosh(qx)\cos(qx) \ , \tag{4.106}$$

$$I(x) = \sinh(qx)\sin(qx) \ , \tag{4.107}$$

the solution of the differential equation system can be written

$$y(x) = y(0)H(x) - z(0)I(x) \tag{4.108}$$

$$z(x) = z(0)H(x) + y(0)I(x) \ . \tag{4.109}$$

Here $y(0)$ and $z(0)$ are the solution of the linear system

$$a_1 y(0) - a_2 z(0) = 2b_1 \tag{4.110}$$

$$a_2 y(0) + a_1 z(0) = 2b_2 \tag{4.111}$$

with

$$b_1 = k_1 p_0 \sin\phi \tag{4.112}$$

$$b_2 = k_1 p_0 \cos\phi \tag{4.113}$$

and

$$a_1 = 2\left\{qD_2\left[F(d) - G(d)\right] + 2k_2 c_{2e} H(d)\right\} \tag{4.114}$$

$$a_2 = 2\left\{qD_2\left[F(d) + G(d)\right] + 2k_2 c_{2e} I(d)\right\} \ . \tag{4.115}$$

The determinant of the system given by (4.110) and (4.111) is

$$C = a_1^2 + a_2^2 \tag{4.116}$$

and the solution is

$$y(0) = \frac{2}{C}\left(a_1 b_1 + a_2 b_2\right) \tag{4.117}$$

$$z(0) = \frac{2}{C}\left(a_1 b_2 - a_2 b_1\right) \ . \tag{4.118}$$

Recalling the definition of y and z (4.92), (4.93), the amplitude $c_{20}(x)$ is found by squaring and summing, i.e. $c_{20}^2 = y^2(x) + z^2(x)$. This gives

$$c_{20} = 2\frac{k_1 p_0}{\sqrt{C}} \quad . \tag{4.119}$$

Similarly, the phase is such that $\tan\phi_2(x) = y(x)/z(x)$. By introducing the angles λ and $\sigma(x)$ such that

$$\tan\lambda = \frac{a_2}{a_1} \quad , \tag{4.120}$$

$$\sigma(x) = \frac{H(x)}{I(x)} \tag{4.121}$$

the phase is expressed by

$$\tan\phi_2(x) = \tan\left[\phi_2(0) - \sigma(x)\right] \quad , \tag{4.122}$$

where

$$\tan\phi_2(0) = \tan\left[\phi + \lambda\right] \quad . \tag{4.123}$$

The diffusion problem in the coating has thus been solved, and the link between phase and amplitude of the concentration oscillation in the coating and phase and amplitude of the pressure oscillation has been found. The next step is to make use of this link to determine the pressure phase lag and amplitude as functions of the surface and bulk material parameters.

4.3.4 Phase lag ϕ and amplitude ratio Λ

The pressure oscillations are characterised by a phase lag ϕ, as already mentioned, and by an amplitude ratio Λ which measures the degree of attenuation of the pressure oscillation with respect to that of the volume. The amplitude ratio is defined as

$$\Lambda = \frac{p_0}{p_e}\frac{V_e}{V_0} \quad . \tag{4.124}$$

At this stage it is necessary to make use of the gas balance equation (4.86) and to account for hydrogen dissolved in the substrate by recalling that $c_1(t) = k\ c_2(0,t)$, where $c_2(0,t)$ is obtained from the solution given in the previous subsection.

The linearised gas balance equation then reads

$$\sin\Omega t\left\{\frac{\Omega}{RT}\left[p_0V_e\sin\phi - V_0p_e\sin\epsilon\right]\right\} - \cos\Omega t\left\{\frac{\Omega}{RT}\left[V_0p_e\cos\epsilon - p_0V_e\cos\phi\right]\right\} =$$
$$A\left\{\left[k_1p_0\sin\phi - 2k_2c_{2e}y(d)\right]\cos\Omega t - \left[k_1p_0\cos\phi - 2k_2c_{2e}z(d)\right]\sin\Omega t\right\}$$
$$-kV_1\Omega\left[z(0)\cos\Omega t + y(0)\sin\Omega t\right] \tag{4.125}$$

and it holds again $\forall\ t$. Equating separately to zero the coefficients of $\sin\Omega t$ and $\cos\Omega t$ yields

$$\frac{\Omega}{RT}\left[p_0V_e\sin\phi - V_0p_e\sin\epsilon\right] =$$
$$A\left[2k_2c_{2e}z(d) - k_1p_0\cos\phi\right] - kV_1\Omega y(0)\ , \tag{4.126}$$
$$-\frac{\Omega}{RT}\left[V_0p_e\cos\epsilon - p_0V_e\cos\phi\right] =$$
$$A\left[k_1p_0\sin\phi - 2k_2c_{2e}y(d)\right] - kV_1\Omega z(0)\ . \tag{4.127}$$

It is useful to define

$$X = \Lambda\sin\phi \tag{4.128}$$

and

$$Y = \Lambda\cos\phi\ . \tag{4.129}$$

By substituting in (4.126) and (4.127) the expression of $y(0), z(0), y(d), z(d)$ previously obtained, the linear system is deduced

$$\alpha X + \beta Y = \frac{\Omega V_e}{RT}\sin\epsilon \tag{4.130}$$
$$\beta X - \alpha Y = -\frac{\Omega V_e}{RT}\cos\epsilon\ , \tag{4.131}$$

where

$$\alpha = \frac{\Omega V_e}{RT} + \frac{2k_1a_1}{C}\left[kV_1\Omega - 2Ak_2c_{2e}I(d)\right] + 4Ak_1k_2c_{2e}\frac{a_2}{C}H(d) \tag{4.132}$$

$$\beta = \frac{2k_1a_2}{C}\left[kV_1\Omega - 2Ak_2c_{2e}I(d)\right] - 4Ak_1k_2c_{2e}\frac{a_1}{C}H(d)\ . \tag{4.133}$$

The determinant of the linear system is

$$\mathcal{D} = -(\alpha^2 + \beta^2) \tag{4.134}$$

and its solution is

$$X = \frac{\Omega V_e}{\mathcal{D}RT}(\beta \cos\epsilon - \alpha \sin\epsilon) \tag{4.135}$$

$$Y = -\frac{\Omega V_e}{\mathcal{D}RT}(\beta \sin\epsilon + \alpha \cos\epsilon) \ . \tag{4.136}$$

The phase lag ϕ is obtained from (4.128), (4.129) as follows:

$$\tan\phi = \frac{X}{Y} = -\frac{\beta\cos\epsilon - \alpha\sin\epsilon}{\beta\sin\epsilon + \alpha\cos\epsilon} \ , \tag{4.137}$$

which, upon introduction of the phase advance θ defined as

$$\tan\theta = \frac{\beta}{\alpha} \ , \tag{4.138}$$

becomes

$$\tan\phi = -\tan(\theta - \epsilon) \tag{4.139}$$

or equivalently

$$\phi = \epsilon - \theta \ . \tag{4.140}$$

In other words $-\theta$ coincides with the phase lag ϕ when the system response time τ_{SR} is equal to zero, i.e. $\epsilon = 0$.

As for the amplitude ratio Λ, by squaring (4.128), (4.129) adding the resulting equalities and taking the square root, one obtains

$$\Lambda = \sqrt{X^2 + Y^2} = \frac{\Omega V_e}{RT\sqrt{\mathcal{D}}} \ . \tag{4.141}$$

At this stage, the following important parameters have to be introduced:

- the diffusion time in the coating, τ_d

$$\tau_d = \frac{d^2}{D_2} \ , \tag{4.142}$$

  which is different from the analogous diffusion time (4.41) used to model the experiments carried out at Ispra;

- the modified partition coefficient u, defined by (4.50);

- the pseudo-volume V_{H_2}

$$V_{H_2} = RTAd\frac{c_{2e}}{p_e} \tag{4.143}$$

and the ratio

$$R_{He} = \frac{V_{H_2}}{V_e} \ ; \tag{4.144}$$

it is worth noticing that V_{H_2} is the volume that the amount of hydrogen dissolved in the coating would occupy at the temperature T and at the pressure p_e;

- the surface time τ_s, characteristic of specimen charge-up in surface-limited regimes

$$\tau_s = \frac{d}{4k_2c_{2e}} \ . \tag{4.145}$$

The flow regime number

$$\gamma = 2\frac{\tau_s}{\tau_d} \tag{4.146}$$

then discriminates between surface- and diffusion-dominated regimes; by recalling (4.87) it can be rewritten as

$$\gamma = \frac{D_2K_s\sqrt{p_e}}{2k_1p_ed} \ . \tag{4.147}$$

Accordingly, the flow of hydrogen is controlled by bulk diffusion at large values of the thickness d, of the equilibrium pressure p_e, of the surface constant k_1 or for small diffusivities D_2 or Sieverts' constants K_s in the coating. The opposite holds for surface-controlled flow.

It is worth pointing out that from (4.147), γ is the ratio of the steady-state diffusion-limited permeation flux $j_{\infty,\mathrm{DL}} = D_2K_s\sqrt{p_e}/d$ through a symmetric membrane continuously pumped downstream and of thickness d, to four times that in surface-limited conditions $j_{\infty,\mathrm{SL}} = k_1p_e/2$.

Another noteworthy point is the dependence of V_{H_2}, R_{He}, τ_s and γ on the equilibrium pressure p_e: all these parameters scale as $1/\sqrt{p_e}$, after recalling (4.87).

In order to simplify an otherwise cumbersome notation, the following quantities are introduced:

$$\mathcal{W}_1 = \cosh(2qd) - \cos(2qd) \ , \tag{4.148}$$

$$\mathcal{W}_2 = \cosh(2qd) + \cos(2qd) \ , \tag{4.149}$$

$$\mathcal{U}_1 = \sinh(2qd) - \sin(2qd) \ , \tag{4.150}$$

$$\mathcal{U}_2 = \sinh(2qd) + \sin(2qd) \ , \tag{4.151}$$

$$\mathcal{N} = R_{He}\{\gamma\Omega\tau_d\mathcal{W}_1 + qd\mathcal{U}_1 + 2u\Omega\tau_d[\gamma qd[F(d) + G(d)] + I(d)]\} \ , \tag{4.152}$$

$$\mathcal{D}_0 = 2\Omega\tau_d[\mathcal{W}_2 + \gamma\Omega\tau_s\mathcal{W}_1 + 2\gamma qd\mathcal{U}_1] \ , \tag{4.153}$$

$$\mathcal{D}_1 = R_{He}qd\mathcal{U}_2 \ , \tag{4.154}$$

$$\mathcal{D}_2 = 2uR_{He}\Omega\tau_d\{\gamma qd[F(d) - G(d)] + H(d)\} \ , \tag{4.155}$$

$$\mathcal{D}_E = \mathcal{D}_0 + \mathcal{D}_1 + \mathcal{D}_2 \ . \tag{4.156}$$

With these provisions, the phase advance θ is given by

$$\tan\theta = \frac{\mathcal{N}}{\mathcal{D}_E} \tag{4.157}$$

and the amplitude ratio reads

$$\Lambda = \frac{\mathcal{D}_0}{\sqrt{\mathcal{N}^2 + \mathcal{D}_E^2}} \ . \tag{4.158}$$

It can be shown that the phase lag ϕ tends to zero both as $\Omega \to 0$ and as $\Omega \to \infty$. This can be interpreted physically by noticing that as the frequency is diminished, the system tends to approach the equilibrium conditions existing exactly only at $\Omega = 0$, while for very large oscillation frequencies the specimen does not interact with the impinging pressure wave, which oscillates too quickly for the specimen dynamics to react.

4.3.5 Influence of physical parameters on ϕ

In order to elucidate the influence of the many parameters involved in the analytical expression of phase lag and amplitude ratio, it is useful to examine some particular cases. This is the subject of the next subsubsections and the treatment is restricted only to the phase advance $\theta = \epsilon - \phi$ for simplicity. Plots of $\phi\ |_{\epsilon=0} = -\theta$ versus $\sqrt{\nu/\mathrm{mHz}}$, where $\nu = \Omega/(2\pi)$ is the oscillation frequency, are used in the following to help understanding the parameters' influence on ϕ.

Diffusion-limited case

The diffusion-controlled case is obtained in the limit $\gamma \to 0$. This approximation gives, for the phase advance θ

$$\tan\theta = R_{He}\frac{\mathcal{U}_1 + 4uqd\,I\,(d)}{4qd\mathcal{W}_2 + R_{He}\,[\mathcal{U}_2 + 4uqd]} \quad . \tag{4.159}$$

Figures 4.3 and 4.4 show the way varying the parameters R_{He} and τ_d respectively

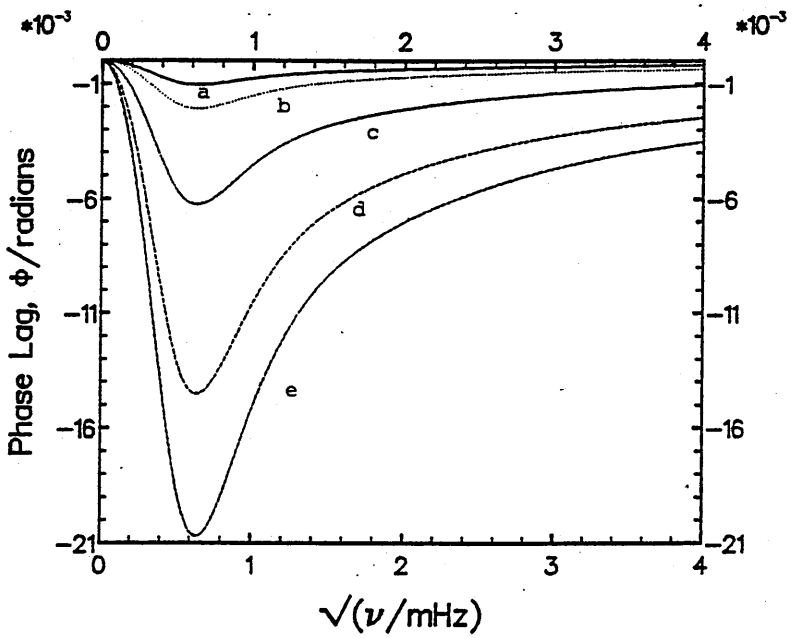

Figure 4.3 Effect of varying R_{He} on ϕ in diffusion-limited conditions. Parameters are $\tau_d = 1000$ s, $u = 0$ and R_{He}: a – 0.005, b – 0.01, c – 0.03, d – 0.07, e – 0.1 .

affect the ϕ versus $\sqrt{\nu}$ curves, for a non-absorbing-substrate case, $u = 0$. Increasing R_{He} produces larger values, in magnitude, of ϕ by deepening the minimum and by slightly shifting it towards larger frequencies. Augmenting the time τ_d does not vary the magnitude of ϕ but solely compresses the whole curve, and therefore shifts the minimum, towards lower frequencies.

Figure 4.5 shows the effect of varying the substrate parameter u for fixed values of R_{He} and τ_d. An increase in u provokes effects that are qualitatively similar to those caused by an increase in R_{He} but

- the changes are only appreciable for frequencies smaller than a threshold value,

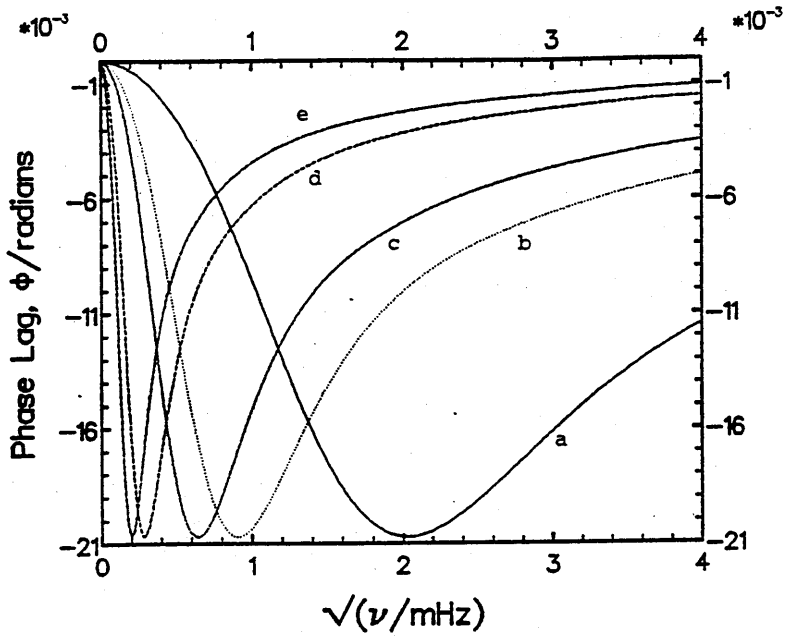

Figure 4.4 Effect on ϕ versus $\sqrt{\nu}$ curve of varying the diffusion time τ_d in diffusion-limited conditions. Parameters values are $u = 0$, $R_{He} = 0.1$ and τ_d/s : a – 100, b – 500, c – 1000, d – 5000, e – 10000.

- the minimum is not shifted,
- the valley width is only slightly increased,
- an additional "shoulder" and possibly a minimum are added for large values of u,
- in contrast with the increase in ϕ caused by R_{He}, that produced by an increase of u does not depend on p_e .

Surface-limited case

The surface-controlled case is obtained in the limit $\gamma \to \infty$. This approximation gives, for the phase advance θ

$$\tan\theta = 2R_{He}\frac{(u+1)\,\Omega\tau_s}{4\Omega^2\tau_s^2 + (u+1)\,R_{He} + 2} \quad . \tag{4.160}$$

It is interesting to note that, for $u = 0$, on rearranging one has

$$\Omega^2 = \frac{1}{2\tau_s^2}\left[R_{He}\frac{\Omega\tau_s}{\tan\theta} - \frac{1}{2}R_{He} - 1\right] \quad . \tag{4.161}$$

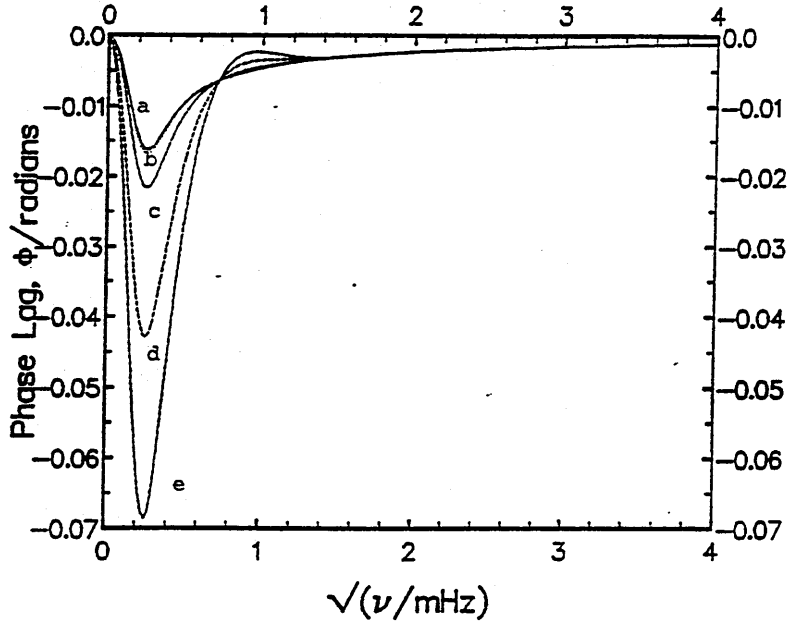

Figure 4.5 Effect on ϕ versus $\sqrt{\nu}$ curve of varying the modified partition coefficient u, in diffusion-limited conditions. Parameters values are $\tau_d = 6000$ s, $R_{He} = 0.08$ and u: a – 0, b – 0.023, c – 0.23, d – 1.17, e – 2.34.

Therefore, a plot of Ω^2 versus $\Omega/\tan\theta$ would give a straight line with slope equal to $R_{He}/(2\tau_s)$ and intercept equal to $-(R_{He}+2)/(4\tau_s^2)$. Such plot would allow the determination of K_s and k_1.

Figures 4.6 and 4.7 show the way varying the parameters R_{He} and τ_s respectively affects the ϕ versus $\sqrt{\nu}$ curves, for a non-absorbing-substrate case, $u = 0$. The effects produced are the same as those obtained in the diffusion-limited case by varying R_{He} and τ_d.

Figure 4.8 shows the effect of varying the modified partition coefficient u for fixed values of R_{He} and τ_s. Again, the effect produced is similar to that obtained in the diffusion-limited case, but for the lack of additional shoulder and minimum, which are not visible in this figure.

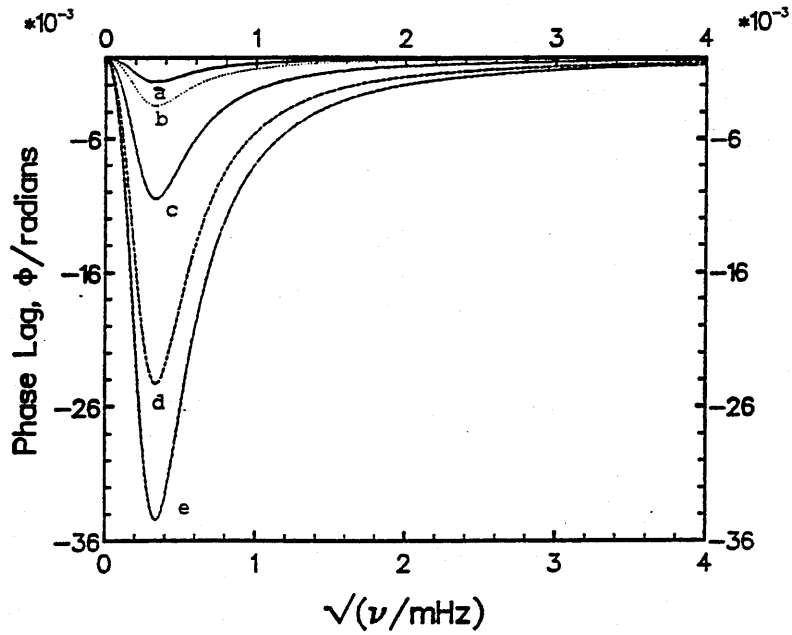

Figure 4.6 Effect of varying the pseudo-volume ratio R_{He}, on ϕ versus $\sqrt{\nu}$ curve, in surface-limited conditions. Parameters values are $\tau_s = 1000$ s, $u = 0$ and R_{He}: a – 0.005, b – 0.01, c – 0.03, d – 0.07, e – 0.1.

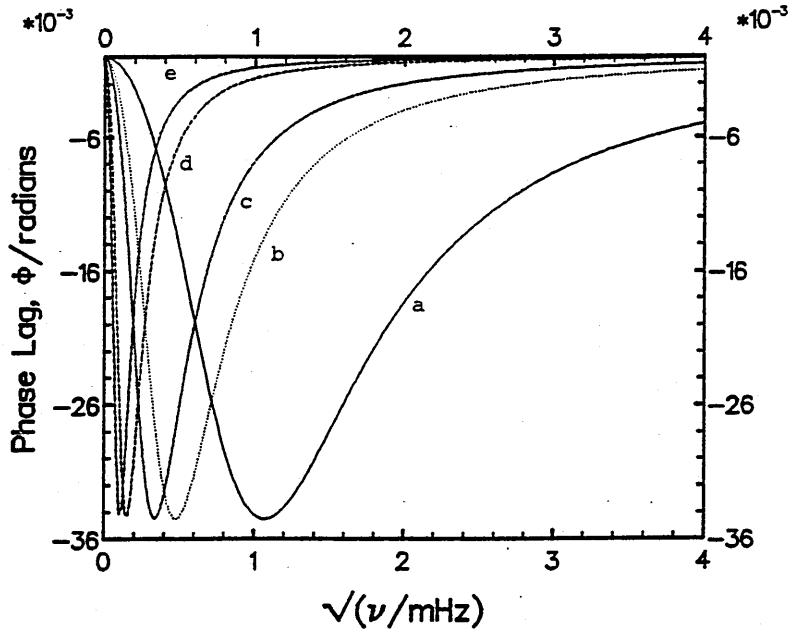

Figure 4.7 Effect on ϕ versus $\sqrt{\nu}$ curve of varying the surface time τ_s in surface-limited conditions. Parameters values are $u = 0$, $R_{He} = 0.1$ and τ_s/s : a – 100, b – 500, c – 1000, d – 5000, e – 10000.

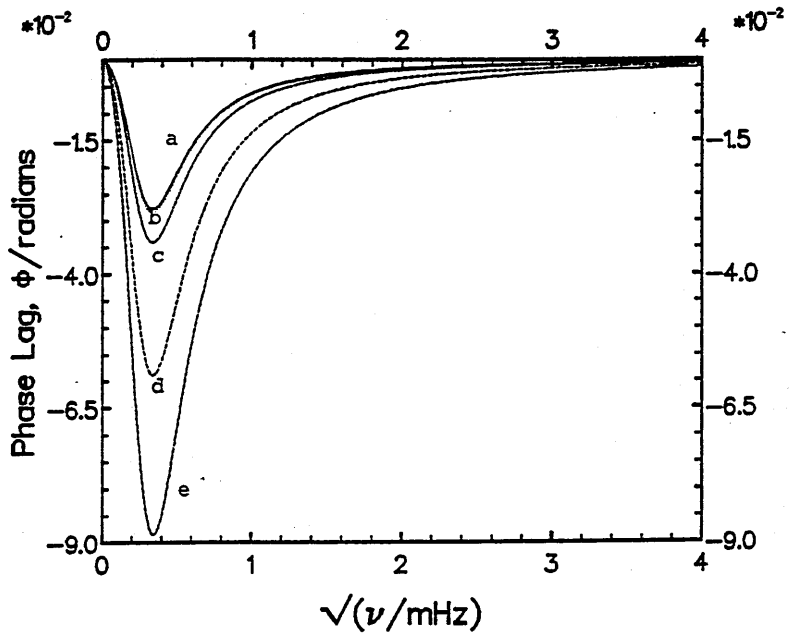

Figure 4.8 Effect on ϕ versus $\sqrt{\nu}$ curve of varying the modified partition coefficient u, in surface-limited conditions. Parameters values are $\tau_s = 1000$ s, $R_{He} = 0.08$ and u: a – 0, b – 0.023, c – 0.23, d – 1.17, e – 2.34.

Mixed regime and the diffusion- to surface-limited transition without substrate absorption ($u = 0$)

A mixed regime, where diffusion and surface effects have the same importance for the kinetics of the overall process, is present when γ is neither too small nor too large. There is no clear-cut boundary between diffusion- and surface-control and it can be approximately stated that the transition between these two regimes occurs slowly over a range $0.01 < \gamma < 100$, which then defines the mixed regime condition.

In this case there is no simple formula for the phase advance θ, which has to be evaluated by means of (4.157). Setting $u = 0$ has the simplifying effect of giving $\mathcal{D}_2 = 0$.

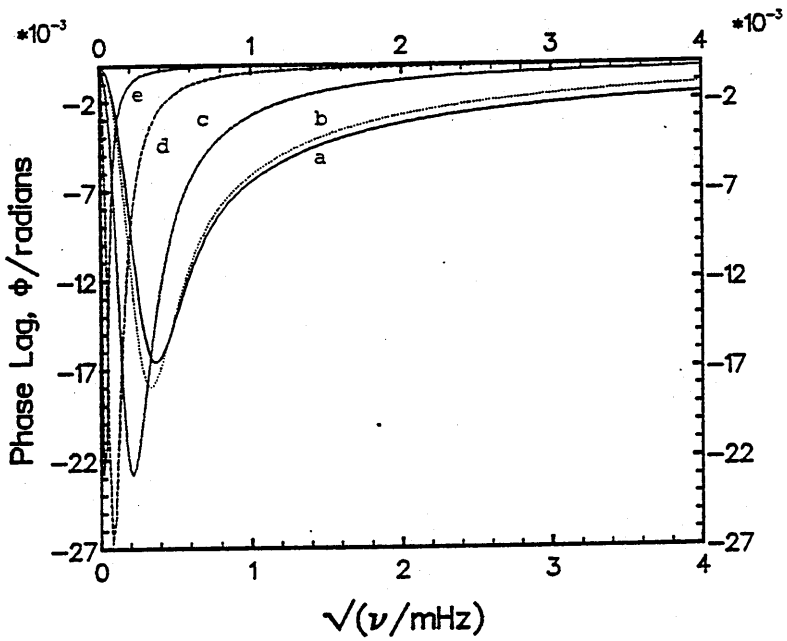

Figure 4.9 Evidence for the surface- to diffusion-control transition obtained for ϕ versus $\sqrt{\nu}$ curves by varying the flow regime number γ, with a non-absorbing substrate. Parameters values are $\tau_d = 3000$ s, $R_{He} = 0.08$, $u = 0$ and γ: a – 0, b – 0.1 , c – 1, d – 10, e – 100.

Figure 4.9 shows the way the transition from diffusion- to surface-control affects the ϕ versus $\sqrt{\nu}$ curves, for a non-absorbing-substrate case, $u = 0$ and for fixed values of R_{He} and τ_d. It is evident that increasing γ has the effect of compressing the phase lag curve towards lower frequencies, of making the valley steeper and

deeper.

Mixed regime with substrate absorption ($u \neq 0$)

The real case of an absorbing substrate, $u \neq 0$, has to be treated by means of the full formula (4.157), for the phase advance θ. Figure 4.10 shows how an absorbing

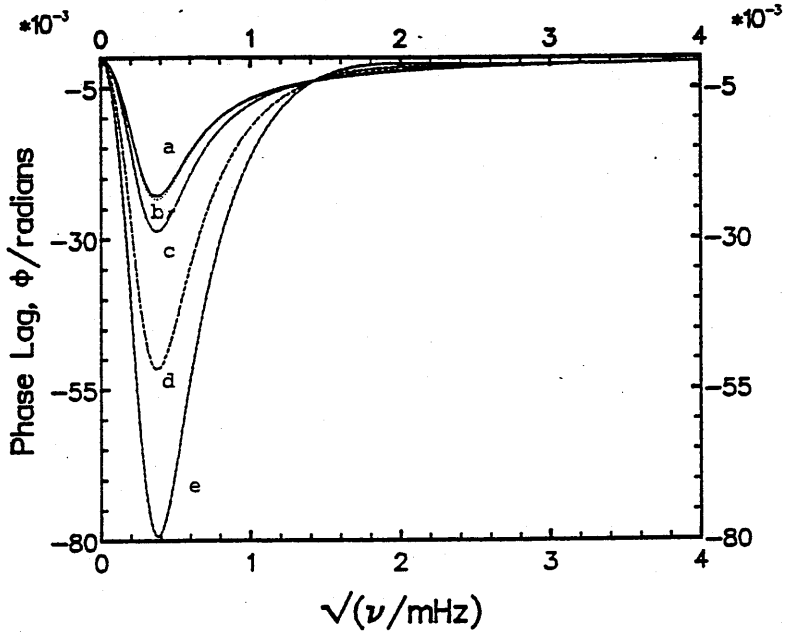

Figure 4.10 Effect of an absorbing substrate on the ϕ versus $\sqrt{\nu}$ curves in a mixed regime. Parameters values are $\tau_d = 1000$ s, $R_{He} = 0.08$, $\gamma = 1$ and u: a – 0, b – 0.023 , c – 0.23, d – 1.17, e – 2.34.

substrate affects the ϕ versus $\sqrt{\nu}$ curves, in a mixed regime, $\gamma = 1$, and for fixed values of R_{He} and τ_d. The effect of increasing u is the same as for the diffusion-limited case.

4.4 Summary

Two models have been developed to interpret hydrogen release experiments carried out at the JRC Ispra, in the bulk- and surface-controlled limits. These have been described for bare and coated specimen. A model including both diffusion and

surface reactions, at the same time, would require the use of computer numerical algorithms. Work is under way on this topic.

A comprehensive model, which includes substrate absorption, surface processes and bulk diffusion, has been developed and described for interpretation of the volume-modulation experiments carried out at the Oxford Research Unit.

The nature of the experiments carried out at Oxford is such that the interaction of hydrogen with thin coatings deposited on short cylinders can be modelled by reduction to a slab diffusion problem. Uncoated short cylindrical samples would require additional modelling, beyond the scope of this work. Spherical symmetry would be simpler and could also be used as a first approximation for short uncoated cylinders.

Chapter 5

Results and Discussion

5.1 Introduction

This chapter reports the experimental findings of this thesis. The results obtained at Ispra are detailed first, on hydrogen release from TZM, from TiC-coated steel and from TiC-coated TZM. One separate section is devoted to each one of the three combinations of materials. Results of the volume modulation work carried out at Oxford with TiC-coated TZM are reported in a fourth section.

In each section, an opening subsection gives some preliminary considerations based on a scrutiny of raw data, without resorting to models of the experiment. A second subsection contains the results from model-to-data fitting and discusses them briefly.

Results for the hydrogen-TZM system are given first and are then used to interpret the experiments with TiC coated specimens.

5.2 Work with bare TZM

5.2.1 Preliminary considerations

As anticipated in chapter 3, each release experiment carried out with the Ispra technique contains information on the dynamics and about the equilibrium state of the processes involved. It is reasonably assumed that the equilibrium state is independent of the type of dynamics involved. It was also stated in chapter 1 that

the equilibrium state can give information on relevant physics, such as the state of dissolved hydrogen. It is then useful to devote attention first to final pressures P_f and solubilities S, then to the shape and the behaviour of transient release curves.

Solubility and departure from Sieverts' law

For the experiments on hydrogen in TZM, at a given temperature T, the solubility $S(T, p_0)$ computed from the final pressure P_f with equation (4.22), presents an unexpected feature, as it can be seen in Figure 5.1. The experimental points lie

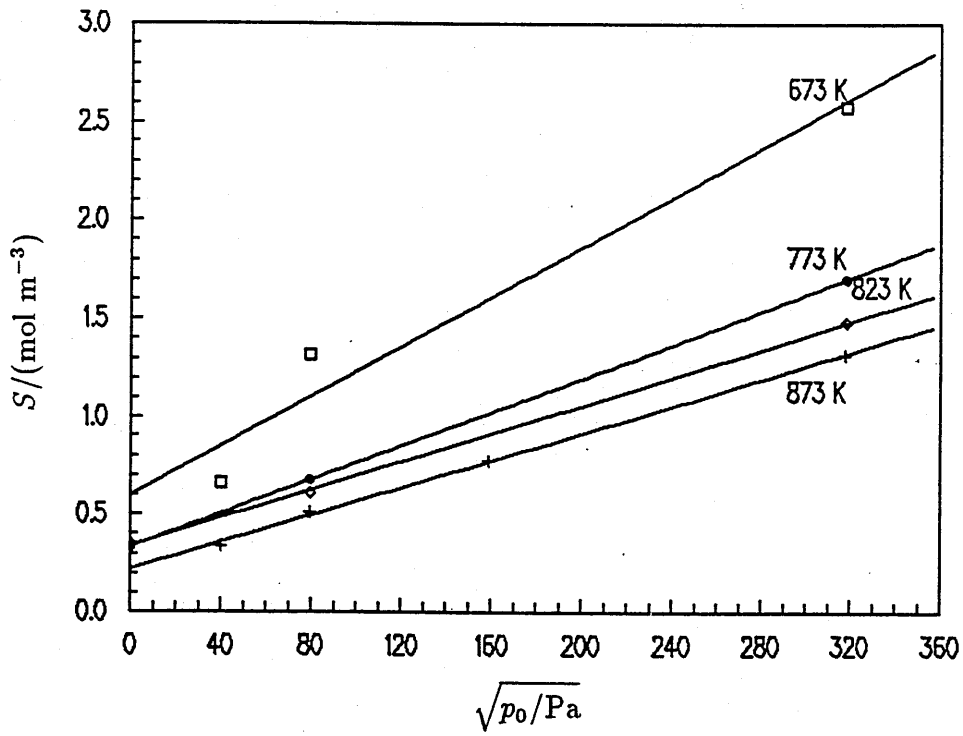

Figure 5.1 Variation of the hydrogen solubility S in TZM with the square root of the loading pressure p_0 at different temperatures.

remarkably close to a straight line which does not pass through the origin. In fact, a linear fit of S vs $\sqrt{p_0}$ gives an intercept S_0 at $p_0 = 0$ significantly different from zero, between 0.2 and 0.6 mol m^{-3}. It has to be noted that S_0 varies with the temperature and increases as the temperature is decreased. It is useful to compare the values of S_0 to the equivalent concentration coming from a unit hydrogen surface coverage:

using a surface roughness of 3, a value of $\theta = 1$ would be equivalent to $c_\theta = 0.02$ mol m^{-3}, so the hydrogen adsorbed on the two dimensional sample surface cannot be responsible for S_0. In addition, the term c_θ should also be expected to be linear with $\sqrt{p_0}$.

In other words, the term S_0 does not fit the expectations based on Sieverts' law. Two possibilities have to be considered, depending on whether the term S_0 is confirmed by experiments carried out at lower pressures, or not. Such measurements would be needed to determine the pressure dependence of the solubility close to $p_0 = 0$.

1) First case: $S_0 \neq 0$ even at very low pressure. The case in which the linear pressure dependence $S = S_0 + K_s\sqrt{p_0}$ remains unchanged even at virtually zero pressure is considered first.

To find a possible explanation in such a case, it is worth observing that the equilibrium concentration at the end of the loading phase c_i, which is equivalent to the solubility S, can be written as

$$c_i = S_0 + K_s\sqrt{p_0} \tag{5.1}$$

and in an equivalent way

$$k_2(c_i - S_0)^2 = k_1 p_0 \ . \tag{5.2}$$

This equates the equilibrium desorption and absorption fluxes; when plotted on a p_0 versus c_i graph, (5.2) is represented by a parabola having a minimum on the c_i axis, with abscissa $c_{i,min} = S_0$. Such a plot is shown in Figure 5.2, for the experimental data measured at 873 K. It turns out however that the data can be described by one branch of the parabola $p_0 = \alpha + \beta c_i + \gamma c_i^2$ where the minimum has ordinate $p_{min} = \alpha - \beta^2/(4\gamma) = 620$ Pa. This value is really small in this case, but it is not negligible compared to $S^2 k_2/k_1$ where S is the solubility of low pressure points. By re-defining $S_0 = c_{i,min} = -\beta/(2\gamma)$ and $K_s = 1/\sqrt{\gamma}$, the new parabola can be expressed by the equation

$$k_2(c_i - S_0)^2 + k_1 p_{min} = k_1 p_0 \ , \tag{5.3}$$

which replaces the equilibrium condition expressed by equation (5.2). From (5.3) one has that $p_0 > p_{min}$. Equation (5.3) can also be written as

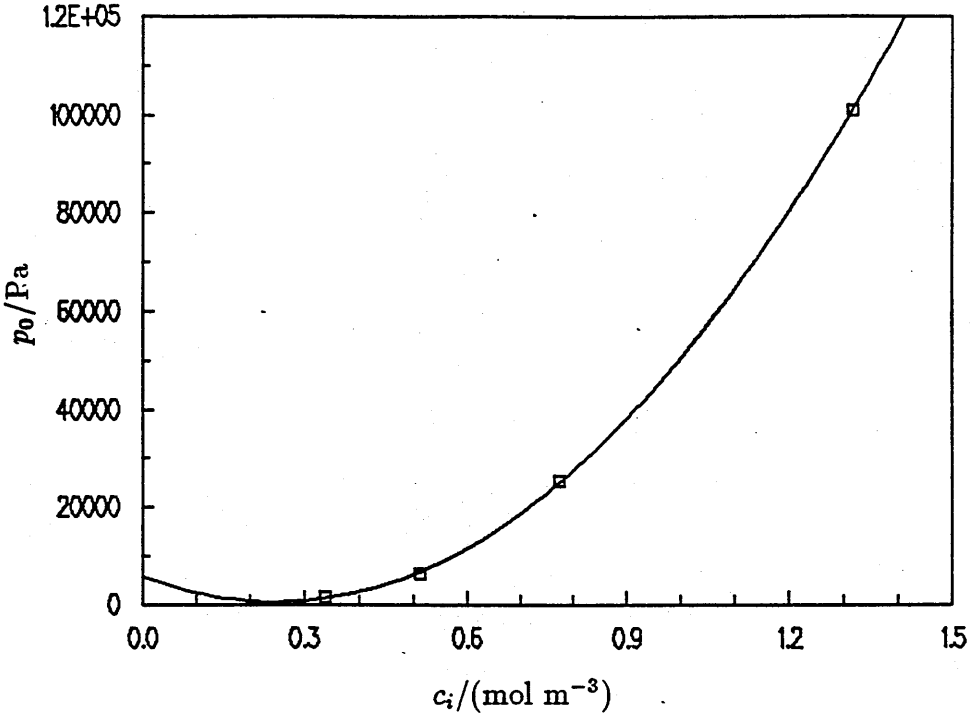

Figure 5.2 Plot of the loading pressure p_0 versus the equilibrium initial concentration c_i at 873 K; a parabola is fitted to the data points, to obtain the residual solubility S_0 as abscissa of the minimum and the additional term p_{min} as the ordinate of the minimum.

$$c_i = S_0 + K_s\sqrt{p_0 - p_{min}} \ , \tag{5.4}$$

which expresses a deviation from Sieverts' law.

Thus, if again c_i or S are plotted versus $\sqrt{p_0}$, as shown in Figure 5.3 for the data obtained at 673 K, the trend for pressures much higher than p_{min} is linear with $\sqrt{p_0}$, while as the pressure is decreased a departure from linearity can be observed. One should bear in mind this fact when judging the low pressure data points in Figure 5.1. The attempt shown in Figure 5.3, at fitting the data at 673 K with equation (5.4) suggests that the lowest pressure point might be underestimated. In Figure 5.3 the best choice is for $p_{min} = 1600$ Pa and for an effective Sieverts' constant 20 per cent lower than the one quoted in the next section.

An additional absorption-desorption flux $f_{ad} = k_1 p_{min}$ can be introduced to represent adsorption and desorption of an additional hydrogen population existing

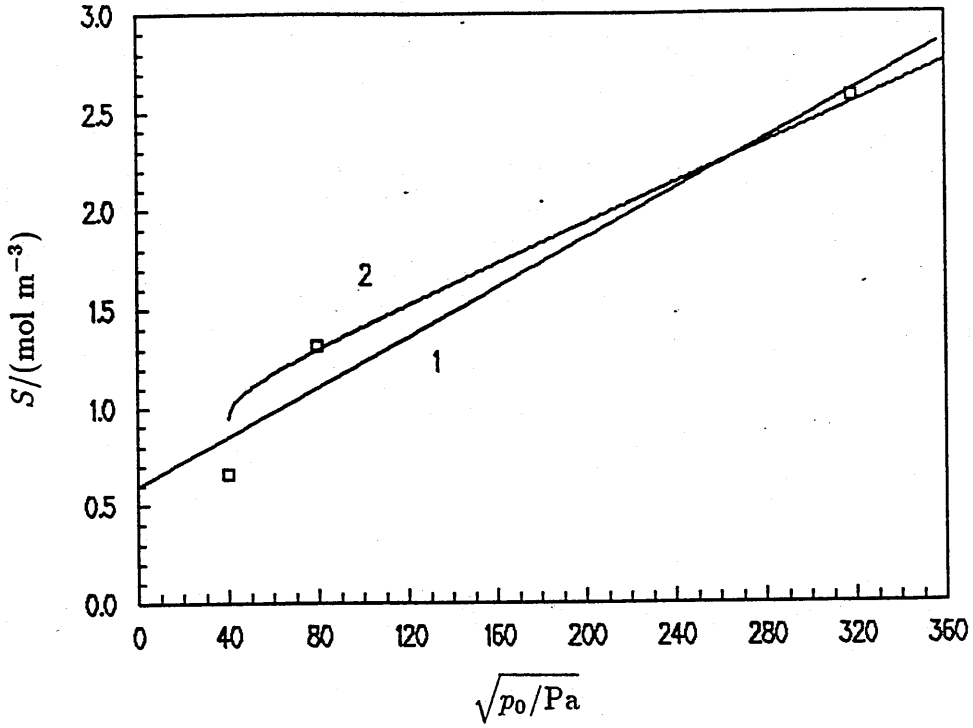

Figure 5.3 Square root of pressure dependence of the solubility at 673 K, obtained from equation (5.4), showing a departure from Sieverts' law at low pressures. The straight line 1 was obtained by a linear fit to the points while curve 2 is an attempt at fitting the points with equation (5.4), using $p_{min} = 1600$ Pa. As a consequence, the low pressure data seem underestimated, as well as the values of S_0, whereas K_s turns out to be overestimated by about 20 per cent.

on the specimen surface. Such a hydrogen population is not included in equation (5.2), where the total hydrogen concentration c_i in the sample is not fully available for the recombinative desorption flux. Indeed, in equation (5.2) only an effective concentration $c_i - S_0$ is contained in the desorption term. The term f_{ad} represents the absorption-desorption flux for the amount of hydrogen $V_s S_0$. A mechanism for the additional flux f_{ad} is suggested in the discussion section.

It is concluded that (5.1) only holds for large pressures, $p_0 \gg p_{min}$, and for lower pressures this model reveals a departure from a linear dependence on $\sqrt{p_0}$.

2) Second case: the pressure dependence of S changes as p_0 approaches zero. A second possibility arises when the pressure dependence of S changes as the pressure is decreased. It has been shown in 1.2.2 that such a behaviour is predicted by a model which accounts for nonlinear trapping in the host matrix. The steric factor $(1 - zN_A/N)$ in this case is responsible for the term S_0. This means that trap occupation is high and the equations describing the transient behaviour are nonlinear because of the product cz. Therefore these equations cannot be solved by analytical methods. Nevertheless, the diffusivity D can be extracted from high pressure data and the Sieverts' constant K_s can be found by plotting S versus $\sqrt{p_0}$ and computing the slope of the resulting high pressure straight line .

At this stage there are not enough data to decide which of the two possible explanations is the right one.

Summary. As final comment to this subsubsection, it can be recalled that the raw data on solubility are affected by the unexpected term S_0, which is not dependent on the loading pressure p_0. Two possible explanations have been given for this and accordingly, two ways have been shown to extract Sieverts' constant, provided more data for different loading pressures at a given temperature are available. Departures from Sieverts' law are therefore possible if there is an additional desorption flux from the specimen surface or if nonlinear trapping is present. In the next section it will be suggested that in the first case, such a flux can be associated with an additional hydrogen population existing on the specimen surface.

Transient release

The normalised hydrogen release curves at 873 K are shown in Figure 5.4, for loading pressures in the range 10^3 - 10^5 Pa. It is evident that for loading pressures p_0 higher than 2.5×10^4 Pa the release curves overlap, in agreement with the diffusion-limited model developed in chapter 4. The release becomes slower at lower loading pressures, a fact which can be ascribed to surface processes becoming dominant over bulk diffusion. Such behaviour is in qualitative agreement with the surface-limited model developed in chapter 4. The release curves have shown a similar trend with the loading pressure also at lower temperatures.

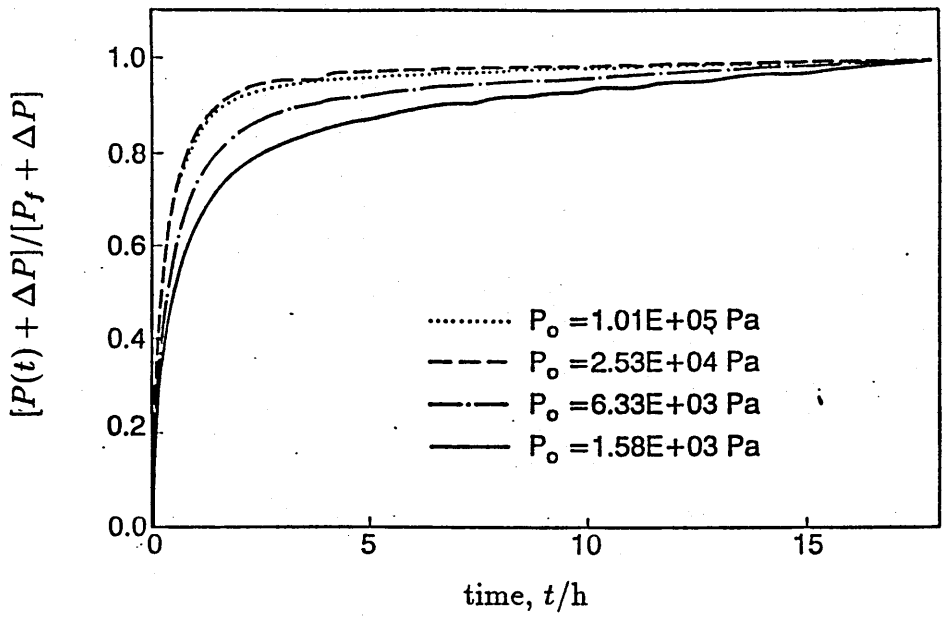

Figure 5.4 Pressure effects on the hydrogen normalised release from TZM at 873 K.

From the release curves it appears that the release and loading times chosen were long enough to reach equilibrium at temperatures between 773 K and 873 K. At 673 K the release times turned out to be too short and so probably were also the loading times. As a consequence the solubility at 673 K obtained here may turn out to be underestimated, as anticipated in the previous subsubsection by means of considerations on the equilibrium state.

5.2.2 Results

Fits to data of both the surface-limited (SL) and the diffusion-limited (DL) models for a homogeneous solid were carried out.

In general and from a qualitative point of view, the SL model could produce a better fit to the data than the DL model. The agreement between fitted and experimental curve was excellent with both models till roughly 90 per cent of the final pressure was reached. Then the approach to equilibrium in the experimental curve was gentle since the remaining 10 per cent of the hydrogen was given off at a rate almost constant in time. This was better modelled by the SL model which allows such gentle approach to equilibrium after the release has reached 90 per cent of the steady state. Indeed, the DL model predicts a much more abrupt approach to

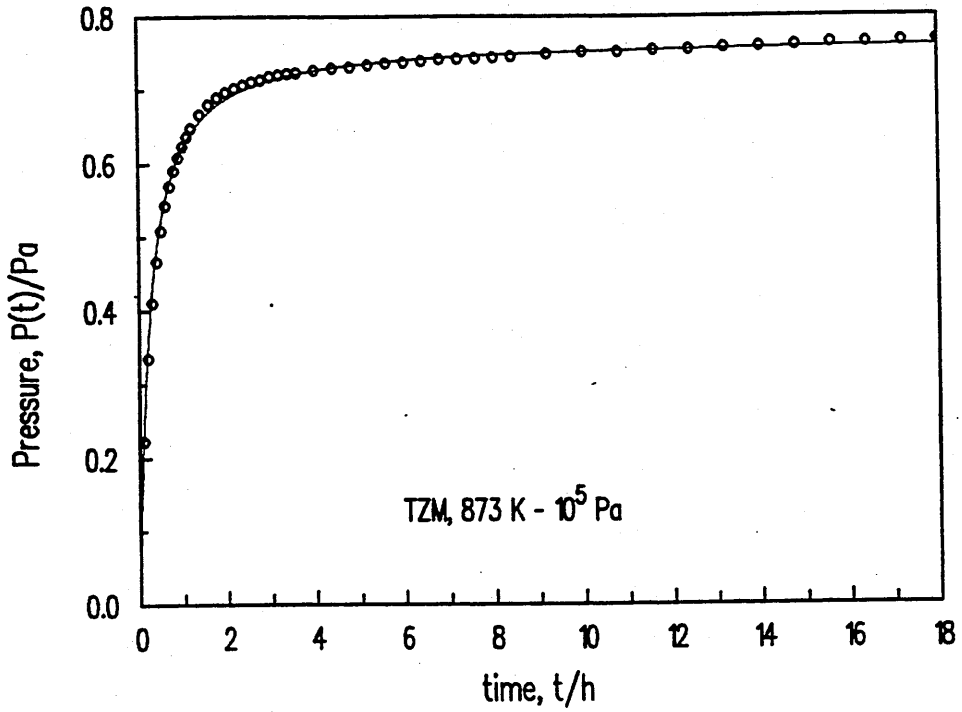

Figure 5.5 Fit by the SL model to the normalised pressure curve, for hydrogen released by TZM at 873 K and 10^5 Pa. Key to symbols: o o o experiment, — fitted curve.

equilibrium. This fact can be understood by comparing the fitted curves produced with the two models, for the same release run at 873 K and 10^5 Pa, as shown in Figure 5.5 for the SL model and in Figure 5.6 for the DL model. The DL model gave a closer fit at high loading pressures and low temperatures, whereas the opposite was true for the SL model. This is interpreted as evidence of the fact that surface processes become important at low hydrogen concentrations in the sample.

The residual solubility S_0 was found to vary with the temperature according to

$$S_0/(\text{mol m}^{-3}) = 1.55 \times 10^{-2} \exp\left(\frac{2450}{T/\text{K}}\right) , \tag{5.5}$$

which implies that the processes, if any, associated with the residual solubility are exothermic, with an activation energy of 20.37 kJ mol^{-1}.

The Sieverts' constant, computed as $K_s = (S - S_0)/\sqrt{p_0}$, was found to vary with the temperature as follows

$$K_s/(\text{mol m}^{-3}\ \text{Pa}^{-1/2}) = 3.68 \times 10^{-4} \exp\left(\frac{1900}{T/\text{K}}\right) , \tag{5.6}$$

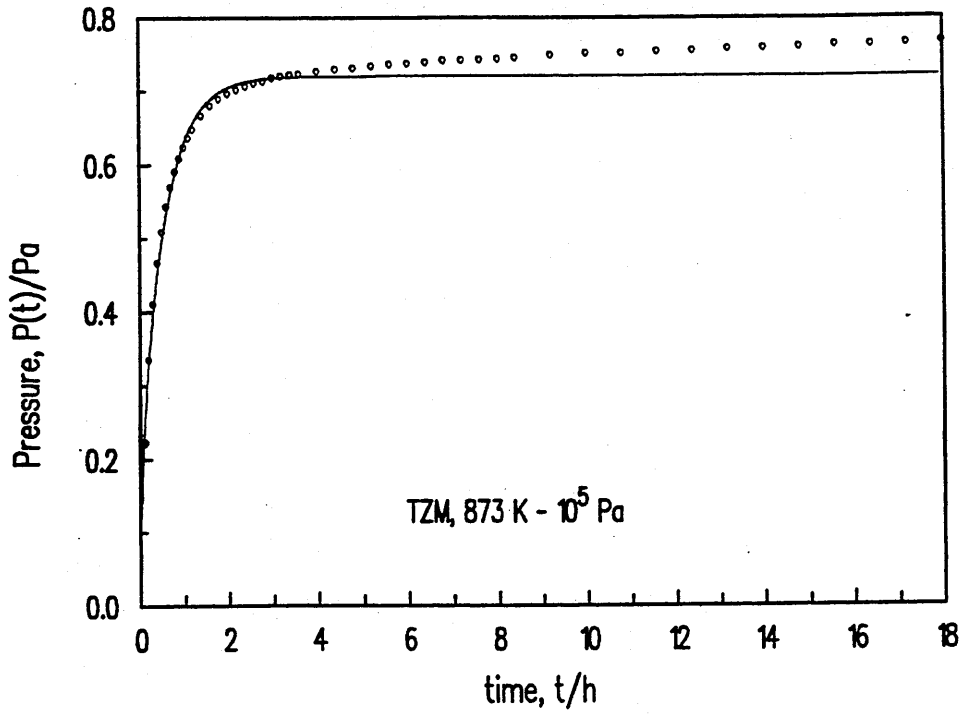

Figure 5.6 Fit to data by the DL model to the normalised pressure curve for hydrogen released by TZM at 873 K and 10^5 Pa. Key to symbols: o o o experiment, — fitted curve.

from which a solution heat Q_s of 15.8 kJ mol^{-1} is deduced. The temperature dependence of both S_0 and K_s is shown in Figure 5.7. The solubility coefficient K_s decreases with increasing temperature which means that, in contrast with the case of molybdenum, hydrogen solution in TZM is exothermic.

The term S_0 can be interpreted as a contribution from surface contaminants that liberate hydrogen on reacting with the metal [56, 57], as discussed at the end of this section.

Alternatively, S_0 can be ascribed to nonlinear trapping. In such a case the trap density $N = N_A S_0$ is obtained as

$$N/(\text{traps m}^{-3}) = 9.33 \times 10^{21} \exp\left(\frac{2450}{T/\text{K}}\right) \quad , \tag{5.7}$$

which at 873 K gives $N_{873\,K} = 1.54 \times 10^{23}$ m^{-3} , while at 673 K it is $N_{673K} = 3.56 \times 10^{23}$ m^{-3}. These two values are equivalent to a trap-to-atom ratio of 2.4×10^{-6} traps per host atom and 5.6×10^{-6} traps per host atom, respectively. The temperature dependence of N might express some trap annealing. Such conclusion is

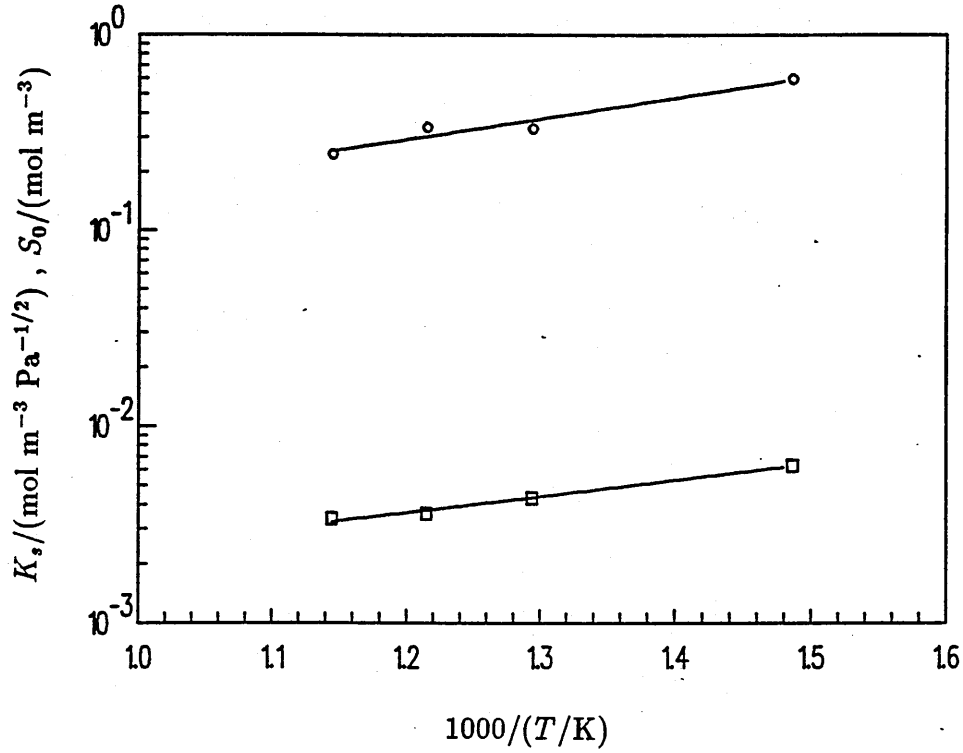

Figure 5.7 Temperature dependence of hydrogen residual solubility S_0 and Sieverts' constant K_s in TZM. Key to symbols: □ – K_s, ○ – S_0.

however suspicious, as TZM is a high temperature material, with a recrystallisation temperature well over 1300 K. Temperature cycling between room temperature and 873 K, to which the specimens had been subjected, should have no effect on N.

The apparent diffusion coefficient D_{app}, obtained by fitting to data the pressure law obtained by the DL model, varies with the loading pressure p_0, as shown in Figure 5.8. This figure also presents the apparent Sieverts' constant $K_{s,app} = S/\sqrt{p_0}$ and the apparent permeability $\Phi_{app} = D_{app}K_{s,app}$. For all three, there seems to be a trend towards saturation for high values of p_0, which is interpreted as an indication that the experimental conditions approach a diffusion-limited regime, unaffected by traps. The variation of Φ_{app} with p_0 is small, but still there is a trend to decrease with p_0. This might be caused by surface processes.

The high pressure values of D_{app} should therefore represent more closely the true diffusivity D, whether D_{app} is influenced by trapping or by surface reactions, as

shown in chapter 1 for trapping. Such values were used to find the temperature dependence, presented in Figure 5.9, which is given by .

$$D/(\mathrm{m^2 s^{-1}}) = 4.78 \times 10^{-5} \exp\left(-\frac{10100}{T/\mathrm{K}}\right) \quad . \tag{5.8}$$

This gives an activation energy for diffusion of 83.97 kJ mol^{-1}.

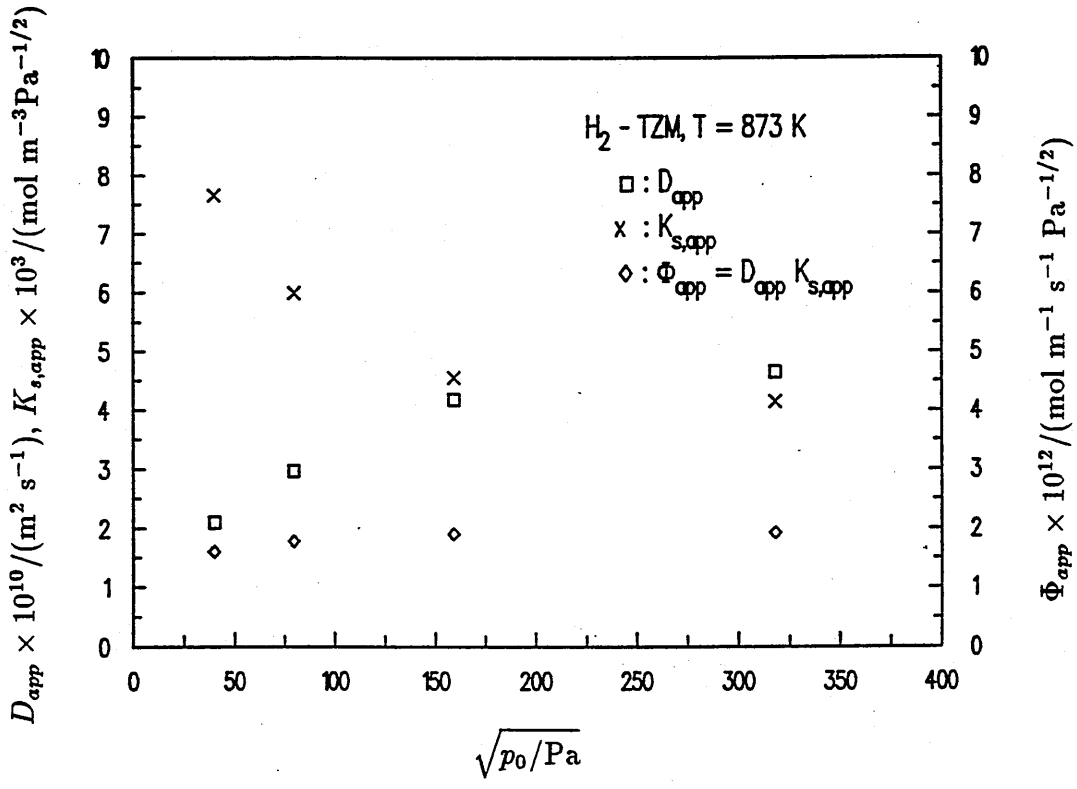

Figure 5.8 Influence of the loading pressure p_0 on the apparent hydrogen diffusivity D_{app}, Sieverts' constant $K_{s,app}$ and permeability Φ_{app} in TZM at 873 K.

Fitting to data of the SL model pressure curves gave values of k_1 that are slightly pressure dependent, with a marked trend towards saturation for low pressures, as shown in Figure 5.10. This behaviour is exactly opposite to that of the apparent diffusivity D_{app}. The low pressure results were used to find the temperature dependence of the surface rate coefficients. They are presented in Figure 5.11 in Arrhenius' plot and they are given by

$$k_1/(\mathrm{mol\ m^{-2}\ s^{-1}\ Pa^{-1}}) = 1.34 \times 10^{-6} \exp\left(-\frac{9700}{T/\mathrm{K}}\right) \quad , \tag{5.9}$$

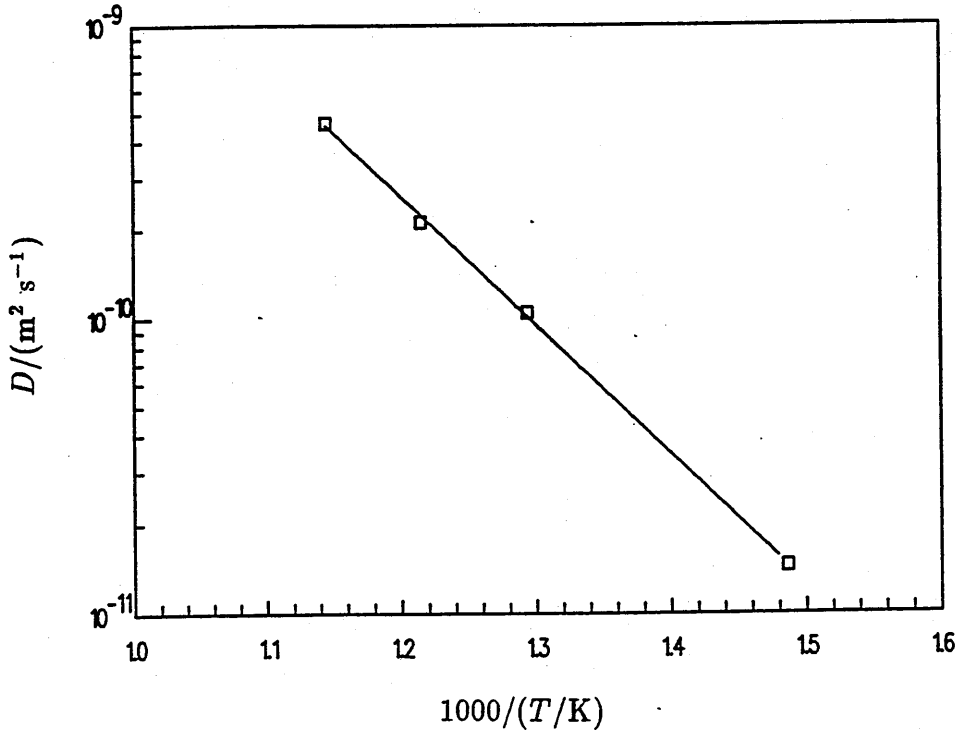

Figure 5.9 Temperature dependence of hydrogen diffusivity D in TZM.

yielding an activation energy for absorption of 80.64 kJ mol^{-1} and

$$k_2/(\mathrm{m}^4\ \mathrm{mol}^{-1}\ \mathrm{s}^{-1}) = 3.33\ \exp\left(-\frac{12600}{T/\mathrm{K}}\right)\ , \tag{5.10}$$

from which an activation energy for recombinative desorption of 105 kJ mol^{-1} is obtained.

Using the values of D and K_s found, the diffusion-limited permeability DK_s is obtained

$$DK_s/(\mathrm{mol\ m}^{-1}\ \mathrm{s}^{-1}\ \mathrm{Pa}^{-1/2}) = 1.76 \times 10^{-8}\ \exp\left(-\frac{8200}{T/\mathrm{K}}\right)\ , \tag{5.11}$$

which gives an activation energy for permeation of 68.2 kJ mol^{-1}. From the values of k_1, the sticking coefficient $s = k_1/\phi$ already defined in chapter 1 is

$$s = 1.97 \times 10^{-5} \exp\left(-\frac{10050}{T/\mathrm{K}}\right)\ , \tag{5.12}$$

which gives 6.44×10^{-12} and 1.95×10^{-10} at 673 K and 873 K respectively. The activation energy for adsorption is therefore $2E_C = 83.55$ kJ mol^{-1}.

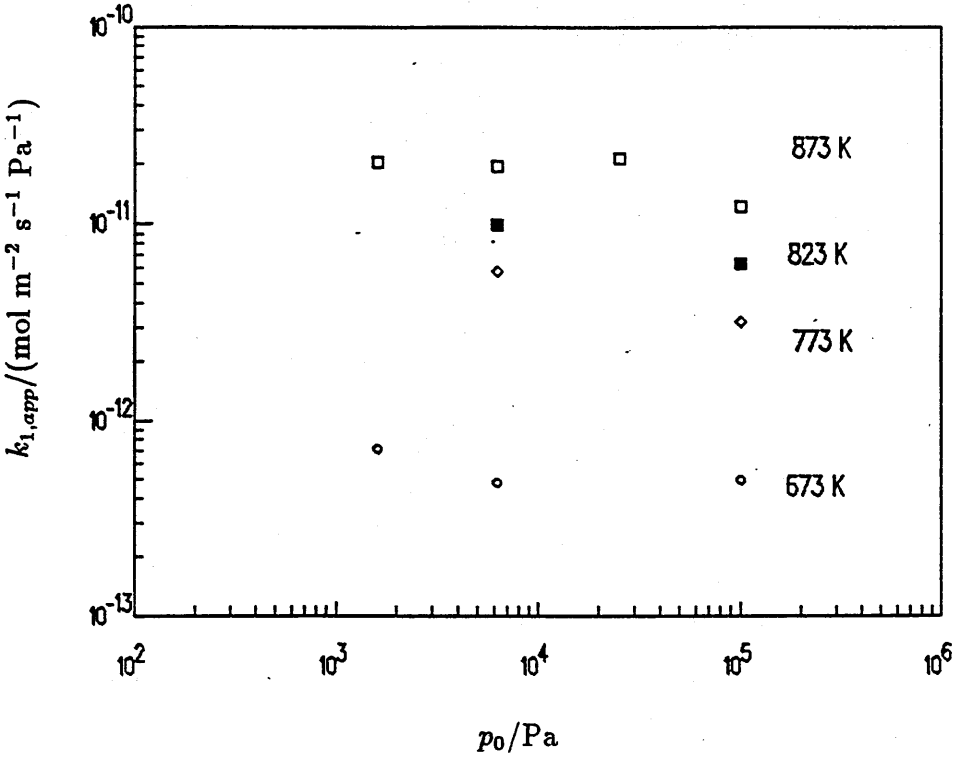

Figure 5.10 Influence of the loading pressure p_0 on the apparent hydrogen surface rate $k_{1,app}$ in TZM at different temperatures.

Discussion

The results presented show that TZM has a low hydrogen solubility, probably slightly higher than that of molybdenum owing to the small Ti and Zr additions. These also change the solution behaviour into exothermic, a fact that does not fit with earlier work on binary alloys (see chapter 1), since the electron to atom ratio e/A estimated for TZM is 5.97, thus very close to that of molybdenum.

The residual solubility S_0 can be interpreted in two different ways: either as due to trapping or as an additional signal, coming for instance from reactions such as oxidation of the surface. In fact, enthalpy values of about 30 kJ mol^{-1} have been reported [58, 59] for the exothermic oxidation of molybdenum, according to the reaction

$$\frac{1}{2}\mathrm{Mo} + \mathrm{H_2O} = \frac{1}{2}\mathrm{MoO_2} + \mathrm{H_2}\ . \tag{5.13}$$

Such enthalpy values have to be compared to the value of 20 kJ mol^{-1} obtained

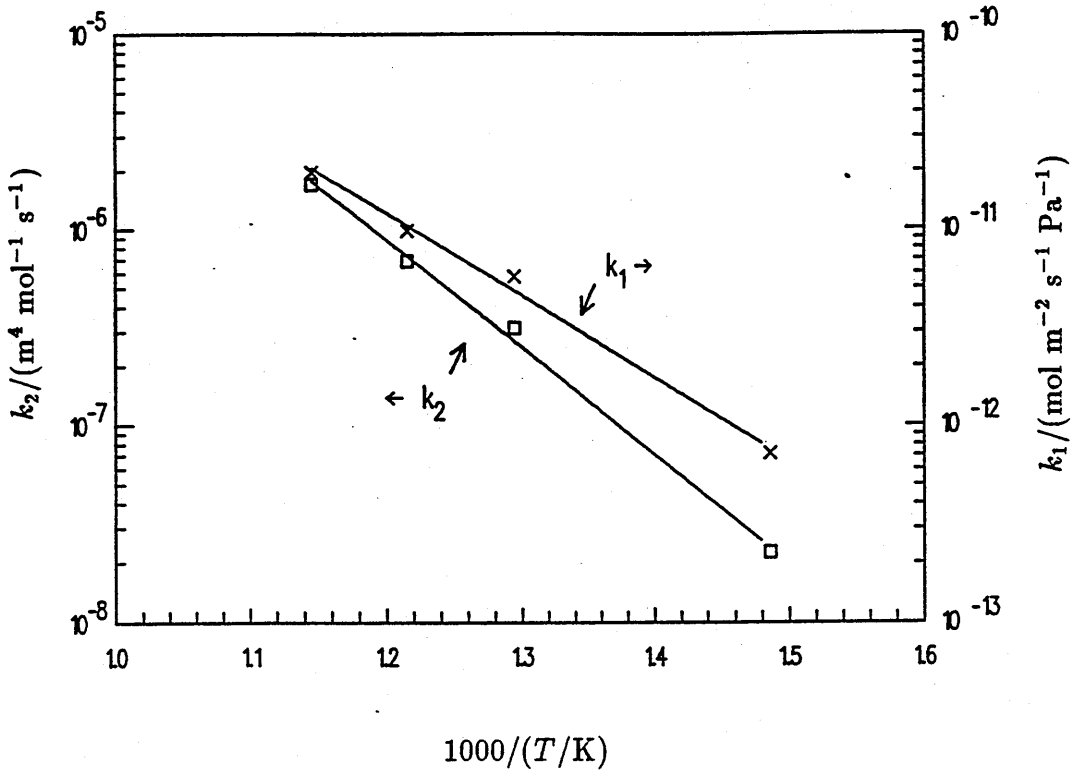

Figure 5.11 Temperature dependence of hydrogen surface constants k_1, k_2 in TZM. Key to symbols: $\times$ – k_1, $\square$ – k_2.

from the temperature dependence of S_0.

Trapping has been reported for hydrogen in TZM, with an energy of 67.5 kJ mol^{-1} [26] and the term S_0 can be explained by trapping. However, trapping alone cannot explain the small decrease of Φ_{app} with p_0, which is known [11] to be caused by finite surface reaction rates.

Earlier work with TZM [35] detected no permeation of hydrogen at 873 K, while at 1073 K a value 5 times higher than the value of DK_s extrapolated by means of equation (5.11) was given.

A detailed comparison with molybdenum data is rather difficult, due to the lack of agreement among diffusivities by different authors. The present TZM diffusivity data are a factor of 10 lower than a band containing most high-diffusivity molybdenum results [60].

For solubility, the values obtained are higher than those reported by Katsuta

[28] by a factor of 2 at 873 K and by a factor of 20 at 673 K.

As for permeability, in the temperature range studied the present DK_s results are lower by nearly a factor of 2 [28] and the activation energy of 68.2 kJ mol^{-1} is very close to the value of 73 kJ mol^{-1} reported for molybdenum [28, 61].

When plotted in Figure 1.8, the surface rate constant k_2 found would lie in the low part of the band containing most of the literature data for steels and would be lower than those given graphically by Kitajima [37], for hydrogen in molybdenum. The slope in such an Arrhenius plot would agree with the one expected from Pick's model [8].

Diffusion in a thin carbide/oxide surface layer (about 100 Å thick) is not believed to be important in this study owing to the huge cylinder radius-to-thickness ratio. In fact, the diffusivity in the surface layer would have to be 10^{10} times lower than the already low value for TZM, if diffusion in the surface layer was to be dominant. Further work with much thinner samples would be needed to study the influence of diffusion in the surface layer.

Owing to the low solubility, the exothermic solution behaviour, the low permeability, TZM seems suited for high temperature applications using hydrogen and as a potential hydrogen permeation barrier. Extrapolation of molybdenum data to TZM is not advisable.

Since the solubility is lower than in the austenitic AISI 316L steel by a factor of 10 and the recrystallisation temperature is higher, TZM is definitely a more suited substrate than that steel for the purpose of carrying out experiments on hydrogen release from high temperature CVD coatings.

5.3 Work with TiC-coated AISI 316L steel

5.3.1 Preliminary considerations

Several runs were carried out with steel cylinders coated with 3 μm thick TiC, in order to obtain rough estimates of the time required to saturate the sample with hydrogen. This was defined as the loading time in chapter 3, whereas the release time was defined as the minimum time required for the release to be complete at the equilibrium final pressure P_f. As a rule of thumb, the release and the loading time

are almost the same and depend on the test temperature through the diffusivity. This is true in diffusion-limited regimes, but it may not be so if surface effects are important. In fact, the pressure ratio between loading and release phases can be as high as 10^4, depending on the solubility; therefore, the release pressure may happen to be sufficiently low for the flow regime to become surface-controlled during the release phase.

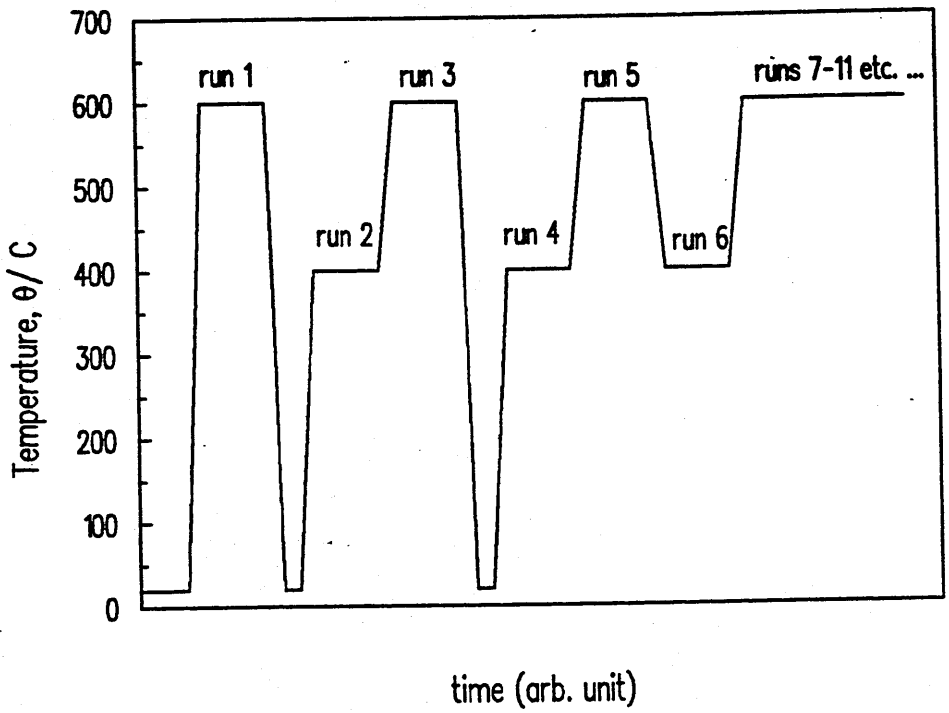

Figure 5.12 Thermal history of AISI 316L samples coated with a 3 μm thick TiC layer.

At 873 K and 10^5 Pa, loading times of 1 day were found and they increased to 7 days at a temperature of 673 K and at the same loading pressure.

The reproducibility of the release experiments after mild thermal cycling from room temperature to the test temperature was also assessed, so as to look into the effects of thermal expansion coefficient mismatch between the substrate and the coating. The thermal history of the samples is detailed graphically in Figure 5.12. Heating and cooling rates of 25 K/hr, which is equivalent to 0.4 K/minute, were used so as not to impose additional thermal stresses on the samples. Good reproducibility was obtained both at 673 K and at 873 K as shown in Figure 5.13. From that figure, an estimate of 24 hours for the release time at 873 K can also be obtained.

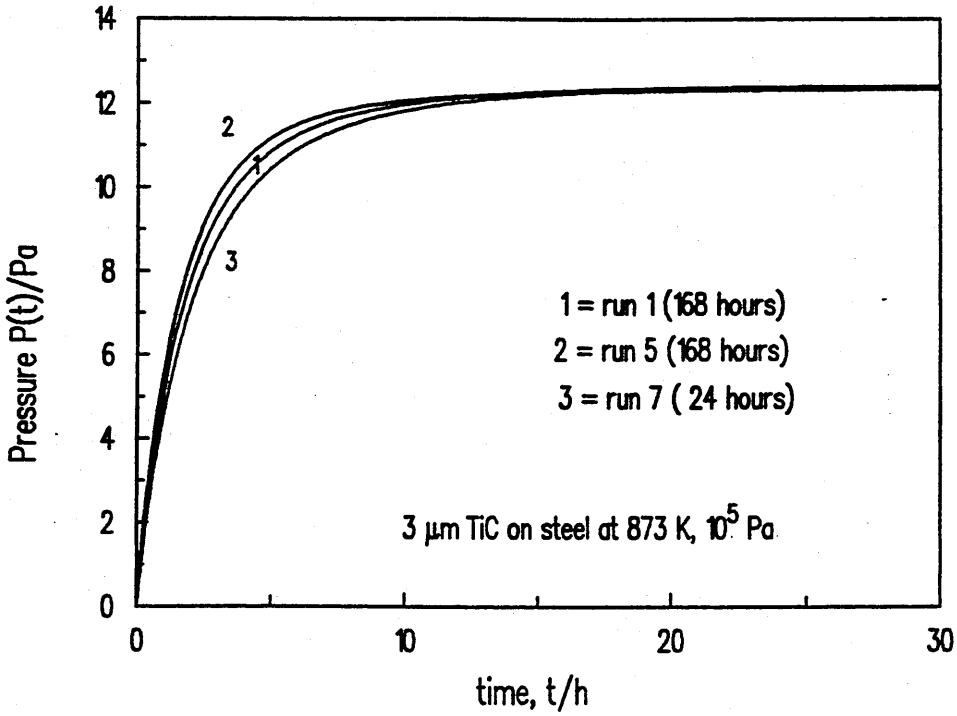

Figure 5.13 Reproducibility of the release curves at 873 K and 10^5 Pa after mild thermal cycling for a 3 μm thick TiC coating on steel. The loading times used are given in parentheses.

The equilibrium final pressure P_f varied as $\sqrt{p_0}$, p_0 being the loading pressure, both at 773 K and 873 K, independently of the thickness of the TiC coating layer. The pressure exponent is obtained by plotting P_f versus p_0 on logarithmic scales. This exponent is is 0.50 at 873 K and 0.53 at 773 K, the latter value likely being affected by underestimated final pressures at low loading pressures. A subsequent plot of P_f versus $\sqrt{p_0}$, presented in Figure 5.14, show that the data points describe a straight line passing through the origin. The outcome is that for both thicknesses, Sieverts' law for the coated sample as a whole still holds. The coated sample has therefore the same macroscopic solution behaviour as that of the bare sample.

The bare steel was tested by a small number of runs which confirmed the data obtained by Reiter and coworkers on the same steel batch [21]. In particular, the release from the coated samples is much slower than from the bare steel as can be seen in Figure 5.15. From that figure, release times of 3 hours, 24 hours and 65 hours are obtained respectively for the bare steel and for the thickness of 3 and of 5 μm. The two thicknesses have times that are scaled by a factor 65/24=2.7, which

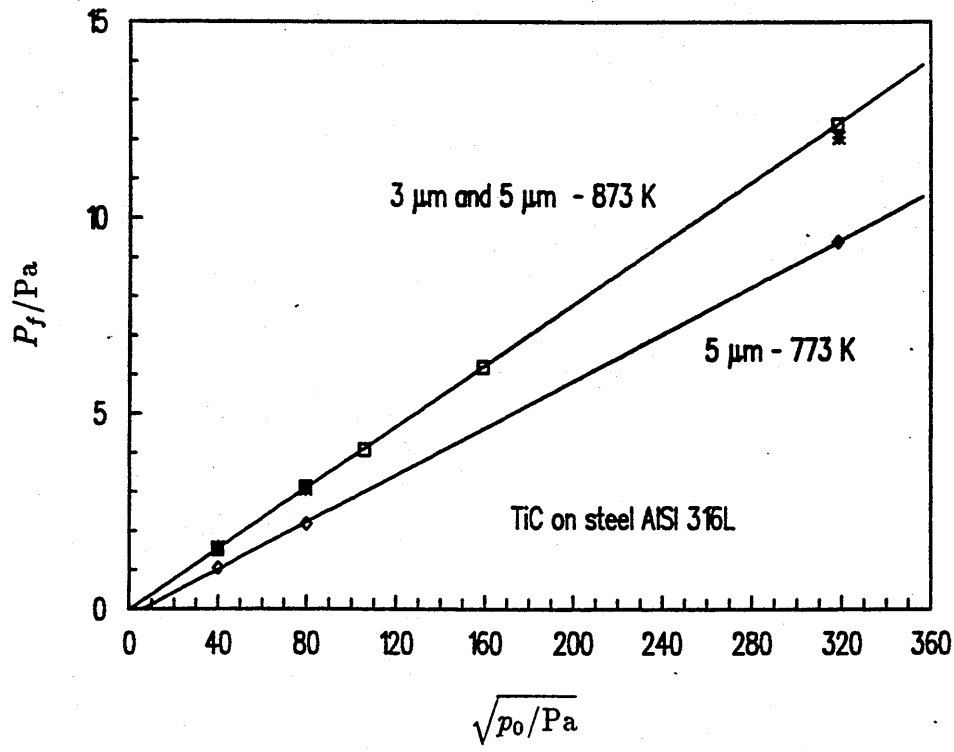

Figure 5.14 Variation of the final pressure P_f with the square root of the loading pressure p_0 for different thickness-temperature combinations: □ – 3 μm, 873 K; $*$ – 5 μm, 873 K; ◇ – 5 μm, 773 K.

is very close to the square of the inverse thickness ratio 25/9=2.78. This suggests that the release times scale as the square of the layer thickness d, as predicted by the diffusion-limited model developed in chapter 4.

The decrease of the release rate is even more pronounced at lower pressures, as observed in Figures 5.16 and 5.17, where the release time is again of 3 hours for the bare steel but increases to values exceeding 24 hours and 72 hours for the coated samples. The scaling of the release times is still close to a square-of-thickness type, being 72/24=3. At 673 K the release time is increased at least fourfold by a 3 μm thick layer, as may be seen in Figure 5.18, from 40 hours to 168 hours.

The d^2 scaling of the time to equilibrium has to fail for sufficiently low thicknesses. For a thickness of 0.5 μm a scaling with d^2 at 823 K would give a release time of less than 5 hours, which is roughly the bare steel release time. In such case, the TiC layer should have no slowing effect on the release. This is not the case as shown in Figure

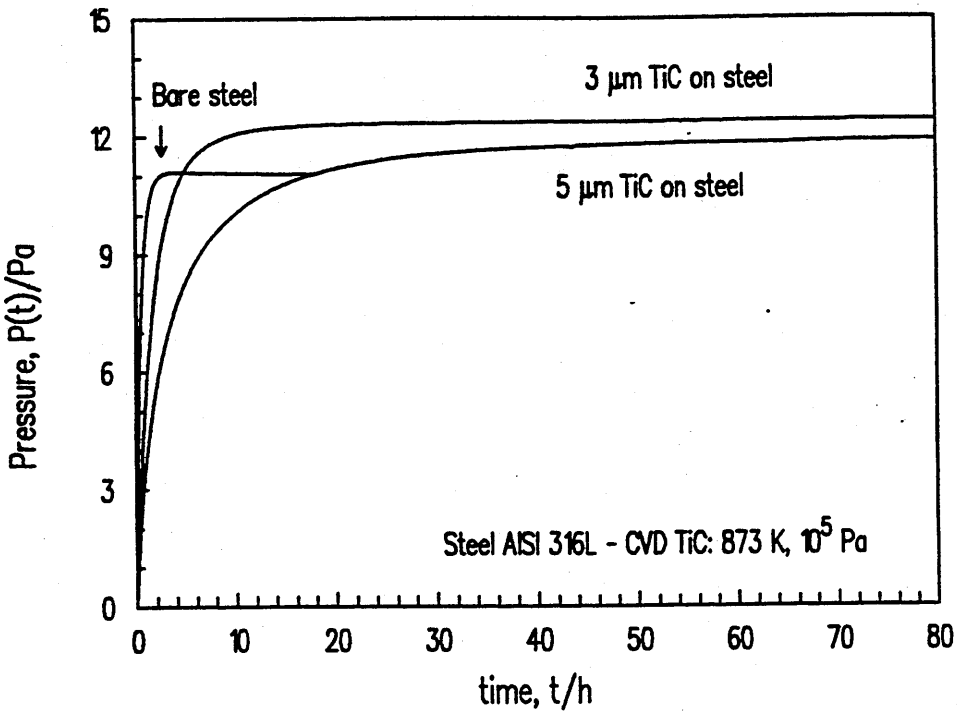

Figure 5.15 Hydrogen release from bare and TiC-coated steel at 873 K and 10^5 Pa. The increase of the release time with the TiC thickness is evident.

5.19. Here, the time $t_{99\%}$ necessary to reach 99 per cent of the final equilibrium, is plotted versus the squared thickness d^2, at 823 K. It can be seen that two data points at a thickness of 3 and 5 μm agree with a d^2 dependence, outlined by the solid straight line, drawn as a guide to the eye. At low enough thicknesses, the DL model has to fail and the experimental points should lie on the curved broken line, to reach the bare steel point at $d = 0$. This does not apply to the point at 0.5 μm, for which the same equilibrium time is obtained as that of a 4 μm in a DL regime.

It is proposed that for the 0.5 μm TiC layer, the slowing down is not due to diffusion in the coating layer, rather that the release regime has likely moved into a surface-limited region. This fact is very important since it implies that reduction of the release rate can also be achieved with very thin layers, which would pose fewer problems from the point of view of mechanical integrity of the layer.

Coating the steel with a TiC layer has enhanced the effects of reactions at the surface. As outlined in a more extensive previous investigation on the AISI 316L steel [21], surface effects begin to show up in this kind of experiment at a loading pressure p_0 lower than 10^3 Pa at 873 K and to be dominant at less than 10 Pa. This

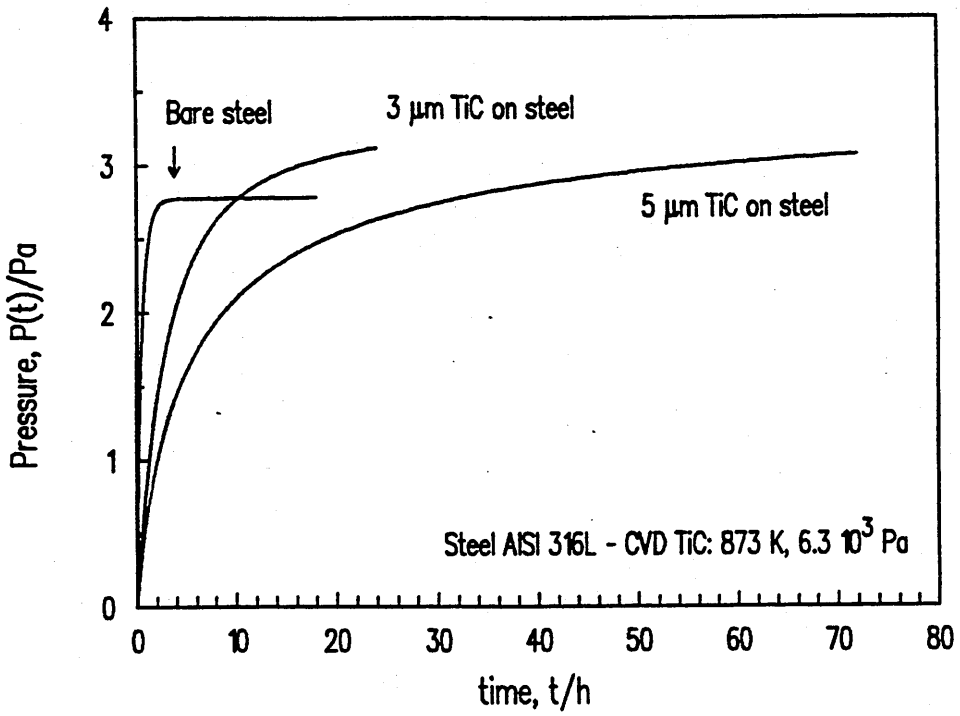

Figure 5.16 Hydrogen release versus time for bare and coated steel at 873 K and 6.3×10^3 Pa. Notice the increase of the release time with the thickness, which is larger than the increase in Figure 5.15.

was confirmed by the test runs carried out to check Reiter's data [21] and an example is shown in Figure 5.20, where the hydrogen release versus time at 873 K is presented for loading pressures of 10^5 Pa and 6.3×10^3 Pa. The release times are exactly the same and in a plot of $P(t)/P_f$ versus time t the two curves would overlap exactly. This is in strong contrast with the same picture for TiC-coated steel at 873 K and in the same pressure range, as shown in Figure 5.21. An important difference between the surface effects in steel and in TZM lies in the different concentrations in steel and TZM. On the other hand pressures and therefore concentrations in the sample, are the same for the TiC-coated steel as for the bare steel. Hence the surface rate constants must be strongly different. As a matter of fact, the material on the surface is different, so one should be prepared to find that also the surface rate constants of TiC are different from those of steel and TZM.

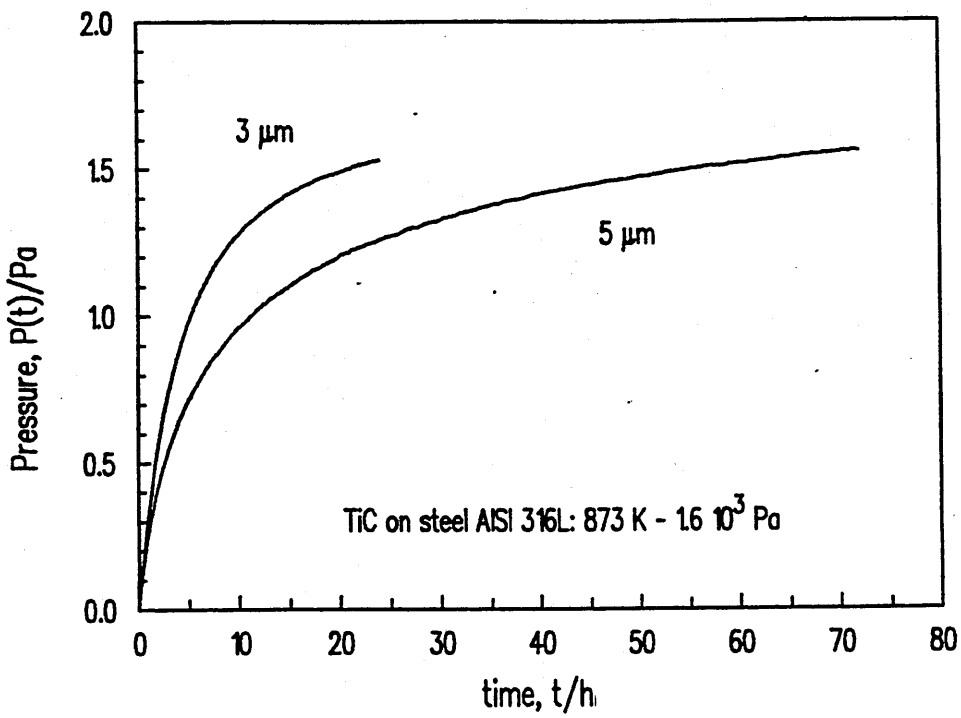

Figure 5.17 Hydrogen release from TiC-coated steel at 873 K and 1.6×10^3 Pa, for different thicknesses.

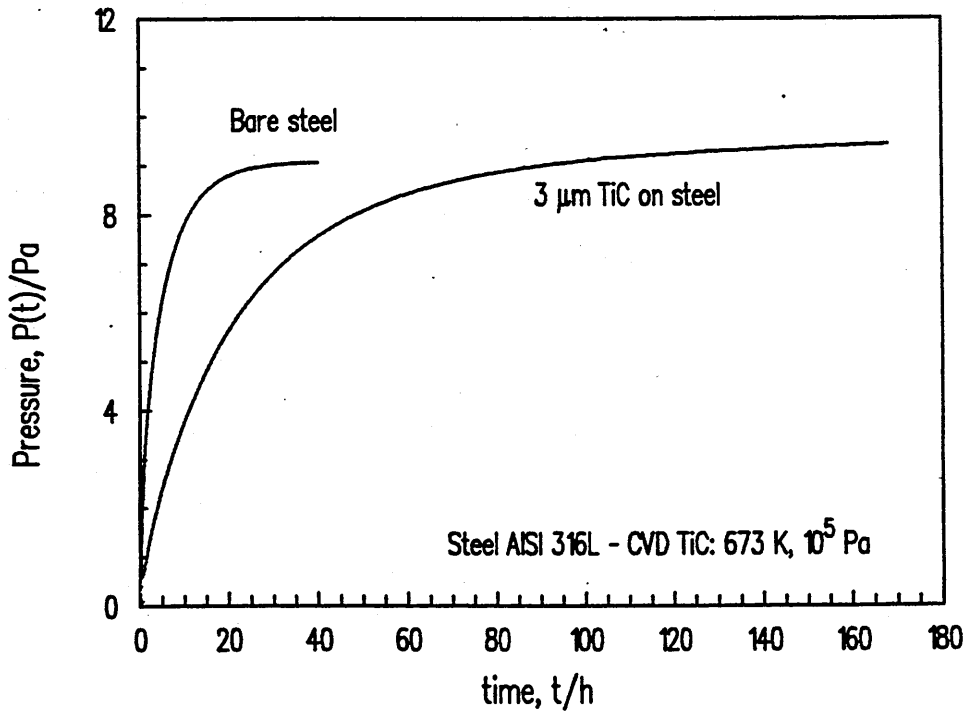

Figure 5.18 Hydrogen release in time from bare and coated steel at 673 K and 10^5 Pa.

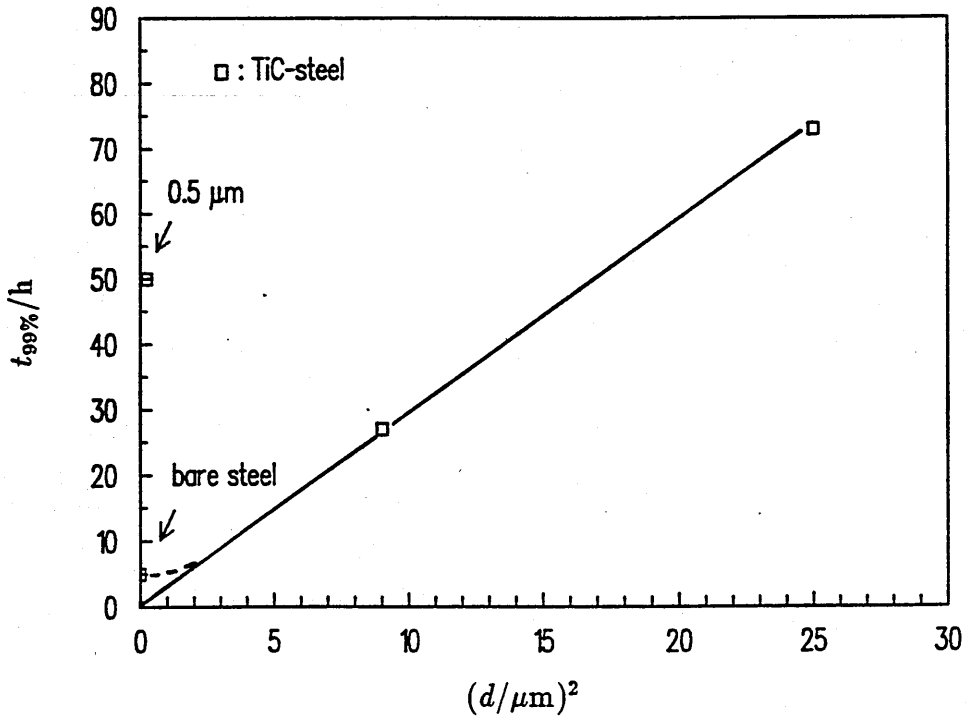

Figure 5.19 Influence of the thickness d on the equilibrium time $t_{99\%}$ for TiC-coated steel at 823 K and 10^5 Pa.

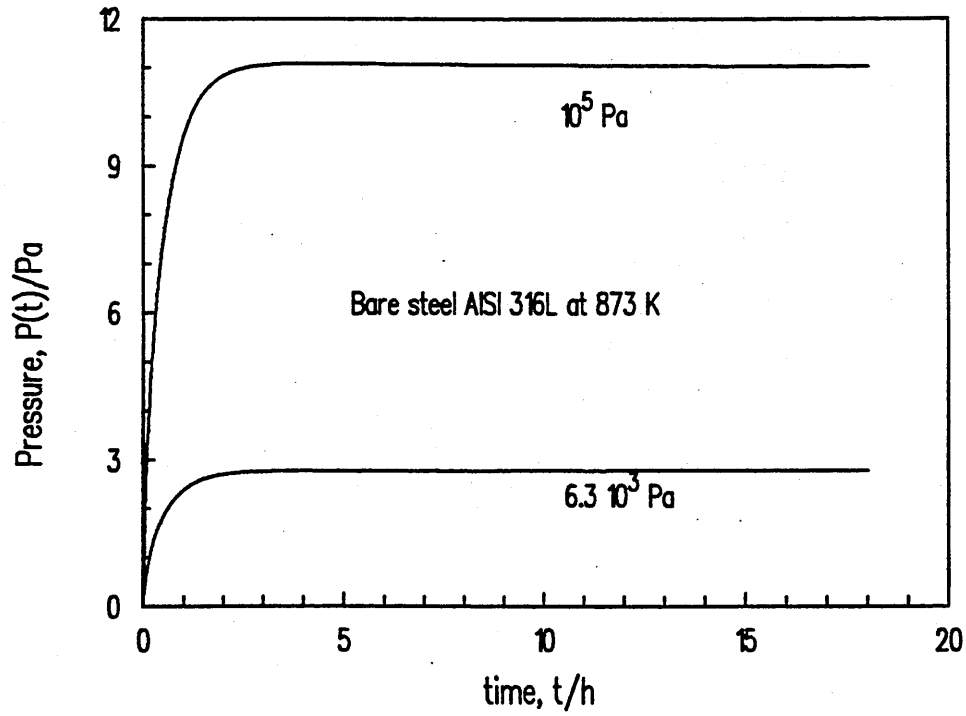

Figure 5.20 Hydrogen release from AISI 316L steel at 873 K for 10^5 Pa and 6.3×10^3 Pa.

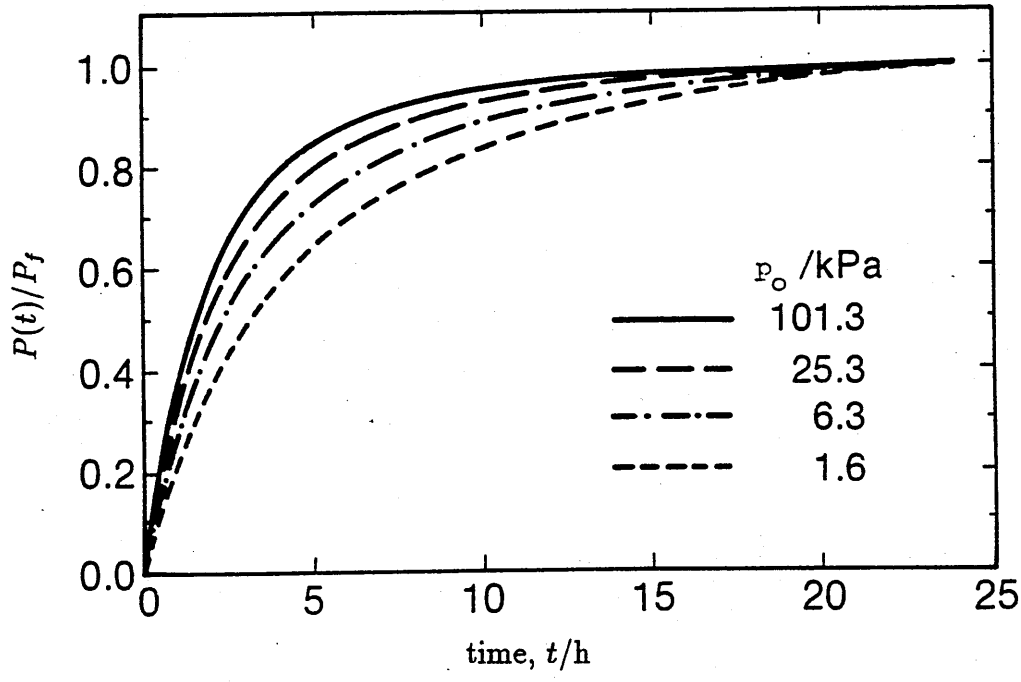

Figure 5.21 Effect of the loading pressure p_0 on the hydrogen release from TiC-coated steel at 873 K.

5.3.2 Data fitting results

The two models developed (SL and DL) were used to interpret the equilibrium and the transient evolution data. Generally speaking, the agreement obtained was better with the DL model at high loading and release pressure, whereas the SL model gave a much better fit at lower pressures. This was due to a change of shape of the evolution curve as pressures were diminished.

A difficulty when dealing with a coated metal is the modelling of the coating/substrate interface behaviour. The partition coefficient k was treated as a free parameter in the DL model and was therefore allowed to vary during the nonlinear fit. This was not possible with the SL model, because of the form of the fitting function and the way k entered it. The parameter in this case was the product $\beta = V_s K_s$, where $K_s = K_{s2}$ is the solubility coefficient of hydrogen in the coating and $V_s = kV_1 + V_2$ is an effective specimen volume, which accounts for the volume of the substrate V_1 and of the coating layer V_2. With the assumption $k = K_{s1}/K_{s2}$, the solubility coefficient in the coating was computed as $K_s = K_{s1}V_1/(\beta - V_2)$, having used for K_{s1} the values measured in previous tests with the bare substrate and given by equation (5.6). The fit was constrained so as to obtain the best agreement between the "dynamic" solubility coefficient K_s and the "equilibrium" one $c_{2i}/\sqrt{p_0}$. In this stance dynamic refers to the value of K_s which is obtained from transient data, as opposed to the one from initial equilibrium data.

An example of the variation of the accuracy of the fit obtained by the SL model is shown in Figure 5.22, at the temperature of 873 K and for various values of the loading pressure p_0. It is noticed that a very good agreement is obtained between experimental and fitted curve at low pressure (line 4) and that the agreement becomes worse as the loading pressure p_0 increases. An important fact is that to achieve a good fit at one fixed temperature, such as the case of Figure 5.22, the parameter $\beta = K_s V_s$ had to be allowed to vary with p_0. In the pressure range investigated, β was found to vary by 50 per cent.

If, on the other hand, the same set of values for the parameters k_1 and β was used at a fixed temperature, and the only difference was attributed to differing final pressures P_f at different loading pressures p_0, the SL model was unable to reproduce equally well all the release curves. In more detail, the release predicted by the SL

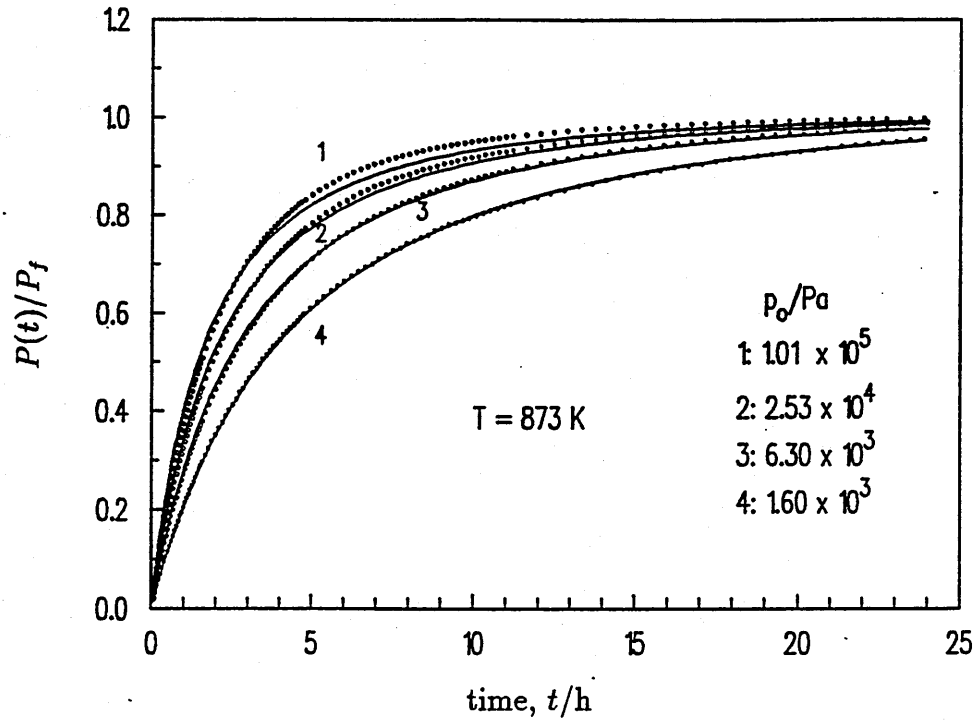

Figure 5.22 Data fitting by the SL model for 3 μm thick TiC on steel at different loading pressure p_0 and at 873 K. Dots represent the experimental values and lines are the fitted curves.

model at the highest pressure, say $p_0 = 10^5$ Pa, and obtained by using the values of k_1 and β which gave the best fit at the lowest pressure, $p_0 = 1.6 \times 10^3$ Pa, was faster than that measured experimentally. This is reproduced in Figure 5.23, where the pressure increase versus time, measured at 873 K and at $p_0 = 10^5$ Pa (line 1) is compared to the curve predicted by the SL model (line 2).

The dependence of the parameter $\beta = K_s V_s$ on p_0, found by data fitting, is presented in Figure 5.24 at the temperature of 873 K and for a coating thickness of 3 μm. This dependence can be represented as

$$\beta/(\text{mol Pa}^{-1/2}) = 3.8 \times 10^{-7} + 3.9 \times 10^{-9}\,(p_0/\text{Pa})^{0.52} \quad . \tag{5.14}$$

Since $\beta = K_s(kV_1 + V_2)$, also the partition coefficient k has the same dependence on p_0 as that of β, because $K_s = K_{s2}$, i.e. the solubility coefficient in the coating is

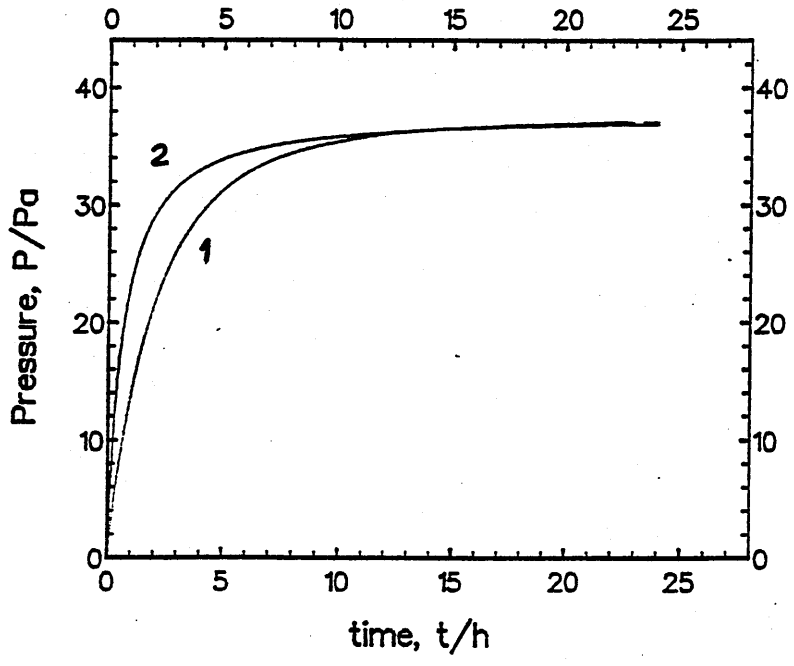

Figure 5.23 Comparison of hydrogen release by steel coated with 3 μm TiC, at 873 K and 10^5 Pa, to the prediction of the SL model using low pressure (1.6×10^3 Pa) values of the parameters k_1 and β. Key: 1 - experiment, 2 - SL model.

not dependent on p_0. In more detail

$$k = \frac{\beta}{K_{s2} V_1} - \frac{V_2}{V_1} \ , \tag{5.15}$$

and by setting $\beta = \beta_0 + \beta_1 \sqrt{p_0}$ one has

$$k = k^0 + k^1 \sqrt{p_0} \ , \tag{5.16}$$

with $k^0 = \beta_0/(K_{s2} V_1) - V_2/V_1$ and $k^1 = \beta_1/(K_{s2} V_1)$.

This suggests that the interface model used here, which does not include a pressure dependence of k and which is based on continuity of chemical potential at the interface, is not capable of describing consistently these measurements with various loading pressures.

The agreement between fitted and experimental curves became worse on increasing the coating thickness from 3 to 5 μm and improved as the thickness was reduced to 0.5 μm.

A combined fit with the two models (DL and SL) was used to find the diffusivity

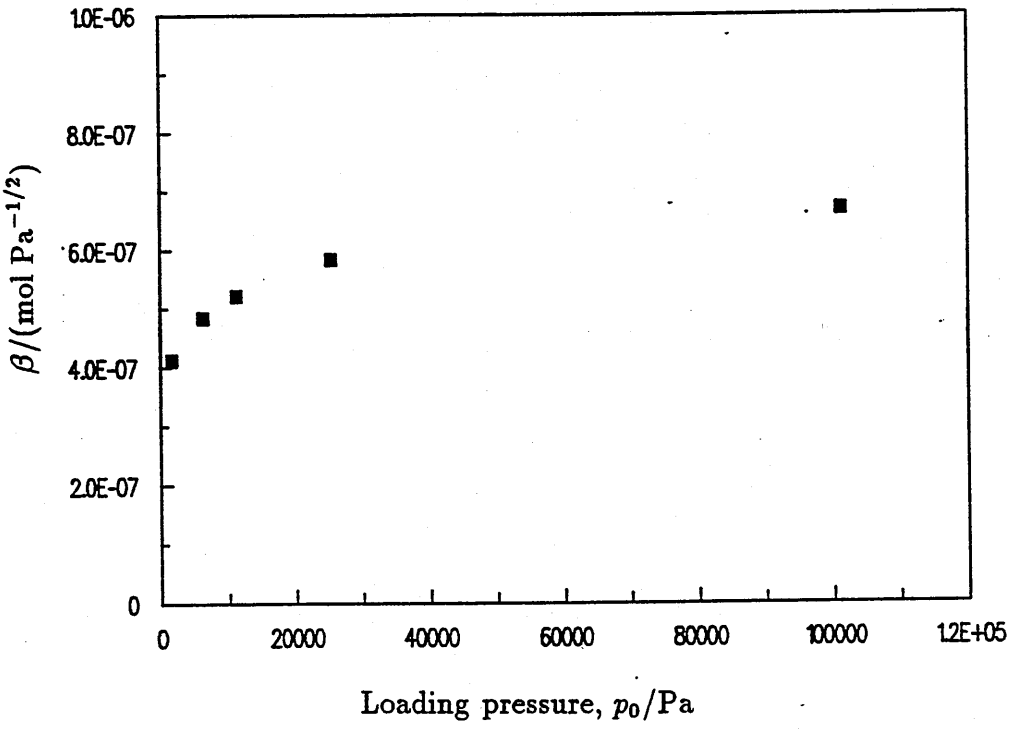

Figure 5.24 Variation of the interface parameter β with the loading pressure p_0 for steel coated with 3 μm TiC, at 873 K.

D and the solubility coefficient K_s from high loading pressure data and to determine the surface rate constant k_1 and again K_s from low pressure release curves.

Hydrogen solubility in steel after coating deposition

From the raw final pressures a solubility value was computed for hydrogen in the coated steel specimen. In this way, the effect of the CVD coating procedure on the equilibrium absorption characteristics has been examined.

It has been found that Sieverts' law still held, and Sieverts' constant has remained practically unchanged. Figure 5.25 shows the solubility constant K_s for hydrogen in bare steel [21] from equation (1.34) and in TiC-coated steel, from data obtained with 0.5, 3 and 5 μm TiC. For the hydrogen Sieverts' constant in TiC-coated steel,

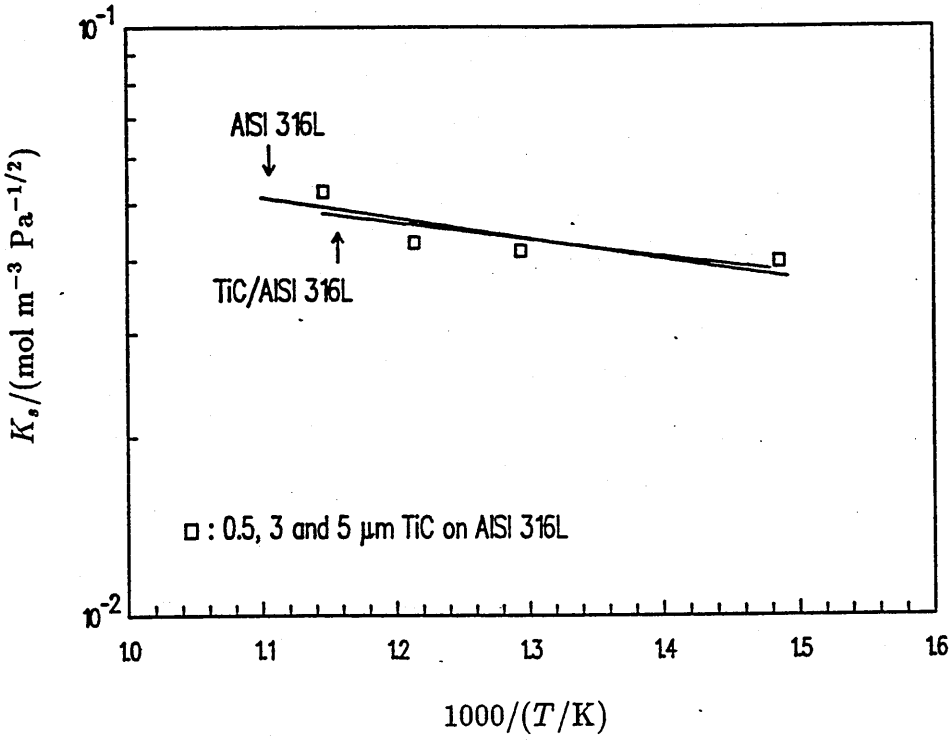

Figure 5.25 Temperature dependence of the apparent Sieverts' constant of hydrogen in TiC-coated steel, from data obtained with thicknesses of 0.5, 3 and 5 μm (□). Compare the Arrhenius straight lines for coated and bare steel.

the Arrhenius relation is given by

$$K_s/(\text{mol m}^{-3}\ \text{Pa}^{-1/2}) = 0.103\ \exp\left(-\frac{664}{T/\text{K}}\right)\ , \tag{5.17}$$

which yields a heat of solution of 5.52 kJ/mol as against 6.9 kJ/mol from (1.34). The pre-exponential factor 0.103 has to be compared to the value of 0.128, again from equation (1.34), for bare steel.

Hence, from the equilibrium absorption viewpoint, TiC-coated steel can be thought of as simply bare steel, provided a very thin coating is used. In other words the equilibrium bulk behaviour is not affected by a thin TiC coating.

Hydrogen solubility in TiC

The solubility S in TiC obtained from the DL model is shown in Figure 5.26 in mol/m^3 as a function of the square root of the loading pressure p_0 expressed in Pa, for steel specimen coated with 3 and 5 μm of TiC, at temperatures of 673 K, 773 K and 873 K. Sieverts' law holds, though it appears that the points at low p_0 or low temperature, especially at 673 K, have been underestimated. The pressure exponent of S can be found by a linear fit of Log S versus Log p_0; the value of the exponent found at 873 K for the 3 μm data is 0.52.

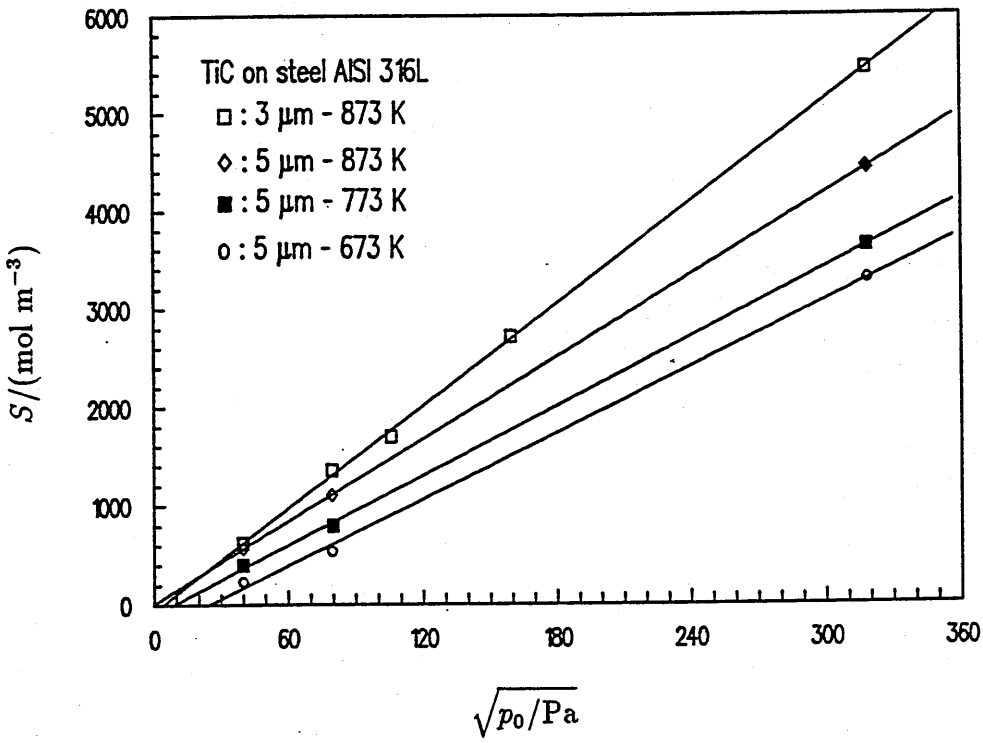

Figure 5.26 Variation of the hydrogen solubility S in TiC with the square root of the loading pressure p_0, for different thicknesses and at different temperatures.

The temperature dependence of Sieverts' constant of hydrogen in TiC is shown in Arrhenius' plot in Figure 5.27, from solubility data obtained by the DL model. It can be represented by the following equation

$$K_s/(\text{mol m}^{-3}\ \text{Pa}^{-1/2}) = 27.3\ \exp\left(-\frac{613}{T/\text{K}}\right)\ , \qquad (5.18)$$

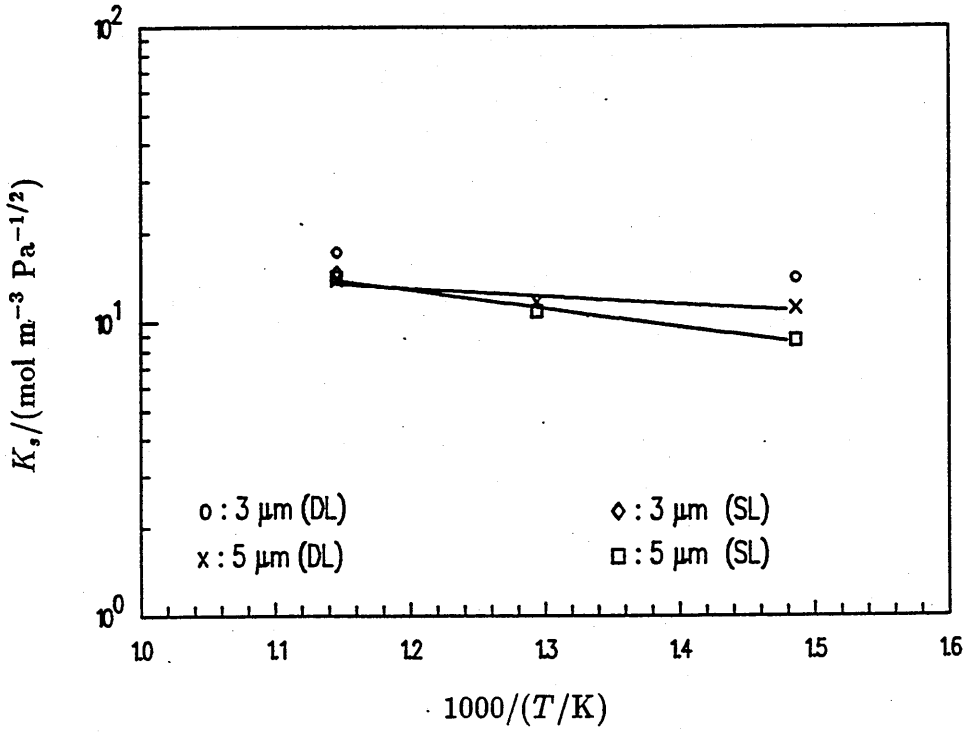

Figure 5.27 Variation of the hydrogen solubility constant K_s in TiC with the inverse temperature 1000/T for thicknesses of 3 and 5 μm.

obtained by a linear least squares fit. Figure 5.27 also presents the values of K_s in TiC as obtained by means of data fitting with the SL model, for the lowest values of the loading pressure p_0. In this case the temperature dependence is given by

$$K_s/(\text{mol m}^{-3}\ \text{Pa}^{-1/2}) = 71.4\ \exp\left(-\frac{1426}{T/\text{K}}\right) \quad . \tag{5.19}$$

Despite the fact that these SL results heavily rely on transient modelling and on previously measured substrate data, it has to be noticed the agreement, within a factor of 2, for single values of K_s with those obtained by the DL model (see Figure 5.27). Anyway, these results should not be extrapolated to temperatures outside the current experimental range.

There is however a small endothermic temperature dependence, as the solution heat is Q_s = 5.1 kJ/mol from the DL fit and Q_s = 11.9 kJ/mol from the SL fit. It is worth recalling that other studies (see chapter 1) [36, 38] reported an

exothermal behaviour for SiC. Therefore, although silicon and titanium belong to different groups in the periodic table of elements and a comparison with ZrC would be more appropriate, a marginal doubt remains on the present solubility coefficient in TiC, as it was obtained from fitting to a model and not as a direct measurement. It ought to be confirmed by means of direct equilibrium absorption measurements.

It is also worth noticing that the values of Sieverts' constant K_s are very large when compared to those for the metallic substrates, TZM and steel. They are 200 times larger than in steel and 1000 to 3000 times higher than in TZM. These figures do not fully agree with the values of the partition coefficient k obtained from fitting to data with the DL model, which are 3 to 6 times smaller than the ratio K_{s1}/K_{s2}. For the SL fit, k values are smaller again than the ratio K_{s1}/K_{s2}, by a factor of up to 4. A doubt may therefore arise about the solubility in steel after coating by CVD. It has to be ascertained whether K_{s1}, i. e. the solubility coefficient in the steel substrate, has been changed by the high temperature coating procedure. Alternatively, the interface model may be too simple.

Diffusivity in TiC

The diffusion coefficient obtained from data fitting turned out to vary with the loading pressure p_0, in opposition to the hypothesis of the DL model. The dependence of this "apparent" diffusivity D_{app} on the loading pressure is clearly visible in Figure 5.28 for 3 and 5 μm coatings on steel, at 773 K and 873 K. A common feature at all temperatures is the increase of the apparent diffusivity D_{app} with the loading pressure p_0, with a probable trend towards a constant value at the highest pressures. The solid line in the figure is only given as a guide for the eye.

The high pressure values of the apparent diffusivity D_{app} have been taken as the best possible estimate of the diffusivity D and have been used to examine the temperature dependence. This can be seen in Figure 5.29 in an Arrhenius' plot in which the results for 3 and 5 μm TiC on steel and for the bare AISI 316L steel (equation (1.35)) have been grouped, for comparison. It is to be noticed that diffusivity values in TiC are 6 orders of magnitude lower than in the steel substrate. The diffusion coefficient of hydrogen in TiC can be represented by the following equation:

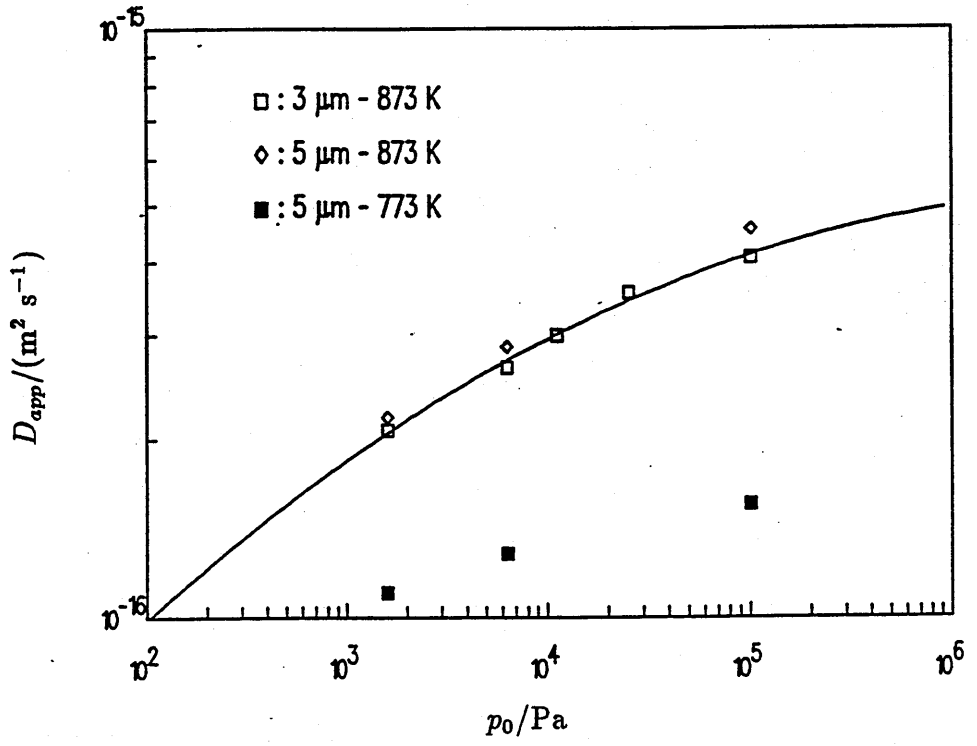

Figure 5.28 Variation of the hydrogen apparent diffusivity D_{app} in TiC with the loading pressure p_0 at different temperatures and for thicknesses of 3 and 5 μm.

$$D/(\mathrm{m^2 s^{-1}}) = 1.08 \times 10^{-12} \exp\left(-\frac{6800}{T/\mathrm{K}}\right) \quad , \tag{5.20}$$

from 3 and 5 μm TiC on steel (line 2). The activation energy for diffusion is then 56.5 kJ/mol. It is recalled that this energy for the case of hydrogen in the AISI 316L steel is 59.9 kJ/mol (see chapter 1).

Surface rate constants for hydrogen in TiC

A set of values for the surface rate constants k_1 and k_2 has been obtained by data fitting the transients measured with specimen having thicknesses of 3 and 5 μm. The value of k_1 has been constrained to be the same at a given temperature and for different loading pressures p_0, while the values of K_s obtained at the lowest p_0 have been used to compute the desorption rate constant $k_2 = k_1/K_s^2$. The temperature dependence of both k_1 and k_2 is presented in Figure 5.30, as function of the inverse

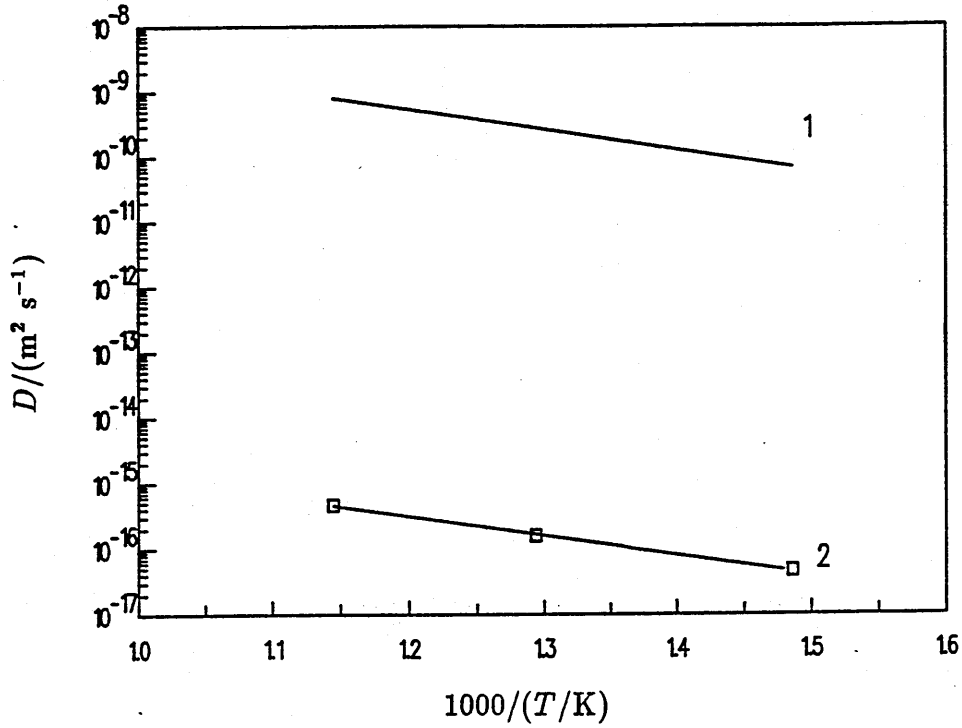

Figure 5.29 Variation of the hydrogen diffusivity D in TiC with the inverse temperature 1000/T for thicknesses of 3 and 5 μm on steel (line 2). Also shown for comparison the diffusivity in the substrate, AISI 316L steel (line 1 - from [21]).

temperature $1000/(T/\mathrm{K})$. The variation with the temperature can be expressed as

$$k_1/(\mathrm{mol\ m^{-2}\ s^{-1}\ Pa^{-1}}) = 4.1 \times 10^{-8}\ \exp\left(-\frac{4560}{T/\mathrm{K}}\right)\ , \qquad (5.21)$$

yielding an activation energy for absorption of 37.90 kJ mol^{-1} and as

$$k_2/(\mathrm{m^4\ mol^{-1}\ s^{-1}}) = 6.9 \times 10^{-12}\ \exp\left(-\frac{1595}{T/\mathrm{K}}\right)\ , \qquad (5.22)$$

from which an activation energy for recombinative desorption of 13.26 kJ mol^{-1} is obtained. It is worth noticing that these rate constants are very low when compared to those commonly found for steels, even if heavily oxidised. A comparison to the values reported in Figure 1.8 reveals that steels have desorption rate constants that are four orders of magnitude higher than the present values for TiC.

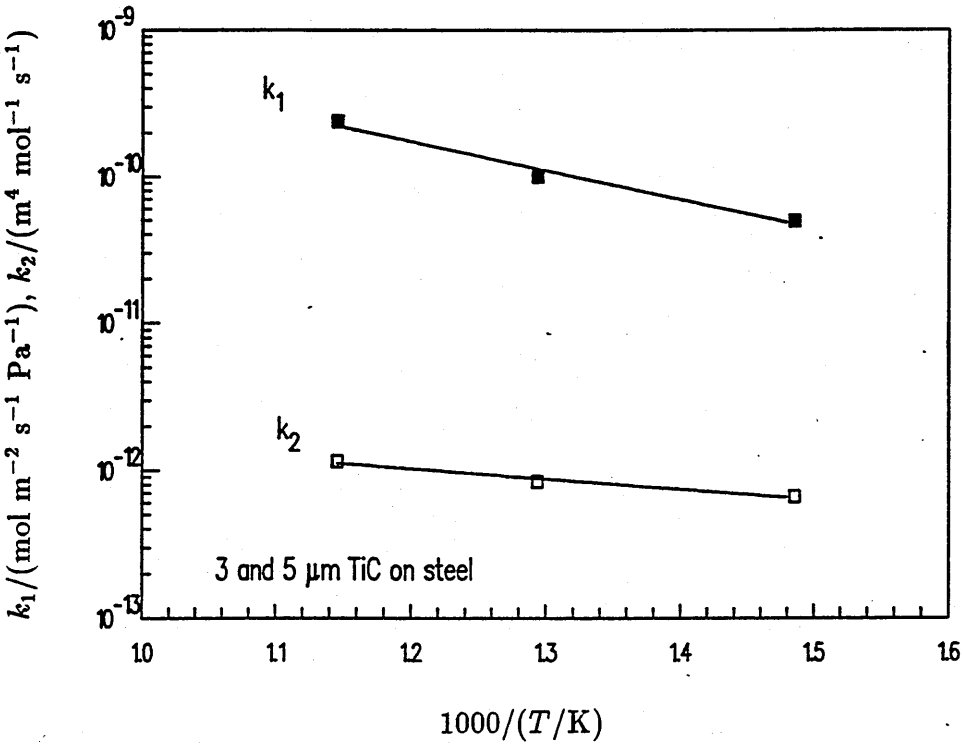

Figure 5.30 Temperature dependence of hydrogen surface constants k_1, k_2 in TiC.

Discussion

The results suggest that in the experimental conditions of this work, surface processes and bulk diffusion are equally important during hydrogen release from the TiC-coated steel specimens and nonlinear trapping can be ruled out. In fact, nonlinear trapping is reflected by a departure from Sieverts' law, which was not detected in these data. Very low estimates for the diffusivity D and for the surface rates k_1, k_2 for TiC have been obtained and they are much smaller than those for the bare steel. The solubility coefficient is much higher than in steel, a fact which would offset the low D values in the diffusion-controlled permeability DK_s. On the other hand, it has been shown that the equilibrium absorption behaviour of the steel substrate is unaffected by a thin TiC coating, the overall "apparent" solubility remaining unchanged.

Fitting the data with simple models has shown that the interface boundary condition used, characteristic of a continuous instantaneous equilibrium at the interface,

cannot describe consistently all the experiments.

A possible explanation for the variation of β and k with $\sqrt{p_0}$ can be obtained by taking account of a steric factor in the chemical potential of hydrogen in the coating at the interface with the substrate.

In fact, the hydrogen chemical potential in the solid phase is expressed by equation (1.8) and for an fcc lattice, such as the AISI steel and TiC, $\epsilon = 1$. Equating the potential in the substrate μ_{s1} to that in the coating $\mu_{s,2}$, having set for simplicity

$$B = \exp\left(\frac{\mu_{s02} - \mu_{s01}}{k^B T}\right) \ , \tag{5.23}$$

gives

$$\frac{\eta_1}{\eta_2} = B\,\frac{1-\eta_1}{1-\eta_2} \ . \tag{5.24}$$

For dilute solutions in the substrate, such as in the case of steel, $\eta_1 \ll 1$, hence

$$\frac{\eta_1}{\eta_2} = B + \eta_1 \ , \tag{5.25}$$

and $\eta_1 = \gamma\sqrt{p_0}$ is the solubility in the substrate expressed in atomic fraction. Then, making use of the host density ρ_s and molar mass A_s, since $k = c_1/c_2$ and $c = \eta\rho_s/(2A_s)$, which gives $k = (\eta_1/\eta_2)(\rho_{s1}/\rho_{s2})(A_{s2}/A_{s1})$, it is found that

$$k = \frac{A_{s2}\rho_{s1}}{A_{s1}\rho_{s2}}\,(B + \gamma\sqrt{p_0}) \ , \tag{5.26}$$

in qualitative agreement with the experimental finding given by equation (5.16). It is worth pointing out that the solubility value obtained for hydrogen in TiC is equivalent to a concentration $\eta_2 = 5.4 \times 10^{-2}$ atomic fraction at 873 K and 10^5 Pa. Thus, the steric factor $1 - \eta_2$ may really be important.

This explanation should however be verified by further work in which surface effects can be separated from bulk diffusion, so to make sure that the $\sqrt{p_0}$ dependence of β is not caused by the superposition of surface processes and lattice diffusion.

5.4 Work with TiC-coated TZM

A limited number of release runs were carried out with TiC-coated TZM specimen. These experiments displayed some anomalies, which will be described later on. The

amount of experimental work was judged insufficient for data fitting with the SL and DL models, as it will be explained later in this section. In fact, a model including diffusion, nonlinear trapping and surface effects would probably be needed. No final results will be given therefore, in terms of solubilities, diffusivities or surface rate constants. Nevertheless, the work carried out is worthy of consideration as it may give some qualitative information to complement the previous and more extensive work on TiC-coated steel.

5.4.1 Qualitative observations

Work with TiC coatings having only one thickness of 1 μm was carried out, at temperatures of 673 K, 773 K, 823 K and 873 K. As for the rest of the experimental work reported, loading pressure were varied between 1.6×10^3 Pa and 10^5 Pa.

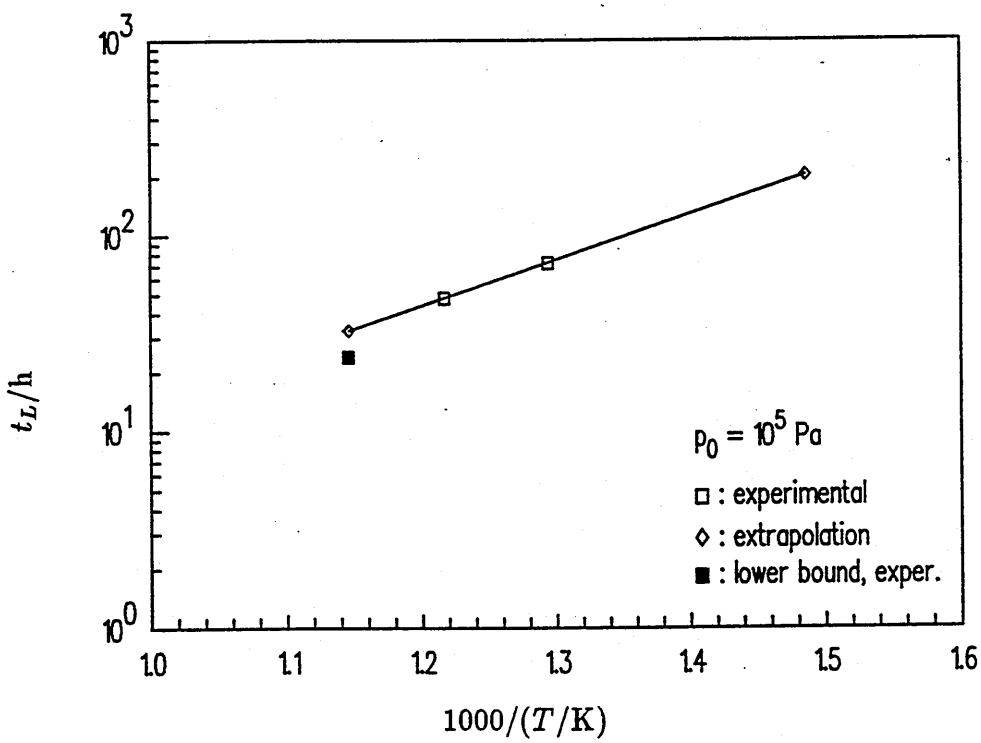

Figure 5.31 Temperature dependence of the loading time t_L for hydrogen in 1 μm TiC on TZM, at a loading pressure $p_0 = 10^5$ Pa.

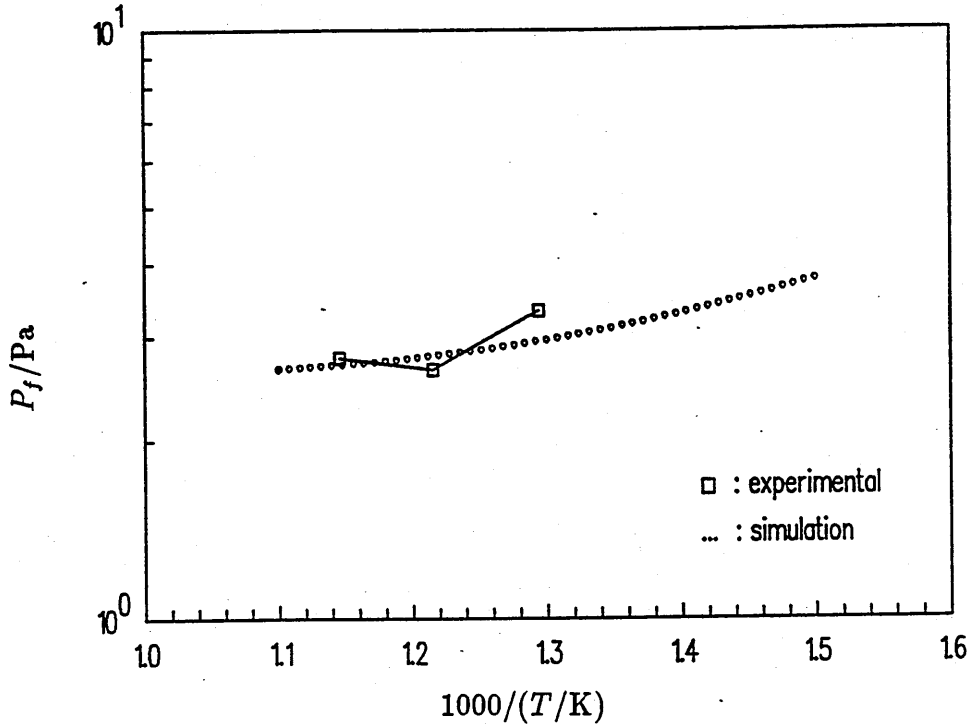

Figure 5.32 Temperature dependence of the final pressure P_f for hydrogen in 1 μm TiC on TZM, at a loading pressure $p_0 = 10^5$ Pa.

Minimum loading times t_L are shown in an Arrhenius plot in Figure 5.31, together with a straight line used for extrapolation to 673 K and to 873 K. The minimum loading time was determined at 10^5 Pa for temperatures of 773 K and 823 K and it was of 72 and 48 hours. At 873 K and 10^5 Pa, a lower bound of 24 hours was found. This value does not disagree with 33 hours, which is the value extrapolated to 873 K from the two points at 773 and 823 K. Extrapolation to 673 K gave 205 hours, a time much too long compared to the maximum experimental times actually used at this temperature. Therefore, runs carried out at 673 K cannot be taken into consideration in this analysis as it is reckoned that the specimens had not been fully charged with hydrogen at the end of the loading phase.

The first anomaly in these data can be observed in Figure 5.32, where the final pressure P_f at a loading pressure of 10^5 Pa is shown versus the inverse temperature. It is worth recalling that P_f is proportional to the amount of gas absorbed by the

specimen at the end of the loading phase, therefore also to the solubility of hydrogen in the specimen when this is considered as being composed of one material only. It is evident from Figure 5.32 that the middle data point, at 823 K, is not in line with the increasing trend displayed by the other two points. If this data point is correct, this anomaly can be explained by assuming that the total P_f signal comprised one contribution by an endothermic material, i.e. the coating, and one contribution from an exothermic material, the substrate. Under these assumptions, the final pressure P_f can be written as the sum of two Arrhenius exponentials having temperature factors, therefore energies, of opposite sign

$$P_f = f_1 \exp\left(\frac{Q_1}{RT}\right) + f_2 \exp\left(-\frac{Q_2}{RT}\right). \tag{5.27}$$

In this equation, the subscripts 1 and 2 refer to the substrate and to the coating, respectively. The dotted curve in Figure 5.32 is an example obtained by (5.27) with $Q_1 = 16$ kJ/mol, $Q_2 = 10$ kJ/mol, $f_1 = 0.075$ Pa and $f_2 = 8$ Pa. The values of Q_1 and Q_2 have been taken from the results reported in the previous section on the solubility of hydrogen in bare TZM and in TiC, while f_1 and f_2 were adjusted to obtain a reasonable fit to the three data points. If the value of $(f_1/f_2)\ \exp[(Q_1+Q_2)/RT]$ is identified with $u = kV_1/V_2$ then, for a 1 μm TiC deposited on four TZM cylinders with height of 0.06 m and diameter of 0.005 m, the value of k obtained at 873 K is $k = 3.9 \times 10^{-4}$. This is in the same range of the value found by the DL model for TiC on steel. It is recalled that at 873 K the solubility in steel is 15 times higher than in TZM, thus the value of k just found by this very crude approximation is a factor of 7 higher than expected. It is however in good agreement with the value of 2.4×10^{-4} computed at 873 K for the ratio K_{s1}/K_{s2}, using (5.6) for Sieverts' constant K_{s1} in TZM and (5.18) for Sieverts' constant K_{s2} in TiC.

The second anomaly can be observed in Figure 5.33. This shows the variation with the square root of the loading pressure p_0 of the final pressure P_f at 773 K and 873 K. The straight line obtained by a linear fit does not pass through the origin, a fact already observed with bare TZM data. The intercepts are 0.14 Pa at 873 K and 0.23 Pa at 773 K. These value, when converted to solubility in the "whole" specimen, give 0.27 and 0.44 mol/m^3 respectively. It is interesting to recall that at these temperatures S_0 for TZM has been found (see 5.2.2) to be 0.22 and 0.34

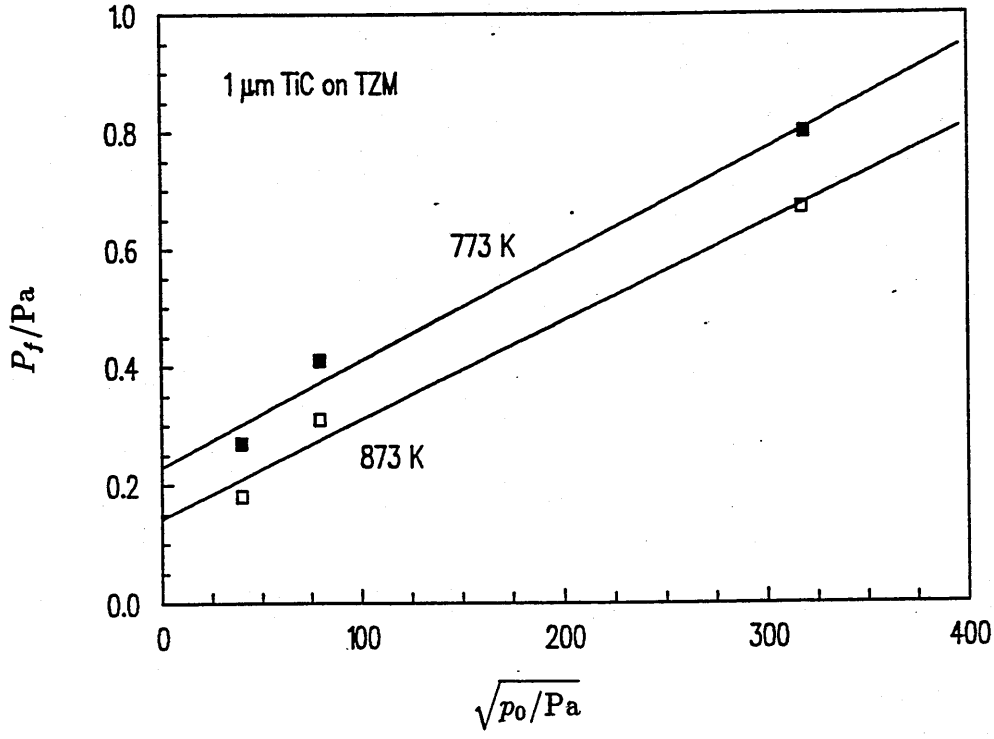

Figure 5.33 Dependence of the final pressure P_f on the loading pressure p_0 at 773 K and 873 K for hydrogen in 1 μm TiC on TZM.

mol/m^3. Such values are about 20 - 30 per cent lower than those just found for TiC-TZM data. At this stage, interpreting S_0 as due to contributions from surface contaminants is hard to accept. More likely, these points confirm the presence of nonlinear trapping in TZM.

The release transients for 1 μm TiC on TZM are compared to those for bare TZM in Figure 5.34, at the same loading pressure of 10^5 Pa and for temperatures of 773 K, 823 K and 873 K. Here, the release curves for TZM have been rescaled by dividing the original pressure $P(t)$ by 1.11, as TZM work had been carried out in a similar rig, having a volume greater by that factor.

From the absolute values of pressure and from the level of noise in this figure, it can be understood that experiments with TZM and with TiC-coated TZM were very close to the detectability threshold of the technique.

It can also be seen that at all temperatures, equilibrium release times t_R are

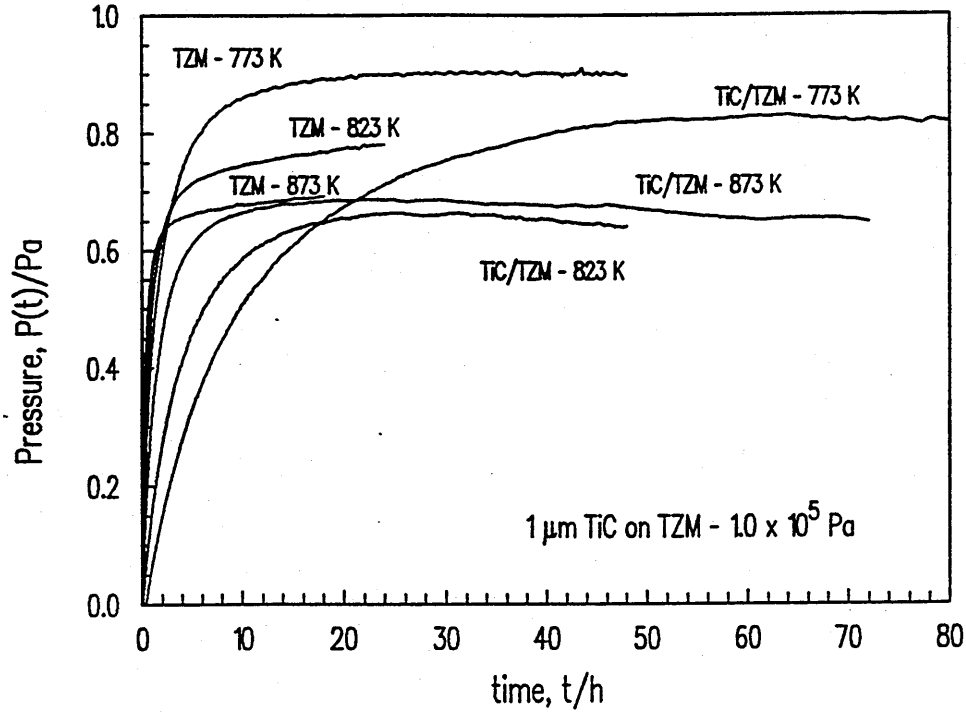

Figure 5.34 Comparison of hydrogen release transients for TiC/TZM to those of bare TZM at 10^5 Pa and various temperatures.

higher for coated specimens than for bare TZM samples, by a factor of three at least. In more detail, release times are about 70 h at 773 K, 30 h at 823 K and 24 h at 873 K. This is the third anomaly in these data, as release times appear significantly smaller than the loading times t_L quoted earlier. In general, the opposite should be expected as surface effects would slow down the absorption and desorption of hydrogen more effectively at low pressures, i.e. during release transients. Instead, this might be a pointer towards irreversible trapping, for which $k_A \gg k_B$ and the traps cannot be emptied. This does not seem compatible with the variation of P_f with $\sqrt{p_0}$ which suggests the presence of reversible trapping, unless two different type of traps are assumed to exist in the coated specimen.

The equilibrium release times can be compared to those found for TiC on steel, given in Figure 5.19. It is noticed that at 823 K, the release time for 1 μm on TZM is larger than that for a 3 μm coating on steel.

Final pressures are quite close to those for bare TZM runs, and are about 20 - 30 per cent lower. However, the rescaling carried out, by a factor 1.11, was a rough one and a more complex scaling ought to be used to carry out a detailed comparison

of final pressures.

Figure 5.35 shows release transients at 873 K and for different loading pressures, both for bare TZM and for TiC-coated TZM. The same scaling as that previously

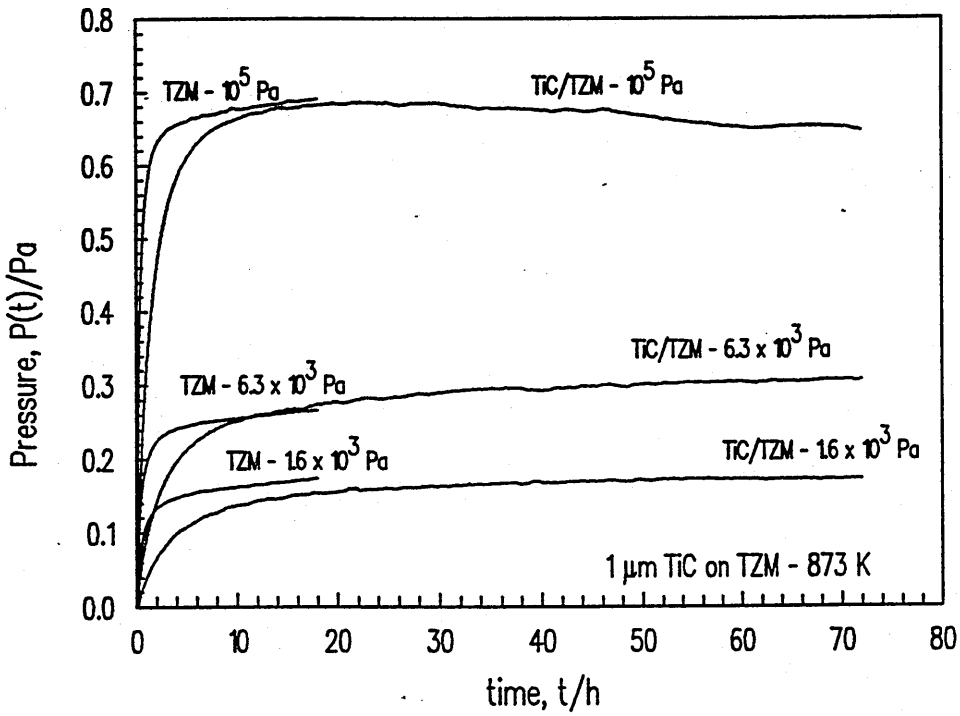

Figure 5.35 Comparison of hydrogen release transients for TiC/TZM to those of bare TZM at 873 K and various loading pressures.

mentioned has been carried out on TZM pressure values . Even as the loading pressure p_0 is decreased, the slowing effect of TiC persists and becomes even stronger.

The latter point is more evident when the normalised pressure $P(t)/P_f$ is plotted versus time t at different loading pressures p_0. Two such plots are shown in Figures 5.36 and 5.37.

Discussion

Some qualitative information has been obtained from a small number of release runs with TZM specimen coated by 1 μm TiC.

Such runs confirm that the coating layer slows hydrogen release by the substrate and has a small influence on the equilibrium final pressure.

Anomalies detected in these data, cast some doubts on the data and on their interpretation, but in some cases they confirm previous results or suggest a better

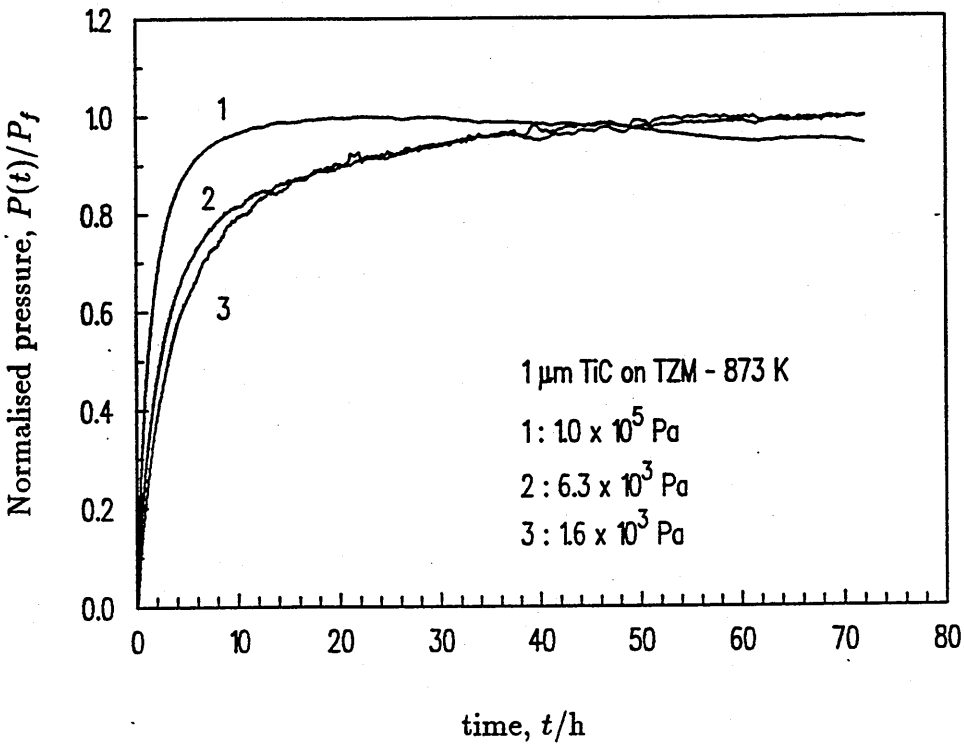

Figure 5.36 Variation of hydrogen normalised release with loading pressure for TiC/TZM at 873 K.

interpretation of the data, because for some anomaly a resonable explanation has been given. An important example is the interpretation of the anomaly in the final pressure at 823 K with respect to the other temperatures, as due to a combination of contributions by an exothermal (TZM) and an endothermal (TiC) hydrogen occluder. Another example is the pointer towards trapping in TZM constituted by the dependence of P_f on $\sqrt{p_0}$.

A slowing of the release as the loading pressure was decreased was also found here, which is attributed to surface effects caused by low concentrations of hydrogen in the substrate and therefore low pressures during the release transient, coupled to slow surface kinetics of the coating layer.

An attempt to fit the high pressure curves with the DL model gives very low diffusivities, confirming the hint from a comparison of release times that this TiC coating is more impervious than that deposited on the AISI 316L steel.

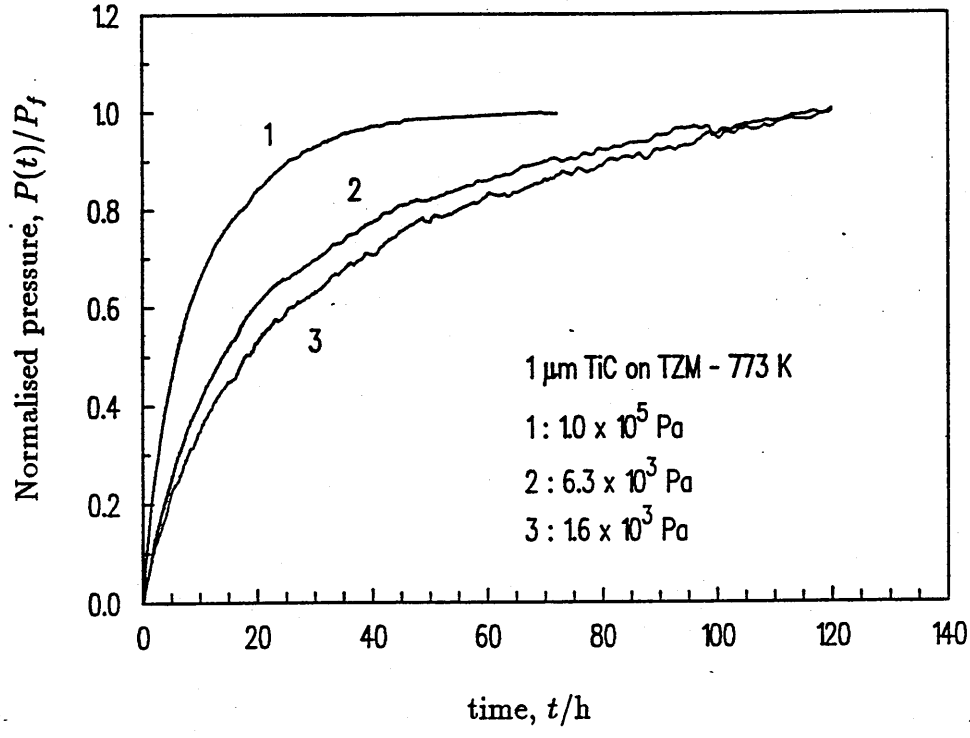

Figure 5.37 Variation of hydrogen normalised release with loading pressure for TiC/TZM at 773 K.

More quantitative work is certainly needed on this combination of coating and substrate. In particular, the importance of nonlinear trapping in the substrate has to be examined. In addition, the effect of finite surface rates has to be separated from bulk diffusion in order to obtain more reliable data on the coating absorption characteristics. For this, it is also desirable to restrict the interaction of hydrogen to a shallow superficial layer within the coating, so that coating/substrate interface effects can be neglected. This can be achieved with a different type of experiment and is the subject of the next section.

5.5 Volume-modulation on TiC-coated TZM

5.5.1 Preliminary considerations

A small number of experiments have been carried out on TiC-coated TZM, with a coating thickness of 8 μm, in the temperature range 883 K - 1083 K and for equilibrium pressures p_e between 4 Pa and 74 Pa. The temperature range had to be shifted to higher values, with respect to the range used in the Ispra experiments, in order to increase the phase lag signal. In fact, the thickness of the coating is so small that in these experiments the signal is very close to the threshold level for detectability, which is mainly determined by the system noise level. Experiments performed at temperatures below 883 K showed no significant difference from those executed without samples. Increasing the sample temperature made the phase lag become distinguishable from the system background signal.

Times to reach equilibrium conditions, that is to reach a constant pressure value in the experimental chamber, have been found to vary with the specimen temperature and with p_e. At a fixed temperature, times increased as p_e was decreased while at a fixed pressure times decreased as the temperature was increased.

The blank run response (with no sample in the rig) has been found to be similar to the response obtained with samples in the rig at the highest frequencies, where almost no interaction between hydrogen and the specimen is to be expected.

On increasing the temperature to reach a new equilibrium state prior to starting a run, a nonlinear (in temperature) pressure increase was recorded and it was much larger than what should have been expected if caused by the increased thermal agitation. This means that desorption of hydrogen was triggered. It can be concluded that the overall solubility of the specimens decreases as the temperature is increased, in agreement with the behaviour expected for the bare substrate, TZM, which the Ispra work has shown to be an exothermal occluder of hydrogen.

Pressure dependence of the measured phase lag

The effect on the measured phase lag ϕ of varying the equilibrium pressure p_e is shown in Figure 5.38 at the temperature of 1083 K and for values of p_e between 8 Pa and 74 Pa. The curved lines represent the fitted values, and are discussed in the

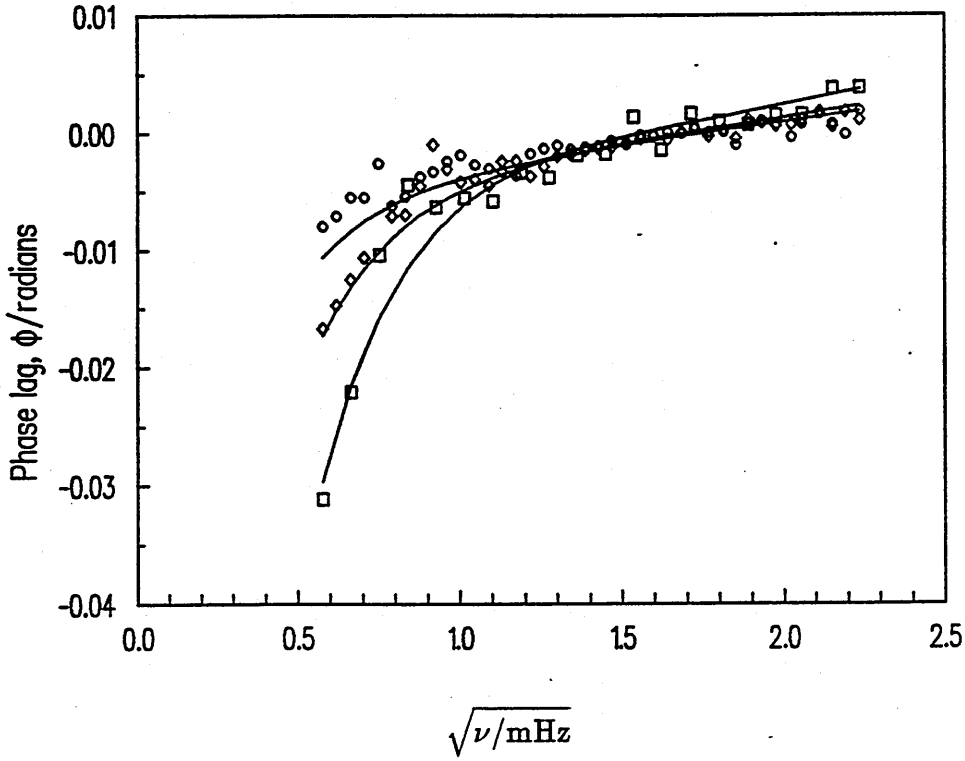

Figure 5.38 Influence of pressure on the measured phase lag ϕ at 1083 K. Pressures p_e are as follows: □ – 8.5 Pa, ◇ – 33 Pa, ○ – 74 Pa.

next subsection.

It is evident that, at a fixed frequency ν, the signal becomes larger, i.e. $|\phi|$ increases, as p_e is diminished. This happens at all the temperatures investigated and the effect is stronger as the temperature is increased.

It is recalled that, with the provision $c_e = K_s\sqrt{p_e}$, the parameters V_{He} and γ defined by (4.143), (4.144) and (4.146) are the only ones to vary with p_e. They both scale with the pressure as $1/\sqrt{p_e}$. It has been shown in 4.3.5 that an increase of $|\phi|$ at a fixed frequency can be generated by increasing V_{He} (see Figures 4.3 and 4.6) or by decreasing γ (see Figure 4.9). The trend of ϕ with varying p_e shown in Figure 5.38 is compatible with an increase of V_{He} as p_e diminishes, to dominate the effect on ϕ of the corresponding increase of γ.

Temperature dependence of the measured phase lag

The effect of varying the specimen temperature on the measured phase lag ϕ is shown in Figure 5.39 for p_e values around 8 - 8.5 Pa at 983 K and 1083 K, respectively. Again, curved lines represents fitted points and are discussed in the next subsection.

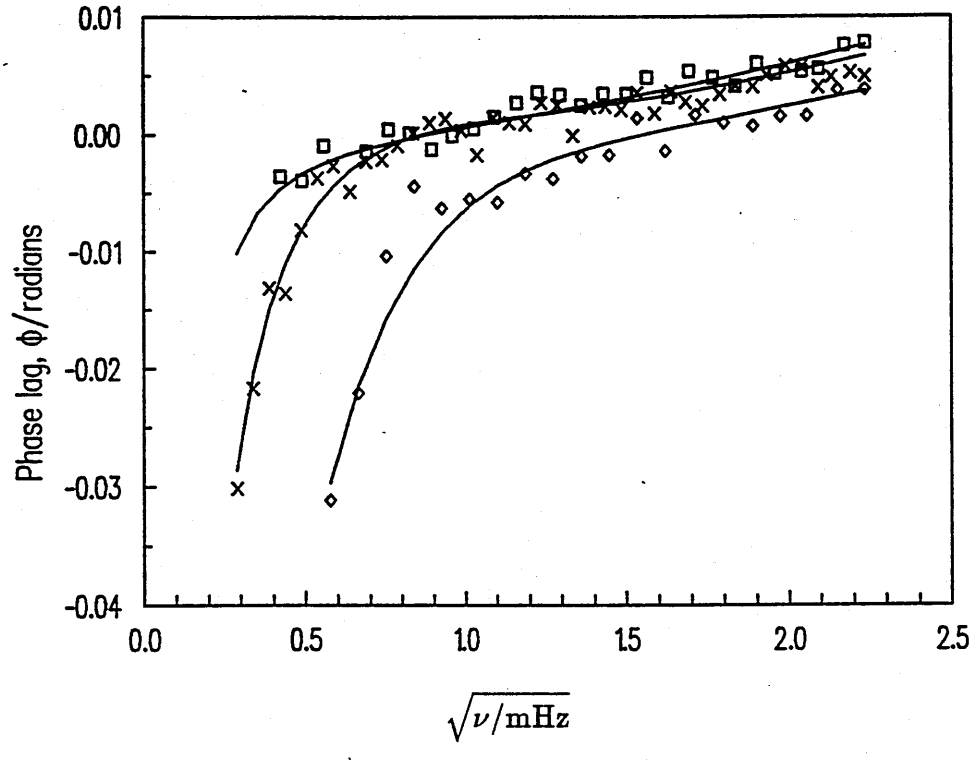

Figure 5.39 Influence of temperature on the measured phase lag ϕ at low pressure. Temperatures and pressures are as follows: □ – 883 K, 4.5 Pa; × – 983 K, 8 Pa; ◇ – 1083 K, 8.5 Pa.

The phase curve at 883 K was obtained with a pressure of 4.5 Pa, because the signal at 8 Pa and 883 K was too small to be detected. This is in agreement with what has been shown in the previous subsubsection, i.e. that $|\phi|$ decreases as p_e is increased.

As can be noticed in Figure 5.39, the effect of increasing the temperature is to shift the phase curve towards larger frequencies ν, by diminishing the times τ_d and/or τ_s. This is equivalent to increasing the diffusivity D or the product $k_2 K_{s,2}$ with the temperature.

A second effect is to increase $|\phi|$, which is compatible with an augmented value

of V_{He} caused by an increase of K_{s2} with the temperature. Notice that the modified partition parameter u cannot be responsible for such increase of $|\phi|$ as u is expected to decrease as the temperature is increased, because solution in TZM is exothermal.

5.5.2 Data fitting results

The model developed in chapter 4, which combines surface reactions and bulk diffusion, has been applied to fitting to the phase lag data in several consecutive steps.

In the first step, at a given pressure and temperature, the system response time τ_{SR} has been found, by simulating an empty rig, that is by setting $V_{He} = 0$ and by using very large values, of the order of 10^9 s, for the characteristic time τ_d in a diffusion limited regime. For this, the diffusion-limited approximation (4.159) for the phase advance θ has been used. The values found for τ_{SR} are in good agreement with those obtained experimentally without samples in the rig and they appear to be slightly pressure-dependent, as they increase with decreasing p_e. The influence of temperature is much weaker, probably due to the size of the heated region which is much smaller than that of the whole experimental vessel.

With the second step, several attempts have been made to fit the data by using the diffusion-limited approximation (4.159) and, failing that, the surface-limited approximation (4.160). As both have been unable to produce a good fit to the data over the whole frequency range, even if the substrate-absorption term u was varied, in the third step the fit has been carried out including both diffusion and surface reactions at the same time, by means of (4.157) and with u set equal to zero. In this way a much better fit than in step 2 has been obtained, sometimes over the whole frequency range. The value of the flow regime number γ obtained diminished with increasing pressure, and it varied between 2 and 0.7 at 1083 K and between 1.2 and 4 at 983 K and 883 K, according to which the flow regime was mixed, with both diffusion and surface reactions having the same importance.

The fourth step involved improving the fit agreement at the lowest frequencies by increasing the value of the modified partition coefficient parameter u. This additional step has been necessary as the temperature was increased and as the pressure was diminished. An interpretation for these facts is that as the temperature is increased the effective penetration depth by diffusion also increases; as the pressure

falls, experimental conditions are shifted towards a surface-limited regime, in which the penetration depth is equal to the coating thickness as in a true surface-limited regime the concentration evolves in time remaining always flat, that is without space gradients.

Values of the partition coefficient k thus obtained are however higher than what expected from the work carried out at Ispra, by a factor ranging between 3 and 20. Since with TZM as a substrate, recrystallisation during coating deposition can be ruled out, this confirms that the treatment of hydrogen interface behaviour is not good enough. Further improvement of the interface is beyond the scope of this work.

An example of the fit quality achieved is given in Figure 5.38 for variable pressure at the temperature of 1083 K and in Figure 5.39 for variable temperature, at pressure p_e of 4.5 Pa, 8 Pa and 8.5 Pa.

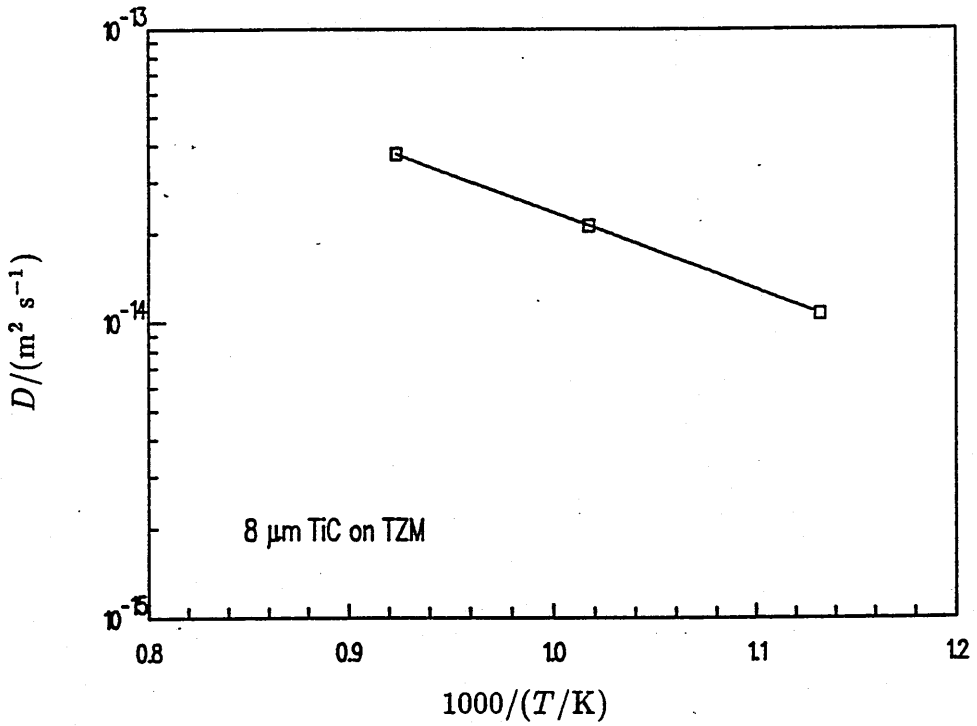

Figure 5.40 Temperature dependence of the hydrogen diffusivity D in TiC.

The temperature dependence of the diffusivity obtained by data-fitting is shown in Figure 5.40 in an Arrhenius plot. The straight line has been obtained by linear

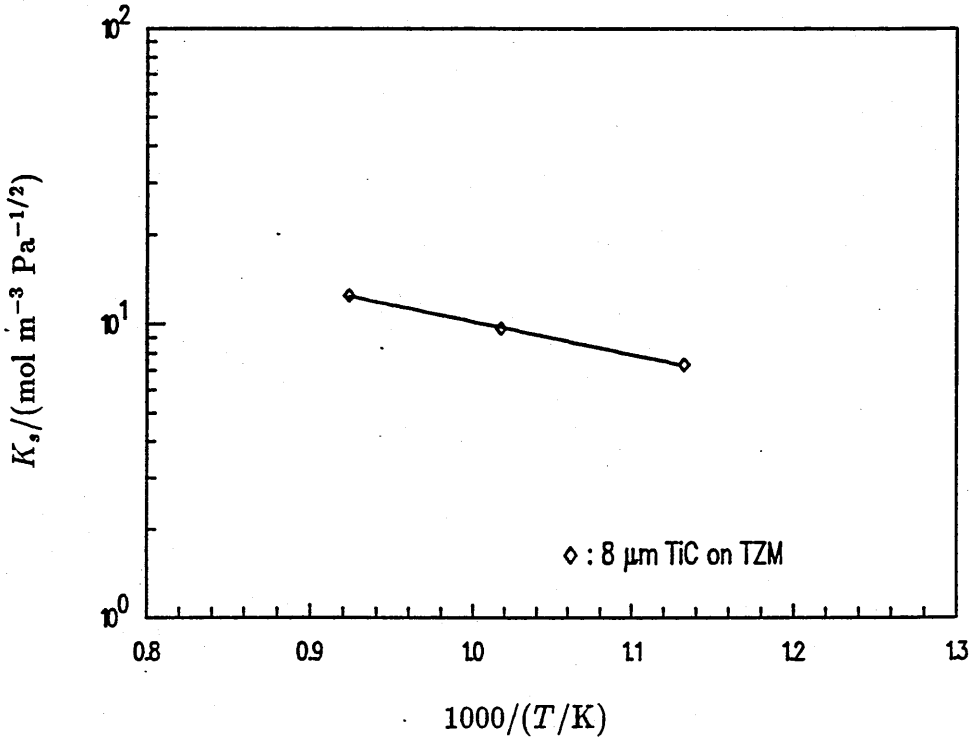

Figure 5.41 Temperature dependence of the hydrogen Sieverts' constant K_s in TiC.

least-squares analysis. The variation with the temperature can be expressed as

$$D/(\mathrm{m^2\ s^{-1}}) = 9.6 \times 10^{-12}\ \exp\left(-\frac{6010}{T/\mathrm{K}}\right)\ , \tag{5.28}$$

which gives values of 9.9×10^{-15} m^2 s^{-1} at 873 K and of 1.3×10^{-15} m^2 s^{-1} at 673 K. Though being much smaller than the diffusivity in TZM or in steel, these values are a factor of 100 higher than those measured at Ispra, on other TiC coatings obtained by a different supplier.

The temperature dependence of Sieverts' constant K_s obtained is shown in Figure 5.41, together with the least-squares straight line, in an Arrhenius plot. The variation with the temperature can be expressed as

$$K_s/(\mathrm{mol\ m^{-3}\ Pa^{-1/2}}) = 135.6\ \exp\left(-\frac{2590}{T/\mathrm{K}}\right)\ , \tag{5.29}$$

which gives values of 7 mol m^{-3} Pa$^{-1/2}$ at 873 K and of 2.9 mol m^{-3} Pa$^{-1/2}$ at

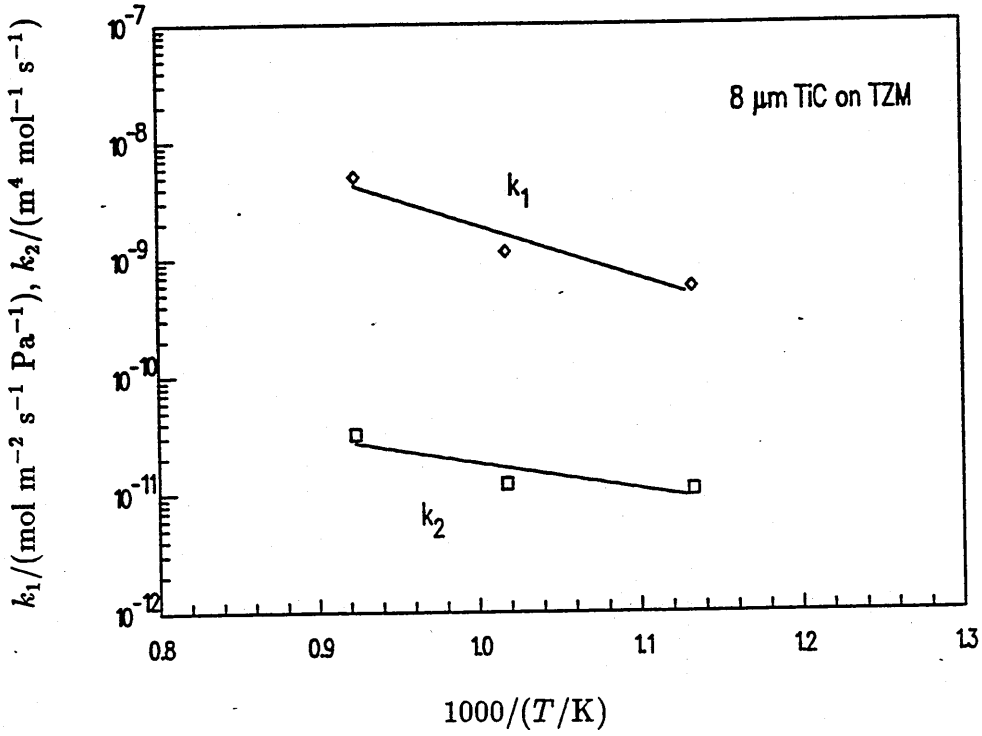

Figure 5.42 Temperature dependence of hydrogen surface constants k_1, k_2 in TiC.

673 K. These are about 2 and 3 times lower, respectively, than the values given in a previous section for TiC deposited on steel as obtained at Ispra.

The surface rate constants k_1, k_2 found by data-fitting vary with the inverse temperature, $1000/(T/K)$, in the way shown in Figure 5.42. The variation with the temperature can be expressed as

$$k_1/(\text{mol m}^{-2}\ \text{s}^{-1}\ \text{Pa}^{-1}) = 5.4 \times 10^{-5}\ \exp\left(-\frac{10250}{T/\text{K}}\right) \tag{5.30}$$

and by

$$k_2/(\text{m}^4\ \text{mol}^{-1}\ \text{s}^{-1}) = 2.9 \times 10^{-9}\ \exp\left(-\frac{5070}{T/\text{K}}\right)\ . \tag{5.31}$$

Such values are about a factor 10 lower than those previously given for TiC on steel as measured at Ispra.

5.5.3 Discussion

The small amount of volume-modulation work reported in this section confirms the exothermic character of hydrogen solution in TZM. It also shows that during volume oscillations, hydrogen mainly interacts with the TiC coating and that as the frequency is lowered at fixed pressure and temperature, substrate absorption becomes more and more important. This effect is stronger as the pressure in decreased.

The model developed allows one to work in flow regimes where bulk diffusion and surface effects have the same weight. It then permits the evaluation of diffusion coefficients, surface rate constants and solubility constants for the coating.

The measured phase lag scales qualitatively in agreement with the model expectations as the pressure is varied, but in some cases at the lowest frequencies, it is required to also consider substrate absorption. The interface model used here seems however inadequate.

The results confirm that TiC has low diffusivity D and surface rate constants k_1, k_2 and that the Sieverts' constant is high. A source of concern lies in the strong difference in the diffusivity between the TiC coating studied at Oxford and that studied at Ispra.

5.6 Summary

The results obtained at Ispra with a gas evolution technique on the interaction of hydrogen with TZM, TiC-coated steel and TiC-coated TZM have been reported. A qualitative interpretation has been given for the data on TiC-coated TZM.

Such results have been completed by results from a more limited work carried out at Oxford, by means of a volume-modulation technique, on hydrogen interaction with TiC-coated TZM.

The work carried out at Ispra shows that

- TZM has a low and exothermic hydrogen solubility, while the diffusivity is similar to that of the AISI 316L steel;
- nonlinear trapping and surface effects affect the TZM experiments;

- coating the AISI 316L steel with TiC results in slowing the release of hydrogen from the steel substrate, leave almost unchanged the overall equilibrium absorption behaviour and introduces pressure effects, which are interpreted as caused by surface reactions;
- no evidence is found for trapping to affect diffusion in the coating layer and very low diffusivity are thus determined;
- coating TZM with TiC also slows hydrogen release from the substrate and leaves the global solution behaviour qualitatively unchanged; some anomaly in the measurements are detected; one of them might suggest the presence of additional irreversible traps in the coating or in the substrate.

The results of the volume-modulation work at Oxford

- qualitatively confirm the results obtained at Ispra for TiC, i.e. low D, k_1, k_2 and high K_s, by allowing the separation of surface effects from bulk diffusion in the coating;
- do not provide strong evidence for linear trapping in the coating;
- confirm that the substrate/coating interface model used is not adequate to entirely model the data;
- generate some concern about the strong difference between diffusivities obtained at Ispra and at Oxford.

On the last point, it is recalled that the TiC coatings used at Oxford were obtained from a different supplier.

Chapter 6

Conclusion

This thesis has presented experimental investigations, accompanied by models for their interpretation, carried out with two markedly different techniques and in two different laboratories. Accordingly, most of the work reported has been split into two parts, one for each technique. At the end of the work, it is felt necessary to draw a unified conclusion, on the basis of the whole work. This is accomplished in this chapter, where some thoughts and suggestions are put forward about importance, applicability and consequences of the results obtained.

The first section briefly addresses the steady state permeation through a coated metallic membrane and the conditions required for achieving permeation reduction by means of a thin coating layer. The second suggests some applications of the results and for the material studied in this work. A concluding section outlines possible work as a further step in this line of research.

6.1 Steady state permeation through a metallic membrane

In order to outline the way the physics deployed in this thesis can be applied to a practical problem, the steady state permeation through a coated metallic membrane, separating two chambers at pressures p_1 and p_2 respectively, is considered. A schematic cross-sectional view of such a membrane is presented in Figure 6.1. The metallic foil is referred to as medium 1 whereas the coating layer is labelled by a 2. Thus concentrations in the metal and in the coating are c_1 and c_2, respectively. With

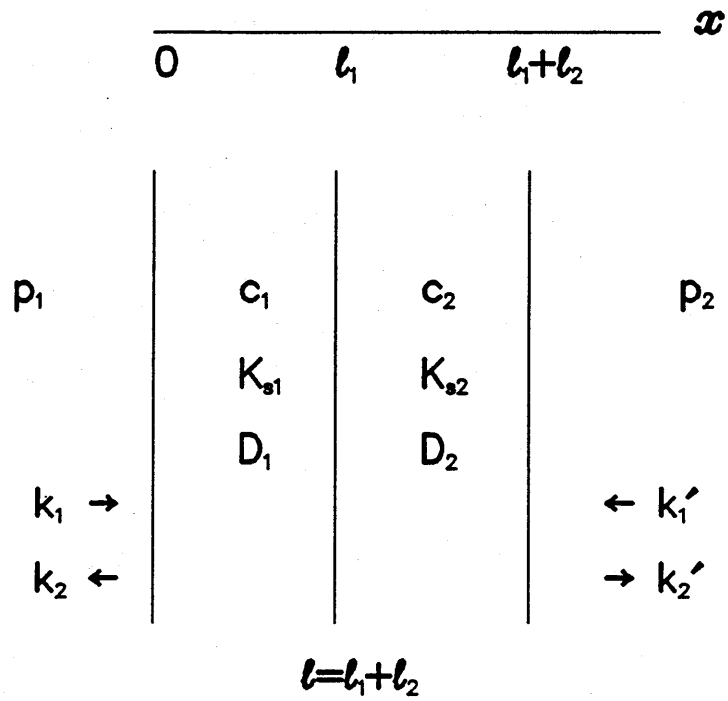

Figure 6.1 Schematic representation of a bilayer permeation membrane of total thickness ℓ

the provision $n = 1, 2$, Sieverts' constants are $K_{s,n}$, diffusivities D_n, diffusion-limited permeabilities $\Phi_n = D_n K_{s,n}$ and thicknesses ℓ_n. As for surface rate constants, defined by (1.1), they are k_1, k_2 at the free surface of the metallic foil and k_1', k_2' on the coating free surface. Atomic solution is assumed to occur in the layer, as well as in the metal. No trapping is included in this simple example and the interface kinetics is taken to be in dynamic equilibrium. In addition, the simplest cases of diffusion- and surface-limited flow are considered.

6.1.1 Diffusion-limited flow on both sides of the membrane

The steady state permeation flux through the coated membrane is found by solving the diffusion equation (1.14) subject to the condition $\partial/\partial t = 0$. Interface conditions are (1.30), which represents dynamic equilibrium, and (1.29) to account for flux continuity. The partition coefficient k is taken to be equal to the ratio of solubilities in the two media, i.e. $k = K_{s,1}/K_{s_2}$.

The stationary permeation flux at either sides of the membrane is $j_d = -D_2\,(\partial c_2/\partial x)$

where $\ell = \ell_1 + \ell_2$ is the membrane total thickness. The origin of the space axis x coincides with the metal free surface.

Explicitly

$$j_d = H_d \frac{\Phi_1}{\ell} (\sqrt{p_1} - \sqrt{p_2}) \quad , \tag{6.1}$$

where the reduction factor H_d is given by

$$H_d = \frac{\ell_1 + \ell_2}{\ell_1 + \ell_2 \Phi_1 / \Phi_2} \quad . \tag{6.2}$$

If $H_d = 1$ equation (6.1) reduces to Richardson's law for an uncoated membrane.

Notice that, provided the diffusivities D_1 and D_2 do not depend on the hydrogen concentration [62], these results do not depend on the direction of permeation with respect to the position of the coating, i.e. they are the same if the coating and the metal are interchanged. This can be achieved either by imposing $p_2 > p_1$ or by interchanging the subscripts 1 and 2 in (6.1) and (6.2).

Equations (6.1) and (6.2) can also be applied to the case of plasma-driven-permeation (PDP), or more generally when hydrogen in the upstream chamber impinges on the membrane surface only in atomic form. In such a case, if the atomic flux impinging on the upstream wall is $\phi = \phi_r + \phi_i$ and the reflected fraction is ϕ_r, the upstream pressure has to be substituted for by the equivalent pressure $p_i = \phi_i / k_1$. Thus, the permeation flux becomes dependent on the permeation direction because of the term k_1. Hence, the lower k_1 the higher j_d and the membrane becomes a pump if the plasma faces a material with a low absorption rate k_1. Since $k_1 = k_2 K_s^2$, for a PDP experimental set up, the material on the plasma facing side of the membrane needs to have a large solubility and/or a large release rate constant k_2 if permeation is to be reduced. Highly pure and clean palladium would be such a material. Unfortunately, palladium has a high permeability Φ, therefore the reduction factor would probably not be small enough. This drawback can be overcome by depositing a thin layer of palladium on top of a layer of a low permeability material, itself deposited on or joined to the metallic foil.

In diffusion limited regimes, a large reduction of the permeation by means of a coated membrane relies on large thicknesses and small permeabilities of the materials constituting the membrane. For a coating, brittleness rules out large coating thicknesses, hence the burden is entirely on the permeability of the coating. As an

example, for a coating thickness $\ell_2 = 5$ μm on a metal foil having thickness $\ell_1 = 5$ mm, a reduction in the permeation by a factor of 100 requires $\Phi_1/\Phi_2 > 10^5$. In the case of TiC, roughly $\Phi_1/\Phi_2 > 10^4$ which would give $H_d < 1/11 = 0.09$.

6.1.2 Surface-limited flow on both sides of the membrane

When surface reactions entirely control the permeation through the membrane, the concentration of hydrogen in the solid phase can be assumed to vary in time through a sequence of flat spatial profiles, as the concentration gradients are instantaneously made to vanish because of high diffusivities. Concentrations are therefore only functions of time t, $c_n = c_n(t)$ and the permeation flux through the membrane is given by (1.1). Making use of the partition coefficient $k = c_1/c_2$, the steady state permeation flux is found to be

$$j_s = H_s \frac{k_1}{2} (p_1 - p_2) \quad , \tag{6.3}$$

where H_s is the reduction factor in surface-limited regimes

$$H_s = 2\frac{k_1'}{k_1 + k_1'} \quad . \tag{6.4}$$

Notice that when $H_s = 1$, (6.3) reduces to the permeation flux for a symmetric uncoated membrane. The effect of a coating is actually to break this symmetry.

As for the diffusion-limited case, (6.3) and (6.4) imply that the permeation flux is independent of the permeation direction. This again does not hold for an atomic upstream flux impinging on the membrane, or for a PDP set-up. In such a case a low absorption coating would act as a pump if placed on the plasma side of the membrane, or as a permeation barrier if placed on the downstream side.

Two limiting cases are worth considering for the reduction factor H_s:

1. if $k_1 \ll k_1'$ then $H_s = 2$ and the membrane would pump hydrogen;
2. if $k_1 \gg k_1'$ then $H_s = 2k_1'/k_1$ and the membrane would act as a permeation barrier.

In the second case, a reduction factor equal to 0.01 would require $k_1/k_1' = 200$. This is a much less demanding requirement than the equivalent for a diffusion-limited regime. By using values of k_1 for ion-beam cleaned steel reported by Grant

et al [22] together with those reported in the previous chapter for TiC deposited on the AISI 316L steel and studied at Ispra, the reduction factor takes the value $H_s = 5 \times 10^{-3} = 1/200$ at 673 K and $H_s = 9 \times 10^{-4} = 1/1100$ at 873 K.

It appears therefore that TiC would be a more effective permeation barrier in surface-limited regimes than in diffusion-limited regimes.

6.2 Possible applications

In the previous section a possible application of a low absorption coating as hydrogen permeation barrier has been suggested. It has also been shown that the same coating may act as a pump if facing a plasma in a PDP set-up. However, the analysis carried out was very simple and only restricted to extreme limiting cases where either bulk diffusion or surface reactions are dominant. Furthermore, the application was for an ideal case constituted by a metallic membrane separating either two gas phases or a plasma phase from a gas phase.

In this section, two examples of application of coatings to more realistic cases are given. They are extensions of the pump and permeation barrier cases considered in the previous section.

The first example is related to the permeation of tritium into the coolant in a NET-type[1] fusion reactor. In such a device, fusion neutrons (n) will interact with a lithium-based compound to produce tritium and helium via (n,Li) fusion reactions. Such a compound will be located in a breeding blanket, just outside the first wall enclosing the deuterium-tritium plasma. One of the current candidate lithium compounds is the eutectic alloy Pb-17Li, for which the melting point is at 508 K. Lead added to lithium in this alloy reduces the reactivity of lithium in air and acts as a neutron multiplier.

The tritium produced in the blanket will be recovered outside the toroidal chamber enclosing the plasma, as the lithium alloy will be circulated by keeping it in the liquid state at temperatures in the range 550 K - 650 K. At these temperatures, permeation of tritium into the coolant through the steel piping containing the liquid Pb-17Li alloy is really an issue to be considered. In fact, radioactive tritium can

[1]NET is the acronym of Next Experimental Torus, the next machine after JET in the european plan towards a power thermonuclear fusion reactor.

easily form tritiated water, HTO, which is 25000 times more harmful than gaseous tritium (HT or T_2), as it easily enters the human biological cycle[2]

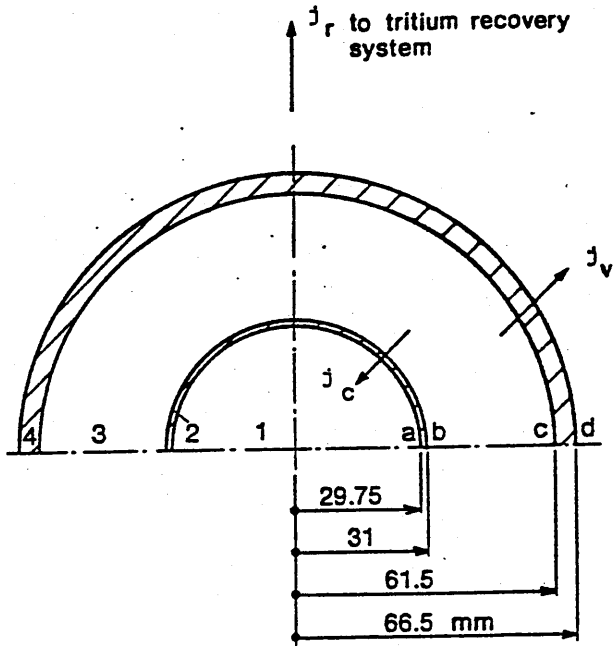

Figure 6.2 Schematic representation of a cross-section of the simplified blanket module used for numerical simulation of the permeation reduction achieved by thin coatings. Key to symbols: 1 – coolant, 2 – coolant tube, 3 – liquid breeder, 4 – external wall; j_r – tritium flux to the recovery system, j_c – tritium flux into the coolant, j_v – tritium flux to the outside (vacuum) [63].

One possible way of reducing the tritium losses to the coolant, would be to apply thin coatings having low hydrogen permeation to the metallic piping in the blanket system. This possibility has been numerically simulated at JRC Ispra [63]. Figure 6.2 shows a cross-sectional view of the simplified blanket unit used in the numerical simulation. It represents two concentric cylindrical steel tubes, between which the liquid breeder is made to flow perpendicularly to the page. The cooling water is contained in the innermost tube. The tubes are enclosed in an evacuated or helium-purged chamber. Tritium from the liquid alloy is recovered with an associated flux j_r

[2]Molecular hydrogen and tritium have a very low solubility in water and less than 0.004 per cent of inhaled tritium gas is absorbed into the body. Essentially 100 per cent of the HTO vapour inhaled is absorbed into the body and mixed uniformly to the body's water within a few hours. Tritiated water vapour in air is also quite rapidly absorbed through the skin.

outside the reactor, or permeates through the external tube wall, with an associated flux j_v, where it is recovered by helium-purging. The permeation flux j_c to the coolant through the inner tube wall has to be minimised.

The onedimensional numerical algorithm used for this simulation includes bulk diffusion in the solid walls, surface reactions at the solid/gas surface and a tritium source term in the liquid alloy to account for tritium production via (n,Li) fusion reactions. An average tritium production rate of 1.023×10^{18} atoms m^{-3} s^{-1} was used, while temperatures were 553 K in the coolant tube, 568 K in the liquid alloy and 583 K in the outer tube wall.

Solubility, diffusivity and surface rate constants determined for TiC in this thesis were used as input data in the numerical simulation. The coating thickness used was 10 μm. The results of the numerical simulation are shown in Figure 6.3, where the variation with time t of the integrated permeation flux Φ_c is presented, for different position of the coating. In that figure, two things have to be considered, namely the value of the steady state of Φ_c, which should be minimised, and the time to reach such a value. This time should be maximised.

Obviously, coating the external tube wall is ineffective, while the best solution would be coating both tubes on both surfaces, so that recovery in the external vacuum or by helium purging would not be crucial. However, this solution might be impractical from the point of view of production and very expensive. Hence, an alternative would be to coat only the coolant tube.

This simulation cannot have the final say on the problem, but it helps understanding the possible application of coatings in this area.

The second examples is related to the work by Shmayda et al [64], as already anticipated in the previous section. That work relies on the pump/compression which can be obtained when atomic hydrogen impinges on a membrane for which k_1 is low and k_1' is high. This condition can be achieved, as already mentioned, by coating with TiC the upstream side of a metallic foil. In addition, since TiC has also a low k_2, the backflow should also be low.

Such a pump/compressor would be important for use with tritium. It would in fact be tritium-compatible owing to the absence of oil and elastomers. It is reported [65] that it would also work efficiently to separate small amounts of tritium present

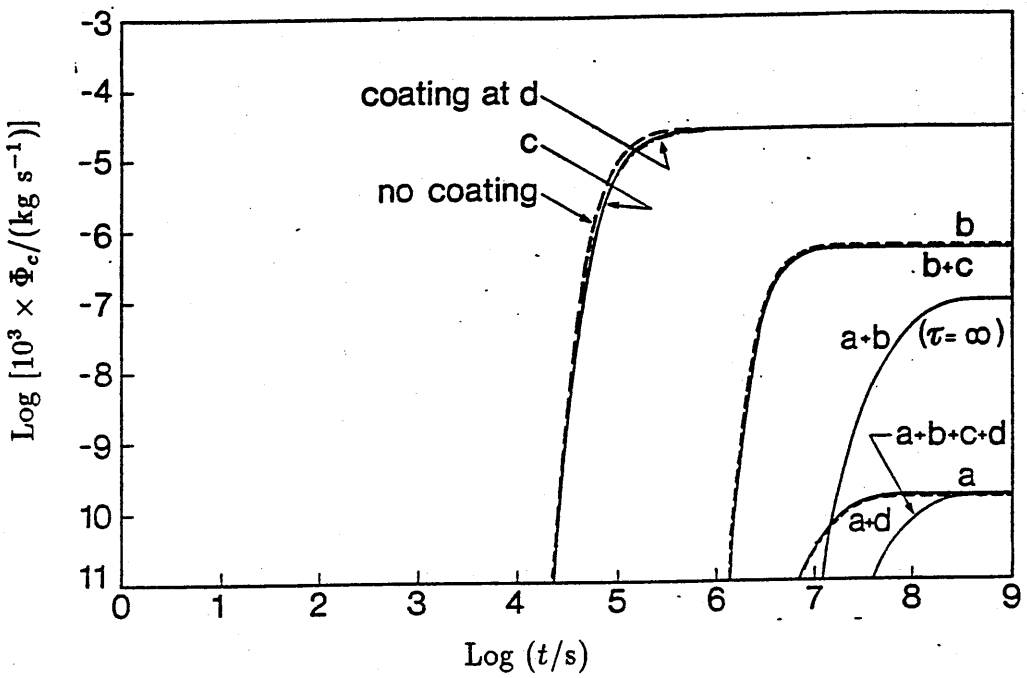

Figure 6.3 Effect of coating layers on the time dependence of the integrated tritium permeation flux Φ_c to the coolant. The position of the coating layers are indicated by the letters a,b,c,d which refer to Figure 6.2. The liquid alloy recycling time is $\tau = 10^4$ s, apart from the static case when the coating is on a and b (labelled a+b) [63].

in a tritium-helium mixture, a very important application in view of the blanket design mentioned in the previous example.

6.3 Future work

The work reported in this thesis is a first attempt at studying and modelling the interaction of hydrogen with thin carbon-based coatings deposited on metals. There is space for more work on this important topic, which is crucial in particular to plasma-wall problems in current carbon-based tokamaks first walls. If the hydrogen behaviour in the coating only is of interest, a technique such as that used at Oxford is particularly useful, because it allows one to restrict the penetration of hydrogen

to a superficial region of the solid. This type of study would be particularly useful if coupled to a study of the same materials with a gas- or plasma-driven-permeation apparatus, where the effectiveness of the data measured and the models developed could be verified and tested.

The Oxford rig can be however improved, according to the points suggested at the end of chapter 3. This type of apparatus would allow one to study transients between two equilibrium states, as it was done at Ispra, and to run volume-modulation experiments.

The difference in results found with different TiC coatings, obtained from different suppliers, suggests a strong need for either a closer collaboration with the supplier or the own production and characterisation of the coating to be studied. In addition, more reliable data might be obtained by working with one specimen with a given initial thickness which could be decreased by ion-beam milling. This type of work would be more easily carried out in a permeation apparatus, either modulated or step-like.

On the modelling side, there is a need to include bulk diffusion, surface reactions and nonlinear trapping in a single comprehensive model. This seems easier with the Oxford technique, owing to the possibility of linearising the equations defining the model, whereas it calls for numerical algorithms with the technique available at Ispra. The TZM data obtained at Ispra should also be re-analysed by means of such a model.

From the experimental viewpoint, the next step would be to run experiments at Oxford with bare TZM samples and with other coating thicknesses.

6.4 Summary

Some considerations have been put forward concerning the importance and application of the results of this work in the fusion technology area. In particular, the cases of tritium permeation reduction, of tritium purification and pumping by means of coated metallic membranes have been treated. Examples based on analytical expressions for simple surface- and diffusion-limited regimes have been given. More complex and realistic situations have to be tackled with the help of numerical al-

gorithms. One example of this kind has also been given, for the permeation of tritium to the coolant in a NET-type fusion device. Some suggestions have been given concerning possible future work.

References

[1] **G. Saibene, R. Sartori, A. Tanga, A. Peacock, M. Pick, P. Gaze, 1990**: J. Nucl. Mater., 176-177, 618

[2] **R.A. Langley, 1984**: J. Nucl. Mater., 128-129, 622

[3] **W. Möller, 1984**: in "*Physics of Plasma-Wall Interaction in Controlled Fusion*", NATO AISI series, p 439

[4] **P.M. Richards, 1988**: J. Nucl. Mater., 152, 246

[5] **J.S. Wang, 1936**: Proc. Camb. Phil. Soc., 32, 657

[6] **F. Waelbroeck, 1984**: *Influence of bulk and surface phenomena on the hydrogen permeation through metals*, KFA Jülich report Jül-1966

[7] **M.A. Pick, J.W. Davenport, M. Strongin, G.J. Dienes, 1979**: Phys. Rev. Lett., 43, 286

[8] **M.A. Pick, K. Sonnenberg, 1985**: J. Nucl. Mater., 131, 208

[9] **A. Winkler, K.D. Rendulic, 1982**: Surface Sci., 118, 19

[10] **E.I. Ko, R.J. Madix, 1981**: Surface Sci. 104, 221

[11] **A.D. Le Claire, 1983**: Permeation of Gases Through Solids, I - Principles, in "*Diffusion and Defect Data*", 33, 1

[12] **F. Waelbroeck, I. Ali-Khan, K.J. Dietz, P. Wienhold, 1979**: J. Nucl. Mater. 85-86, 345

[13] **J. Crank, 1975**: *The Mathematics of Diffusion*, Oxford University Press

[14] **M. Caorlin, 1984**: Tesi di laurea in Fisica, Università degli Studi di Milano, a.a. 1982-1983 (unpublished)

[15] **D.F. Sherman, D.R. Olander, 1989**: J. Nucl. Mater., 166, 307

[16] **P.M. Richards, S.M. Myers, W.R. Wampler, D.M. Follstaedt, 1989**: J. Appl. Phys., 65, 180

[17] **H.R. Ihle, C.H. Wu, 1984**: J. Nucl. Mater., 122-123, 901

[18] **H. Katsuta, S. Konishi, H. Yoshida, 1983**: J. Nucl. Mater., 116, 244

[19] **R.D. Siegel, R.W. Coughlin, 1970**: J. Appl. Polym. Sci., 4, 3145

[20] **K.S. Forcey, D.K. Ross, J.C.B. Simpson, D.S. Evans, 1988**: J. Nucl. Mater., 160, 117

[21] **F. Reiter, J. Camposilvan, M. Caorlin, G. Saibene, R. Sartori, 1985**: Fus. Technol., 8, 2344

[22] **D.M. Grant, D.L. Cummings, D.A. Blackburn, 1988**: J. Nucl. Mater., 152, 139

[23] **M. Yamawaki, K. Yamaguchi, S. Tanaka, T. Namba, T. Kiyoshi, Y. Takahashi, 1989**: J. Nucl. Mater., 162-164, 1071

[24] **Metallwerk Plansee, 1986**: *TZM, A High Temperature Molybdenum Alloy*, Metallwerk Plansee GmbH technical note, Reutte-Tirol, Austria

[25] **E. Zolti, 1988**: J. Nucl. Mater., 155-157, 386

[26] **M.I. Baskes, A.E. Pontau, K.L. Wilson, W.L. Barr, 1984**: J. Nucl. Mater., 122-123, 1511

[27] **G.R. Caskey, M.R. Louthan, R.G. Derrick, 1975**: J. Nucl. Mater., 55, 279

[28] **H. Katsuta, R.B. McLellan, K. Furukawa, 1982**: J. Phys. Chem. Solids, 43, 533

[29] **A.P. Zakharov, V.M. Sharapov, E.I. Evko, 1975**: Sov. Mat. Sci., 9, 149

[30] **W.A. Oates, R.B. McLellan, 1972**: Scr. Metall., 6, 349

[31] **T. Eguchi, S. Morozumi, 1974**: Nippon Kinzoku Gakkaishi, 38, 1019

[32] **H. Katsuta, R.B. McLellan, 1979**: J. Phys. Chem. Solids, 40, 845

[33] **C.L. Huffine, J.M. Williams, 1960**: Corrosion, 16, 430t

[34] **T. Noda, M. Okada, 1987**: Trans. JIM, 28, 517

[35] **A. Semeniuk, G.R. Brady, 1974**: Weld. J., 53, 454s

[36] **R.A. Causey, J.D. Fowler, C. Ravanbakht, T.S. Elleman, K. Verghese, 1978**: J. Amer. Cer. Soc., 61, 221

[37] **M. Kitajima, M. Fukutomi, A. Hasegawa, M. Okada, 1986**: J. Nucl. Mater., 141-143, 234

[38] **K. Verghese, L.R. Zumwalt, C.P. Feng, T.S. Elleman, 1979**: J. Nucl. Mater., 85-86, 1161

[39] **H. Katsuta, Y. Katano, T. Morita, S. Tanaka, 1986**: Proc. Int. Symp. on Fusion Reactor Blanket and Fuel Cycle Engineering, Tokai-mura, Tokyo, p. 233

[40] **M.P. Riehm, W.W. Smeltzer, D.A. Thompson, 1986**: CFFTP Rep. No. G-86041

[41] **K. Sone, Y. Murakami, 1984**: J. Nucl. Mater., 121, 254

[42] **B.M. Kramer, 1983**: Thin Solid Films, 108, 117

[43] **L. E. Toth, 1971**: *Transition Metal Carbides and Nitrides*, Academic Press, New York

[44] **J.F. Lynch, et al., 1966**: *Engineering Properties of Selected Ceramic Materials*, Am. Cer. Soc. Publ., Columbus, Ohio

[45] **H. Preston-Thomas, Ed., 1976**: Metrologia, 12, 7

[46] **P.R. Bevington, 1969**: *Data Reduction and Error Analysis for the Physical Sciences*, McGraw-Hill

[47] **Cragoe, 1948**: Procés Verbaux Comité Int. Poids Mésures, 21,T84

[48] **J.P. Pratt, D.C. Ailion, 1969**: Rev. Sci. Instr., 40, 1614

[49] **R. Matera, 1984**: *AISI 316 Reference Book*, Technical Note No. I.07.B1.84.62, CEC - JRC Ispra

[50] **D.L. Cummings, D.A. Blackburn, 1987**: J. Nucl. Mater., 144, 81

[51] **W. Eichenauer, 1960**: Mem. Sci. Rev. Met., LVII, 943

[52] **P. Lin, et al, 1987**: J. Vac. Sci. Technol. A, 5, 2372

[53] **H.S. Carslaw, J.C. Jaeger, 1959**: *Conduction of Heat in Solids*, Oxford University Press

[54] **J.C. Jaeger, 1941**: Phil. Mag., 32, 324

[55] **M. Caorlin, 1992**: internal report, The Open University, in preparation

[56] **G.L. Powell, 1974**: in "*Hydrogen in Metals*", ASM, Bernstein, Thompson eds., p 585

[57] **H.A. Jehn, K.K. Schulze, 1985**: in "*Physical Metallurgy and Technology of Molybdenum and its Alloys*", AMAX Special. Metals Corp., 131, 208

[58] **E. Best, I. Hinz, 1983**: Molybdenum: Metal. Chemical Reactions, in "*Gmelin Handbook of Inorganic Chemistry*", Springer Verlag, 53 A3, 121

[59] **V. Seshadri, S.P. Mehrotra, E.A. Villegas, 1980**: Metal ABM, 36, 653

[60] **T. Tanabe, Y. Furuyama, N. Saitoh, S. Imoto, 1987**: Trans. JIM, 28, 706

[61] **J.W. Guthrie, L.C. Beavis, D.R. Begeal, W.G. Perkins, 1974**: J. Nucl. Mater., 53, 313

[62] **R. Ash, R. M. Barrer, 1959** : Phil. Mag., 4, 1197

[63] **F. Reiter, 1989**: private communication

[64] **W.T. Shmayda, F. Waelbroeck, J. Winter, P. Wienhold, T. Banno, N.P. Kherani, 1985**: Fus. Technol., 8, 2285

[65] **W.T. Shmayda, N.P. Kherani, 1987**: private communication